THE UNIVERSITY OF CHICAGO

RARE EARTH ISOTOPE VARIATIONS AND IMPLICATIONS FOR THE EVOLUTION OF THE EARLY SOLAR SYSTEM

A DISSERTATION SUBMITTED TO

THE FACULTY OF THE DIVISION OF THE PHYSICAL SCIENCES

IN CANDIDACY FOR THE DEGREE OF

DOCTOR OF PHILOSOPHY

DEPARTMENT OF THE GEOPHYSICAL SCIENCES

BY

JINGYA HU

CHICAGO, ILLINOIS

AUGUST 2021

TABLE OF CONTENTS

LIST OF FIGURES

LIST OF TABLES

ACKNOWLEDGEMENT

I would like to first thank my advisor, Nicolas Dauphas, not only for the knowledge and skills that I have learned during my PhD but also for the attitude towards research: following questions with deep, long-lasting impacts on our understanding of the Earth and the solar system, and answering the questions with carefully designed experiments and well-thought-out modeling. I am deeply grateful for the energy and time he spent on guiding me. His office door is always open. I can drop by anytime whenever I get any questions and challenges. Thanks for his insightful suggestions, I have never left his office disappointedly.

I would like also to express my sincere thanks to the members of my committee, Andrew Davis, Fred Ciesla, and Andrew Campbell, for both the insightful comments on career development and valuable discussion in research. The comments and discussion is very useful and points out the direction that I need to make improvement.

I would like to extend my thanks to my collaborator and Collegues, Reika Yokochi, Ruslan Mendybaev, Mathieu Roskosz, Thomas Ireland, Bruce Charlier, Esen Alp, Michael Hu, and Jiyong Zhao, Lawrence Grossman, Douglas MacAyeal, Dorian Abbot, Philipp Heck, Richard Lyons, Krysten Villalon, Hailu Kong, Jennika Greer, Ziwei Wang, Xin Yang, Bowen Fan, Fei Wu, Xiufeng Ma, Yuchen Liu, Hong Yang. I enjoy the time we have spent on the research topics and look forward to more exciting discoveries.

I am grateful to the previous and current administrative staff, Brian Lynch, David Taylor, James Eason, Susan Hubbard, Jolene Hanchar, Sarah Lippert, Victor Gavin.

I would like also to thank my former and current colleagues at the Origins Lab, Christoph Burkhardt, Haolan Tang, Corliss Sio, Nicolas Greber, Francois Tissot, Sarah Aarons, Xike Nie, Timo Hopp, Aleisha Johnson, Xi Chen, Andrew Heard, Hao Zeng, Matous Ptacek, Zhe Zhang, Xinyi Liu, and Andrew Regula.

Finally, I would like to acknowledge my family for supporting me over these years, Conghuan Hu, and Mingyu Wang.

ABSTRACT

The depletion in both the most volatile and most refractory rare earth elements (REEs) in meteoritic refractory inclusions known as group II calcium-, aluminum-rich inclusions (CAIs), was originally thought to be a direct manifestation of high-temperature (over 1700 K) solar nebula condensation.

In this scenario, the fractionation in REE abundances arose from: (1) partial equilibrium condensation and removal of the most refractory REEs in ultrarefractory grains prior to CAI formation; (2) complete condensation of the moderately refractory REEs in CAIs; and (3) incomplete condensation of the most volatile REEs (Eu and Yb) that remained in the gas until after CAIs formed.

The stable isotopic compositions of 8 REEs (Ce, Nd, Sm, Eu, Gd, Dy, Er, Yb) in 8 CAIs (7 with highly fractionated group II REE abundance patterns) are measured to unravel the evaporation/condensation processes that those CAIs experienced. Contrary to expectation for the equilibrium condensation scenario outlined above, significant light isotope enrichment has been found for the most refractory REEs and more subdued isotopic variations for the less refractory REEs. This suggests that group II CAIs formed by a two-stage process involving fast evaporation of pre-existing materials, followed by near-equilibrium recondensation.

The astrophysical context where this could have happened is uncertain, but could have involved episodic intense heating in one or several energetic events akin to EX Lupi type outbursts of eruptive pre-main-sequence stars.

In Chapter 2, I introduce the principle of the double-spike (DS) technique and discuss the correction of DS in the presence of isotopic anomalies. In Chapter 3, Analytical methods for REE isotope analyses are discussed. A series of geostandards were measured using DS technique to define the REE isotopic compositions of the bulk silicate Earth. In Chapter 4, the range of equilibrium isotopic fractionation of Eu and Dy in nature is estimated using the synchrotron technique of nuclear resonance inelastic X-ray scattering (NRIXS) and *Ab initio* calculations. The equilibrium fractionation factors of Eu and Dy are extrapolated to all REEs to estimate the range of REE equilibrium isotopic fractionation in nature including the nebular condition. In Chapter 5, REE isotopic compositions in 8 CAIs are reported. The REE isotopic fractionations are discussed. The timescale of the event responsible for the CAI formation is estimated based on modeling.

1. INTRODUCTION

1.1. The Challenge of Chondritic Earth Assumption

A cornerstone of cosmochemistry and early solar system chronology is the assumption that refractory lithophile elements (RLEs; *e.g.*, Al, Ca, Sc, Ti, Y, Zr, Hf, lanthanides) are in "chondritic" proportions in planetary bodies (Allègre et al., 1995a; McDonough and Sun, 1995). However, discoveries of the isotopic anomalies for a variety of refractory lithophile elements (*e.g.*, Ti: Niederer et al., 1980, 1985; Trinquier et al., 2009; Zhang et al., 2011; lanthanides: Schönbächler et al., 2003; Andreasen and Sharma, 2007; Carlson et al., 2007; Simon et al., 2009; Ca: Chen et al., 2010; Dauphas et al., 2014; Zr: Akram et al., 2015; Albalat et al., 2015), Ca stable isotopic fractionation (Simon et al., 2009; Valdes et al., 2014), and Tm abundance anomalies (Dauphas and Pourmand, 2015; Barrat et al., 2016) in chondrites indicate that, to some extent, refractory lithophile elements are not uniformly distributed. Some of these signatures were most likely produced by thermal processing and associated evaporation/condensation processes. This is evidenced by the enriched light Ca isotope composition (Huang et al., 2012) and large chemical fractionation among rare earth elements in group II calcium-aluminum-rich inclusions (CAIs; Boynton, 1975; Davis and Grossman, 1979).

1.2. Geochemical Behaviors of the Rare Earth Elements

The rare earth elements (REEs) are a group of RLEs with similar chemical properties that exhibit a significant range in terms of volatilities. Rare earth elements condense early in the evolution of the solar nebula, partitioning into solid solutions of refractory minerals such as hibonite and perovskite (Boynton, 1975; Davis and Grossman, 1979; Lodders, 2003). Hibonite

first appears at 1742 K in solar nebula condition. Most heavy REEs (Gd, Tb, Dy, Ho, Er, Tm, and Lu; most refractory REEs) partition into hibonite at approximately 1659 K, followed by the condensation of light REEs (La, Pr, Nd, Sm; moderately refractory REEs) from 1602 K to 1478 K (Lodders, 2003). The most volatile REE are Eu and Yb, which condensed at 1356 K and 1487 K respectively. The whole set of REEs covers a substantial range of volatilities, with 50% condensation temperatures ranging from 1356 K to 1659 K.

The chemical properties and geochemical behaviors of REEs are commonly controlled by their ionic radii, which decrease with increasing atomic numbers, a phenomenon known as lanthanide contraction. In addition to ionic radii, the relative volatility of each REE also influences their species presenting in solid and gas (Boynton, 1975; Davis and Grossman, 1979). However, the relative volatilities are not a smooth function of ionic radius. Most lanthanides show trivalent states as solids and exist as monoxides (La, Pr, Nd, Sm, Gd, Tb, Dy, Er and Lu) in nebular gas. The equilibrium reaction of these REEs between solid and gas can be written as:

$$\mathrm{LnO(g)} + \frac{1}{2}\mathrm{O(g)} = \mathrm{LnO_{1.5}(s)}, \qquad (1.1)$$

where $\mathrm{LnO(g)}$ is the monoxide of REEs in the gas, $\mathrm{LnO_{1.5}(s)}$ refers to the lanthanides that partition into minerals (*e.g.*, hibonite), and $\mathrm{O(g)}$ is the gas-phase carrying oxygen (*e.g.*, water vapor). Increasing oxygen fugacity can generally make REEs more refractory, but the volatility of REEs, relative to each other, is not affected. Increasing oxygen fugacity drives all equilibrium reactions like Eq. 1.1 to the right to roughly the same extent.

The exceptions are Ce, Eu, Yb and Tm, for which the most abundant gas and solid species are not monoxides and sesquioxides, respectively. Cerium tends to form tetravalent ions in oxidizing environments. A substantial amount of CeO_2 is able to exist in either gas or solid in the condensation from solar system composition (Davis et al., 1982). The dominant reactions are

$$CeO_2(g) = CeO_{1.5}(s) + \frac{1}{2}O(g), \qquad (1.2)$$

$$CeO_2(g) = CeO_2(s). \qquad (1.3)$$

The preference for forming tetravalent ions makes Ce react in a direction opposite to most REEs when the oxygen fugacity changes: increasing oxygen fugacity decreases the volatility of most lanthanides, but increases or does not affect the volatility of Ce. This, in turn, gives rise to Ce negative anomalies in the evaporated residues or condensates under oxidizing environments. Europium, on the other hand, tends to exhibit divalent states under reducing environments in solid (Lodders, 2003). In the gas, Eu is present in monoatomic form in equilibrium condensation from a gas of the solar composition. Decreasing oxygen fugacity generally makes Eu more volatile than neighboring REEs and leads to negative Eu abundance anomalies in the REE patterns. Ytterbium behaves like Eu but is slightly more refractory compared to Eu. Thulium is mostly monatomic in solar composition gas. As oxygen fugacity is increased, Tm becomes more refractory compared to Eq. 1.1,

$$Tm(g) + \frac{3}{2}O(g) = TmO_{1.5}(s). \qquad (1.4)$$

1.3. CAIs with Group II REE Patterns

Calcium-aluminum-rich inclusions are widely distributed in different groups of chondrites, with the abundance varying from <0.1 to ~3 vol% (McSween, 1977; Hezel et al., 2008). CAIs are mainly composed of the minerals that are predicted to condense from a cooling gas of solar composition at temperatures 1300-1450 K and total pressure of 10^{-5} to 10^{-3} bar, a composition similar to the first 5% of condensates from the nebular gas based on equilibrium condensation calculations (Grossman, 1972; Grossman et al., 2000). The extremely old age (4.56 Ga; Allègre et al., 1995b; Amelin et al., 2002; Amelin et al., 2009; Amelin et al., 2010) and the existence of isotopic anomalies (*e.g.*, Birck and Lugmair, 1988; Chen et al., 2010; Fahey et al., 1987; Huang et al., 2012; Leya et al., 2009; Loss and Lugmair, 1990; Niederer and Papanastassiou, 1984) suggest that CAIs are among the most primitive materials preserved in the solar system.

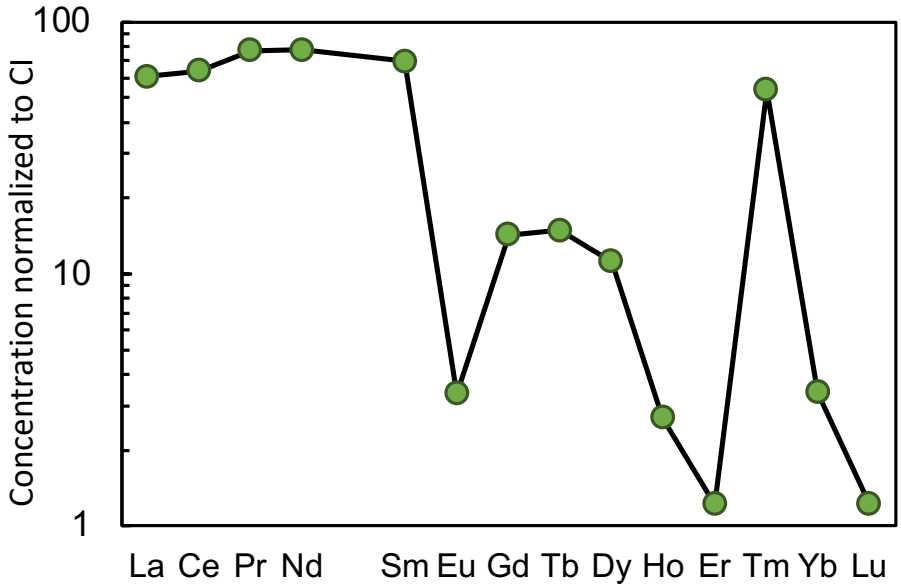

Figure 1.1 Typical REE pattern of a group II CAI from Allende meteorite (FG-FT-8; Tissot et al. 2016).

Calcium-aluminum-rich inclusions with group II REE patterns were first discovered by Tanaka and Masuda (1973), in the pink portion of a CAI in Allende. This kind of REE pattern was later found in many CAIs, most commonly of the fine-grained CAIs that are widely distributed in most chondrite varieties. These group II REE patterns are characterized by a relative depletion in the most refractory REEs (heavy REEs Gd-Lu with the exception of Tm and Yb), a uniform enrichment in moderately refractory REEs (Tm and light REEs La-Sm), and a depletion in the most volatile REEs (Eu and Yb). Thulium, which is of intermediate refractoriness, shows up as a prominent positive anomaly, relative to the neighbor HREEs which are either more volatile (Yb) or more refractory (most of the heavy REEs). Europium, which is more volatile than neighbor LREEs, shows up as a prominent negative anomaly (Mason and Taylor, 1982). These group II REE patterns are thought to represent a snapshot in the condensation sequence, whereby the most refractory and most volatile REEs are depleted, and only those REEs of intermediate refractoriness are present in their full complement (Boynton, 1975; Davis and Grossman, 1979; Kornacki and Fegley, 1986).

Calcium-aluminum-rich inclusions with group II REE patterns have a history of thermal processing that can be tracked by the highly fractionated REE patterns. Such a pattern can be produced by either condensation or evaporation (Boynton, 1975; Davis and Grossman, 1979). A close look at isotope composition of REEs in CAIs can help to distinguish these two scenarios. Among REEs, Ce and Eu bears more than one valence state and is sensitive to change of redox states (Drake, 1975; Evensen et al., 1978). Studies on Ce and Eu isotope composition can improve our comprehension on redox conditions of the solar system at the time of CAI formation. Many other RLEs (*e.g.*, Ca, Ti, Ba) have 50% condensation temperatures that overlap with the volatility

range of REEs (approximately 1356-1659 K; Lodders, 2003). The geochemical behaviors of these RLEs are likely influenced by the thermal processes that also control the isotopic fractionations of REEs. This has important consequences for estimating the budgets of heat producing elements in planets and for early solar system chronology (ratios of RLEs such as Lu/Hf and Sm/Nd are often assumed to be chondritic at a bulk scale).

The discovery of Tm abundance anomaly in REE patterns (Dauphas and Pourmand, 2015; Barrat et al., 2016), Ca stable isotope fractionation (Simon et al., 2009; Valdes et al., 2014), and various isotopic anomalies (Warren, 2011) documented in a series of elements suggest the existence of heterogeneity in the bulk meteorite level. In particular, carbonaceous chondrites (with the exception of CO chondrites) show difference from other groups of chondrites as well as the bulk Earth. Such difference can be due to the heterogeneous distribution of interplanetary dust which has a composition similar to group II CAIs. If this is the case, potential REE isotope signatures produced in early condensation/evaporation processes may also be inherited in different planetary bodies.

1.4. Isotope Analyses of Rare Earth Elements

Despite the scientific merits and enormous potential of REE isotope systematics in early solar system studies, analyzing the stable isotope fractionation of the whole set of REEs is challenging. The challenge partially arises from the lack of an efficient and clean approach for separating each REE. Although many approaches have been developed and refined to separate REEs from each other through either traditional column chemistry or the HPLC system (*e.g.*, Gast et al., 1970; Strelow and Jackson, 1974; Crock et al., 1984; Baker et al., 2002; Pourmand et al., 2012), these approaches are only suitable for bulk concentration data. They cannot be applied to

high precision isotope analyses, due to potential isobaric interferences. Thus, present measurements on REE isotopic fractionations have been compromised by either focusing on a single REE of interest, or by separating all REEs through multiple columns (e.g., Moynier et al., 2006; Albalat et al., 2015). The former may overlook potentially valuable information preserved in REE isotopes, while the latter is rather time-consuming and introduces unnecessary tedious work in isotope analyses. Even only focusing on one element, a clean separation with a high yield can still be challenging due to the similar characteristics of REEs in resin.

Another concern is the precision of the REE isotope analyses. Due to the high mass number of REEs, the predicted mass-dependent fractionation that may occur in the solar nebula is on the order of ‰ or sub ‰ level. Such small isotope variations can be easily masked by laboratory-produced isotopic fractionation during sample processing and instrumental analyses (Albarède and Beard, 2004). Many current studies on REE isotope analyses focus on radiogenic effects and isotopic anomalies, which can be properly corrected by internal normalization, assuming a constant value of a certain isotope ratio. However, for stable isotopic fractionation, low yields in REE separation and the status of mass spectrometry can both affect the precision and accuracy of REE isotope analysis. This makes it difficult to detect the subtle isotope variations in samples. Because of the challenge on isotope analyses of REEs, a systematic survey on the isotopic compositions of the REEs in the terrestrial rocks is lacking, which hinders our understanding on the isotopic composition of the bulk silicate Earth. The isotopic compositions of the bulk silicate Earth for REEs also have important bearings in interpreting the isotopic fractionation of extraterrestrial samples such as CAIs.

1.5. Equilibrium Fractionation Estimation of REEs Using NRIXS

The europium abundance anomaly relative to neighboring REEs (*i.e.*, Sm and Gd) has long been used as an indicator of reducing environments. The magnitudes of Eu abundance anomalies are not only controlled by the valence states of Eu but also depends on the behaviors of the neighboring REEs, hindering the possibility of a more quantitative interpretation. A potentially more reliable choice is to use Eu stable isotope fractionation as a new proxy for redox change. The NRIXS technique provides a unique insight into Eu stable isotopic fractionation by directly measuring the strength of the chemical bonds (*i.e.*, the mean force constant) of Mössbauer isotope ^{151}Eu, which controls the equilibrium isotopic fractionation between co-existing phases. Another REE isotope that can be measured by NRIXS is ^{161}Dy. Analyzing pure oxide, minerals, and synthesized glass samples of igneous composition provide insights into equilibrium fractionations that can happen in nature. The fractionation factors determined by NRIXS can be used to estimate the extent of equilibrium fractionation that happen during the condensation and evaporation in the early solar system and help to distinguish equilibrium and kinetic fractionation in the CAIs.

1.6. Isotopic Compositions of REE Isotopes in CAIs for Tracking Heating Events in the Early Solar System

The prevalent view on the REE patterns of the group II CAIs is that the nebular gas experienced a prior condensation of ultra-refractory phases in equilibrium with the ambient gas before a complete condensation of REEs except for the least refractory ones. If this snapshot scenario were correct, one would expect relatively restricted stable isotopic fractionations in the group II CAIs that were mainly caused by equilibrium fractionation. In the case that kinetic process

has played a role, the prior ultrarefractory phase would be enriched in light isotopes for refractory REEs, leaving behind a gas residue enriched in heavy isotopes to form the group II CAIs. The condensation origin of group II CAIs has been the cornerstone to support the equilibrium condensation view of the solar nebula.

This scenario can be tested by analyzing the REE stable isotopic fractionations in the group II CAIs. The depletion levels of the REE and the isotopic fractionation can be used to determine the timescales of the evaporation or condensation that are responsible for the CAI formation, which can help to pin down to the astrophysical setting of the CAI formation.

1.5. References

Akram, W., Schönbächler, M., Bisterzo, S., Gallino, R., 2015. Zirconium isotope evidence for the heterogeneous distribution of s-process materials in the solar system. Geochimica et Cosmochimica Acta 165, 484-500.

Albalat, E., Blichert-Toft, J., Telouk, P., Albarède, F., 2015. The lunar neutron energy spectrum inferred from the isotope compositions of rare-earth elements and hafnium in Apollo samples. Earth and Planetary Science Letters 429, 147-156.

Albarède, F., Beard, B., 2004. Analytical methods for non-traditional isotopes. Reviews in mineralogy and geochemistry 55, 113-152.

Allègre, C.J., Poirier, J.-P., Humler, E., Hofmann, A.W., 1995a. The chemical composition of the Earth. Earth and Planetary Science Letters 134, 515-526.

Allègre, C.J., Manhès, G., Göpel, C., 1995b. The age of the Earth. Geochimica et Cosmochimica Acta 59, 1445-1456.

Amelin, Y., Krot, A.N., Hutcheon, I.D., Ulyanov, A.A., 2002. Lead isotopic ages of chondrules and calcium-aluminum-rich inclusions. Science 297, 1678-1683.

Amelin, Y., Connelly, J., Zartman, R., Chen, J., Göpel, C., Neymark, L., 2009. Modern U–Pb chronometry of meteorites: Advancing to higher time resolution reveals new problems. Geochimica et Cosmochimica Acta 73, 5212-5223.

Amelin, Y., Kaltenbach, A., Iizuka, T., Stirling, C.H., Ireland, T.R., Petaev, M. and Jacobsen, S.B., 2010. U–Pb chronology of the Solar System's oldest solids with variable 238U/235U. Earth and Planetary Science Letters, 300(3-4), pp.343-350.

Andreasen, R., Sharma, M., 2007. Mixing and homogenization in the early solar system: clues from Sr, Ba, Nd, and Sm isotopes in meteorites. The Astrophysical Journal 665, 874.

Baker, J., Waight, T., Ulfbeck, D., 2002. Rapid and highly reproducible analysis of rare earth elements by multiple collector inductively coupled plasma mass spectrometry. Geochimica et Cosmochimica Acta 66, 3635-3646.

Barrat, J.-A., Dauphas, N., Gillet, P., Bollinger, C., Etoubleau, J., Bischoff, A., Yamaguchi, A., 2016. Evidence from Tm anomalies for non-CI refractory lithophile element proportions in terrestrial planets and achondrites. Geochimica et Cosmochimica Acta 176, 1-17.

Birck, J.L., Lugmair, G., 1988. Nickel and chromium isotopes in Allende inclusions. Earth and Planetary Science Letters 90, 131-143.

Boynton, W.V., 1975. Fractionation in the solar nebula: condensation of yttrium and the rare earth elements. Geochimica et Cosmochimica Acta 39, 569-584.

Carlson, R.W., Boyet, M., Horan, M., 2007. Chondrite barium, neodymium, and samarium isotopic heterogeneity and early earth differentiation. Science 316, 1175-1178.

Chen, H., Chen, J., Lee, T., Shen, J., 2010. Calcium isotopic anomalies in the Allende CAIs and the angrite Angra dos Reis, Lunar and Planetary Science 41, #2088.

Connelly, J.N., Bizzarro, M., Krot, A.N., Nordlund, Å., Wielandt, D. and Ivanova, M.A., 2012. The absolute chronology and thermal processing of solids in the solar protoplanetary disk. Science, 338(6107), pp.651-655.

Crock, J., Lichte, F., Wildeman, T., 1984. The group separation of the rare-earth elements and yttrium from geologic materials by cation-exchange chromatography. Chemical Geology 45, 149-163.

Dauphas, N., Chen, J.H., Zhang, J., Papanastassiou, D.A., Davis, A.M., Travaglio, C., 2014. Calcium-48 isotopic anomalies in bulk chondrites and achondrites: Evidence for a uniform isotopic reservoir in the inner protoplanetary disk. Earth and Planetary Science Letters 407, 96-108.

Dauphas, N., Pourmand, A., 2015. Thulium anomalies and rare earth element patterns in meteorites and Earth: Nebular fractionation and the nugget effect. Geochimica et Cosmochimica Acta 163, 234-261.

Davis, A.M., Grossman, L., 1979. Condensation and fractionation of rare earths in the solar nebula. Geochimica et Cosmochimica Acta 43, 1611-1632.

Davis, A.M., Tanaka, T., Grossman, L., Lee, T., Wasserburg, G., 1982. Chemical composition of HAL, an isotopically-unusual Allende inclusion. Geochimica et Cosmochimica Acta 46, 1627-1651.

Drake, M.J., 1975. The oxidation state of europium as an indicator of oxygen fugacity. Geochimica et Cosmochimica Acta 39, 55-64.

Evensen, N.M., Hamilton, P., O'nions, R., 1978. Rare-earth abundances in chondritic meteorites. Geochimica et Cosmochimica Acta 42, 1199-1212.

Fahey, A., Goswami, J., McKeegan, K., Zinner, E., 1987. ^{26}Al, ^{244}Pu, ^{50}Ti, REE, and trace element abundances in hibonite grains from CM and CV meteorites. Geochimica et Cosmochimica Acta 51, 329-350.

Gast, P., Hubbard, N., Wiesmann, H., 1970. Chemical composition and petrogenesis of basalts from Tranquillity Base. Proceedings of the Apollo 11 Lunar Science Conference, 1143-1163.

Grossman, L., 1972. Condensation in the primitive solar nebula. Geochimica et Cosmochimica Acta 36, 597-619.

Grossman, L., Ebel, D.S., Simon, S.B., Davis, A.M., Richter, F.M., Parsad, N.M., 2000. Major element chemical and isotopic compositions of refractory inclusions in C3 chondrites: The separate roles of condensation and evaporation. Geochimica et Cosmochimica Acta 64, 2879-2894.

Hezel, D.C., Russell, S.S., Ross, A.J., Kearsley, A.T., 2008. Modal abundances of CAIs: Implications for bulk chondrite element abundances and fractionations. Meteoritics & Planetary Science 43, 1879-1894.

Huang, S., Farkaš, J., Yu, G., Petaev, M.I., Jacobsen, S.B., 2012. Calcium isotopic ratios and rare earth element abundances in refractory inclusions from the Allende CV3 chondrite. Geochimica et Cosmochimica Acta 77, 252-265.

Kornacki, A.S., Fegley, B. Jr., 1986. The abundance and relative volatility of refractory trace elements in Allende Ca, Al-rich inclusions: implications for chemical and physical processes in the solar nebula. Earth and Planetary Science Letters 79, 217-234.

Leya, I., Schoenbaechler, M., Kraehenbuehl, U., Halliday, A.N., 2009. New titanium isotope data for Allende and Efremovka CAIs. The Astrophysical Journal 702, 1118-1126.

Lodders, K., 2003. Solar system abundances and condensation temperatures of the elements. The Astrophysical Journal 591, 1220-1247.

Loss, R., Lugmair, G., 1990. Zinc isotope anomalies in Allende meteorite inclusions. The Astrophysical Journal 360, L59-L62.

Mason, B., Taylor, S.R., 1982. Inclusions in the Allende meteorite. Smithsonian Contributions to the Earth Sciences 25, 1-30.

McDonough, W.F., Sun, S.-S., 1995. The composition of the Earth. Chemical Geology 120, 223-253.

McSween, H.Y. Jr., 1977. Petrographic variations among carbonaceous chondrites of the Vigarano type. Geochimica et Cosmochimica Acta 41, 1777-1790.

Moynier, F., Bouvier, A., Blichert-Toft, J., Telouk, P., Gasperini, D., Albarede, F., 2006. Europium isotopic variations in Allende CAIs and the nature of mass-dependent fractionation in the solar nebula. Geochimica et Cosmochimica Acta 70, 4287-4294.

Niederer, F., Papanastassiou, D., Wasserburg, G., 1980. Endemic isotopic anomalies in titanium. Astrophysical Journal Letters 240, L73-L77.

Niederer, F., Papanastassiou, D., Wasserburg, G., 1985. Absolute isotopic abundances of Ti in meteorites. Geochimica et Cosmochimica Acta 49, 835-851.

Niederer, F.R., Papanastassiou, D., 1984. Ca isotopes in refractory inclusions. Geochimica et Cosmochimica Acta 48, 1279-1293.

Pourmand, A., Dauphas, N., Ireland, T.J., 2012. A novel extraction chromatography and MC-ICP-MS technique for rapid analysis of REE, Sc and Y: Revising CI-chondrite and Post-Archean Australian Shale (PAAS) abundances. Chemical Geology 291, 38-54.

Schönbächler, M., Lee, D.-C., Rehkämper, M., Halliday, A.N., Fehr, M.A., Hattendorf, B., Günther, D., 2003. Zirconium isotope evidence for incomplete admixing of r-process components in the solar nebula. Earth and Planetary Science Letters 216, 467-481.

Simon, J.I., DePaolo, D.J., Moynier, F., 2009. Calcium isotope composition of meteorites, Earth, and Mars. The Astrophysical Journal 702, 707-715.

Strelow, F.W.E., Jackson, P., 1974. Determination of trace and ultratrace quantities of rare earth elements by ion exchange chromatography-mass spectrography. Analytical Chemistry 46, 1481-1486.

Tanaka, T., Masuda, A., 1973. Rare-earth elements in matrix, inclusions, and chondrules of the Allende meteorite. Icarus 19, 523-530.

Tissot, F.L.H., Dauphas, N., Grossman, L., 2016. Origin of uranium isotope variations in early solar nebula condensates. Science Advances 2, #e1501400 (7pp).

Trinquier, A., Elliott, T., Ulfbeck, D., Coath, C., Krot, A.N., Bizzarro, M., 2009. Origin of nucleosynthetic isotope heterogeneity in the solar protoplanetary disk. Science 324, 374-376.

Valdes, M.C., Moreira, M., Foriel, J., Moynier, F., 2014. The nature of Earth's building blocks as revealed by calcium isotopes. Earth and Planetary Science Letters 394, 135-145.

Warren, P.H., 2011. Stable-isotopic anomalies and the accretionary assemblage of the Earth and Mars: A subordinate role for carbonaceous chondrites. Earth and Planetary Science Letters 311, 93-100.

Zhang, J., Dauphas, N., Davis, A.M., Pourmand, A., 2011. A new method for MC-ICPMS measurement of titanium isotopic composition: Identification of correlated isotope anomalies in meteorites. Journal of Analytical Atomic Spectrometry 26, 2197-2205.

2. PRINCIPLE OF DOUBLE-SPIKE DATA REDUCTION AND CORRECTION IN THE PRESENCE OF ISOTOPIC ANOMALIES

2.1. Introduction

Non-traditional stable isotope systems refer to elements that are measured for variations in their non-radiogenic isotopic compositions by instruments other than gas-source mass spectrometers. The last two decades have seen an explosion in the use of these systems to address very diverse topics, ranging from human diseases to solar nebula evolution (Teng et al., 2017, and references therein). Natural isotope variations of heavy elements, however, are subtle and can be easily masked by artificial fractionation produced during sample processing and mass spectrometry. For example, incomplete recovery during column chromatography can impart large isotopic fractionation and the presence of matrix elements can affect instrumental bias in both Multi Collector Inductively Plasma Mass Spectrometers (MC-ICPMS) and Thermal Ionization Mass Spectrometers (TIMS). TIMS has long been the instrument of choice for high precision isotopic analyses, especially of isotopes produced by radioactive decay, or those that are affected by isotopic anomalies. Indeed, in those cases the isotopic fractionation induced in the laboratory and mass spectrometer can be normalized out by fixing a ratio to a constant value in a process known as internal normalization. TIMS is less suited for measurement of mass-dependent isotopic fractionation because while the instrumental fractionation is relatively small, it is highly variable. MC-ICPMS on the other hand shows large instrumental mass fractionation but it is much more stable so it can be reliably corrected for by bracketing the sample measurement with standard measurements run in the same conditions (sample-standard bracketing; SSB; Albarède and Beard, 2004). For major elements that are easy to purify, SSB can achieve excellent precisions that allow one to resolve even minute isotopic variations. This is the case for $^{56}Fe/^{54}Fe$ iron isotope ratios,

which can be routinely measured with a precision of better than ±0.03 ‰ (Dauphas et al., 2009), revealing significant isotopic variations in igneous rocks that were previously thought to have uniform isotopic composition based on lower precision (Dauphas et al., 2017 and references therein). In its simplest implementation, the SSB technique suffers from several shortcomings, which are that it is sensitive to the presence of matrix elements that could affect instrumental mass bias, it is unable to correct for isotopic fractionation induced by the purification process, and its precision is limited by fluctuations in instrumental mass bias. Variations on SSB have been developed that address some of these shortcomings, most notably the method of element doping that consists in adding an element of similar mass to the sample and standard to monitor and correct for instrument-induced mass fractionation (Maréchal et al., 1999; Albarède and Beard, 2004). For example, Ni-doping or Cu-doping are sometimes used in Fe isotopic analyses (Poitrasson and Freydier, 2005; Schoenberg and von Blanckenburg, 2005). This helps address the issue of plasma instability and the presence of matrix elements but it does nothing to address the issue of isotopic fractionation produced during the purification. It also suffers from other issues, such as the requirement to purify the solution for the element that is used for doping and the fact that peak jumping is often needed during mass spectrometry between the element of interest and the doping element.

Overall, the MC-ICPMS technique of SSB (and its variations involving element doping) has been successful in addressing the needs of the geochemical community except for rare cases where improper correction of lab-induced isotopic mass-fractionation led to the reporting of erroneous results. However, some nontraditional stable isotope systems cannot be easily measured with this technique. In particular, for trace elements, a tradeoff is often encountered between purity

of the final solution and chemical yield, such that either matrix elements remain or some of the element is lost during the separation. Among these elements, many have 4 or more non-radiogenic elements and are therefore amenable to isotopic analysis by the double-spike method. In TIMS, double-spike is the only option for high-precision stable isotopic analyses (see Johnson and Beard, 1999, and Millet et al., 2012, for applications to Fe).

The double-spike (DS) technique was established in 1963 by Dodson (1963) and has been perfected since then (Russell et al., 1978; Johnson and Beard, 1999; Siebert et al., 2001; Rudge et al., 2009; John, 2012; Lehn et al., 2013; Millet and Dauphas, 2014; Lehn and Jacobson, 2015). The purpose of the DS technique is to correct the isotopic measurements for any isotopic fractionation produced by the purification procedure and the mass spectrometer. This is achieved by mixing with the sample some synthetic mixture of 2 isotopes (triple spike does not show any benefit relative to DS; Millet and Dauphas, 2014) early in the sample processing scheme; ideally during digestion. It is important that sample-spike equilibration be achieved early, meaning that the atoms of the DS have the same speciation as the sample atoms, so that the DS atoms experience the same isotopic fractionation as the sample atoms during laboratory processing. By measuring the 3 (or more) independent isotopic ratios formed by the 4 (or more) isotopes, it is possible to calculate the isotopic composition of the sample prior to purification and isotopic analysis.

An assumption often made in DS is that the original sample composition is related to the composition of the terrestrial standard by the laws of mass-dependent fractionation. This helps with data reduction as only one isotopic analysis of the sample + spike mixture is needed. Unlike terrestrial rocks, which for the most part follow mass-dependent fractionation (notable exceptions are O, S, and Hg), planetary materials can display isotopic anomalies inherited from incomplete

mixing of the products of stellar nucleosynthesis (Dauphas and Schauble, 2016 and references therein). By isotopic anomalies, we mean departures from the laws of mass-dependent fractionation. In those cases, one has to measure the isotopic composition of the unspiked sample. The laboratories that study isotopic anomalies often do not combine those measurements with DS measurements because the isotopic anomalies are small (down to a few parts per million relative deviations on isotopic ratios; Bouvier and Boyet, 2016; Burkhardt et al., 2016) and any spike contamination in the laboratory or mass spectrometer would jeopardize future measurements of natural materials. For example, the large excess ^{150}Nd measured by Bouvier and Boyet, (2016) in enstatite chondrites is presumably not real but due to contamination by the ^{150}Nd spike used for determination of the Sm/Nd ratio. Furthermore, some extraterrestrial samples are precious and avoiding duplication of measurements is desirable. For these reasons, it can be beneficial for DS studies to use previously published patterns of isotopic anomalies in the data reduction. Measurements of isotopic anomalies are almost always done by internal normalization. Previously, the approach used to take into account those isotopic anomalies in the DS data reduction was empirical, meaning that isotopic anomalies would be added to a terrestrial standard composition to numerically derive a relationship between these anomalies and the correction that needed to be applied to the DS procedure (Burkhardt et al., 2014). In this chapter, we provide introduction on the data reduction of the DS technique. The theoretical frameworks of the DS technique is used for isotope analyses of Ce, Nd, Sm, Gd, Dy, Er, and Yb on an MC-ICPMS for terrestrial samples. We rigorously derive formulas to correct DS measurements for the presence of isotopic anomalies. The true isotopic ratio can be obtained through a simple correction of the routine DS data reduction algorithm that assumes terrestrial mass-dependent fractionation. The formula for correction is

useful for extraterrestrial samples such as meteorites and their components, especially for nucleosynthetic anomalies.

2.2. Formula for Double-Spike Data Reduction and Correction

The DS technique involves doping the sample before digestion with a synthetic DS solution that contains at least two isotopes of the element of interest. The choice of the isotopes, their proportions in the DS mixture, and the proportion of the DS and sample have been extensively studied and the reader is referred to the literature for further details (Galer, 1999; Johnson and Beard, 1999; Rudge et al., 2009; John, 2012; Lehn et al., 2013; Millet and Dauphas, 2014). Suffice to say is that these can be optimized to reduce the risk of isobaric interferences and minimize the magnification of errors. After mixing and equilibrating the DS with the sample, the DS-sample mixture is purified and isotopic ratios are measured on a mass spectrometer. The measured isotope ratio is simply,

$$R_m^{i/k} = \left[(1-f)R_{smp}^{i/k} + fR_{sp}^{i/k}\right]\left(\frac{m_i}{m_k}\right)^{\beta}, \qquad (2.1)$$

where i is an isotope of the element of interest, k is the reference isotope relative to which all isotopic ratios are reported, $R_m^{i/k}$, $R_{smp}^{i/k}$ and $R_{sp}^{i/k}$ are measured, sample and spike isotopic ratios, f is the proportion of isotope k in the spike-sample mixture, β is the instrumental mass bias (assuming that mass fractionation follows the exponential law (Russell et al., 1978; Hart and Zindler, 1989; Maréchal et al., 1999; Dauphas and Schauble, 2016), and m_i is the mass of the i^{th} isotope. An assumption that is often made and is mostly valid for terrestrial rocks is that the isotopic composition of the sample is related to that of the standard by the laws of mass-dependent

fractionation. In the case of isotopic anomalies, this is obviously not the case and our aim here is to assess the extent of the correction that needs to be applied to the DS data reduction when such mass-dependence is assumed. If no isotopic anomaly is present, the sample isotope ratios can be related to the standard isotope ratios through the following expression,

$$R_{smp}^{i/k} = R_{std}^{i/k}\left(\frac{m_i}{m_k}\right)^{\alpha}, \qquad (2.2)$$

where α is the exponent of the exponential mass fractionation corresponding to natural fractionation of the sample relative to the standard. This is the quantity of interest in the DS approach. Substituting Eq. 2.2 into Eq. 2.1, one gets,

$$R_{m}^{i/k} = \left[(1-f)R_{std}^{i/k}\left(\frac{m_i}{m_k}\right)^{\alpha} + fR_{sp}^{i/k}\right]\left(\frac{m_i}{m_k}\right)^{\beta}. \qquad (2.3)$$

Equation 2.3 is a canonical equation for the double-spike reduction. The unknowns in this equation are f, α and β. Therefore, the system can be solved using a set of three equations, which can be obtained by applying Eq. 2.3 to three different isotope ratios, hence the requirement for at least 4 isotopes in the DS approach. However, in the presence of isotopic anomalies, one cannot assume that sample and standard isotopic ratios are related by mass-dependent fractionation. Instead, the isotope ratio of the standard $R_{std}^{i/k}$ needs to be adjusted to account for the presence of isotopic anomalies, so that the mass-dependent relationship between standards and samples takes the form,

$$R_{smp}^{i/k} = R_{std}^{i/k}\left(1+\frac{\varepsilon_{i/k}}{10^4}\right)\left(\frac{m_i}{m_k}\right)^{\alpha}, \qquad (2.4)$$

$\varepsilon_{i/k}$ in Eq. 2.4 indicates the size of the isotopic anomalies. The isotopic anomaly $\varepsilon_{i/k}$ is determined from an independent, unspiked measurement. It corresponds to the relative difference of the standard and sample isotopic ratio after fixing one ratio to a fixed value by internal normalization,

$$\varepsilon_{i/k} = (r_{smp}^{i/k*}/R_{std}^{i/k*} - 1) \times 10^4, \qquad (2.5)$$

where $r_{smp}^{i/k*}$ and $R_{std}^{i/k*}$ are the measured ratios of the unspiked sample and unspiked standard after internal normalization. The internally normalized ratio is related to the measured ratio by mass-fractionation, which is assumed to follow the exponential law,

$$r_{smp}^{i/k*} = r_{smp}^{i/k}/\left(\frac{m_i}{m_k}\right)^{\zeta}, \qquad (2.6)$$

The exponent of the exponential law ζ is calculated by arbitrarily fixing the ratio $r_{smp}^{j/k}$ to the ratio of a previous measured reference material $R_{ref}^{j/k}$ in a process known as internal normalization,

$$\zeta = \ln\left(\frac{r_{smp}^{j/k}}{R_{ref}^{j/k}}\right)/\ln\left(\frac{m_j}{m_k}\right), \qquad (2.7)$$

We wish to emphasize that the choice of an internal normalization scheme in the DS data reduction is inconsequential as the only requirement for the unspiked composition is to lie on a mass-fractionation relationship with the true ratio, a condition that internal normalization fulfills. With Eq. 2.4, a modified version of Eq. 2.3 can be written that accounts for the fact that standard and sample isotopic ratios are related through both isotopic anomalies and mass-dependent fractionation,

$$R_m^{i/k} = \left[(1-f)R_{std}^{i/k}\left(1+\frac{\varepsilon_{i/k}}{10^4}\right)\left(\frac{m_i}{m_k}\right)^{\alpha} + fR_{sp}^{i/k}\right]\left(\frac{m_i}{m_k}\right)^{\beta}. \qquad (2.8)$$

As $\varepsilon_{i/k}/10^4 \ll 1$, Eq. 2.8 is equivalent to adding a small value (denoted $dR_{std}^{i/k}$) on the standard ratio $R_{std}^{i/k}$ in Eq. 2.3. The addition of the $dR_{std}^{i/k}$ will lead to a shift in the calculated values of f, α and β. If a relationship can be derived between $dR_{std}^{i/k}$ and the corresponding changes of the unknowns df, $d\alpha$ and $d\beta$, then the α value calculated by the routine DS data reduction procedure can be corrected for $d\alpha$. Below, we derive such a relationship by taking the differential of Eq. 2.3 with respect to f, α, β and $R_{std}^{i/k}$,

$$\left[R_{sp}^{i/k} - R_{std}^{i/k}\left(\frac{m_i}{m_k}\right)^{\alpha}\right]df + (1-f)R_{std}^{i/k}\left(\frac{m_i}{m_k}\right)^{\alpha}\ln\left(\frac{m_i}{m_k}\right)d\alpha + \left[(1-f)R_{std}^{i/k}\left(\frac{m_i}{m_k}\right)^{\alpha} + fR_{sp}^{i/k}\right]\ln\left(\frac{m_i}{m_k}\right)d\beta = -(1-f)dR_{std}^{i/k}\left(\frac{m_i}{m_k}\right)^{\alpha}. \qquad (2.9)$$

The fact that the differential form of Eq. 2.3 is used means that the final formula will only be valid over a limited range of isotopic anomalies, which is discussed in Sect. 2.3. In the following, we replace $dR_{std}^{i/k}$ with $R_{std}^{i/k}\frac{\varepsilon_{i/k}}{10^4}$ to obtain a relationship between the unknowns df, $d\alpha$, $d\beta$ and the isotopic anomalies. Eq. 2.9 is changed accordingly,

$$\left[R_{sp}^{i/k} - R_{std}^{i/k}\left(\frac{m_i}{m_k}\right)^{\alpha}\right]df + (1-f)R_{std}^{i/k}\left(\frac{m_i}{m_k}\right)^{\alpha}\ln\left(\frac{m_i}{m_k}\right)d\alpha + \left[(1-f)R_{std}^{i/k}\left(\frac{m_i}{m_k}\right)^{\alpha} + fR_{sp}^{i/k}\right]\ln\left(\frac{m_i}{m_k}\right)d\beta = -\frac{1}{10^4}(1-f)R_{std}^{i/k}\left(\frac{m_i}{m_k}\right)^{\alpha}\varepsilon_{i/k}. \qquad (2.10)$$

We introduce the notation $\mu_{i/k} = \ln\left(\frac{m_i}{m_k}\right)$, such that Eq. 2.10 takes a more compact form,

$$\left[\frac{R_{sp}^{i/k}}{R_{std}^{i/k}}\Big/\left(\frac{m_i}{m_k}\right)^{\alpha} - 1\right]df + (1-f)\mu_{i/k}d\alpha + \left[(1-f) + f\frac{R_{sp}^{i/k}}{R_{std}^{i/k}}\Big/\left(\frac{m_i}{m_k}\right)^{\alpha}\right]\mu_{i/k}d\beta = -\frac{1}{10^4}(1-f)\varepsilon_{i/k}. \qquad (2.11)$$

For elements affected by isotopic anomalies, $\left(\frac{m_i}{m_k}\right)^{\alpha}$ is very close to one (*e.g.*, for Ti isotopes, the ratio of masses of the lightest and heaviest isotopes is 50/46=1.09). We therefore use the approximation $\frac{R_{sp}^{i/k}}{R_{std}^{i/k}}\Big/\left(\frac{m_i}{m_k}\right)^{\alpha} - 1 \approx \frac{R_{sp}^{i/k}}{R_{std}^{i/k}} - 1$. With $t_{i/k} = \frac{R_{sp}^{i/k}}{R_{std}^{i/k}} - 1$, Eq. 2.11 can be rewritten as,

$$t_{i/k}df + (1-f)\mu_{i/k}d\alpha + \left(1 + f\,t_{i/k}\right)\mu_{i/k}d\beta = -\frac{1}{10^4}(1-f)\varepsilon_{i/k}. \quad (2.12)$$

Applying Eq. 2.12 to three different isotope ratios 2/1, 3/1 and 4/1, one obtains a set of three linear equations of unknowns df, dα and dβ. Using Cramer's rule to solve the system of equations for dα, we get,

$$d\alpha = \frac{\begin{vmatrix} t_{2/1} & -\frac{1}{10^4}(1-f)\varepsilon_{2/1} & (1+f\,t_{2/1})\mu_{2/1} \\ t_{3/1} & -\frac{1}{10^4}(1-f)\varepsilon_{3/1} & (1+f\,t_{3/1})\mu_{3/1} \\ t_{4/1} & -\frac{1}{10^4}(1-f)\varepsilon_{4/1} & (1+f\,t_{4/1})\mu_{4/1} \end{vmatrix}}{\begin{vmatrix} t_{2/1} & (1-f)\mu_{2/1} & (1+f\,t_{2/1})\mu_{2/1} \\ t_{3/1} & (1-f)\mu_{3/1} & (1+f\,t_{3/1})\mu_{3/1} \\ t_{4/1} & (1-f)\mu_{4/1} & (1+f\,t_{4/1})\mu_{4/1} \end{vmatrix}}. \quad (2.13)$$

Equation 2.13 can be simplified by transposing the matrices, switching the order of the rows and columns, and factorizing some terms in the numerator and denominator,

$$d\alpha = -\frac{1}{10^4}\frac{\begin{vmatrix} \varepsilon_{2/1} & \varepsilon_{3/1} & \varepsilon_{4/1} \\ t_{2/1} & t_{3/1} & t_{4/1} \\ \left(t_{2/1}+\frac{1}{f}\right)\mu_{2/1} & \left(t_{3/1}+\frac{1}{f}\right)\mu_{3/1} & \left(t_{4/1}+\frac{1}{f}\right)\mu_{4/1} \end{vmatrix}}{\begin{vmatrix} \mu_{2/1} & \mu_{3/1} & \mu_{4/1} \\ t_{2/1} & t_{3/1} & t_{4/1} \\ t_{2/1}\mu_{2/1} & t_{3/1}\mu_{3/1} & t_{4/1}\mu_{4/1} \end{vmatrix}}. \quad (2.14)$$

We now introduce the $\delta_{i/k}$ notation corresponding to the natural fractionation of isotope ratio i/k,

$$\delta_{i/k} = \left(\frac{R_{smp}^{i/k}}{R_{std}^{i/k}} - 1\right) \times 10^3. \qquad (2.15)$$

The relation between $\delta_{i/k}$ and the natural fractionation factor α can be written as,

$$\delta_{i/k} = \left(\frac{R_{smp}^{i/k}}{R_{std}^{i/k}} - 1\right) \times 10^3 \approx \ln\left(\frac{R_{smp}^{i/k}}{R_{std}^{i/k}}\right) \times 10^3 = \alpha\mu_{i/k} \times 10^3. \qquad (2.16)$$

Differentiating both sides of Eq. 2.17, one obtains a relationship between dα and $d\delta_{i/1}$,

$$d\delta_{i/1} = \mu_{i/1} d\alpha \times 10^3. \qquad (2.17)$$

Combining Eq. 2.14 and Eq. 2.17, it follows that,

$$d\delta_{i/1} = -\frac{\mu_{i/1}}{10} \frac{\begin{vmatrix} \varepsilon_{2/1} & \varepsilon_{3/1} & \varepsilon_{4/1} \\ t_{2/1} & t_{3/1} & t_{4/1} \\ \left(t_{2/1}+\frac{1}{f}\right)\mu_{2/1} & \left(t_{3/1}+\frac{1}{f}\right)\mu_{3/1} & \left(t_{4/1}+\frac{1}{f}\right)\mu_{4/1} \end{vmatrix}}{\begin{vmatrix} \mu_{2/1} & \mu_{3/1} & \mu_{4/1} \\ t_{2/1} & t_{3/1} & t_{4/1} \\ t_{2/1}\mu_{2/1} & t_{3/1}\mu_{3/1} & t_{4/1}\mu_{4/1} \end{vmatrix}}. \qquad (2.18)$$

Expanding the determinant on the numerator of Eq. 2.18, one can write,

$$d\delta_{i/1} = -\frac{\mu_{i/1}}{10} \frac{\begin{vmatrix} t_{3/1} & t_{4/1} \\ \left(t_{3/1}+\frac{1}{f}\right)\mu_{3/1} & \left(t_{4/1}+\frac{1}{f}\right)\mu_{4/1} \end{vmatrix}\varepsilon_{2/1} + \begin{vmatrix} t_{4/1} & t_{2/1} \\ \left(t_{4/1}+\frac{1}{f}\right)\mu_{4/1} & \left(t_{2/1}+\frac{1}{f}\right)\mu_{2/1} \end{vmatrix}\varepsilon_{3/1} + \begin{vmatrix} t_{2/1} & t_{3/1} \\ \left(t_{2/1}+\frac{1}{f}\right)\mu_{2/1} & \left(t_{3/1}+\frac{1}{f}\right)\mu_{3/1} \end{vmatrix}\varepsilon_{4/1}}{\begin{vmatrix} \mu_{2/1} & \mu_{3/1} & \mu_{4/1} \\ t_{2/1} & t_{3/1} & t_{4/1} \\ t_{2/1}\mu_{2/1} & t_{3/1}\mu_{3/1} & t_{4/1}\mu_{4/1} \end{vmatrix}}. \qquad (2.19)$$

After expanding the determinant in Eq. 2.19 and combining like terms, $d\delta_{i/1}$ can be written as a linear combination of isotopic anomalies,

$$d\delta_{i/1} = -\frac{u_{i/1}}{10D}\left(F_{2/1}\varepsilon_{2/1} + F_{3/1}\varepsilon_{3/1} + F_{4/1}\varepsilon_{4/1}\right), \qquad (2.20)$$

where,

$$D = t_{2/1}t_{3/1}\mu_{3/2}\mu_{4/1} + t_{4/1}t_{2/1}\mu_{2/4}\mu_{3/1} + t_{3/1}t_{4/1}\mu_{4/3}\mu_{2/1}, \qquad (2.21)$$

$$F_{2/1} = t_{3/1}t_{4/1}\mu_{4/3} + \left(t_{3/1}\mu_{4/1} - t_{4/1}\mu_{3/1}\right)/f, \qquad (2.22)$$

$$F_{3/1} = t_{4/1}t_{2/1}\mu_{2/4} + \left(t_{4/1}\mu_{2/1} - t_{2/1}\mu_{4/1}\right)/f, \qquad (2.23)$$

$$F_{4/1} = t_{2/1}t_{3/1}\mu_{3/2} + \left(t_{2/1}\mu_{3/1} - t_{3/1}\mu_{2/1}\right)/f. \qquad (2.24)$$

The reason for expanding the determinant in this manner is that it shows explicitly how the correction depends linearly on the measured isotopic anomalies (ε values). We tested the validity of Eq. 2.20 by calculating the correction for some simulated data and comparing it with that obtained from a numerical solution. Equation 2.20 is found to be valid as long as the isotopic anomalies are within several epsilon units, a range covering most nucleosynthetic anomalies in meteorites. The quantity f in Eq. 2.18 is the fraction of isotope 1 from the spike in the sample-spike mixture. It can be obtained from the DS data reduction. A first order estimate of f is sufficient for use in this equation, which can be obtained by writing an approximate version of Eq. 2.3,

$$R_m^{i/k} \approx (1 - f)R_{std}^{i/k} + fR_{sp}^{i/k}. \qquad (2.25)$$

It follows that,

$$f \approx \frac{R_m^{i/k}/R_{std}^{i/k}-1}{R_{sp}^{i/k}/R_{std}^{i/k}-1}. \qquad (2.26)$$

Introducing the notation $s_{i/k} = R_m^{i/k}/R_{std}^{i/k} - 1$, Eq. 2.26 takes the form,

$$f \approx \frac{s_{i/k}}{t_{i/k}}. \qquad (2.27)$$

Substituting Eq. 2.27 into Eq. 2.18, one gets,

$$d\delta_{i/1} \approx -\frac{\mu_{i/1}}{10}\frac{\begin{vmatrix} \varepsilon_{2/1} & \varepsilon_{3/1} & \varepsilon_{4/1} \\ t_{2/1} & t_{3/1} & t_{4/1} \\ \left(1+\frac{1}{s_{2/1}}\right)t_{2/1}\mu_{2/1} & \left(1+\frac{1}{s_{3/1}}\right)t_{3/1}\mu_{3/1} & \left(1+\frac{1}{s_{4/1}}\right)t_{4/1}\mu_{4/1} \end{vmatrix}}{\begin{vmatrix} \mu_{2/1} & \mu_{3/1} & \mu_{4/1} \\ t_{2/1} & t_{3/1} & t_{4/1} \\ t_{2/1}\mu_{2/1} & t_{3/1}\mu_{3/1} & t_{4/1}\mu_{4/1} \end{vmatrix}}. \qquad (2.28)$$

Expanding the determinant on the numerator of Eq. 2.28, it follows,

$$d\delta_{i/1} = -\frac{\mu_{i/1}}{10}\frac{\begin{vmatrix} t_{3/1} & t_{4/1} \\ \left(1+\frac{1}{s_{3/1}}\right)t_{3/1}\mu_{3/1} & \left(1+\frac{1}{s_{4/1}}\right)t_{4/1}\mu_{4/1} \end{vmatrix}\varepsilon_{2/1} + \begin{vmatrix} t_{4/1} & t_{2/1} \\ \left(1+\frac{1}{s_{4/1}}\right)t_{4/1}\mu_{4/1} & \left(1+\frac{1}{s_{2/1}}\right)t_{2/1}\mu_{2/1} \end{vmatrix}\varepsilon_{3/1} + \begin{vmatrix} t_{2/1} & t_{3/1} \\ \left(1+\frac{1}{s_{2/1}}\right)t_{2/1}\mu_{2/1} & \left(1+\frac{1}{s_{3/1}}\right)t_{3/1}\mu_{3/1} \end{vmatrix}\varepsilon_{4/1}}{\begin{vmatrix} \mu_{2/1} & \mu_{3/1} & \mu_{4/1} \\ t_{2/1} & t_{3/1} & t_{4/1} \\ t_{2/1}\mu_{2/1} & t_{3/1}\mu_{3/1} & t_{4/1}\mu_{4/1} \end{vmatrix}}. \qquad (2.29)$$

Expanding the determinant in Eq. 2.29 and combining like terms, one can write,

$$d\delta_{i/1} = -\frac{u_{i/1}}{10D}\left(M_{2/1}\varepsilon_{2/1} + M_{3/1}\varepsilon_{3/1} + M_{4/1}\varepsilon_{4/1}\right), \quad (2.30)$$

where,

$$M_{2/1} = t_{3/1}t_{4/1}\left(\mu_{4/3} + \mu_{4/1}/s_{4/1} - \mu_{3/1}/s_{3/1}\right), \qquad (2.31)$$

$$M_{3/1} = t_{2/1}t_{4/1}\left(\mu_{2/4} + \mu_{2/1}/s_{2/1} - \mu_{4/1}/s_{4/1}\right), \quad (2.32)$$

$$M_{4/1} = t_{2/1}t_{3/1}\left(\mu_{3/2} + \mu_{3/1}/s_{3/1} - \mu_{2/1}/s_{2/1}\right), \quad (2.33)$$

As a reminder, $d\delta_{i/1}$ is the shift associated with the presence of isotopic anomalies (*i.e.*, $\delta_{true} - \delta_{calc}$). Equation 2.20 shows that the correction that needs to be applied to the isotopic fractionation calculated by the DS procedure in the presence of isotopic anomalies is a simple linear combination of the anomalies affecting the 3 isotopic ratios used in the DS data reduction. In planetary materials, isotopic anomalies are often correlated, as they correspond to binary mixing between an average solar system component and a pure nucleosynthetic component. If this is the case, then the correction that needs to be applied is proportional to the magnitude of the anomalies on just one isotope. This will be illustrated in the case of Mo. Note that the presence of such a correlation between anomalies is not a prerequisite to the application of either Eq. 2.20 or Eq. 2.30; it just brings further simplifications.

Isotopic anomalies are measured with some uncertainty, which should be taken into account in the uncertainty assessment of the mass-dependent fractionation. The formulas that we derived provide a straightforward way to propagate isotopic anomaly uncertainties on mass fractionation determinations. Assuming that the uncertainties on all ε values are independent, their errors translate into an error on the correction $\Delta^{i/1}$ of,

$$\sigma_{\Delta^{i/1}} = \frac{\mu_{i/1}}{10}\sqrt{\left(F_{2/1}\sigma_{\varepsilon_{2/1}}\right)^2 + \left(F_{3/1}\sigma_{\varepsilon_{3/1}}\right)^2 + \left(F_{4/1}\sigma_{\varepsilon_{4/1}}\right)^2}. \quad (2.34)$$

This uncertainty can be added quadratically to the uncertainty associated with the sample-DS analysis itself. As discussed above, the choice of a normalization scheme is inconsequential for the calculation of absolute ratios (see McCulloch and Wasserburg, 1978 for an expression to convert data from one internal normalization scheme to another).

One of the limitations of the formula that we derived is that it is best suited to elements that possess 4 abundant isotopes. When exactly 4 isotopes are used, the DS correction can be calculated analytically through Eq. 2.20. When more than 4 isotopes are used, the system is over-constrained and cannot be exactly resolved. Instead, one relies on χ^2-minimization algorithms where the measurements are weighted by the inverse of their variance. In those situations, the only option is to calculate the influence of isotopic anomalies numerically. The analytical is still useful in those cases as it provides a test to ground-trust these numerical calculations.

2.3. Applications to Isotopic Measurements of Planetary Materials

2.3.1. Molybdenum

Molybdenum is a refractory and moderately siderophile element that has seven stable isotopes. Sub per-mil level mass-dependent isotopic fractionations of Mo have been reported in chondrites, iron meteorites and differentiated planetary bodies, which reflect solar nebula and planetary differentiation processes (Hin et al., 2013; Burkhardt et al., 2014). Such fractionation can be precisely determined through the DS technique if the effect of Mo isotopic anomalies can be properly accounted for. Molybdenum isotopic anomalies in meteorites are dominated by an *s*-deficit process (Dauphas et al., 2002a, b; Burkhardt et al., 2011; Dauphas and Schauble, 2016) but higher precision measurements have recently shown that not all meteorites follow the exact same

pattern (Budde et al., 2016; Nagai and Yokoyama, 2016; Poole et al., 2017). Nevertheless, to first order, Mo nucleosynthetic anomalies are well correlated in bulk planetary materials.

Burkhardt et al., (2014) numerically modeled the effects of nucleosynthetic anomalies (Table S2 in Burkhardt et al., 2014) and obtained a relationship between the size of the anomaly and the correction in the DS data reduction. The manner in which they tackled this question was to subtract or add variable amounts of an *s*-deficit component to a standard composition and to run the routine DS algorithm procedure on this simulated composition. They empirically concluded that the correction for the presence of anomalies could be expressed as,

$$\delta^{98/95}\mathrm{Mo}_{\mathrm{corrected}} = \delta^{98/95}\mathrm{Mo}_{\mathrm{uncorrected}} - 0.066\varepsilon^{96/95}\mathrm{Mo}_{\mathrm{nucleosynthetic}}, \qquad (2.35)$$

where $\delta^{98/95}\mathrm{Mo}_{\mathrm{corrected}}$ and $\delta^{98/95}\mathrm{Mo}_{\mathrm{uncorrected}}$ are the corrected and uncorrected δ values, and $\varepsilon^{96/95}\mathrm{Mo}_{\mathrm{nucleosynthetic}}$ is the nucleosynthetic anomaly on the ^{96}Mo/^{95}Mo ratio after internal normalization to a fixed ^{97}Mo/^{95}Mo value (0.602083). To test and compare our derivation with the relationship established by Burkhardt et al. (2014), we calculate the correction using Eq. 2.20. The standard and spike compositions and optimum spike proportion are from Burkhardt (2012). The pattern of isotopic anomalies is that considered by Burkhardt et al. (2014) (their Table S2). The relationship between the correction and isotopic anomalies takes the form,

$$\Delta^{98/95}\mathrm{Mo} = -0.0304\varepsilon^{97/95}\mathrm{Mo} - 0.1136\varepsilon^{98/95}\mathrm{Mo} + 0.0206\varepsilon^{100/95}\mathrm{Mo}, \qquad (2.36)$$

where $\Delta^{98/95}$Mo is the correction that needs to be added if one does the data reduction without accounting for the presence of isotopic anomalies (*i.e.*, $\delta_{true} - \delta_{calc}$). Because Mo isotopic anomalies are relatively well correlated, corresponding to an *s*-deficit pattern, Eq. 2.36 can be simplified to,

$$\delta^{98/95}\text{Mo}_{\text{corrected}} = \delta^{98/95}\text{Mo}_{\text{uncorrected}} - 0.070\varepsilon^{96/95}\text{Mo}_{\text{nucleosynthetic}}, \quad (2.37)$$

which is consistent with the numerical solution Eq. 2.35 provided in Burkhardt et al. (2014).

Table 2.1Effect of nucleosynthetic anomalies on Mo DS mass fractionation correction.

	SRM 3134 Mo	**-0.005%s**[a]	**-0.01%s**	**-0.05%s**
	Modeled isotopic abundances			
^{92}Mo	14.7339	14.7352	14.7365	14.7468
^{94}Mo	9.2129	9.2137	9.2146	9.2214
^{95}Mo	15.8922	15.8920	15.8918	15.8900
^{96}Mo	16.6717	16.6700	16.6683	16.6549
^{97}Mo	9.5685	9.5683	9.5682	9.5671
^{98}Mo	24.2256	24.2245	24.2234	24.2145
^{100}Mo	9.6952	9.6962	9.6972	9.7054
	Modeled nucleosynthetic anomalies			
$\varepsilon^{92/95}$Mo	0	1.01	2.03	10.14
$\varepsilon^{94/95}$Mo	0	1.07	2.13	10.67
$\varepsilon^{95/95}$Mo	0	0	0	0
$\varepsilon^{96/95}$Mo	0	-0.86	-1.72	-8.63
$\varepsilon^{97/95}$Mo	0	0	0	0
$\varepsilon^{98/95}$Mo	0	-0.31	-0.63	-3.13
$\varepsilon^{100/95}$Mo	0	1.19	2.38	11.93
	Apparent fractionation induced by nucleosynthetic anomalies			
$\delta^{98/95}$Mo (Burkhardt *et al.* 2014)	0	-0.06	-0.12	-0.60
$\delta^{98/95}$Mo (This work)	0	-0.06	-0.12	-0.60

a. s-process deficit simulated by subtracting various amount of s-process Mo (ref. 43) from the isotopic abundances of the Mo standard SRM3134.

An important step in the derivation of Eq. 2.20 is that the isotopic anomalies are small, such that Eq. 2.9 can take a differential form in $R_{std}^{i/k}$. Eq. 2.20 is therefore only valid over a certain range of anomalies. To evaluate the range of applicability of Eq. 2.20, we have generated synthetic Mo isotope data sets containing various levels of anomalies by adding or subtracting an *s*-deficit

component in a manner similar to what was done by Burkhardt et al. (2014), and arbitrarily setting some natural/instrumental mass fractionation. The induced isotopic fractionation calculated by Eq. 2.37 is found to be consistent with the true fractionation over a large range of isotopic anomalies. The precision of $\delta^{98/95}$Mo isotopic analyses is ~ ±0.05 ‰ (Burkhardt et al., 2014). As shown in Table 2.1 and Fig. 2.1, the analytical equation derived here provides an accurate correction for isotopic anomalies at the ~ ±0.05 ‰ level as long as they do not exceed several tens of ε-units.

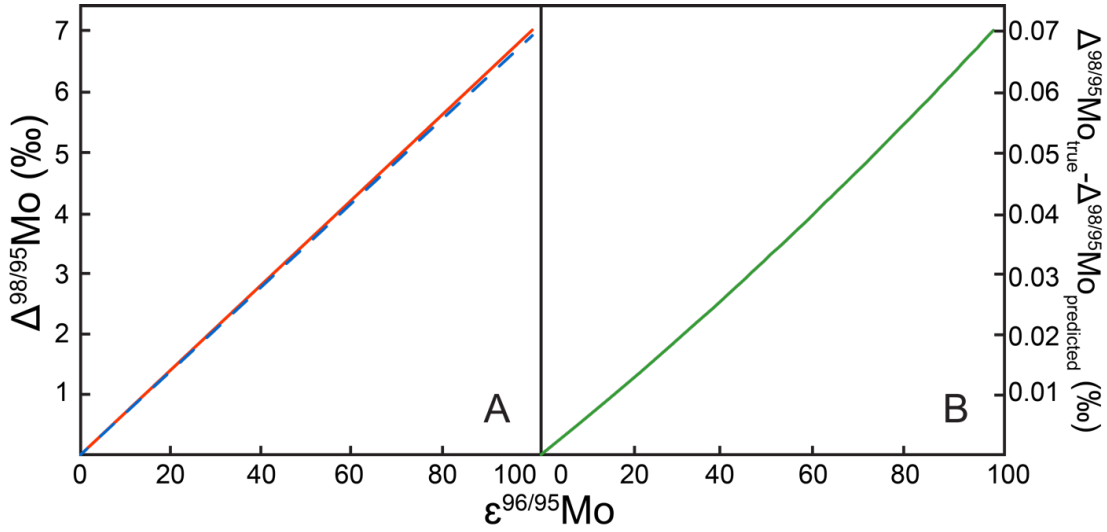

Figure 2.1Predicted (blue dashed line) and true (red solid line) induced apparent fractionation in the DS data reduction with increasing $\varepsilon^{96/95}$Mo (A). The predicted fractionation is calculated using Eq. 2.37 while the true fractionation is based on a DS reduction that uses a simulated composition corresponding to addition of an s-deficit nucleosynthetic component to the terrestrial standard composition. Difference between the true and the predicted mass-dependent fractionation with increasing $\varepsilon^{96/95}$Mo (B). This is the difference between the blue dashed and solid red lines in panel A.

2.3.2. Titanium

Titanium is a refractory lithophile element that condensed early in the evolution of the solar system (Grossman, 1972, 1973; Lodders, 2003). Titanium isotopic anomalies are ubiquitous in meteorites (Davis et al., 2018; Leya et al., 2009; Niederer et al., 1980, 1985; Trinquier et al., 2009;

Zhang et al., 2011) and found to be correlated with other isotope systems, most notably ^{48}Ca (Dauphas et al., 2014). Titanium anomalies affect primarily ^{50}Ti but other isotopes also display anomalies. Isotopic anomaly measurements are usually performed by applying a mass-fractionation correction that fixes the ^{49}Ti/^{47}Ti ratio to a constant value by internal normalization. More recently, some studies have focused on documenting Ti mass-dependent isotopic fractionation in rocks and products of laboratory experiments. These studies have shown that Ti stable isotope systematics could be used to understand evaporation-condensation processes that occurred in the early solar nebula stage (Zhang et al., 2014), and trace magmatic processes in terrestrial planets, the Moon, and differentiated asteroids (Millet et al., 2016; Greber et al., 2017). Analyses of mass-dependent variations of Ti isotopes for extraterrestrial materials are complicated, however, by the ubiquitous existence of nucleosynthetic anomalies (Niederer et al., 1980; Leya et al., 2009; Trinquier et al., 2009) as well as cosmogenic effects (Zhang et al., 2012). Titanium isotope systematics thus represents an excellent case study to test Eq. 2.20.

Most recent Ti isotope measurements have defined the δ-value as the deviation of the ^{49}Ti/^{47}Ti ratio relative to a terrestrial reference material (OL-Ti; Millet and Dauphas, 2014). Isotopic anomalies $\varepsilon^{i/47}$Ti are reported by internal normalization to the same ^{49}Ti/^{47}Ti ratio (Leya et al., 2009; Trinquier et al., 2009; Zhang et al., 2011; Zhang et al., 2014; Davis et al., 2018). Because ^{50}Ti is the Ti isotope most affected by nucleosynthetic anomalies (Leya et al., 2009; Trinquier et al., 2009; Zhang et al., 2011; Zhang et al., 2014; Davis et al., 2018), it is better avoided during DS data reduction of extraterrestrial materials. The other isotopes of Ti also display subtle isotopic anomalies that correspond to a correction on δ-values of Eq. 2.20,

$$\Delta^{48/47}\mathrm{Ti} = +0.0590\varepsilon^{46/47}\mathrm{Ti} - 0.0565\varepsilon^{48/47}\mathrm{Ti} + 0.0085\varepsilon^{49/47}\mathrm{Ti}. \qquad (2.38)$$

Setting $\varepsilon^{49/47}$Ti=0 and using the fact that the anomalies on $\varepsilon^{46/47}$Ti are much larger than those on $\varepsilon^{48/47}$Ti in bulk meteorites, this correction is well approximated by

$$\delta^{48/47}\mathrm{Ti}_{\mathrm{corrected}} = \delta^{48/47}\mathrm{Ti}_{\mathrm{uncorrected}} + 0.059\varepsilon^{46/47}\mathrm{Ti}_{\mathrm{nucleosynthetic}}. \quad (2.39)$$

In bulk meteorites, the anomalies on $\varepsilon^{46/47}$Ti vary between ~ −0.3 and +0.7 (Zhang et al., 2011; Zhang et al., 2012) with uncertainties of ~±0.1. The associated correction on δ-value is between −0.041 and +0.018, which is small but not completely negligible. Similarly to Mo, we assessed the range of applicability of Eq. 2.39 to Ti isotope measurements (Fig. 2.2).

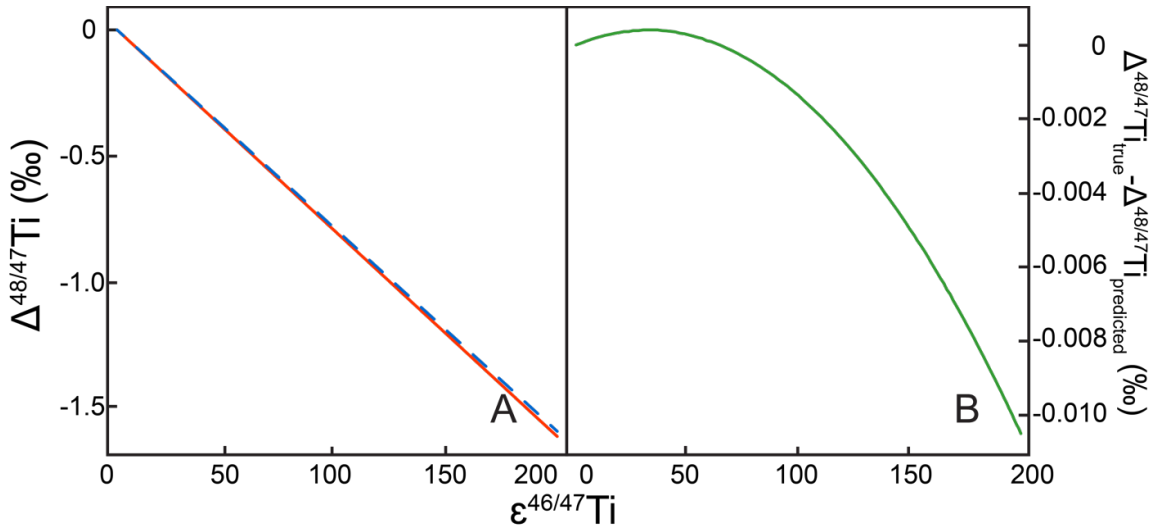

Figure 2.2 Predicted (blue dashed line) and true (red solid line) induced apparent fractionation in the DS data reduction with increasing $\varepsilon^{46/47}$Ti (A). The predicted fractionation is calculated using Eq. 2.39 while the true fractionation is based on a DS reduction that uses a simulated composition with various $\varepsilon^{46/47}$Ti values. Difference between the true and the predicted mass-dependent fractionation with increasing $\varepsilon^{46/47}$Ti (B). This is the difference between the blue dashed and solid red lines in panel A.

The precision of Ti isotopic mass fractionation measurements is typically 0.02 ‰ on the ^{49}Ti/^{47}Ti ratio. As long as the anomalies in $\varepsilon^{46/47}$Ti do not exceed 200, Eq. 2.39 will provide an

accurate correction within the above mentioned precision (Fig. 2.2). For comparison, the $\varepsilon^{46/47}$Ti anomalies reported in calcium-aluminum-rich inclusions extend to ±3 (Leya et al., 2009; Trinquier et al., 2009; Davis et al., 2018) and the formula can be applied to these materials.

2.3.3. Chromium

Chromium is a moderately siderophile element with four stable isotopes (^{50}Cr, ^{52}Cr, ^{53}Cr and ^{54}Cr). Early studies of Cr isotope variations in extraterrestrial samples mainly focused on radiogenic variations in ^{53}Cr (Birck and Allègre, 1988; Lugmair and Shukolyukov, 1998; Trinquier et al., 2008) and nucleosynthetic anomalies in ^{54}Cr (Rotaru et al., 1992; Trinquier et al., 2007). These measurements involved correcting for mass-fractionation (natural and instrumental) by internal normalization using the ^{52}Cr/^{50}Cr as reference. A reason for normalizing to this pair of isotopes is that they show less variations than the other isotopes (Dauphas et al., 2010; Qin et al., 2011). Mass-dependent isotopic fractionation has been the focus of more recent studies (Qin and Wang, 2017). In particular, Moynier et al. (2011) reported Cr isotopic analyses of chondrites using the sample-standard bracketing technique and they argued that the stable Cr isotopic composition of chondrites was systematically lighter than that of the bulk silicate Earth, possibly reflecting the partitioning of Cr in Earth's core. The isotopic variations documented by Moynier et al. (2011) are small and the purification chemistry of Cr is complex, which prompted several groups to reevaluate this question using the DS technique (Moynier et al., 2011; Bonnand et al., 2016; Schoenberg et al., 2016). The conclusion of these studies is that the shift seen in Moynier et al. (2011) is not real and that the bulk silicate Earth has the same Cr isotopic composition of the Earth.

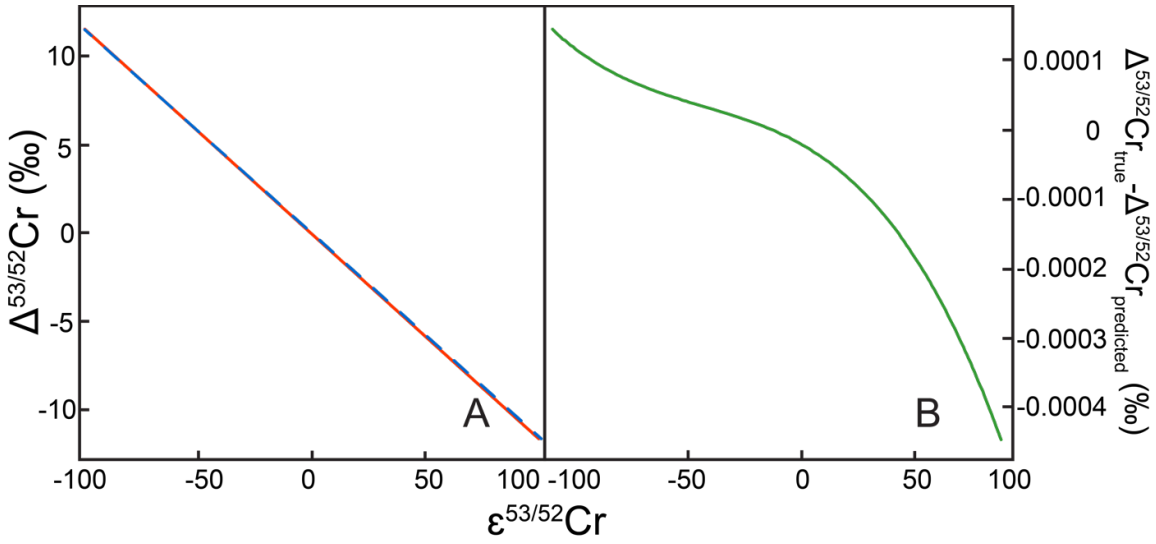

Figure 2.3 Predicted (blue dashed line) and true (solid red line) induced apparent fractionation in the DS data reduction with increasing $\varepsilon^{53/52}$Cr (A). The predicted fractionation is calculated using Eq. 2.41 while the true fractionation is based on a DS reduction that uses a simulated composition with various $\varepsilon^{53/52}$Cr values. Difference between the true and the predicted mass-dependent fractionation with increasing $\varepsilon^{53/52}$Cr (B). This is the difference between the blue dashed and solid red lines in panel A.

Meteorites are affected by both radiogenic ingrowths of ^{53}Cr and nucleosynthetic anomalies of ^{54}Cr, which must be taken into account when reducing DS data for characterization of Cr isotopic fractionation. For the calculation below, we use the DS isotopic composition from Bonnand et al. (2011) and assume an optimal spike proportion of 0.32. Equation 2.20 gives the correction caused by isotopic anomalies and radiogenic ingrowth:

$$\Delta^{53/52}\mathrm{Cr} = -0.0036\varepsilon^{50/52}\mathrm{Cr} - 0.1154\varepsilon^{53/52}\mathrm{Cr} + 0.0040\varepsilon^{54/52}\mathrm{Cr}. \qquad (2.40)$$

Accordingly, the correction is mainly controlled by $\varepsilon^{53/52}$Cr so Eq. 2.40 can be further simplified to,

$$\delta^{53/52}\mathrm{Cr}_{\mathrm{corrected}} = \delta^{53/52}\mathrm{Cr}_{\mathrm{uncorrected}} - 0.1154\varepsilon^{53/52}\mathrm{Cr}. \qquad (2.41)$$

The range of applicability of Eq. 2.41 was tested by comparing the result of this equation with a numerical calculation done on synthetic data (Fig. 2.3). The correction is valid for $\varepsilon^{53/52}\mathrm{Cr}$ below 100 parts per 10^4, which is well within the range of values documented in meteorites. For the samples measured in Bonnand et al. (2011), the correction that needs to be applied varies between 0.013 and 0.119, which is small but not negligible.

2.4. Conclusion

We introduce an analytical formula that gives the correction that needs to be applied to conventional double-spike data reduction when isotopic anomalies are present. When all samples are related by the laws of mass-dependent fractionation, then one single measurement of a spike-sample mixture is sufficient to calculate the absolute isotopic composition. When this assumption is not fulfilled, meaning that the samples display isotopic anomalies relative to the standard, our formula gives the shift induced by assuming that samples and standards are related by a mass-fractionation relationship when they are not. The typical range of isotopic anomalies that the formula can handle depends on the element considered but is sufficient for correction of nucleosynthetic anomalies in bulk meteorites and some of their constituents. Three applications are presented to demonstrate the usefulness of the derived formula: Mo, Ti and Cr in meteoritic materials. The formula gives corrections that agree with the original publications. One virtue of this formula is that it provides a quick and reliable means of using previously published isotopic anomaly measurements to correct the double-spike procedure for the presence of isotopic anomalies. Furthermore, it provides an easy way to propagate uncertainties. The main shortcoming of the formula is that it is only applicable when only 4 isotopes are used and the double-spike data reduction assumes an exact solution.

2.5. References

Albarède, F., Beard, B., 2004. Analytical methods for non-traditional isotopes. Reviews in Mineralogy and Geochemistry 55, 113-152.

Birck, J.-L., Allègre, C.J., 1988. Manganese-chromium isotope systematics and the development of the early Solar System. Nature 331, 579-584.

Bonnand, P., Parkinson, I.J., James, R.H., Karjalainen, A.M., Fehr, M.A., 2011. Accurate and precise determination of stable Cr isotope compositions in carbonates by double spike MC-ICP-MS. Journal of Analytical Atomic Spectrometry 26, 528-535.

Bonnand, P., Williams, H., Parkinson, I., Wood, B., Halliday, A., 2016. Stable chromium isotopic composition of meteorites and metal–silicate experiments: Implications for fractionation during core formation. Earth and Planetary Science Letters 435, 14-21.

Bouvier, A., Boyet, M., 2016. Primitive Solar System materials and Earth share a common initial ^{142}Nd abundance. Nature 537, 399-402.

Budde, G., Burkhardt, C., Brennecka, G.A., Fischer-Gödde, M., Kruijer, T.S., Kleine, T., 2016. Molybdenum isotopic evidence for the origin of chondrules and a distinct genetic heritage of carbonaceous and non-carbonaceous meteorites. Earth and Planetary Science Letters 454, 293-303.

Burkhardt, C., Borg, L., Brennecka, G., Shollenberger, Q., Dauphas, N., Kleine, T., 2016. A nucleosynthetic origin for the Earth's anomalous ^{142}Nd composition. Nature 537, 394-398.

Burkhardt, C., Hin, R.C., Kleine, T., Bourdon, B., 2014. Evidence for Mo isotope fractionation in the solar nebula and during planetary differentiation. Earth and Planetary Science Letters 391, 201-211.

Burkhardt, C., Kleine, T., Oberli, F., Pack, A., Bourdon, B., Wieler, R., 2011. Molybdenum isotope anomalies in meteorites: constraints on solar nebula evolution and origin of the Earth. Earth and Planetary Science Letters 312, 390-400.

Burkhardt, C.N., 2012. Molybdenum isotopes and solar nebula evolution. PhD dissertation, ETH Zurich.

Dauphas, N., Chen, J.H., Zhang, J., Papanastassiou, D.A., Davis, A.M., Travaglio, C., 2014. Calcium-48 isotopic anomalies in bulk chondrites and achondrites: Evidence for a uniform isotopic reservoir in the inner protoplanetary disk. Earth and Planetary Science Letters 407, 96-108.

Dauphas, N., John, S.G., Rouxel, O., 2017. Iron isotope systematics. Reviews in Mineralogy and Geochemistry 82, 415-510.

Dauphas, N., Marty, B., Reisberg, L., 2002a. Molybdenum evidence for inherited planetary scale isotope heterogeneity of the protosolar nebula. The Astrophysical Journal 565, 640-644.

Dauphas, N., Marty, B., Reisberg, L., 2002b. Molybdenum nucleosynthetic dichotomy revealed in primitive meteorites. The Astrophysical Journal Letters 569, L139-L142.

Dauphas, N., Pourmand, A., Teng, F.Z., 2009. Routine isotopic analysis of iron by HR-MC-ICPMS: How precise and how accurate? Chemical Geology 267, 175-184.

Dauphas, N., Remusat, L., Chen, J.H., Roskosz, M., Papanastassiou, D.A., Stodolna, J., Guan, Y., Ma, C., Eiler, J., 2010. Neutron-rich chromium isotope anomalies in supernova nanoparticles. The Astrophysical Journal 720, 1577-1591.

Dauphas, N., Schauble, E.A., 2016. Mass fractionation laws, mass-independent effects, and isotopic anomalies. Annual Review of Earth and Planetary Sciences 44, 709-783.

Davis, A.M., Zhang, J., Greber, N.D., Hu, J., Tissot, F.L., Dauphas, N., 2018. Titanium isotopes and rare earth patterns in CAIs: evidence for thermal processing and gas-dust decoupling in the protoplanetary disk. Geochimica et Cosmochimica Acta 221, 275-295.

Dodson, M., 1963. A theoretical study of the use of internal standards for precise isotopic analysis by the surface ionization technique: Part I-General first-order algebraic solutions. Journal of Scientific Instruments 40, 289-295.

Galer, S.J., 1999. Optimal double and triple spiking for high precision lead isotopic measurement. Chemical Geology 157, 255-274.

Greber, N.D., Dauphas, N., Puchtel, I.S., Hofmann, B.A., Arndt, N.T., 2017. Titanium stable isotopic variations in chondrites, achondrites and lunar rocks. Geochimica et Cosmochimica Acta 213, 534-552.

Grossman, L., 1972. Condensation in the primitive solar nebula. Geochimica et Cosmochimica Acta 36, 597-619.

Grossman, L., 1973. Refractory trace elements in Ca-Al-rich inclusions in the Allende meteorite. Geochimica et Cosmochimica Acta 37, 1119-1140.

Hart, S.R., Zindler, A., 1989. Isotope fractionation laws: a test using calcium. International Journal of Mass Spectrometry and Ion Processes 89, 287-301.

Hin, R.C., Burkhardt, C., Schmidt, M.W., Bourdon, B., Kleine, T., 2013. Experimental evidence for Mo isotope fractionation between metal and silicate liquids. Earth and Planetary Science Letters 379, 38-48.

John, S.G., 2012. Optimizing sample and spike concentrations for isotopic analysis by double-spike ICPMS. Journal of Analytical Atomic Spectrometry 27, 2123-2131.

Johnson, C.M., Beard, B.L., 1999. Correction of instrumentally produced mass fractionation during isotopic analysis of Fe by thermal ionization mass spectrometry. International Journal of Mass Spectrometry 193, 87-99.

Lehn, G., Jacobson, A., Holmden, C., 2013. Precise analysis of Ca isotope ratios ($\delta^{44/40}$Ca) using an optimized ^{43}Ca-^{42}Ca double-spike MC-TIMS method. International Journal of Mass Spectrometry 351, 69-75.

Lehn, G.O., Jacobson, A.D., 2015. Optimization of a ^{48}Ca-^{43}Ca double-spike MC-TIMS method for measuring Ca isotope ratios ($\delta^{44/40}$Ca and $\delta^{44/42}$Ca): limitations from filament reservoir mixing. Journal of Analytical Atomic Spectrometry 30, 1571-1581.

Leya, I., Schönbächler, M., Krähenbühl, U., Halliday, A.N., 2009. New titanium isotope data for Allende and Efremovka CAIs. The Astrophysical Journal 702, 1118-1126.

Lodders, K., 2003. Solar system abundances and condensation temperatures of the elements. The Astrophysical Journal 591, 1220-1247.

Lugmair, G., Shukolyukov, A., 1998. Early solar system timescales according to ^{53}Mn-^{53}Cr systematics. Geochimica et Cosmochimica Acta 62, 2863-2886.

Maréchal, C.N., Télouk, P., Albarède, F., 1999. Precise analysis of copper and zinc isotopic compositions by plasma-source mass spectrometry. Chemical Geology 156, 251-273.

McCulloch, M.T., Wasserburg, G., 1978. Barium and neodymium isotopic anomalies in the Allende meteorite. Astrophysical Journal Letters 220, L15-L19.

Millet, M.-A., Baker, J.A., Payne, C.E., 2012. Ultra-precise stable Fe isotope measurements by high resolution multiple-collector inductively coupled plasma mass spectrometry with a ^{57}Fe-^{58}Fe double spike. Chemical Geology 304, 18-25.

Millet, M.-A., Dauphas, N., 2014. Ultra-precise titanium stable isotope measurements by double-spike high resolution MC-ICP-MS. Journal of Analytical Atomic Spectrometry 29, 1444-1458.

Millet, M.-A., Dauphas, N., Greber, N.D., Burton, K.W., Dale, C.W., Debret, B., Macpherson, C.G., Nowell, G.M., Williams, H.M., 2016. Titanium stable isotope investigation of magmatic processes on the Earth and Moon. Earth and Planetary Science Letters 449, 197-205.

Moynier, F., Yin, Q.Z., Schauble, E., 2011. Isotopic evidence of Cr partitioning into Earth's core. Science 331, 1417-1420.

Nagai, Y., Yokoyama, T., 2016. Molybdenum Isotope Anomalies in Non-Carbonaceous Meteorites, Lunar and Planetary Science 47, #1888.

Niederer, F., Papanastassiou, D., Wasserburg, G., 1980. Endemic isotopic anomalies in titanium. Astrophysical Journal Letters 240, L73-L77.

Niederer, F., Papanastassiou, D., Wasserburg, G., 1985. Absolute isotopic abundances of Ti in meteorites. Geochimica et Cosmochimica Acta 49, 835-851.

Poitrasson, F., Freydier, R., 2005. Heavy iron isotope composition of granites determined by high resolution MC-ICP-MS. Chemical Geology 222, 132-147.

Poole, G.M., Rehkämper, M., Coles, B.J., Goldberg, T., Smith, C.L., 2017. Nucleosynthetic molybdenum isotope anomalies in iron meteorites–new evidence for thermal processing of solar nebula material. Earth and Planetary Science Letters 473, 215-226.

Qin, L., Nittler, L.R., Alexander, C.O.D., Wang, J., Stadermann, F.J., Carlson, R.W., 2011. Extreme ^{54}Cr-rich nano-oxides in the CI chondrite Orgueil–Implication for a late supernova injection into the solar system. Geochimica et Cosmochimica Acta 75, 629-644.

Qin, L., Wang, X., 2017. Chromium isotope geochemistry. Reviews in Mineralogy and Geochemistry 82, 379-414.

Rotaru, M., Birck, J.L., Allègre, C.J., 1992. Clues to early solar system history from chromium isotopes in carbonaceous chondrites. Nature 358, 465-470.

Rudge, J.F., Reynolds, B.C., Bourdon, B., 2009. The double spike toolbox. Chemical Geology 265, 420-431.

Russell, W., Papanastassiou, D., Tombrello, T., 1978. Ca isotope fractionation on the Earth and other solar system materials. Geochimica et Cosmochimica Acta 42, 1075-1090.

Schoenberg, R., Merdian, A., Holmden, C., Kleinhanns, I.C., Haßler, K., Wille, M., Reitter, E., 2016. The stable Cr isotopic compositions of chondrites and silicate planetary reservoirs. Geochimica et Cosmochimica Acta 183, 14-30.

Schoenberg, R., von Blanckenburg, F., 2005. An assessment of the accuracy of stable Fe isotope ratio measurements on samples with organic and inorganic matrices by high-resolution multicollector ICP-MS. International Journal of Mass Spectrometry 242, 257-272.

Siebert, C., Nägler, T.F., Kramers, J.D., 2001. Determination of molybdenum isotope fractionation by double-spike multicollector inductively coupled plasma mass spectrometry. Geochemistry, Geophysics, Geosystems 2, #2000GC000124 (16 pp).

Teng, F.-Z., Dauphas, N., Watkins, J.M., 2017. Non-traditional stable isotopes: retrospective and prospective. Reviews in Mineralogy and Geochemistry 82, 1-26.

Trinquier, A., Birck, J.-L., Allègre, C., Göpel, C., Ulfbeck, D., 2008. ^{53}Mn–^{53}Cr systematics of the early Solar System revisited. Geochimica et Cosmochimica Acta 72, 5146-5163.

Trinquier, A., Birck, J.-L., Allegre, C.J., 2007. Widespread ^{54}Cr heterogeneity in the inner solar system. The Astrophysical Journal 655, 1179-1185.

Trinquier, A., Elliott, T., Ulfbeck, D., Coath, C., Krot, A.N., Bizzarro, M., 2009. Origin of nucleosynthetic isotope heterogeneity in the solar protoplanetary disk. Science 324, 374-376.

Zhang, J., Dauphas, N., Davis, A.M., Leya, I., Fedkin, A., 2012. The proto-Earth as a significant source of lunar material. Nature Geoscience 5, 251-255.

Zhang, J., Dauphas, N., Davis, A.M., Pourmand, A., 2011. A new method for MC-ICPMS measurement of titanium isotopic composition: Identification of correlated isotope anomalies in meteorites. Journal of Analytical Atomic Spectrometry 26, 2197-2205.

Zhang, J., Huang, S., Davis, A.M., Dauphas, N., Hashimoto, A., Jacobsen, S.B., 2014. Calcium and titanium isotopic fractionations during evaporation. Geochimica et Cosmochimica Acta 140, 365-380.

3. ANALYTICAL METHODS FOR REE ISOTOPIC ANALYSIS

3.1 Introduction

Rare earth elements (REEs) comprise 14 naturally occurring lanthanides from La to Lu. The concentrations of REEs plotted against their atomic numbers (*i.e.*, REE pattern) after normalizing to CI chondrites or Post-Archean Australia Shales has been used for tracking geochemical processes in various fields such as low temperature aqueous geochemistry, igneous and metamorphic petrology, and cosmochemistry (Lipin and McKay, 1989).

Rare earth isotopes are most commonly used for radiometric dating and tracing including long-living ^{138}La-^{138}Ce and ^{147}Sm-^{143}Nd, and short-lived ^{146}Sm-^{142}Nd (Lugmair and Marti, 1977; Jacobsen and Wasserburg, 1980; Shimizu et al., 1984; Tanaka et al., 1987; Lugmair and Galer, 1992; Nyquist et al., 1995). The decay of ^{176}Lu to ^{176}Hf is also used for radiogenic dating and tracing. Many REEs have isotopes with large neutron capture cross sections, particularly ^{149}Sm, ^{155}Gd, and ^{157}Gd (Russ III et al., 1971; Sands et al., 2001; Hidaka et al., 2006; Hidaka and Yoneda, 2007; Leya and Masarik, 2013). The isotopic anomalies induced by neutron capture effects from galactic cosmic rays and solar cosmic rays can be recorded in extraterrestrial samples and used to trace cosmogenic effects. Isotopic anomalies of REEs induced by nucleosynthesis have also been observed in meteorites and their components for tracking heterogeneity of the early solar system (Brennecka et al., 2013; Shollenberger et al., 2018; Shollenberger and Brennecka, 2020).

While considerable attention has been paid to REE patterns and isotopic anomalies of some REEs, in general applications of REE isotopes are remain unexplored, especially for mass-dependent fractionations. Rare earth elements span a large range of 50% condensation

temperatures from 1356 to 1647 K in solar nebular condition (Lodders, 2003). Stable isotopic fractionations of REEs induced by condensation and evaporation have been observed in the earliest condensate from the solar nebula, fine-grained calcium aluminum inclusions (Hu et al., 2021). Isotope signatures of REEs induced by condensation of the solar nebula may have also been preserved in meteorites and their components. The stable isotopic compositions of REE of the bulk silicate Earth is also not well known, lacking a baseline to define the isotopic fractionations observed in extraterrestrial samples.

Most REE are present in nature as trivalent cations. Exceptions include Ce, which can also be present as a quadrivalent cation in oxidizing condition, and Eu, which can be present as a divalent cation in reducing environment. Isotopic fractionations of Ce induced by oxidation change have been observed in marine ferromanganese deposits and hot spring precipitates (Nakada et al., 2013, 2016). The equilibrium isotopic fractionation of Eu can be measured by synchrotron technique of nuclear resonance inelastic X-ray scattering (NRIXS), which can be compared to isotope analysis of natural samples (Toellner et al., 2006; Dauphas et al., 2018a). Isotopic fractionations of Eu have also been found to be related with negative Eu abundance anomaly in the REE pattern (Lee and Tanaka, 2021). During igneous processes, how the REE isotopic fractionation evolve in general is also not well known. Isotopic fractionations of REEs are also likely to present especially in the late stage of magma evolution.

Despite the potential application of REE stable isotopic fractionations, very few studies have been focused on REE isotope analyses except for Nd and Sm. One of the major challenges is to separate REEs from each other since they present very similar behavior during partitioning of

chromatography chemistry. Isotopic fractionation of REEs are also very limited, generally in sub-‰ level, requiring high precision analyses.

For the separation of REEs, we have developed a fluoropolymer pneumatic liquid chromatography (FPLC) system, which can use extremely long and thin column and fine resin to separate REEs in one elution (Ireland et al., 2013; Dauphas et al., 2018b; Hu et al., 2021). To distinguish the sub-‰ isotopic fractionation, we have also established approaches to analyze Ce, Nd, Sm, Gd, Dy, and Er using the double-spike (DS) technique while analytical methods of Yb isotopes have been established in a previous study (Tissot, 2015). The analytical methods are tested by measuring a series of geostandards and compared with those measured by sample standard bracketing.

3.2 Samples and Methodology

3.2.1 Isotope Standard Preparation and Determination

We have prepared isotope standards for the isotope measurements of Ce, Nd, Sm, Eu, Gd, Dy, and Er. High purity (>99.99%) powders were purchased from High Purity Metal Specialists (ESPI) in the form of Nd_2O_3, Sm_2O_3, Gd_2O_3, Eu_2O_3, Dy_2O_3, and Er_2O_3. Since CeO_2 cannot be digested completely in diluted HNO_3 and HCl, high purity (>99.995%) $Ce_2(CO_3)_3$ was purchased from Sigma-Aldrich for Ce reference materials. For each of the REE in this study, approximately 1000 ppm stock solution was first prepared in a precleaned FEP vial by dissolving 50 to 200 mg of oxide or carbonate powder in 50 g 3 mol/L HNO_3. A small fraction of the stock solution was then diluted to 1 ppm in a precleaned PFA bottle and used for routine isotope measurement. The

rest of the reference materials is saved for future use and ready to be distributed upon request (named as OL-series, *e.g.*, OL-Eu; Hu et al., 2021).

The stable isotopic fractionation is expressed as the deviation in ‰ per atomic mass unit (‰/amu) relative to the reference material using the following notation (φ superscript refers to the δ notation on a per amu basis),

$$\delta^{\varphi}\mathrm{E} = \left(\frac{R_{\mathrm{smp}}^{\mathrm{i/k}}}{R_{\mathrm{std}}^{\mathrm{i/k}}} - 1\right)\frac{1000}{m_{\mathrm{i}} - m_{\mathrm{k}}}, \qquad (3.1)$$

where m_{i} and m_{j} are the mass numbers of isotopes $^{\mathrm{i}}$E and $^{\mathrm{k}}$E, and $R_{\mathrm{smp}}^{\mathrm{i/k}}$ and $R_{\mathrm{std}}^{\mathrm{i/k}}$ are the isotope ratios for the sample and standard. Unlike TIMS, the true isotope ratios of the reference materials cannot be determined precisely using an MC-ICPMS due to the systematic instrumental shift that varies with time. However, isotope ratios measured in a short time period are subject to the same extent of instrumental shift, allowing for accurate determination of the relative difference of the isotope ratios between the sample and standard (*i.e.*, $\delta^{\varphi}\mathrm{E}$).

Some of the isotope analyses are conducted by sample-standard bracketing (SSB), whereby measurements of samples are interspersed with those of standards. The stable isotopic fractionation is determined by,

$$\delta^{\varphi}\mathrm{E} = \left(\frac{2R_{\mathrm{smp,ms}}^{\mathrm{i/k}}}{R_{\mathrm{std,ms,1}}^{\mathrm{i/k}} + R_{\mathrm{std,ms,2}}^{\mathrm{i/k}}} - 1\right)\frac{1000}{m_{\mathrm{i}} - m_{\mathrm{k}}}, \qquad (3.2)$$

where $R^{\mathrm{i/k}}_{\mathrm{smp,ms}}$ is the measured isotope ratio of the sample, and $R^{\mathrm{i/k}}_{\mathrm{std,ms,1}}$ and $R^{\mathrm{i/k}}_{\mathrm{std,ms,2}}$ are the measured isotope ratios of the standard before and after the sample measurement. The instrumental biases on the sample and standard are thus cancelled by taking the average of the standard ratio before and after the sample ratio. The stable isotopic fractionation $\delta^{\varphi}\mathrm{E}$ of the sample is determined without knowing the true isotope ratios of the standard.

For isotope analysis using the double-spike (DS) technique, the isotope ratios of the reference material are required for the calibration of the DS. In this study, the isotope ratios of the isotope standards are internally normalized to one pair of isotopes, ${}^{\mathrm{j}}\mathrm{E}/{}^{\mathrm{k}}\mathrm{E}$. The ratio of ${}^{\mathrm{j}}\mathrm{E}/{}^{\mathrm{k}}\mathrm{E}$ is first set to be a constant $R^{\mathrm{j/k}}_{\mathrm{ref}}$ (*e.g.*, ${}^{\mathrm{j}}\mathrm{E}/{}^{\mathrm{k}}\mathrm{E}$ of a well-stablished reference material determined by TIMS) as the reference ratio. The fractionation factor between the measured standard ratio $R^{\mathrm{j/k}}_{\mathrm{m}}$ and reference ratio $R^{\mathrm{j/k}}_{\mathrm{ref}}$ can be calculated assuming exponential mass fractionation law,

$$\alpha = \ln\left(R^{\mathrm{j/k}}_{\mathrm{m}}/R^{\mathrm{j/k}}_{\mathrm{ref}}\right)/\ln\left(m_{\mathrm{j}}/m_{\mathrm{k}}\right). \qquad (3.3)$$

The fractionation factor α is then applied to the measured standard isotope ratios ${}^{\mathrm{i}}\mathrm{E}/{}^{\mathrm{k}}\mathrm{E}$ to obtain their $R^{\mathrm{i/k}}_{\mathrm{std}}$ following,

$$R^{\mathrm{i/k}}_{\mathrm{std}} = R^{\mathrm{i/k}}_{\mathrm{m}}/\left(\frac{m_{\mathrm{i}}}{m_{\mathrm{k}}}\right)^{\alpha}. \qquad (3.4)$$

The true isotope ratios of the reference materials are not necessary for DSB since the offset of the double spike data reduction of the sample + DS mixture will be cancelled by bracketing of the standard + DS mixture.

Table 3.1 Composition of the double spike and the optimal proportion of the double spike and standard for Ce, Nd, Sm, Gd, Dy, and Er.

Ce	Proportion	136	138	140	142
Spike 136	44.35%	**50.54%**	0.34%	45.79%	3.33%
Spike 138	55.65%	0.19%	**26.00%**	69.90%	3.84%
Double spike	45.17%	22.52%	14.62%	59.21%	3.61%
Standard	54.83%	0.19%	0.25%	88.45%	11.11%
DS. and std. mixture	-	10.27%	6.74%	75.24%	7.73%

Nd	Proportion	142	143	144	145	146	148	150
Spike 145	41.52%	0.92%	0.70%	2.55%	**91.73%**	3.67%	0.28%	0.15%
Spike 146	58.48%	0.42%	0.29%	0.68%	0.64%	**97.63%**	0.24%	0.10%
Double spike	73.52%	0.63%	0.46%	1.46%	38.46%	58.62%	0.26%	0.12%
Standard	26.48%	27.20%	12.20%	23.80%	8.30%	17.20%	5.70%	5.60%
DS. and std. mixture	-	7.66%	3.57%	7.37%	30.48%	47.65%	1.70%	1.57%

Sm	Proportion	144	147	148	149	150	152	154
Spike 147	62.96%	0.05%	**98.30%**	0.85%	0.36%	0.11%	0.21%	0.12%
Spike 149	37.04%	0.03%	0.38%	0.79%	**97.68%**	0.56%	0.39%	0.17%
Double spike	64.22%	0.04%	62.03%	0.83%	36.41%	0.28%	0.28%	0.14%
Standard	35.78%	3.07%	14.99%	11.24%	13.82%	7.38%	26.75%	22.75%
DS. and std. mixture	-	1.13%	45.20%	4.55%	28.33%	2.82%	9.75%	8.23%

Gd	Proportion	152	154	155	156	157	158	160
Spike 155	61.36%	0.01%	0.23%	**94.31%**	2.85%	1.02%	1.05%	0.53%
Spike 157	38.64%	0.05%	0.31%	4.02%	5.60%	**79.71%**	8.09%	2.28%
Double spike	60.36%	0.03%	0.26%	59.43%	3.91%	31.42%	3.77%	1.21%
Standard	39.64%	0.20%	2.18%	14.80%	20.47%	15.65%	24.84%	21.86%
DS. and std. mixture	-	0.09%	1.02%	41.73%	10.48%	25.17%	12.12%	9.39%

Dy	Proportion	156	158	160	161	162	163	164
Spike 161	62.96%	0.02%	0.07%	0.23%	**95.75%**	2.51%	0.89%	0.55%
Spike 163	37.04%	0.01%	0.01%	0.03%	0.36%	1.25%	**96.84%**	1.52%
Double spike	56.25%	0.02%	0.05%	0.16%	60.41%	2.04%	36.43%	0.91%
Standard	43.75%	0.06%	0.10%	2.34%	18.91%	25.51%	24.90%	28.18%
DS. and std. mixture	-	0.04%	0.07%	1.11%	42.26%	12.31%	31.39%	12.84%

Er	Proportion	162	164	166	167	168	170
Spike 166	76.03%	0.02%	0.06%	**96.31%**	2.78%	0.71%	0.15%
Spike 167	23.97%	0.01%	0.05%	2.81%	**91.77%**	5.05%	0.32%
Double spike	67.50%	0.02%	0.06%	73.90%	24.11%	1.75%	0.19%
Standard	32.50%	0.14%	1.61%	33.61%	22.93%	26.78%	14.93%
DS. and std. mixture	-	0.06%	0.56%	60.80%	23.73%	9.88%	4.98%

3.2.2 Double-Spike Preparation, Calibration, and Doping Tests

The double-spike technique was first introduced by Dodson (1963) to correct for instrumental mass bias induced by surface ionization techniques. This was later used in isotope

analyses in MC-ICPMS, and has been widely applied to a series of isotope systems with 4 or more isotopes. The benefit of using DS technique for isotope measure on MC-ICPMS compared to SSB is that it can correct for isotopic fractionation during sample processing including digestion and purification. The DS technique is also less sensitive to the status of MC-ICPMS and mismatched concentrations, acid molarities, and matrix effects.

The DS technique can correct the isotope analyses for any isotopic fractionation induced by sample processing (digestion, purification, etc.) and instrumental determination. The correction is achieved by mixing the sample with mixture of distinct isotope composition of the same element, which are usually composed of 2 highly enriched isotopes (namely, DS). The DS is ideally added early in the sample processing scheme, such as digestion. The homogenization of the sample and the DS at early stage will ensure that their atoms have the same speciation and subject to the same isotopic fractionation during the later laboratory processing. The choice of the isotopes, their proportions in the DS mixture, and the proportion of the DS and sample have been extensively studied and the reader is referred to the literature cited in Chapter 2. After mixing and equilibrating the DS with the sample, the DS-sample mixture is purified and isotopic ratios are measured on a mass spectrometer. The measured isotope ratio is,

$$R_{\mathrm{m}}^{\mathrm{i/k}} = \left[(1-f)R_{\mathrm{std}}^{\mathrm{i/k}}\left(\frac{m_{\mathrm{i}}}{m_{\mathrm{k}}}\right)^{\alpha} + f\mathrm{R}_{\mathrm{sp}}^{\mathrm{i/k}}\right]\left(\frac{m_{\mathrm{i}}}{m_{\mathrm{k}}}\right)^{\beta}. \quad (3.5)$$

where $R_{\mathrm{m}}^{\mathrm{i/k}}$, $R_{\mathrm{smp}}^{\mathrm{i/k}}$ and $R_{\mathrm{sp}}^{\mathrm{i/k}}$ are measured, sample and spike ratios of isotope $^{\mathrm{i}}$E and $^{\mathrm{k}}$E, f is the proportion of $^{\mathrm{i}}$E in the spike-sample mixture, β is the instrumental mass bias (assuming that mass fractionation follows the exponential law), and m_{i} and m_{k} is the mass of $^{\mathrm{i}}$E and $^{\mathrm{k}}$E. If no isotopic

anomaly is present, the sample isotope ratios can be related to the standard isotope ratios through the following expression,

$$R_{\mathrm{smp}}^{\mathrm{i/k}} = R_{\mathrm{std}}^{\mathrm{i/k}} \left(\frac{m_{\mathrm{i}}}{m_{\mathrm{k}}}\right)^{\alpha}, \quad (3.6)$$

where α is the exponent of the exponential mass fractionation corresponding to natural fractionation of the sample relative to the standard. This is the quantity of interest in the DS approach. Substituting Eq. 3.6 into Eq. 3.5, one gets,

$$R_{\mathrm{m}}^{\mathrm{i/k}} = \left[(1-f)R_{\mathrm{std}}^{\mathrm{i/k}} \left(\frac{m_{\mathrm{i}}}{m_{\mathrm{k}}}\right)^{\alpha} + f\mathrm{R}_{\mathrm{sp}}^{\mathrm{i/k}}\right] \left(\frac{m_{\mathrm{i}}}{m_{\mathrm{k}}}\right)^{\beta}. \quad (3.7)$$

Eq. 3.7 is a canonical equation for DS data reduction. The unknowns in this equation are f, α and β. Therefore, the system can be solved using a set of three equations, which can be obtained by applying Eq. 3.7 to 3 isotope ratios constituted by 4 isotopes.

For the element that have more than 4 abundant isotopes that can be used for DS data reduction, the system is over-constrained. The unknowns f, α and β can be otherwise obtained by performing minimization on

$$\theta = \sum_{\mathrm{i}} \left\{ \frac{R_{\mathrm{m}}^{\mathrm{i/k}} - \left[(1-f)R_{\mathrm{std}}^{\mathrm{i/k}} \left(\frac{m_{\mathrm{i}}}{m_{\mathrm{k}}}\right)^{\alpha} + \mathrm{fR}_{\mathrm{sp}}^{\mathrm{i/k}}\right] \left(\frac{m_{\mathrm{i}}}{m_{\mathrm{k}}}\right)^{\beta}}{\epsilon_{\mathrm{m}}} \right\}^2, \quad (3.8)$$

where ϵ_{m} is the standard deviation of the measured ratio on ${}^{\mathrm{i}}\mathrm{E}/{}^{\mathrm{k}}\mathrm{E}$. Therefore, the measured ratios with large errors will have small weights for DS data reduction. The advantage of using Eq. 3.8

instead of Eq. 3.7 is that more isotopes can be used for elements with more than 4 abundant isotopes, which reduces the potential fluctuation.

Although the isotopic composition of the isotope standard is anchored by the reference value through Eq. 3.3 and 3.4, the true isotope ratios of the isotope standards are not known on MC-ICPMS. The DS measurements are performed in a way like SSB, whereby mixtures of the sample and DS are interspersed by mixtures of the standard and DS (double-spike bracketing, DSB; Albalat et al., 2012). The isotope ratios of the sample and the standards before and after the sample are first determined by DS reduction of their sample-spike or standard-spike mixture. The stable isotopic fractionation of the sample relative to the standard is then obtained by their isotope ratios using Eq. 3.2. The influence of the choice of reference ratio will be cancelled since the standard and sample measured this way are subject to the same extent of instrumental bias like SSB.

To set up the DS technique, spike solutions of each REE need to be prepared from enriched isotopes and calibrated with known isotope standards. For DS preparation, two enriched isotopes for each REE in powder form (*i.e.*, single spikes) were purchased from Oak Ridge National Lab, digested with HNO_3, and mixed according to recommended spike composition based on optimal spike composition from supplementary data in Rudge et al. (2009). The mixed spikes were then diluted in 3 mol/L HNO_3 to 40-140 ppm as stock solutions. Solutions of approximately 20 g were taken from the stock solutions and diluted to 1 ppm using 3 mol/L HNO_3 for calibration and routine isotope analysis.

For calibration, the standard and DS were first mixed in varied proportion, covering a range from 10% DS to 90% DS. The mixtures with different proportion of DS were then heated to dryness on a hot plate to ensure complete homogeneity. The dried standard-spike mixtures were diluted to approximately 30 ppb solutions in 0.3 mol/L HNO_3+0.002 mol/L HF acid and analyzed via MC-ICPMS. The measured ratios of the mixtures were subject to a reversed DS data reduction by switching the position of the standard and DS in Eq. 3.7.

$$R_{\mathrm{m}}^{\mathrm{i/k}} = \left[(1-f)R_{\mathrm{sp,ms}}^{\mathrm{i/k}}\left(\frac{m_{\mathrm{i}}}{m_{\mathrm{k}}}\right)^{\alpha} + fR_{\mathrm{std,ref}}^{\mathrm{i/k}}\right]\left(\frac{m_{\mathrm{i}}}{m_{\mathrm{k}}}\right)^{\beta}. \quad (3.9)$$

Isotope ratios within the optimal range will be averaged and used as the isotope ratio of the DS. It is worth noting that the value of the DS isotope ratio depends on the choice of the reference isotope ratio. However, the stable isotopic fractionations between the sample and standard are not affected by either the reference isotope ratios or the DS isotope ratio used because the influence on both the sample and standard is cancelled by DSB.

Extensive tests have been conducted on DS measurements of Nd, Sm, Gd, Dy, and Er including isobaric interference, and matrix effects by doping elements into the standard-spike mixture. The influences of acid molarity and concentration match during bracketing are also tested by varying the acid molarity and concentration in the standard-spike mixture. The test results are used to interpret their influences on natural samples.

3.2.3 Geostandard Selection and Digestion

Geological standards analyzed in this study include basalts (BIR-1a × 4, BHVO-2 × 3, BCR-2 × 2, W-2 × 2,), andesites (AGV-2 × 3), granites (G-3 × 3), a schist (SDC-1), a limestone

(CCH-1), and marine ferromanganese crusts (NODA-1 × 2, NODP-1). More specifically, 3 geostandards (BIR-1a, BHVO-2, AGV-2) are analyzed using SSB and purified by REE elution of FPLC system; 7 geostandards (BIR-1a × 2, BHVO-2, BCR-2, W-2, AGV-2, G-3) are analyzed using DS and purified once using FPLC; 11 geostandards (BIR-1a, BHVO-2, BCR-2, W-2, AGV-2, G-3, SDC-1, CCH-1, NODA-1 × 2, NODP-1) are analyzed using DS and purified twice using FPLC elution. Some REEs from NODA-1 and NODP-1 have been purified 3 times to eliminate isobaric interferences. We will compare the same geostandards analyzed by SSB and DS to test the reliability of DS technique and compare geostandards that are purified once and twice using FPLC system to interpret the requirement of purification.

For geostandards analyzed using DS technique, variable amounts of Ce, Nd, Sm, Gd, Dy, Er, and Yb DS stock solution were doped into 50 to 150 mg geostandard in a precleaned PTFE beaker based on the optimal mixing ratios and the masses of the REEs in the geostandard. The mixture was evaporated to dryness and digested on a hotplate using HF-HNO_3 (3:1) at 135 °C for 48 hours. The geostandard were then dried again and redissolved in aqua regia to attack remaining fluorides. This step was repeated until the solution is clear. Digested geostandards were then dried and redissolved in 6 to 30 ml of 3 or 11 M HNO_3 depending on the loading media of the chemistry of REE extraction. About 600 mg limestone CCH1 was first digested using concentrated HCl after being doped with DS stock solution and then digested in HF-HNO_3 (3:1) followed by aqua regia. Geostandards analyzed using SSB were digested following a similar procedure except that they are not doped with DS.

3.2.4 Bulk REE Extraction

Before REE were separated from each other, the bulk REEs were first extracted from the digested solution by passing through prepacked TODGA columns (Pourmand et al., 2012). For geostandards that are less than 100 mg, one prepacked TODGA column is enough for REE extraction. The procedure of column chemistry can be found in Pourmand et al. (2012). For geostandards that are larger than 100 mg, two prepacked TODGA columns are combined to increase maximum loading capacity of matrix elements in the solution. The loading media and procedure are also modified. The major difference between the original and modified procedure is that the modified procedure used 11 M instead of 3 M HNO_3, allowing for early elution of Ca to reduce the load on the resin. The yields of the REE TODGA extraction step were near 100%.

3.2.5 FPLC System

Due to their similar partitioning characteristics in resin, lanthanides have long been a challenge to separate from one another. Although progress has been made to separate individual REE using traditional, gravity-driven chromatography, those studies either focus only on a small subset of REE, or cannot provide enough resolution to allow for high precision isotope analyses. An alternative choice is to separate REE through High Performance Liquid Chromatography (HPLC). This method is free of restrictions shared by traditional column chemistry such as limited resin mesh-size and overall length of the column, both of which can cause a severe halt of elution with increasing separating resolution. HPLC is also superior to traditional column chemistry in that it has fine control of acid molarity during elution, and is capable of achieving small-step gradient ramps in elution concentration. Traditional column chemistry, on the contrary, only utilizes coarse-step elution, due to the restricted number of premix eluents that can be used.

Despite those merits, the HPLC system is rarely adopted and applied in nontraditional stable isotope geochemistry. This is because the present commercially available HPLC systems are designed to work in a mild environment, with dilute acids and organic reagent, and are not qualified for surviving the harsh conditions of ultraclean laboratories. Electronic parts for regulating the HPLC systems are placed near the elution body, barely exposed without proper protection from acid fumes, shortening the life span of the apparatus. The flow path in the FPLC system contains a significant amount of material that is easily corroded and dissolved by the concentrated acids that are widely used in isotope geochemistry, and give rise to risks of contamination.

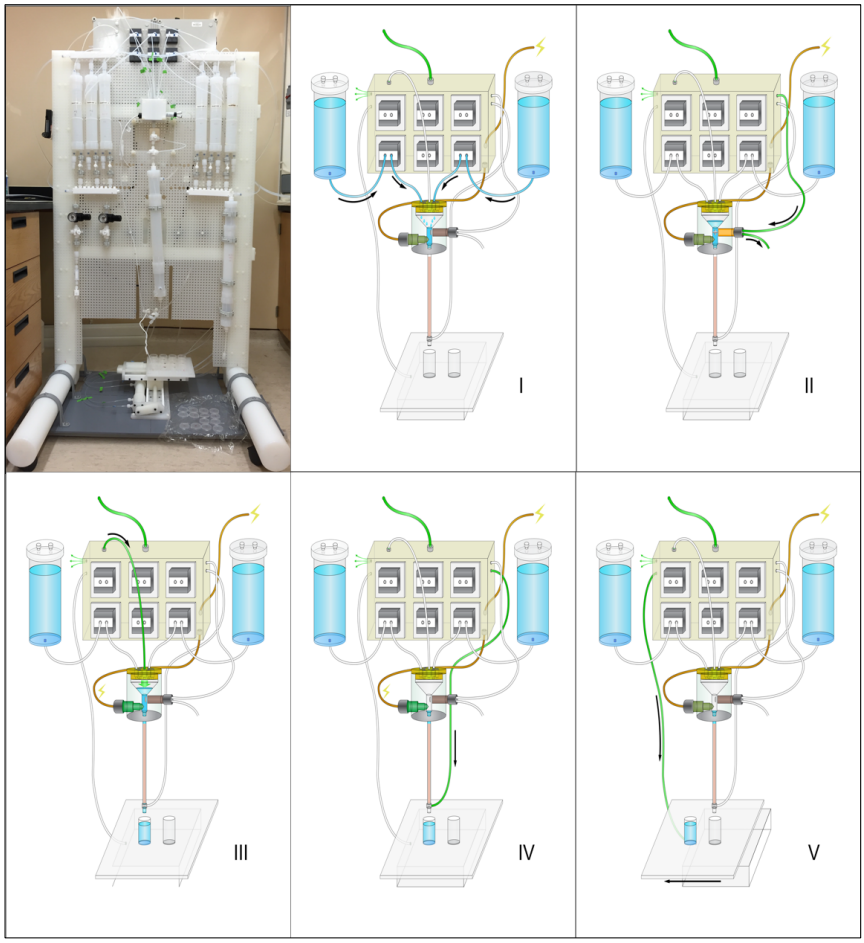

Figure 3.1 Picture and scheme of the FPLC system.

To meet the needs of separating the whole set of REEs, we developed the FPLC system at the University of Chicago (Ireland et al., 2013; Dauphas et al., 2018b; Hu et al., 2021). In the FPLC system, ultrapure reagents (*e.g.*, HF, HCl, HNO_3, H_2O_2, HIBA, or other liquids) are stored in 6 PTFE reservoirs at the top of the system (Fig. 3.1). During elution, the precise volume of reagents is driven to a mixing chamber made of PTFE via pneumatic pumps (Fig. 3.1 I). A PTFE coated stirring magnet is externally activated and mixes the reagents in the chamber (Fig. 3.1 II). Between the chamber and the column is a set of manual valves made of PTFE. When the valves are open, clean N_2 gas will pressurize the mixing chamber and force acids through the column (Fig. 3.1 III). A purge line will employ N_2 gas to purge the tube right below the column, reducing the dead volume of the system. Any solution left in the tube will be forced to beakers to maintain a good yield (Fig. 3.1 IV). Below the column is an X-Y stage with beakers on it. The X-Y stage can be controlled by computer, and can move in X and Y directions to modify the positions of beakers and collect purified solutions (Fig. 3.1 V).

The new system possesses merits of currently available HPLC systems including (1) an adjustable liquid flow path pressurized by clean N_2 gas, allowing for longer columns and finer resin, (2) fully automated elution schemes controlled through LabVIEW software, capable of fine-scale gradient elution, and (3) temperature control of the elution system (room temperature to 70 °C). Additionally, the FPLC system is free of potential problems prevalent in those HPLC systems, due to a series of modifications: (1) the liquid flow path of the FPLC system is made entirely of PTFE, and is immune to potential corrosion caused by concentrated acids and other aggressive reagents, (2) the electronic controls are housed in a box with positive pressure, and isolated from

elution parts, which protects the electronics from acid fumes in the clean laboratory, and (3) all manuals and valves are either manual or activated by clean N_2 gas, free of concerns of corrosion.

The first version of the FPLC system is presented in Ireland et al. (2013). Since the publication of Ireland et al. (2013), a new X-Y stage and a set of manual valves for sample loading has been equipped in the FPLC system. The implementation of X-Y stage (Fig. 3.2) together with a new purge system addresses the dead volume problem possessed by the old manifold solenoid valves. This further improves REE separation performance and elution yields.

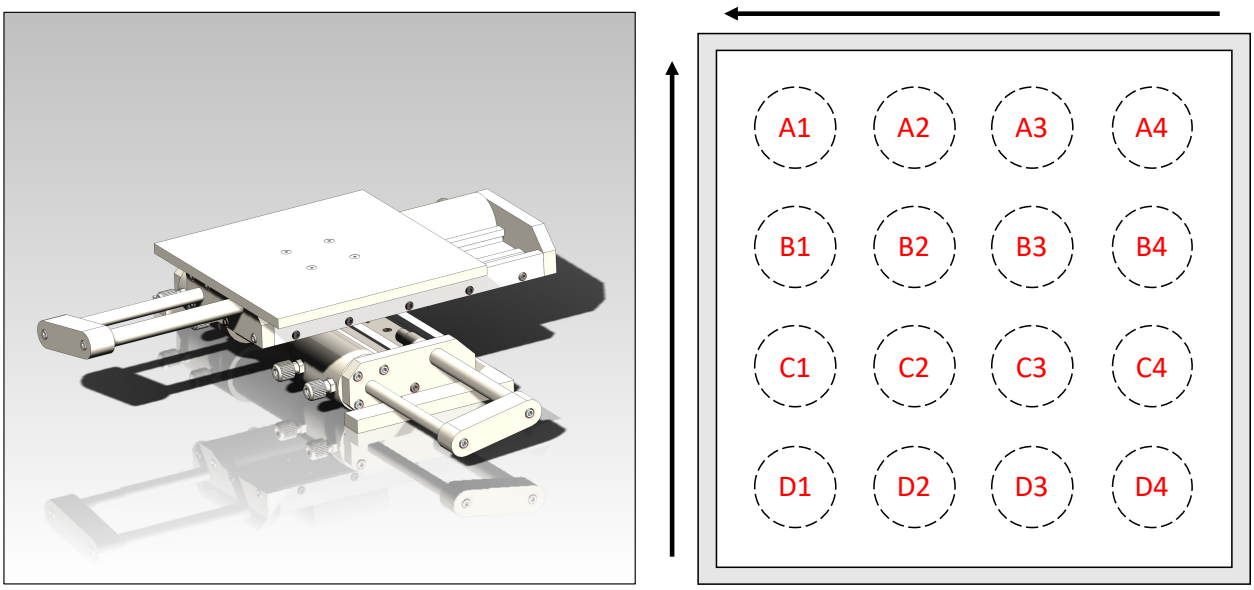

Figure 3.2 Stage for holding the beakers. The stage has 16 positions from A1 to D4.

The old sample loading valve is replaced by a sample introduction loop composed of two fluoropolymer 3-way valves (Fig. 3.3). The new manual valves are arranged in a specific way to switch easily between elution states and loading states, simplifying the sample loading process while maintaining high reliability. By changing the flow paths of the two valves, samples can be injected and stored in a tube between the two valves, to be later connected to the major flow path

of elution. A shorter but equally effective protocol is also applied in REE elution to reduce analytical blanks and improve separation efficiency.

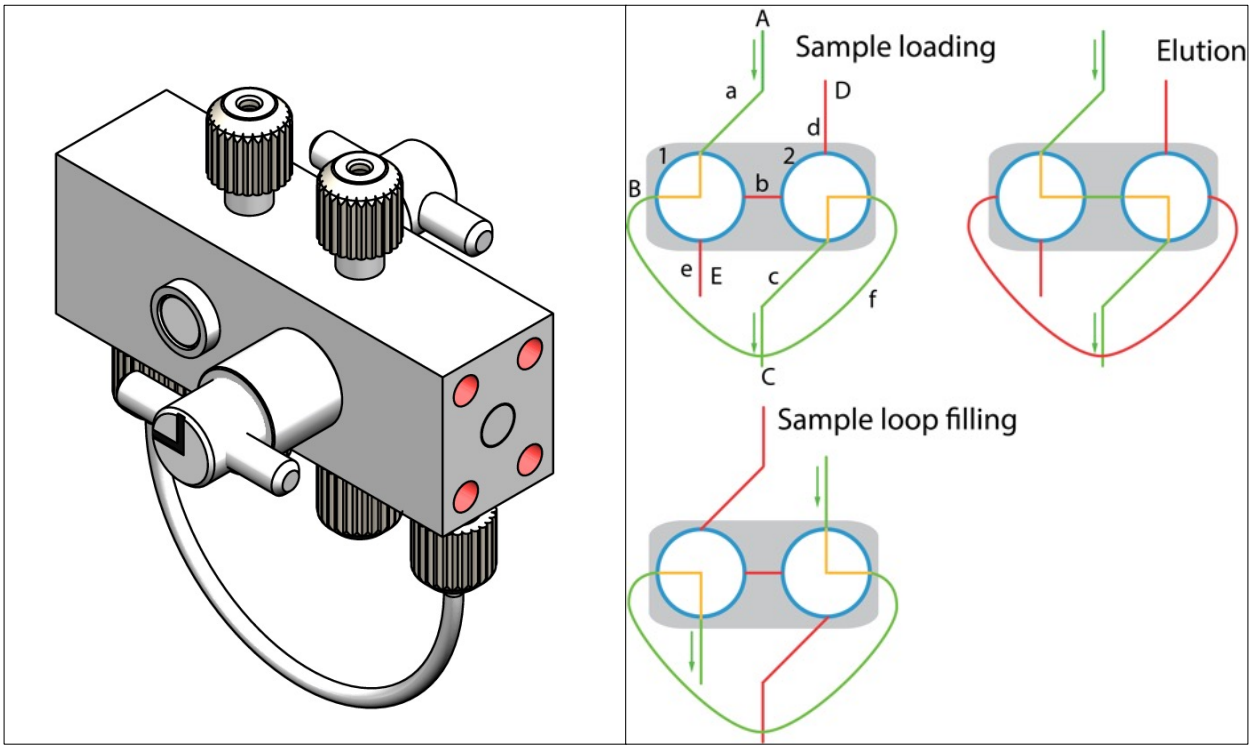

Figure 3.3 Scheme of the sample loading valve. In the sample loading stage, the sample dissolved in 350 to 500 µL reagent is passed from position A through the green line and stored in path f. In the sample loop filling stage, the sample in path f is pushed and introduced into the column by reagents from position D to position E. In the elution stage, reagents are shortcut through path b and directly introduced into the column.

Geostandards that have been purified twice were subjected to a 2-step FPLC elution at 70 °C. In the first step, the bulk of the REEs were dried in a 6 ml PTFE beaker on a hot plate to a tiny drop (<5 µL) and then dissolved in 350 to 500 µL MQ water. The dissolved sample was then loaded onto the FPLC system and subjected to a complete elution (Fig. 3.4). The eluted reagents were collected in 32 cuts ranging from 2 to 20 ml each defined by knowledge gained on a previous calibration. Approximately 5% of each cut was taken and diluted for concentration measurement

by MC-ICPMS. Elution cuts that contained a given REE were then combined based on the concentration measurements. In order to achieve a better separation for geostandard measurements, a second more specific elution step was performed. In this step, REEs that are not neighbor to each other were recombined and loaded onto the FPLC system. This involves 4 FPLC elutions (Ce, Nd, Sm/Gd/Er and Eu/Dy/Yb) ranging from 92 to 188 ml. At the end of each elution, the column was cleaned by elution of 10 mL 6 mol/L HCl followed by 10 ml MQ water at 70 °C to eliminate cross contamination. A few REEs in some geostandards are subject to a third purification to more completely eliminating isobaric interferences following a similar procedure. Geostandards that have been purified once were only subject to the first step of the 2-step FPLC elution.

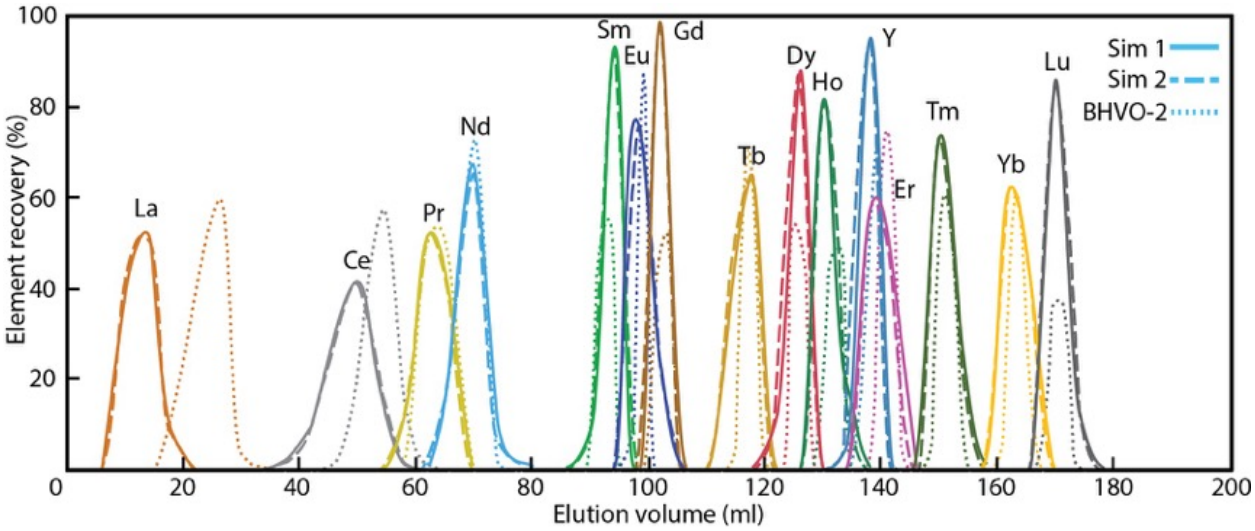

Figure 3.4 Elution curves of the FPLC elution. Sim 1, Sim 2, and BHVO-2 represent elution curves of 10 ppm multiple element solutions and geostandard BHVO-2 respectively.

3.2.6 MC-ICPMS Analysis and Data Reduction

Isotope analysis of REEs were performed using a Thermo Scientific MC-ICPMS upgraded to Neptune Plus specifications with the addition of an OnTool Booster pump. The application of

X skimmer cone and jet cone improves the signals of target isotopes by a factor of 6 compared with routine H skimmer cone + sampler cone. Sample and standard solutions are introduced into the plasma in 0.3 mol/L HNO_3 + 0.002 mol/L HF through an Apex-Q + Spiro TMD desolvating nebulizer (Elemental Scientific Inc.) using a 50 μL/minute self-aspirating PFA nebulizer. Later we switch to Aridus I and Apex Omega for some of the REE measurements. In the case of isotope analyses, major concerns of interference come from the neighboring REEs. Many of the REEs, such as Ce, Nd and Pr, have high preferences to form oxides that causes serious polyatomic isobaric effects on the isotopes of neighboring REEs. The implementation of Spiro TMD significantly enhances the ability to remove water vapor from the sample aerosol stream. This decreases oxygen introduced from sample solutions and suppresses the formation of oxides in the plasma.

For the setting of the isotope analysis, readers are referred to Hu et al. (2021). Briefly, A typical measurement has 60 s take-up time, 60 s baseline, and 40 cycles with an integration time of 8.184 s/cycle. Ce, Nd, Sm, Eu, Gd, and Er were measured in static mode. For Dy and Yb, a subconfiguration was used to monitor isobaric interferences. The subconfiguration was only measured twice at the beginning with integration times of 4.142 s each, and the intensities were averaged and used to correct for isobaric interferences of the following 40 cycles in the main cup configuration after appropriate scaling.

To save sample solution, the idle time between cycles with the same configurations was set to zero while the cycle after a configuration change was preceded by 10 s idle time. Isobaric effects from isotopes of neighboring elements were corrected by monitoring other isotopes of the

same element, calculating intensities assuming natural abundance distribution, and subtracting the intensities from those of interfered isotopes.

For SSB, isotope data reduction was done by copying the raw data into a spreadsheet and correcting for background and isobaric interferences. The DS data reduction is processed by Mathematica code wrapped in a package (CORDS; provided in the supplementary material), which can automatically read the raw ratios of isotope measurements from an input file (CSV, xls, xlsx) and conduct blank correction, isobaric interference corrections, and DS reduction through either exact solving of an equation set of 4 isotopes, or minimization of more than 4 isotopes. For each measurement, the confidence interval can be determined internally through Monte Carlo simulation, through (1) generating a large number of simulated measured ratios based on a normal distribution of the measured ratios of all the cycles in that measurement, (2) conducting the double-spike reduction on the simulated ratios, and (3) calculating the standard deviation of the results from the reduction. The REE with more than 4 abundant isotopes, combinations of 4 isotopes for exact solving are compared for the optimal DS reduction.

For geostandard measurements by both SSB and DSB, the reported δ^{φ}E values were calculated based on 3 to 12 standard-sample-standard bracketings, using each time the average isotopic ratio of the two standard measurements to normalize the isotopic ratio of the sample. The confidence intervals for the isotopic fractionations are reported as 95% confidence intervals using the student *t*-value and the variability of sample δ^{φ}E values. The confidence intervals of DS calibration and doping tests are calculated from the error propagation of the 40 cycles of each measurement based on Monte Carlo simulation.

3.3 Results and Discussion

3.3.1 Double-Spike Calibration and Doping Tests

For calibration, the standard and DS were mixed in varied proportions typically ranging from 10% DS to 90% DS (Fig. 3.5). Mixtures with DS proportions closer to the optimal ratio are supposed to provide more precise isotope analysis. According to the result of calibrations, isotope analyses for REEs show high tolerance in terms of sample-DS ratios. The mixing provides good precision at DS proportions ranging from 40% to 80% for most of the REEs, with the optimal spike proportion varying with the REEs from 60% to 75%.

We performed tests on concentration matching (Fig. 3.6) and acid molarity (Fig. 3.7) to explore the range of tolerance of DSB. For concentration tests, a batch of standard-spike mixtures were prepared, divided, and diluted to aliquots of varied concentrations. These aliquots were bracketed with standard + DS mixtures from the same batch, but at fixed concentrations. The concentration tests show that DS isotope analysis yields consistent and accurate results if the concentration of the sample is between 40% and 200% of that of the bracketing standards. Acid molarity is tested following a similar protocol and found to show negligible effect on isotope analysis with the acid molarity ranging from 0.1 mol/L HNO_3 to 0.5 mol/L HNO_3.

Doping tests on major elements such as Na, Mg, Al, Ca, Ti and Fe were conducted to evaluate the potential matrix effects on isotope analyses (Fig. 3.8-3.12). From the results of doping tests on Na, Mg, Al, Ca, Ti and Fe, the matrix effects on REEs are beyond our concerns: no effect is observed even if the doping ratios reach 100:1, a ratio that is unlikely to be achieved after the chemical purification.

We performed extensive tests on isobaric interferences (direct ones, oxides, hydroxides, nitrides and argides) to evaluate their effects on isotope analyses (Fig. 3.13-3.19). The doping tests show that the effect of compounds causing isobaric effects on isotope analysis is minor for nitrides and argides. The major concern is direct isobaric interferences from neighboring REEs. Isobaric interferences caused by isotopes from another element are usually corrected by monitoring the intensity of another isotope of that element since these two isotopes of that element are generally in proportion of their natural abundances. This, however, is less useful for REE DS measurements since many of the REEs has been doped with DS and the proportion of the isotopes is no longer that of the natural abundances. Thus, high level of purification is required for accurate isotope analyses of REE DS measurements.

Another major concern of accurate isotope analysis arises from the interference of oxides from neighboring REEs. Many REEs (*e.g.*, Ce, Nd and Pr) have a preference to combine with oxygen to form oxides in the plasma. The potential oxides formed therein cannot be corrected in MC-ICPMS, and may cause serious isobaric interference in isotopes of the studied REE. This problem is partially addressed by the application of Spiro TMD in the sample introduction system. The Spiro TMD uses a heated PTFE membrane to effectively remove water vapor from the sample aerosol stream, restricting the amount of oxygen available for oxide formation. An example can be seen from Fig. 3.17 A-D. The Nd and Sm doping test analyzed with Spiro shows substantially less induced isotopic fractionations compared to the same tests without Spiro. Aridus I and Apex Omega was later adopted as the desolvating nebulizers and found to be equally effective in terms of removing oxides.

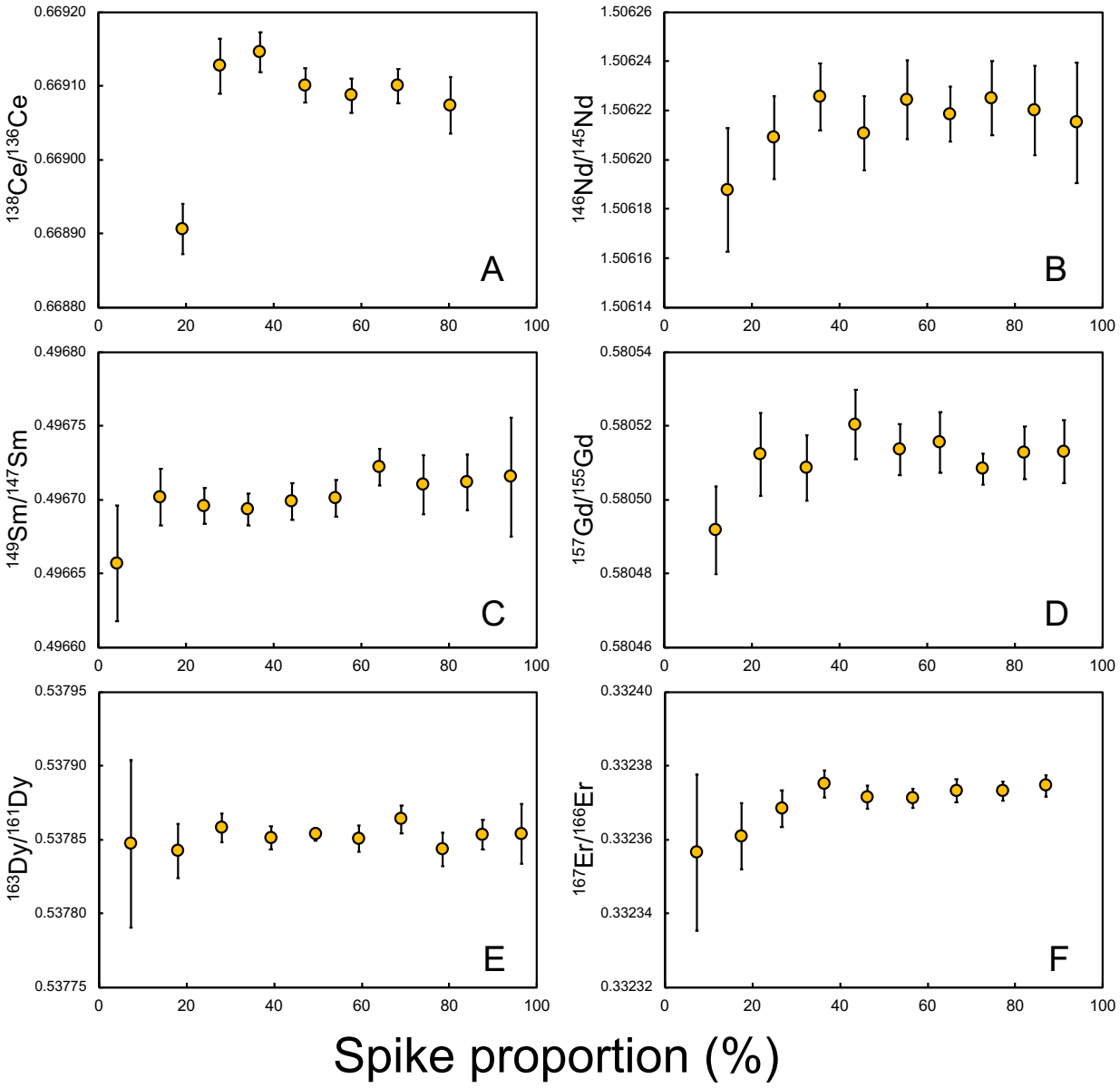

Figure 3.5 DS calibration. The vertical axis is the ratio of the two enriched isotopes of the DS. Horizontal axis is the spike proportion in the standard + DS mixture.

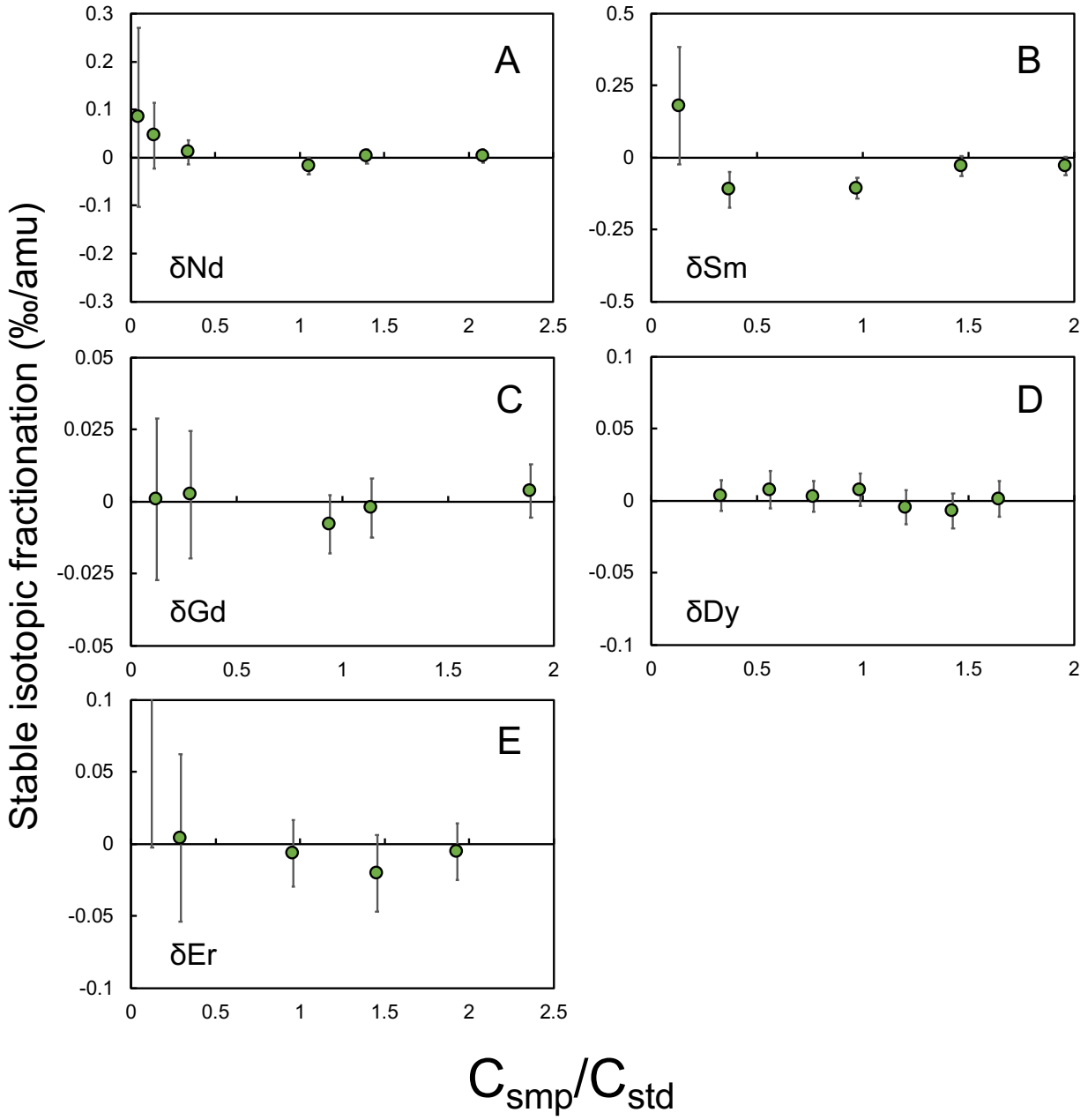

Figure 3.6 Concentration matching test of DS reduction. In the doping test, the sample analyzed using DSB has the same isotopic composition as the bracketing standard. The vertical axis is the isotopic fractionation induced by the difference of concentrations of the sample and standard. The horizontal axis represents the ratio between the concentration of the sample and that of the bracketing standard.

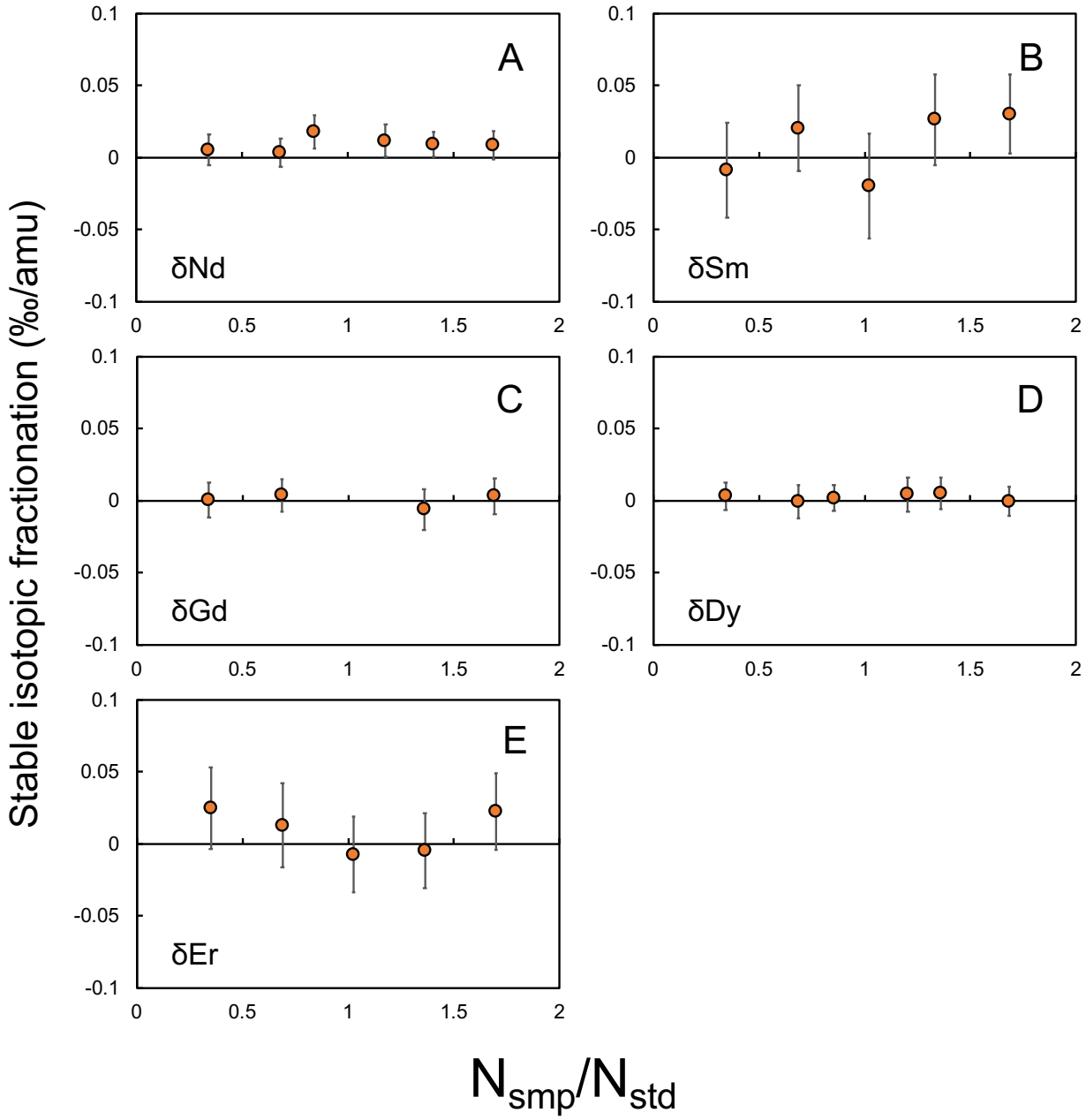

Figure 3.7 Acid molarity test of DS reduction. The sample analyzed using DSB has the same isotopic composition as the bracketing standard. The vertical axis is the isotopic fractionation induced by the difference of acid molarities of the sample and standard. The horizontal axis represents the ratio between the acid molarity of the sample and that of the bracketing standard.

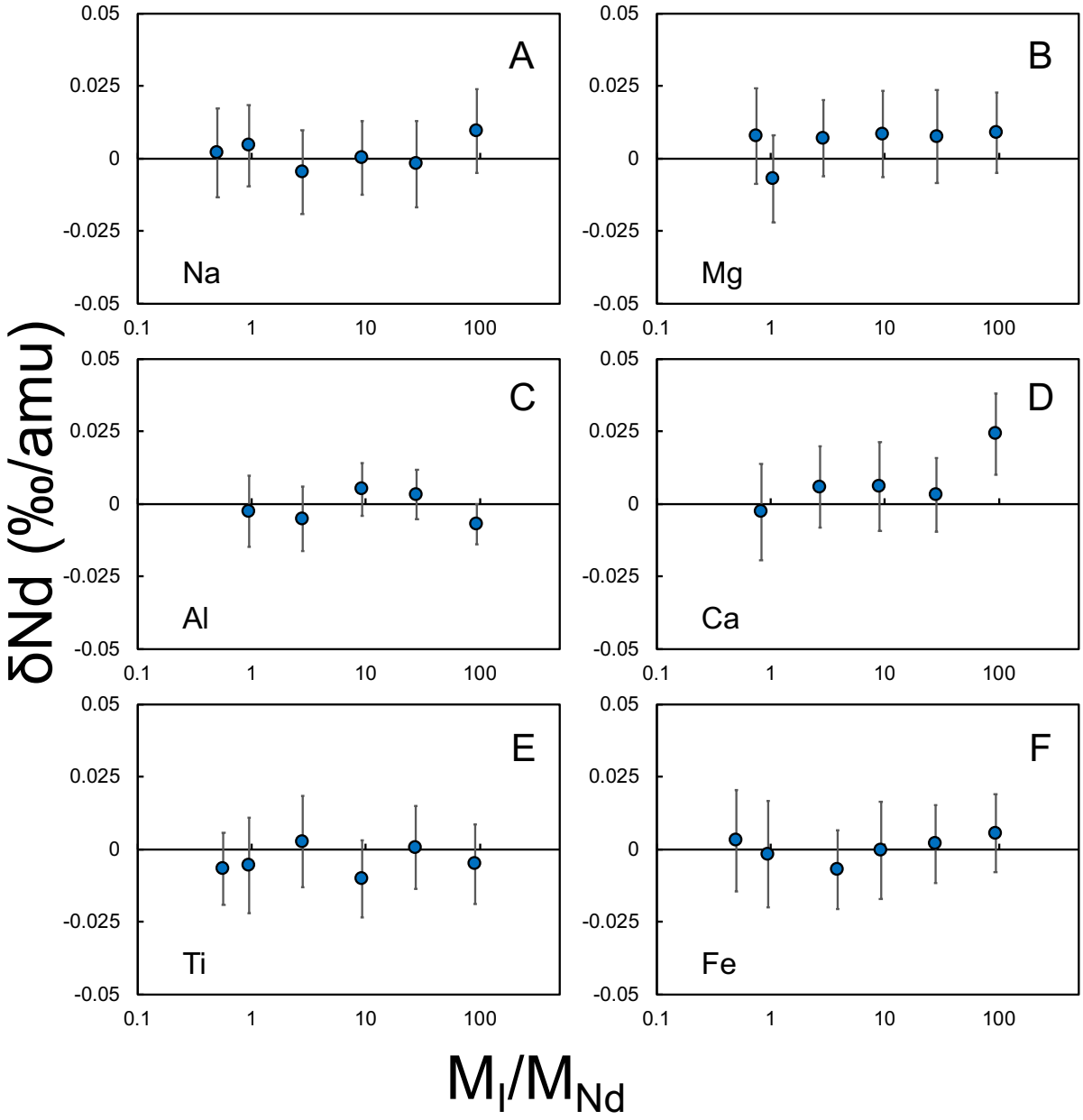

Figure 3.8 Matrix doping test for Nd DS reduction. The sample analyzed using DSB has the same isotopic composition as the bracketing standard. The vertical axis is the isotopic fractionation induced by matrix doping. The horizontal axis represent ratio between the mass of doped element and the mass of Nd.

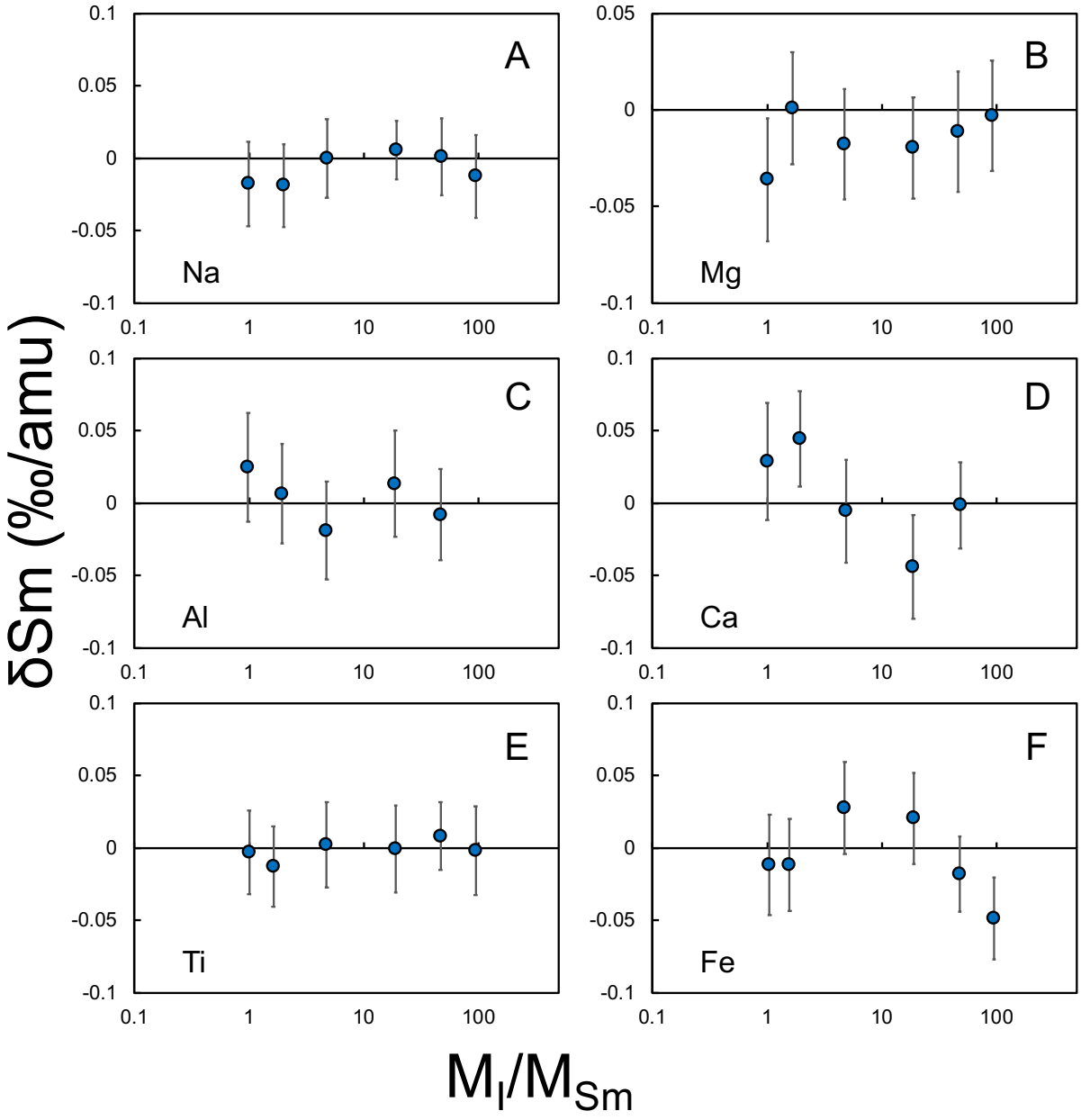

Figure 3.9 Matrix doping test for Sm DS reduction. The sample analyzed using DSB has the same isotopic composition as the bracketing standard. The vertical axis is the isotopic fractionation induced by matrix doping. The horizontal axis represent ratio between the mass of doped element and the mass of Sm.

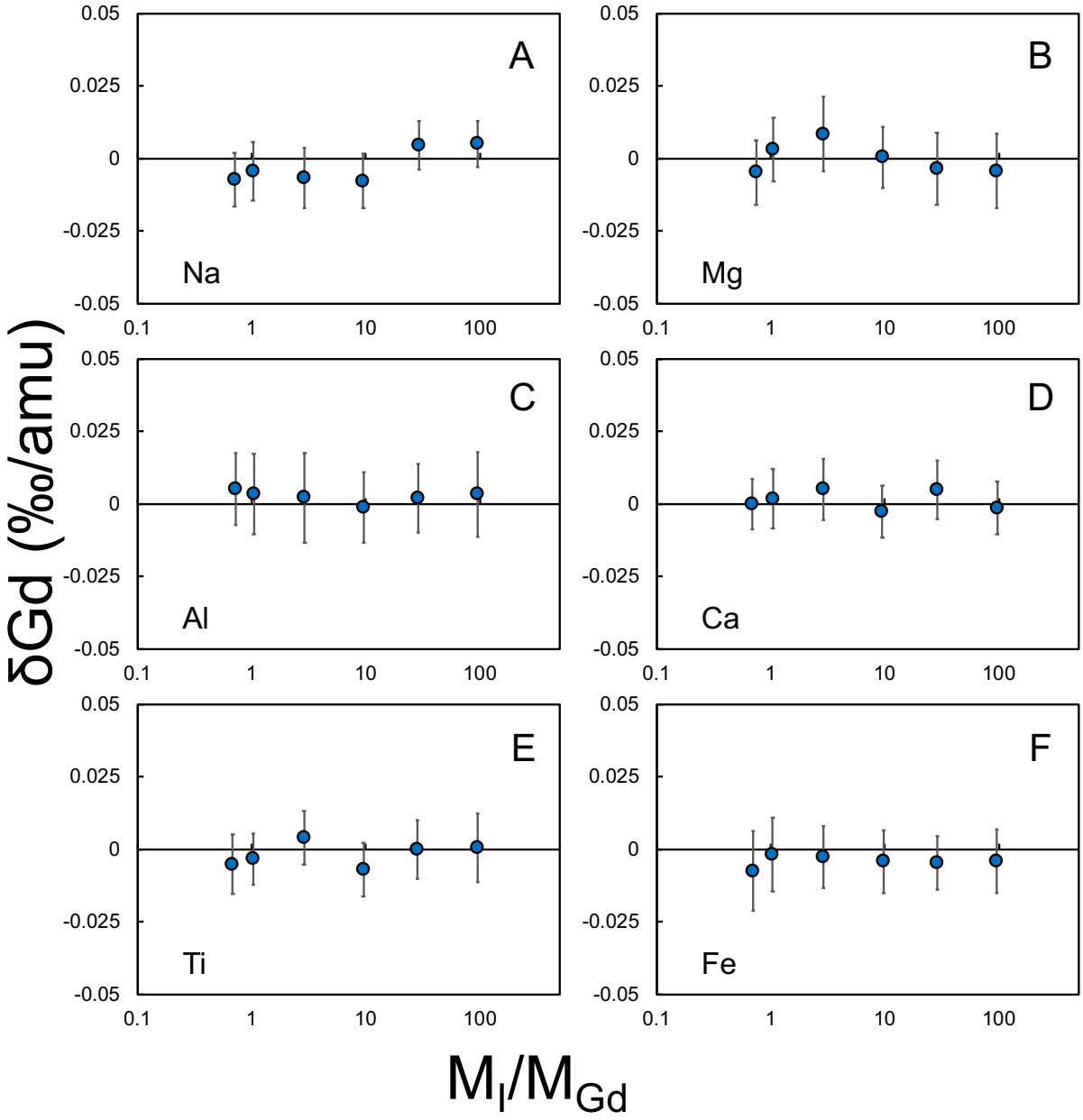

Figure 3.10 Matrix doping test for Gd DS reduction. The sample analyzed using DSB has the same isotopic composition as the bracketing standard. The vertical axis is the isotopic fractionation induced by matrix doping. The horizontal axis represent ratio between the mass of doped element and the mass of Gd.

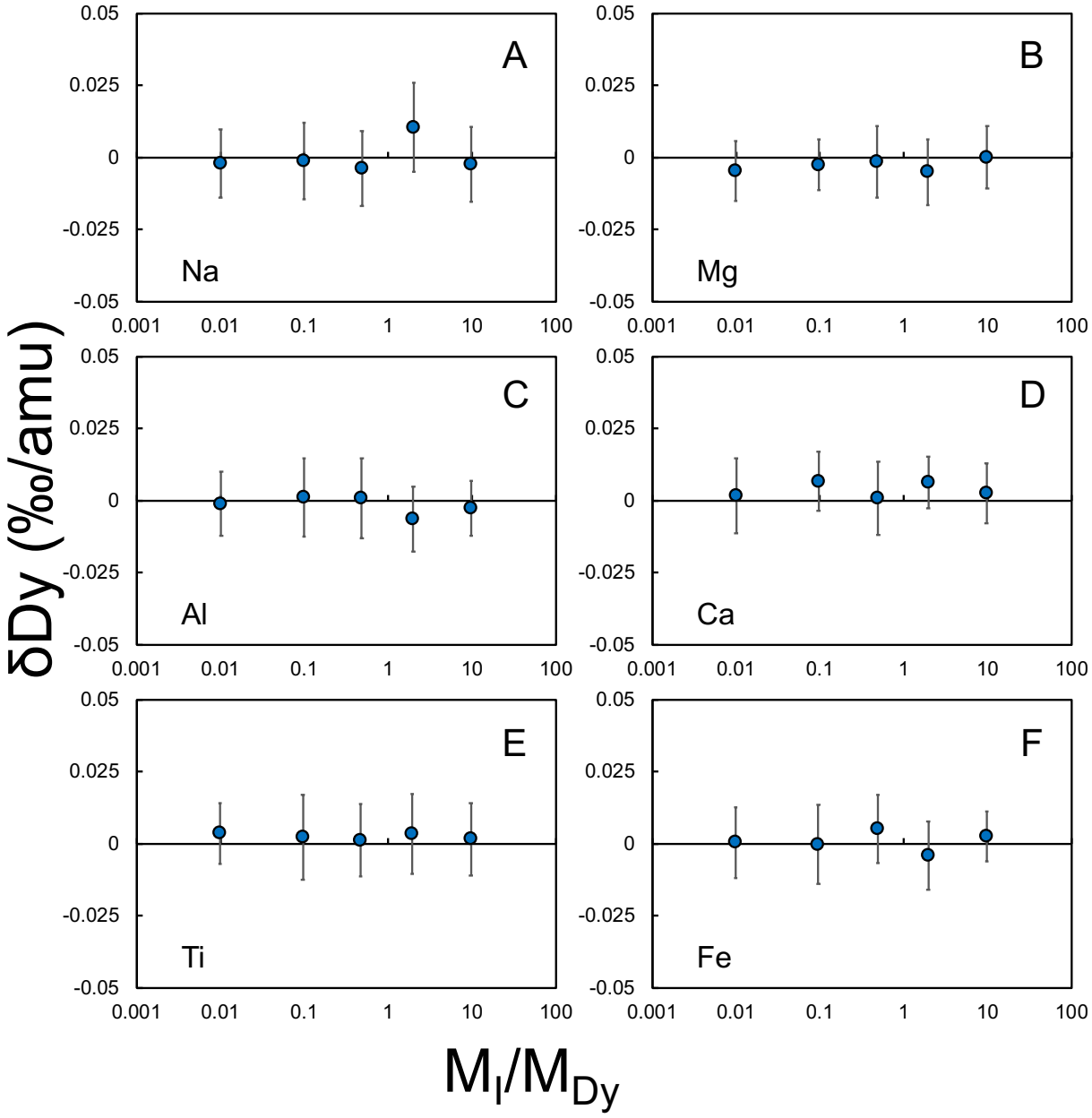

Figure 3.11 Matrix doping test for Dy DS reduction. The sample analyzed using DSB has the same isotopic composition as the bracketing standard. The vertical axis is the isotopic fractionation induced by matrix doping. The horizontal axis represent ratio between the mass of doped element and the mass of Dy.

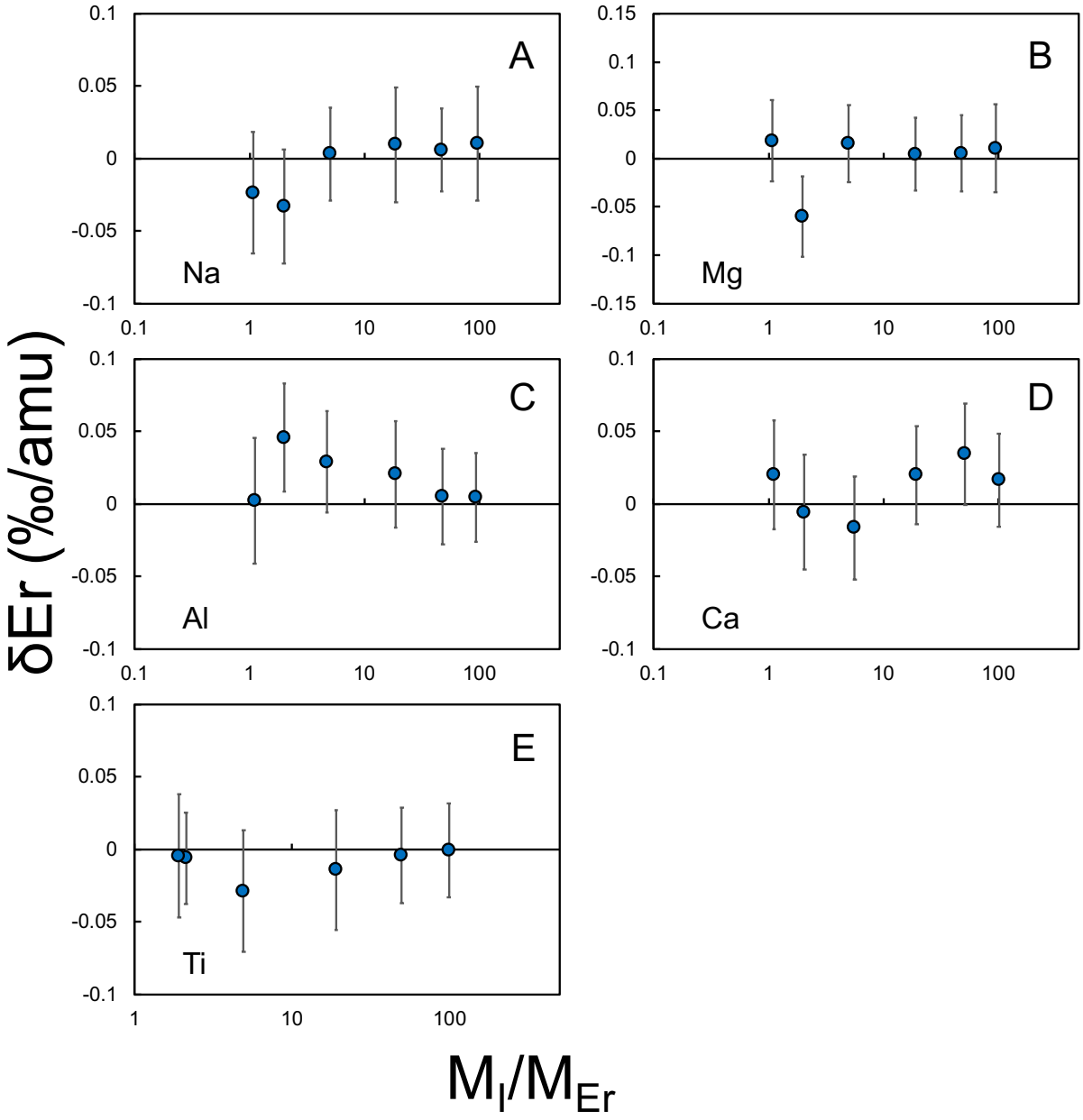

Figure 3.12 Matrix doping test for Er DS reduction. The sample analyzed using DSB has the same isotopic composition as the bracketing standard. The vertical axis is the isotopic fractionation induced by matrix doping. The horizontal axis represent ratio between the mass of doped element and the mass of Er.

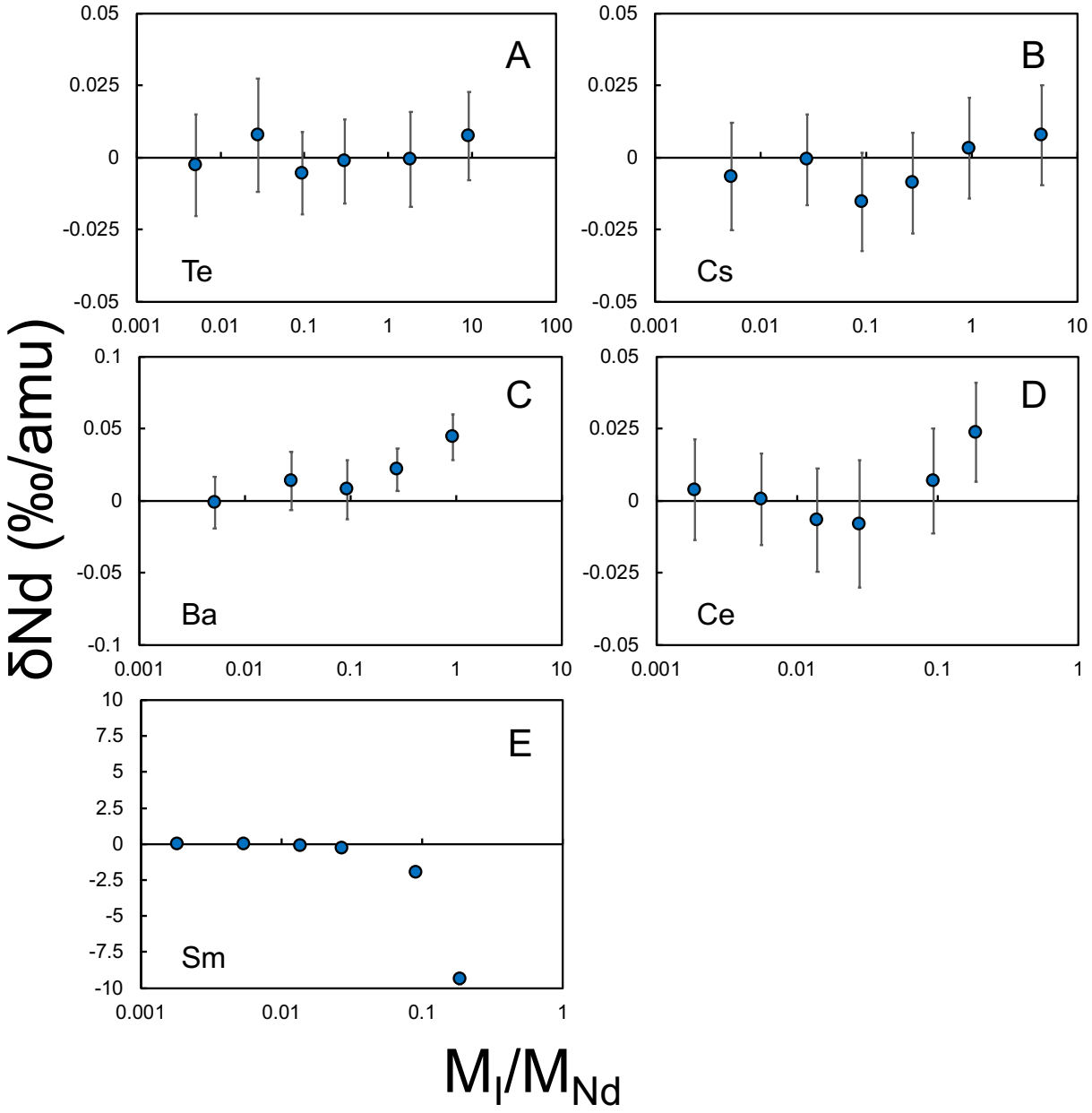

Figure 3.13 Isobaric interference doping test for Nd DS reduction. The sample analyzed using DSB has the same isotopic composition as the bracketing standard. The vertical axis is the isotopic fractionation induced by isobaric inference doping. The horizontal axis represent ratio between the mass of doped element and the mass of Nd.

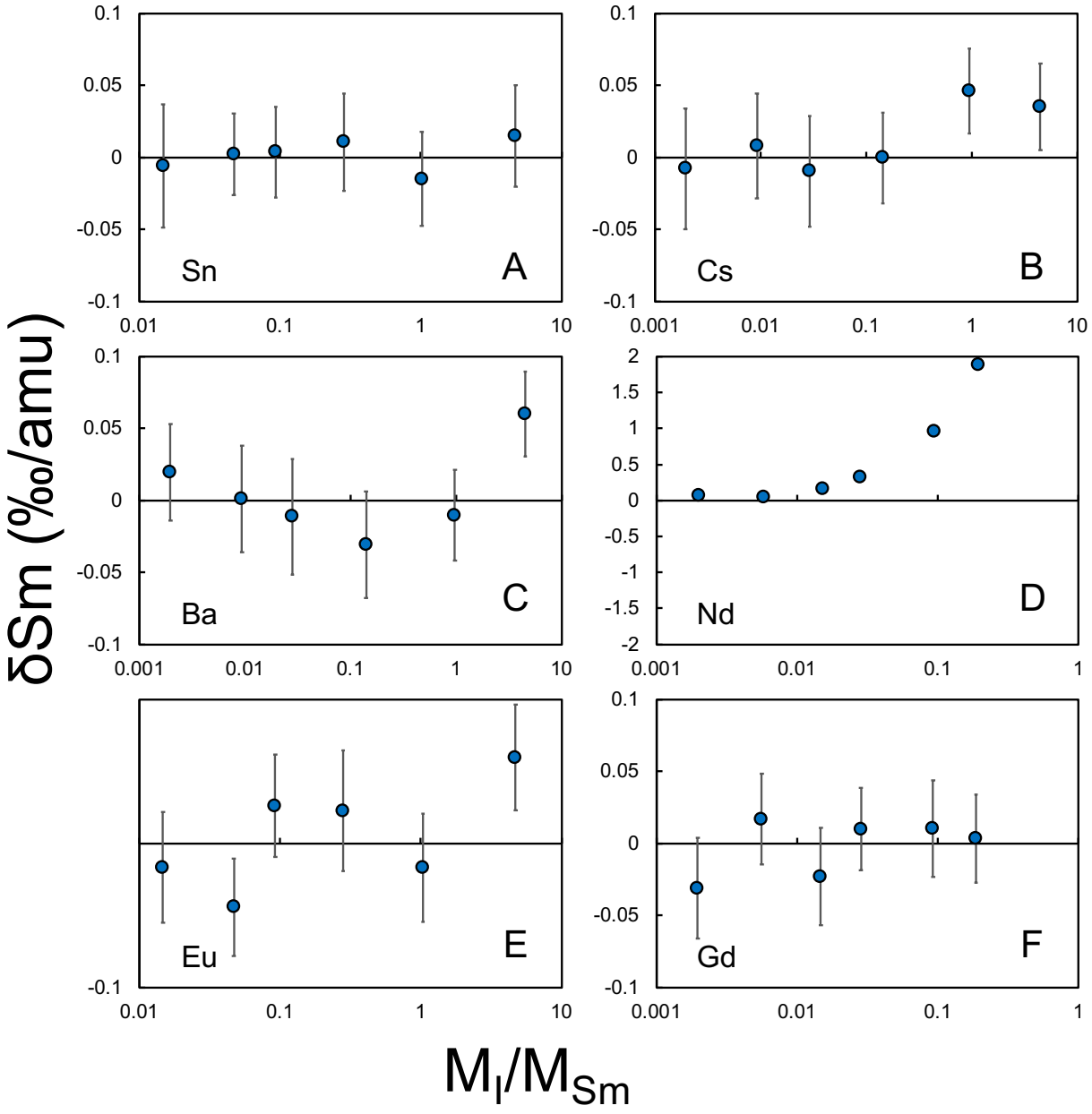

Figure 3.14 Isobaric interference doping test for Sm DS reduction. The sample analyzed using DSB has the same isotopic composition as the bracketing standard. The vertical axis is the isotopic fractionation induced by isobaric inference doping. The horizontal axis represent ratio between the mass of doped element and the mass of Sm.

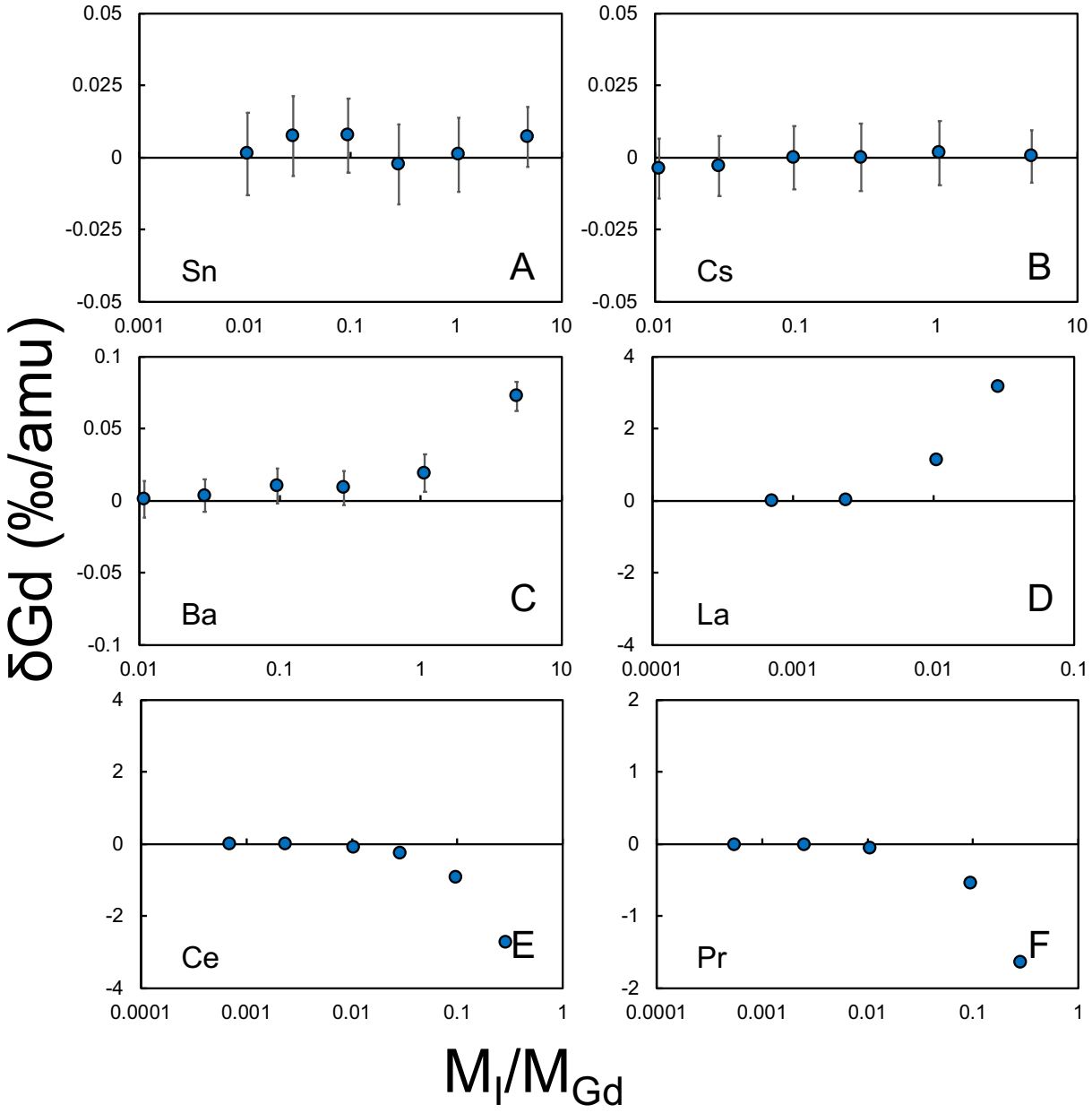

Figure 3.15 Isobaric interference doping test for Gd DS reduction (1). The sample analyzed using DSB has the same isotopic composition as the bracketing standard. The vertical axis is the isotopic fractionation induced by isobaric inference doping. The horizontal axis represent ratio between the mass of doped element and the mass of Gd.

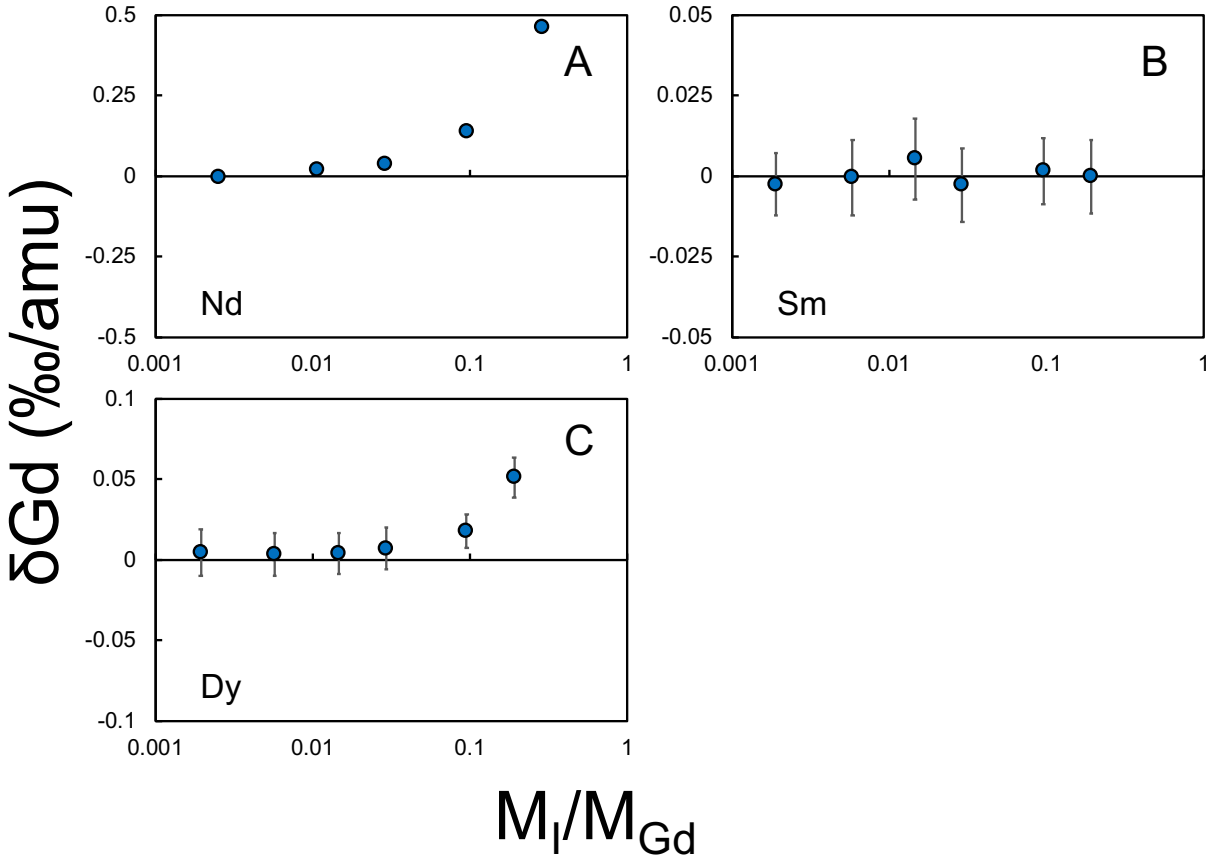

Figure 3.16 Isobaric interference doping test for Gd DS reduction (2). The sample analyzed using DSB has the same isotopic composition as the bracketing standard. The vertical axis is the isotopic fractionation induced by isobaric inference doping. The horizontal axis represent ratio between the mass of doped element and the mass of Gd.

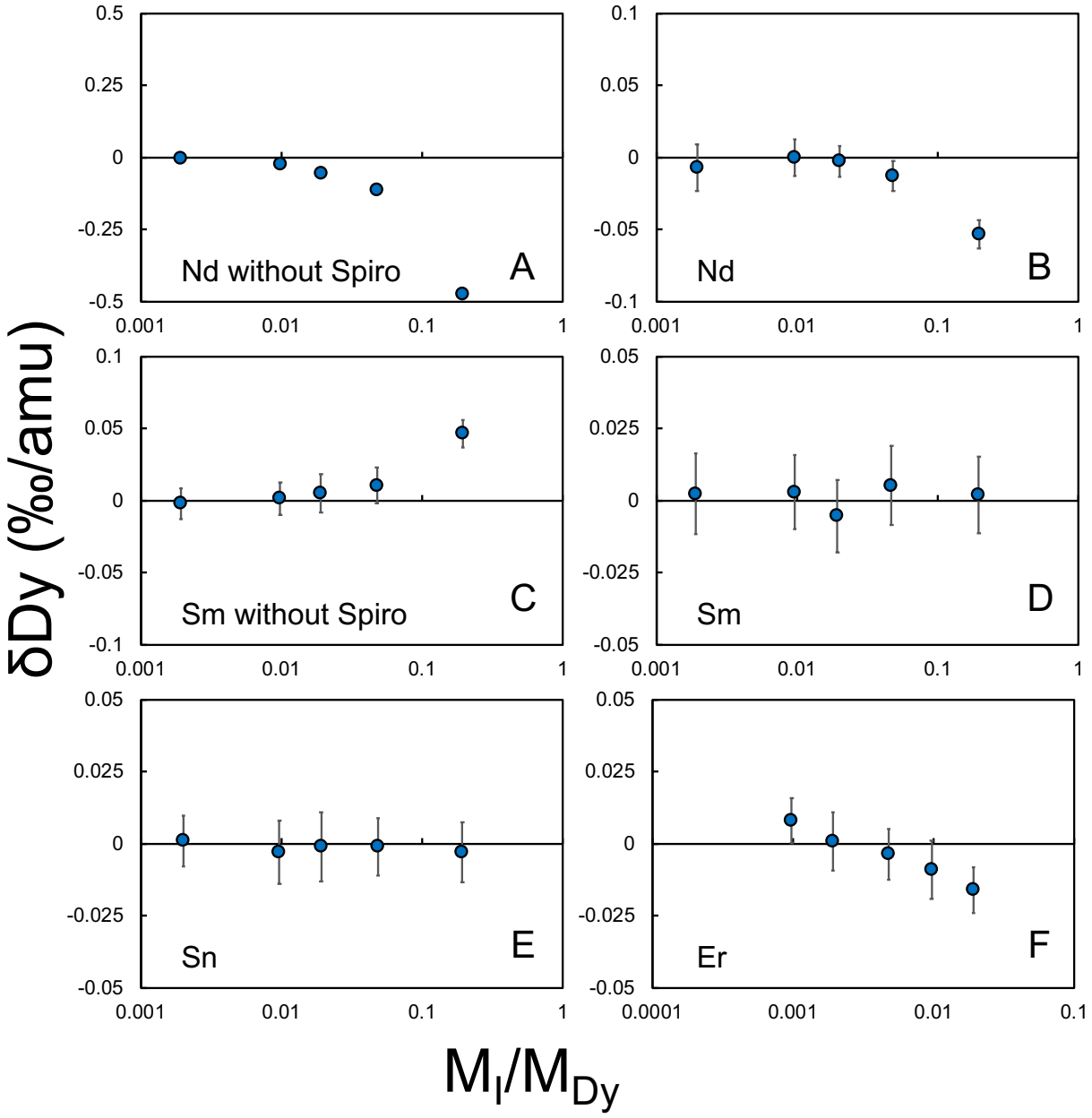

Figure 3.17 Isobaric interference doping test for Dy DS reduction. The sample analyzed using DSB has the same isotopic composition as the bracketing standard. The vertical axis is the isotopic fractionation induced by isobaric inference doping. The horizontal axis represent ratio between the mass of doped element and the mass of Dy.

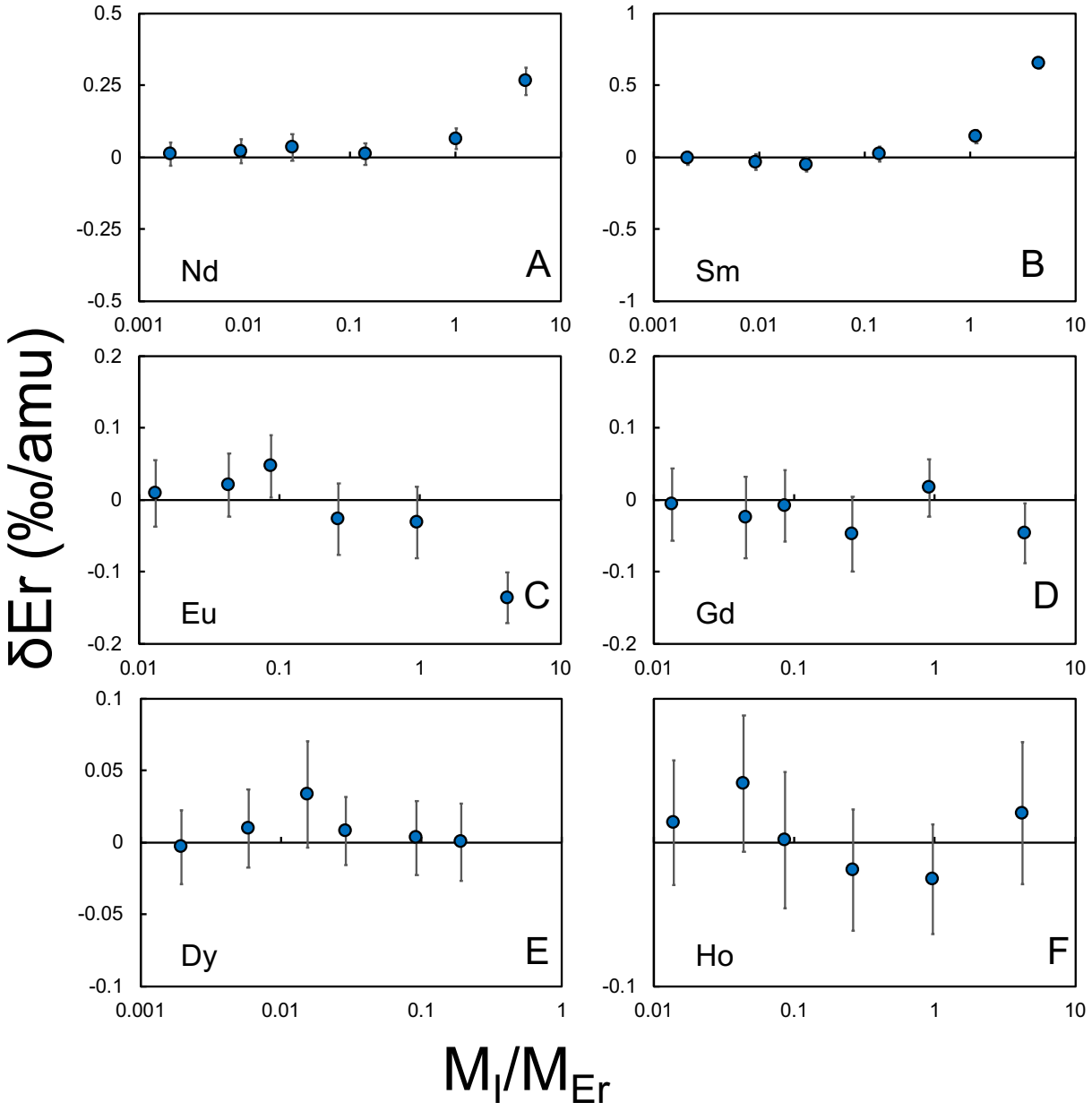

Figure 3.18 Isobaric interference doping test for Er DS reduction (1). The sample analyzed using DSB has the same isotopic composition as the bracketing standard. The vertical axis is the isotopic fractionation induced by isobaric inference doping. The horizontal axis represent ratio between the mass of doped element and the mass of Er.

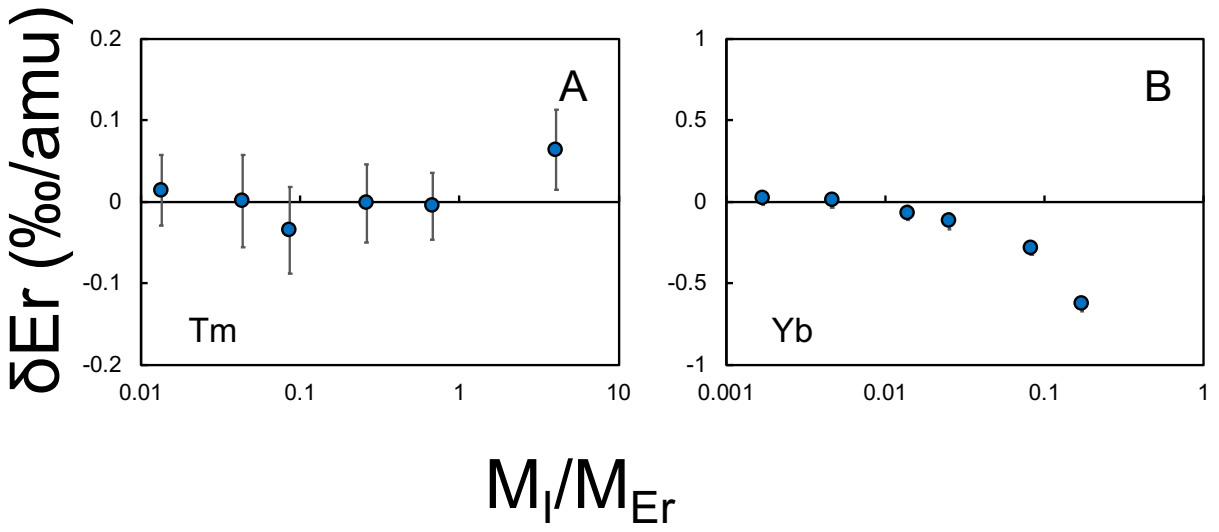

Figure 3.19 Isobaric interference doping test for Er DS reduction (2). The sample analyzed using DSB has the same isotopic composition as the bracketing standard. The vertical axis is the isotopic fractionation induced by isobaric inference doping. The horizontal axis represent ratio between the mass of doped element and the mass of Er.

3.3.2 FPLC Elution

The performance of the FPLC system was first tested and presented in Ireland et al. (2013). In the test, a 70 cm long PTFE column (with an inner diameter of 1.6 mm) was filled with Ln-resin (Eichrom) with 25-50μm resin beads. The overall affinity of REEs for Ln-resin decreases exponentially with increasing acid molarity. A multi-element REE solution containing 10 μg/g of each REE was prepared and loaded into the column. The REEs are eluted sequentially from low (La) to high (Lu) atomic number by ramping up the HCl molarity. A total of 680 mL HCl with molarity increasing from 0.1 mol/L to 10 mol/L was prepared and pumped to elute REEs. The elution was conducted at 70 °C with the pressure adjusted to provide a flow rate of ~0.5 mL/minute. The eluted solution was collected in either 2 mL or 4 mL increments, depending on when elements were predicted to elute. Overall, the FPLC system achieved excellent separation of REEs (La, Ce, Nd, Sm, Eu, Gd, Dy, Er, Yb, and Lu) from each other, with minor overlaps of some

mono-isotopic REEs. According to Ireland et al. (2013), the measured system blanks of the entire elution range from 100 pg for Nd up to 1481 pg for Ce. This may account for 5% for some REEs if less than 100 mg of an average CI chondrite is dissolved and run through the FPLC system.

The FPLC elution is optimized since the upgrade of FPLC with the new stage and sample loading valve. According to the new elution curves by the updated FPLC system (Fig. 3.4), the REE elution is performed at 70 °C and consists of 94 steps of 2 mL each of increasing molarity from 0.1 to 6 mol/L HCl. The flow rate of the elution is 0.17 mL/min. The eluent used for REE separation has been reduced from more than 600 mL to 186 mL, while a similar separation efficiency is maintained. The new elution protocol cuts down almost 2/3 of analytical blank, which reduces the risk of contamination and lowers the detection limits.

One single FPLC elution was sufficient to separate most REEs with only minor overlap of Eu/Dy and Pr/Nd (<20% Dy in the Eu cut and 25% Pr in the Nd cut) and major overlap of Y/Er, none of which showed clear isobaric and matrix effects according to our doping tests. The volume of elution generally do not change for REEs heavier than Sm while the elution volume of La to Nd varies a lot. This is primarily because the partitioning coefficients of LREEs are too small and venerable to variation of acid molarity (they are rinsed at ~ 0.1 mol/L HCl). In order to achieve optimal separation, every elution cut was pipetted and analyzed on MC-ICPMS to ensure the volume of elution for each REE. Since DSB is extremely sensitive to isobaric interferences for some REEs (*e.g.*, Nd on Sm), REEs that are not neighboring to each other were recombined and loaded onto the FPLC system for a second separation, which involves 4 FPLC elutions (Ce, Nd, Sm/Gd/Er, and Eu/Dy/Yb) ranging from 92 to 188 ml.

The overall yields of the 2-step FPLC elution were higher than 95%. However, we found that REEs are difficult be taken back to solution after being dried, especially in the MQ before loading onto the FPLC system. Dissolving REEs in large volume of concentrated HCl can reduce this problem but molarity higher than 0.1 mol/L in the loading HCl will make the elution fail for LREE (La to Nd) because of their extremely low partitioning coefficients in HCl higher than 0.1 mol/L. Typically a few percent to twenty percent of REE can be lost due to the incomplete dissolution in diluted HCl before loading. This has been validated by rinsing the beaker used for loading with concentrated acids and measuring the dissolved REEs. Potential stable isotopic fractionation of some REEs can be induced between the solution and precipitate for SSB measurements but should not affected DS measurements since sample-DS equilibration has been achieved during digestion.

3.3.3 Comparison of SSB and DSB

The benefit of using SSB compared to DSB is that each isotope ratios analyzed can be independently used to determine the stable isotopic fractionation. Since all isotope ratios follow the isotopic fractionation law for terrestrial samples, multiple isotope ratios can be monitored to distinguish the real stable isotopic fractionations from isotopic anomalies induced by isobaric interferences. In comparison, DSB is more vulnerable to isobaric interferences since all the isotope ratios have been used to determine one single stable isotopic fractionation. Isobaric interferences on the isotopes for DS reduction easily induced artificial stable isotopic fractionations that cannot be detected. Isotope analysis using DSB, however, is advantageous over SSB in that the DS is added during digestion and can correct isotopic fractionation induced during sample processing (digestion and chromatography chemistry). The isobaric interferences on the other hand can be

reduced by conducting multiple purifications on the samples. Below we are going to compare SSB after two FPLC elutions, DSB after one FPLC elution, and DSB after two FPLC elutions to interpret the influence of purification and artificial isotopic fractionations during sample processing on both SSB and DSB (Fig. 3.20 and Fig. 3.21).

Although the confidence intervals of DSB estimated by the student *t*-value of the samples are generally very small, approximately 0.01 ‰/amu to 0.02 ‰/amu, the actual confidence interval should be larger than this estimate. Our isotope analyses using SSB have shown that the confidence intervals of internal normalization can be sometimes up to 0.05 ‰/amu. The assumption of DSB is that all samples can be related to the standard using exponential fractionation law. The error bars of DSB can by no means smaller than error of isotopic anomalies. Thus, when we compared the isotope measurements, we only look at measurements with discrepancy larger than 0.05 ‰/amu.

For Ce, DSB after one and two FPLC elutions generally yield consistent results for all samples, with the overall stable isotopic fractionations being within 0.1 ‰/amu of the OL-Ce standard. Isotope analysis using SSB shows slightly heavier isotopic compositions relative to those using DSB for some samples (BHVO-2, 0.21 ‰/amu; BIR-1a, 0.28 ‰/amu) while no isotopic anomalies are observed within the uncertainty. The difference is most likely caused by artificial isotopic fractionations induced during sample processing. Since the yields on FPLC elution are generally over 95%, the artificial isotopic fractionations are most likely caused by incomplete dissolution of Ce while loading onto the FPLC system. In order to elute La to Nd in sequence, the acid molarity of the loading media has to be lower than 0.1 M HNO_3. Rare earth elements are difficult to be completely taken back to solution in such dilute acid. A small fraction of REEs have therefore be lost and potential isotopic fractionations have been induced for some samples.

The same case has also been observed for Nd isotopes. Isotope analysis using SSB showed heavier isotopic fractionation compared to that using DSB for BHVO-2 (0.07 ‰/amu), BIR-1a (0.21 ‰/amu), and G-3 (0.12 ‰/amu) without isotopic anomalies detected. Isotope analysis using DSB shows highly consistent result with little isotopic fractionation relative to OL-Nd standard except for NODP-1. NODP-1 analyzed by DSB after two FPLC elution showed slightly negative isotopic fractionation at about −0.25 ‰/amu. Part of the same sample is passed through column for third purification and yielded −0.04 ‰/amu, which is consistent to OL-Nd standard and igneous rocks. The negative isotopic fractionation after two FPLC elutions are likely to be controlled by isobaric interference caused by Nd. The $^{152}Sm/^{146}Nd$ is 0.00024, which is two orders of magnitude higher than other samples (~0.000005).

For Sm, DSB after two FPLC elutions are generally more consistent with SSB than DSB after one FPLC elution. This is most likely to be controlled by isobaric interference caused by Sm. COQ-1 and G-3 after one FPLC elution both have heavier isotopic composition with $^{145}Nd/^{149}Sm$ one order of magnitude higher (~0.01) than the same samples after two FPLC elutions (~0.0005).

Since Eu has only two isotopes, Eu isotope analyses are conducted using SSB. The results are generally consistent except for BIR-1a, which has shown 0.2 ‰/amu difference for two replicated. The reason is unknown.

All 3 types of measurement show consistent result for Gd. For Dy, all 3 types of measurements are consistent except for G-3. The isotopic fractionations analyzed by DSB after one and two FPLC elutions yield −0.14 ‰/amu while the isotopic fractionation by SSB yield −0.04 ‰/amu. The heavier isotopic composition analyzed by SSB might be affected by incomplete

dissolution. All 3 types of measurements are consistent for Yb except for G-3. Isotope analysis after two FPLC elutions show slightly negative isotopic fractionation compared to DSB after one elution and SSB. The cause is unknown.

Isotope analyses of Er using DSB show highly fractionated isotopic compositions that are substantially different from other REEs while isotope analyses using SSB give negligible isotopic fractionations. Thus, the DSB measurements on Er failed and the cause is unknown. We will not discuss Er isotope measurements using DSB in the later sections.

As is stated previously, REEs can be subject to incomplete digestion for chemistry using Ln-spec resin. Double-spike is thus necessary for analyzing the stable isotopic fractionations especially for LREEs such as Ce and Nd. The major interferences of REE measurements are usually the REE before the one to be measured. Because the abundances of isotopes in the REEs have been changed by the DS, such isobaric interferences are extremely difficult to be corrected and require high level of purification. Thus at least two FPLC elutions are required to obtain reliable results. For the future measurements, it is better to dope only 3 or 4 REEs that are not neighbor to each other to reduce the requirement of purification.

Table 3.2 Summary of REE isotope fractionation of geostandards relative to OL-REE series isotope standard.

Sample	Ce	Nd	Sm	Gd	Dy	Yb
AGV-2	0.04 ± 0.01	-0.01 ± 0.01	-0.06 ± 0.02	0.00 ± 0.01	-0.02 ± 0.01	0.01 ± 0.01
BCR-2	0.02 ± 0.01	-0.01 ± 0.00	-0.02 ± 0.02	0.01 ± 0.01	-0.03 ± 0.01	0.01 ± 0.02
BHVO-2	0.03 ± 0.02	-0.02 ± 0.01	-0.01 ± 0.03	0.02 ± 0.01	-0.01 ± 0.00	0.02 ± 0.01
BIR-1a	-0.04 ± 0.01	0.01 ± 0.01	0.05 ± 0.02	0.03 ± 0.01	0.00 ± 0.01	0.01 ± 0.01
CCH-1	0.03 ± 0.01	0.02 ± 0.02	0.00 ± 0.01	0.03 ± 0.01	0.03 ± 0.00	0.05 ± 0.00
G-3	0.01 ± 0.01	-0.01 ± 0.01	-0.09 ± 0.01	-0.05 ± 0.01	-0.14 ± 0.01	-0.09 ± 0.01
NODA-1	0.07 ± 0.01	0.03 ± 0.01	0.01 ± 0.01	-0.01 ± 0.00	0.01 ± 0.00	0.02 ± 0.00
NODP-1	0.09 ± 0.01	-0.04 ± 0.02	0.00 ± 0.01	0.01 ± 0.00	0.00 ± 0.01	0.05 ± 0.00
SDC-1	0.01 ± 0.02	-0.03 ± 0.01	-0.04 ± 0.03	-0.01 ± 0.00	-0.01 ± 0.00	-0.01 ± 0.01
W-2	0.00 ± 0.01	-0.01 ± 0.01	-0.03 ± 0.01	0.01 ± 0.00	-0.02 ± 0.01	0.01 ± 0.01

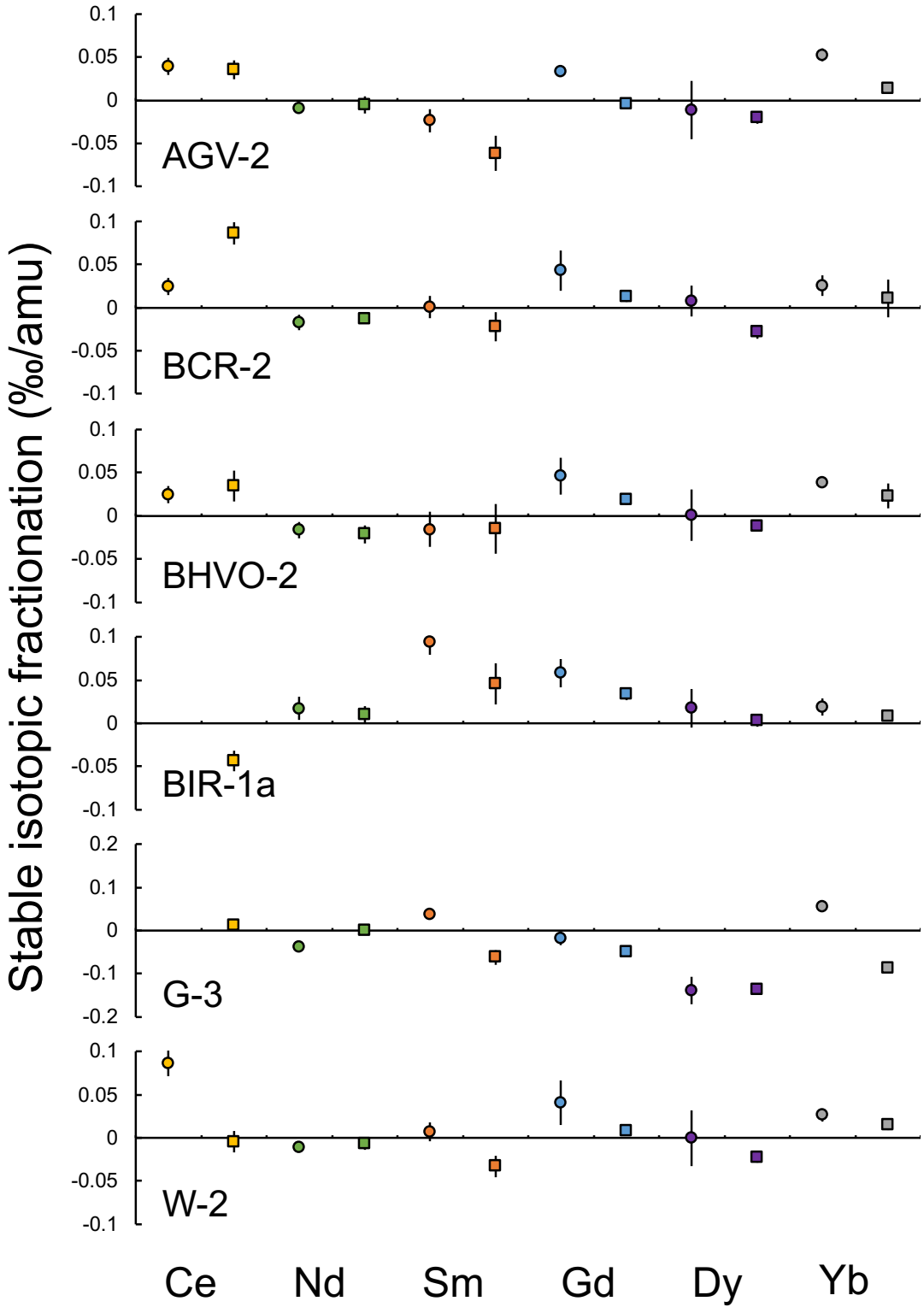

Figure 3.20 Comparison of isotope measurements after one and two FPLC elution. Circles represent measurement after only one FPLC elution while cubes represent measurements after two FPLC elutions.

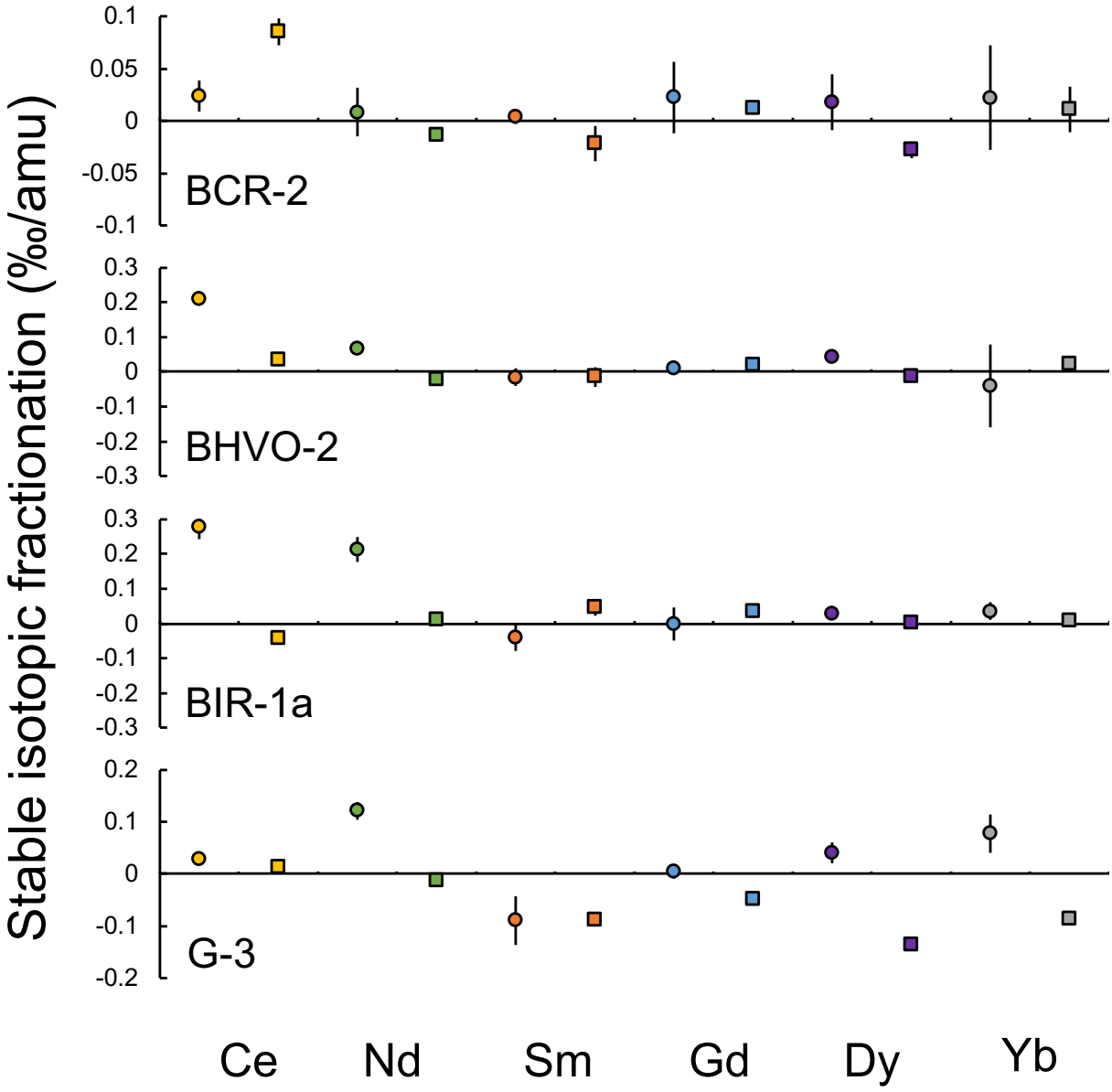

Figure 3.21 Comparison of isotope measurements using SSB and DSB. All geostandards have been passed through two FPLC elutions. Circles represent measurement using SSB while cubes represent measurements after DSB.

3.3.4 Terrestrial REE Isotopic Fractionation

Based on the discussion in Sect. 3.3.2, the isotopic fractionation from DSB after 2 or 3 FPLC elution should be most reliable. We here summarize the stable isotopic composition of REEs in geostandards using DSB in Table 3.2. The SSB data can be affected by the low yields of some

geostandards and hence are not reported. Although our reported isotopic fractionations are relative to our in-lab isotope standard, we still can compare our result with previously published work based on the isotope variations between the geostandards that we share.

AGV-2, BCR-2, BHVO-2, and BIR-2 has been measured by Nakada et al. (2019) and found to show Ce isotopic variations among all 4 geostandards within 0.03 ‰/amu. This is consistent with our measurements on AGV-2, BCR-2, and BHVO-2. Our BIR-1a, however, is lighter by 0.05 ‰/amu compared to BIR-2 in Nakada et al. (2019). The difference is generally very limited and can be either due to sample processing or heterogeneity from different batch of geostandards.

In Nakada et al. (2016), Ce isotope in hydrogenetic marine ferromanganese deposits are measured and found to be slightly heavier than that in igneous geostandards, approximately by 0.05 to 0.15 ‰/amu. In comparison, our NODA-1 and NODP-1 also shows slightly heavier Ce isotopic composition, by 0.05 to 0.10 ‰/amu, which is consistent with the discovery by Nakada et al. (2016).

Albalat et al. (2012) also analyzed Er and Yb isotopes. Unfortunately, the only geostandard that we share is BHVO-2 and thus cannot be compared. From all the basalts that Albalat et al. (2012) have analyzed, the variation of Yb isotopes are within 0.05 ‰/amu, which is also consistent with the range of basalts that we have measured (~0.05 ‰/amu).

From the isotope analyses of geostandards, REE isotopes in terrestrial geostandards show very limited isotopic fractionations, generally within 0.1 ‰/amu. Dy and Yb isotope in granite G-3 is slightly lighter compared to basalts and andesites possibly due to evolution of the magma. In

general, very limited isotopic fractionations found in igneous geostandards indicates that REEs do not fractionation during igneous process. Only one carbonate CCH-1 and one shale SDC-1 is measured and no clear isotopic fractionations have been found. Cerium isotopes in Ferromanganese crust NODA-1 and NODP-1 is slightly enriched in light isotopes, which may be controlled by the oxidative adsorption.

3.4. References

Albalat, E., Telouk, P., Albarède, F., 2012. Er and Yb isotope fractionation in planetary materials. Earth and Planetary Science Letters 355, 39-50.

Brennecka, G.A., Borg, L.E., Wadhwa, M., 2013. Evidence for supernova injection into the solar nebula and the decoupling of r-process nucleosynthesis. Proceedings of the National Academy of Sciences 110, 17241-17246.

Dauphas, N., Hu, M.Y., Baker, E.M., Hu, J., Tissot, F.L.H., Alp, E.E., Roskosz, M., Zhao, J., Bi, W., Liu, J., 2018a. SciPhon: a data analysis software for nuclear resonant inelastic X-ray scattering with applications to Fe, Kr, Sn, Eu and Dy. Journal of synchrotron radiation 25, 1581-1599.

Dauphas, N., Tissot, F.L.H., Yokochi, R., Ireland, T.J., Hu, J., 2018b. Fluoropolymer pneumatically/hydraulically actuated liquid chromatographic system for use with harsh reagents. U.S. Patent No. 9,884,266 (OrLab Chromatography LLC).

Dodson, M., 1963. A theoretical study of the use of internal standards for precise isotopic analysis by the surface ionization technique: Part I-General first-order algebraic solutions. Journal of Scientific Instruments 40, 289-295.

Hidaka, H., Yoneda, S., 2007. Sm and Gd isotopic shifts of Apollo 16 and 17 drill stem samples and their implications for regolith history. Geochimica et Cosmochimica Acta 71, 1074-1086.

Hidaka, H., Yoneda, S., Marti, K., 2006. Regolith history of the aubritic meteorite parent body revealed by neutron capture effects on Sm and Gd isotopes. Geochimica et Cosmochimica Acta 70, 3449-3456.

Hu, J.Y., Dauphas, N., Tissot, F.L.H., Yokochi, R., Ireland, T.J., Zhang, Z., Davis, A.M., Ciesla, F.J., Grossman, L., Charlier, B. L.A., Roskosz, M., Alp, E.E., Hu, M.Y., Zhao, J., 2021.

Heating events in the nascent solar system recorded by rare earth element isotopic fractionation in refractory inclusions. Science Advances 7, eabc2962.

Ireland, T.J., Tissot, F.L.H., Yokochi, R., Dauphas, N., 2013. Teflon-HPLC: A novel chromatographic system for application to isotope geochemistry and other industries. chemical Geology 357, 203-214.

Jacobsen, S.B., Wasserburg, G.J., 1980. Sm-Nd isotopic evolution of chondrites. Earth and Planetary Science Letters 50, 139-155.

Lee, S.-G., Tanaka, T., 2021. Europium isotope fractionation in highly fractionated igneous rocks

with large Eu negative anomaly. Geochemical Journal 55, e9-e17.

Leya, I., Masarik, J., 2013. Thermal neutron capture effects in radioactive and stable nuclide systems. Meteoritics & Planetary Science 48, 665-685.

Lipin, B.R., McKay, G.A., 1989. Geochemistry and mineralogy of rare earth elements. Reviews in Mineralogy and Geochemistry, Vol. 21.

Lodders, K., 2003. Solar system abundances and condensation temperatures of the elements. The Astrophysical Journal 591, 1220-1247.

Lugmair, G.W., Galer, S.J.G., 1992. Age and isotopic relationships among the angrites Lewis Cliff 86010 and Angra dos Reis. Geochimica et Cosmochimica Acta 56, 1673-1694.

Lugmair, G.W., Marti, K., 1977. SmNdPu timepieces in the Angra dos Reis meteorite. Earth and Planetary Science Letters 35, 273-284.

Nakada, R., Asakura, N., Nagaishi, K., 2019. Examination of analytical conditions of cerium (Ce) isotope and stable isotope ratio of Ce in geochemical standards. Geochemical Journal 53, 293-304.

Nakada, R., Takahashi, Y., Tanimizu, M., 2013. Isotopic and speciation study on cerium during its solid–water distribution with implication for Ce stable isotope as a paleo-redox proxy. Geochimica et Cosmochimica Acta 103, 49-62.

Nakada, R., Takahashi, Y., Tanimizu, M., 2016. Cerium stable isotope ratios in ferromanganese deposits and their potential as a paleo-redox proxy. Geochimica et Cosmochimica Acta 181, 89-100.

Nyquist, L., Wiesmann, H., Bansal, B., Shih, C.-Y., Keith, J., Harper, C., 1995. ^{146}Sm-^{142}Nd formation interval for the lunar mantle. Geochimica et Cosmochimica Acta 59, 2817-2837.

Pourmand, A., Dauphas, N., Ireland, T.J., 2012. A novel extraction chromatography and MC-ICP-MS technique for rapid analysis of REE, Sc and Y: Revising CI-chondrite and Post-Archean Australian Shale (PAAS) abundances. Chemical Geology 291, 38-54.

Rudge, J.F., Reynolds, B.C., Bourdon, B., 2009. The double spike toolbox. Chemical Geology 265, 420-431.

Russ, G.P. III, Burnett, D.S., Lingenfelter, R.E., Wasserburg, G.J., 1971. Neutron capture on149Sm in lunar samples. Earth and Planetary Science Letters 13, 53-60.

Sands, D.G., De Laeter, J.R., Rosman, K.J.R., 2001. Measurements of neutron capture effects on Cd, Sm and Gd in lunar samples with implications for the neutron energy spectrum. Earth and Planetary Science Letters 186, 335-346.

Shimizu, H., Tanaka, T., Masuda, A., 1984. Meteoritic ^{138}Ce/^{142}Ce ratio and its evolution. Nature 307, 251-252.

Shollenberger, Q.R., Brennecka, G.A., 2020. Dy, Er, and Yb isotope compositions of meteorites and their components: Constraints on presolar carriers of the rare earth elements. Earth and Planetary Science Letters 529, #115866 (12 pp).

Shollenberger, Q.R., Render, J., Brennecka, G.A., 2018. Er, Yb, and Hf isotopic compositions of refractory inclusions: An integrated isotopic fingerprint of the Solar System's earliest reservoir. Earth and Planetary Science Letters 495, 12-23.

Tanaka, T., Shimizu, H., Kawata, Y., Masuda, A., 1987. Combined La–Ce and Sm–Nd isotope systematics in petrogenetic studies. Nature 327, 113-117.

Tissot, F.L.H., 2015. Geochemistry and cosmochemistry of uranium stable isotopes. The University of Chicago.

Toellner, T.S., Hu, M.Y., Bortel, G., Sturhahn, W., Shu, D., 2006. Four-reflection “nested” meV-monochromators for 20-30 keV synchrotron radiation. Nuclear Instruments and Methods in Physics Research Section A: Accelerators, Spectrometers, Detectors and Associated Equipment 557, 670-675.

4. INSIGHTS OF EQUILIBRIUM FRACTIONATION OF REE ISOTOPES FROM NRIXS AND DFT STUDIES OF EU AND DY

4.1. Introduction

Rare earth elements (REEs) are a group of large ion lithophile elements (LILEs) with similar chemical properties. They comprise the lanthanides La, Ce, Pr, Nd, Pm (all Pm isotopes are short-lived), Sm, Eu, Gd, Tb, Dy, Ho, Er, Tm, Yb, and Lu. In most geological samples, the concentrations of lanthanides normalized either to CI chondrites (Pourmand et al., 2012; Dauphas and Pourmand, 2015) or Post-Archean Australia Shales (Pourmand et al., 2012) show smooth variations as a function of atomic number due to the smooth decrease of ionic number (1.18 to 0.97 Å for a coordination number (CN) of 8; Shannon, 1976). REE abundance patterns are relatively easy to measure by neutron activation analysis (NAA), Secondary Ion Mass Spectrometry (SIMS), and inductively coupled plasma mass spectrometry (ICPMS) and have found many applications across diverse fields, including low temperature aqueous geochemistry, igneous and metamorphic petrology, and cosmochemistry (Lipin and McKay, 1989). In terrestrial environments most lanthanides are present as trivalent cations. However, under oxidizing conditions Ce can also exist as Ce^{4+}, while under reducing conditions Eu can also exist as Eu^{2+}. These peculiar behaviors of Eu and Ce are manifested as excess or deficit abundances relative to neighbor trivalent REEs. Europium abundance anomalies have found important applications in the Earth sciences, for example to (*i*) recognize that a plagioclase flotation crust formed during cooling and crystallization of the lunar magma ocean (Warren, 1985 and references therein), (*ii*) identify the contribution of hydrothermal fluids in Earth's ocean, and (*iii*) constrain redox conditions in extraterrestrial bodies (Wadhwa, 2001).

While considerable insights can be gained by examining REE patterns, some questions remain difficult to tackle with concentrations alone. Indeed, it can be difficult to tell whether the processes that shaped REE abundance patterns took place at thermodynamic equilibrium or were influenced by kinetic or reservoir effects, and what minerals were involved. Some of these questions can be tackled by measuring the stable isotopic compositions of the REEs. Such measurements have recently been used to shed new light on how evaporation and condensation shaped the composition of fine-grained refractory inclusions found in meteorites (Hu et al., 2021), which are thought to be the first solids that formed in the solar system (Grossman, 1972; MacPherson, 2014). These inclusions also known as fine-grained calcium-aluminum-rich inclusions (FG-CAIs). In many FG-CAIs, REEs are strongly fractionated in a manner that does not smoothly follow mass, reflecting the fact REE equilibrium vapor pressures are not smooth functions of mass (Boynton, 1975; Davis and Grossman, 1979; Lodders, 2003; Davis et al., 2018). Such complex patterns are not found in most planetary environments where vapor partitioning plays no role. The REE pattern found in FG-CAIs is marked by depletions in the most volatile (Eu, Yb) and most refractory REEs (Gd-Er and Lu), while the REEs of intermediate refractoriness (La-Sm and Tm) have flat (chondritic) relative abundances (Tanaka and Masuda, 1973; Mason and Taylor, 1982). For a long time, these REE patterns were interpreted to reflect equilibrium condensation from solar gas, whereby the most refractory REEs were sequestered in an earlier generation of ultrarefractory condensates, and the most volatile REEs stayed behind in the gas and were not condensed. Hu et al. (2021) measured the isotopic compositions of Gd, Dy, and Er in these FG-CAIs and found that the most refractory REEs had light isotopic compositions, while other REEs showed more subdued effects. These signatures were interpreted to reflect kinetic effects associated with evaporation under undersaturated conditions, followed by near-equilibrium

condensation. The isotopic data allowed Hu et al. (2021) to constrain the timescales of these processes, shedding new light on the thermal history of the oldest solids formed in the solar system. To interpret their data, they had to quantify the degree of equilibrium isotopic fractionation between condensates and vapor. For REEs dissolved in hibonite, they used the only available data for pure EuO and Eu_2O_3 oxides (Dauphas et al., 2018). Given the high temperatures involved in the formation of refractory inclusions, equilibrium isotopic fractionations are small, and the measurements are dominated by kinetic effects. However, equilibrium isotopic fractionation must not be neglected if one studies REE isotopic variations for lower temperature applications, relevant to terrestrial sedimentary, metamorphic, and igneous rocks.

Four main approaches can be used to estimate equilibrium isotopic fractionation, (*i*) One can study mineral separates in natural samples (typically metamorphic or igneous rocks) that are thought to capture equilibrium conditions at well-characterized P,T conditions. (*ii*) *Ab initio* calculations can be performed to compute reduced partition function ratios. (*iii*) Laboratory experiments can be run under controlled P,T conditions, and the isotopic compositions of the phases can be measured in the experiments, and (*iv*) for some elements with a Mössbauer isotope, Nuclear Resonant Inelastic X-ray scattering (NRIXS) measurements can be acquired to compute reduced partition function ratios as a function of temperature. The REEs have two Mössbauer isotopes, ^{151}Eu and ^{161}Dy, so one can use the fourth approach of examining synthetic samples by NRIXS. In this synchrotron technique, a beam of monochromated X-rays of energy tuned around the nuclear resonant energy of the Mössbauer isotope interacts with the sample, and the scattered X-ray signal resulting from the delayed deexcitation of the Mössbauer isotope is recorded. The energy of the incident X-rays is scanned around the nominal resonance energy, allowing one to

probe lattice vibrations and characterize bond strengths (Polyakov et al., 2007; Polyakov, 2009; Dauphas et al., 2012; Dauphas et al., 2018). Indeed, if the incident X-ray beam has lower or higher energy than the nuclear transition energy, the Mössbauer isotope can still be excited if the lattice gives or takes some energy in the form of phonon (the particle form of lattice vibrations).

From NRIXS, one can estimate the reduced partition functions of Eu and Dy and their temperature dependences (Dauphas et al., 2018), as has been done extensively for Fe (Polyakov et al., 2007; Shahar et al., 2008; Polyakov, 2009; Dauphas et al., 2012; Dauphas et al., 2014) and to a lesser extent for Sn (Roskosz et al., 2020) and Kr (Dauphas et al., 2018). Since the chemical behavior of REEs varies smoothly with increasing atomic number, knowing the equilibrium fractionation factors of two REEs (*i.e.*, Eu and Dy) will provide constraints on those of other REEs. Dauphas et al. (2018) first studied equilibrium isotopic fractionation factor of Eu for a few simple chemical compounds including EuO and Eu_2O_3. In the present study, we improve on existing NRIXS measurements of oxides (Dauphas et al., 2018) and present new data for synthesized glasses with chemical compositions that are representative of diverse igneous rocks from basalt to rhyolite. REEs can be hosted in a variety of materials, including accessory minerals (phosphates like apatite, monazite), silicate (clinopyroxene, amphibole, garnet), carbonates, and can be complexed with carbonate and halogen ions in aqueous systems. Documenting equilibrium isotopic fractionation in all phases involved in REE geochemistry is a formidable task, and we focus here on silicate glasses, which is directly relevant to igneous geochemistry.

4.2. Materials and Methods

4.2.1 Chemical Compounds and Synthesized Glasses

NRIXS is a time-consuming technique. To minimize on acquisition time, it is therefore important to use samples that contain high concentrations of the target isotope. The relative abundances of Mössbauer isotopes ^{151}Eu and ^{161}Dy are 47.8 and 18.9%. Using enriched Eu would increase the signal by a factor of 2 but we decided to use samples with natural Eu isotopic abundance as this allowed us to measure commercially available Eu-bearing pure chemical compounds ($Eu^{2+}O$, $Eu^{2+}S$, $Eu^{2+}Se$, $Eu^{2+}Te$, $Eu^{3+}{}_2(CO_3)_3$, $Eu^{3+}{}_2O_3$, $Eu^{3+}PO_4$). The $EuPO_4$ and $Eu^{3+}{}_2(CO_3)_3$ are obtained from Alfa Aesar, with CAS numbers being 14913-20-3 and 86546-99-8. The product information of EuO, EuS, EuSe, EuTe, Eu_2O_3 are lost and not known. The crystal structure information is listed in Table 4.1.

Table 4.1 Crystal structure of chemical compounds of Eu and Dy.

Chemistry	EuO	EuS	EuSe	EuTe	$Eu_2(CO_3)_3$	$EuPO_4$	Eu_2O_3	Dy	Dy_2O_3
Coodination number	6	5,6,8	6,8	6,8	-	8	6,7	6,12	6,7
Crystal system	Cubic	Cubic, Tetragonal	Cubic	Cubic	-	Monoclinic	Cubic, Monoclinic, Triagonal	Cubic, Trigonal, Hexagonal	Cubic, Monoclinic, Triagonal

We also studied two glass compositions (basalt and rhyolite; Table 4.2) synthesized under two different oxygen fugacities to vary the proportions of Eu^{2+} and Eu^{3+}, corresponding to a total of 4 glass samples. The synthesized glasses are prepared by Mathieu Roskosz. The powder used to prepare the basaltic and rhyolitic glass samples are taken from the same batch used in Dauphas et al. (2014) and Roskosz et al. (2020). These batches of powder were mixed from reagent grade powder of $CaCO_3$, Al_2O_3, MgO, SiO_2, and Fe_2O_3. Each batch of mixed powder was grounded in a mortar for 4 hours for homogenization. The mixed powder was doped with the reference material

OL-Eu in the form of Eu_2O_3 (Hu et al., 2021) and grounded for another 4 hours. The amount of Eu in the mixture accounted for 3% of the total mass of oxides. The Eu-doped mixture was transferred into a furnace and melted for a few minutes, after which the melt was quenched in air and glass was grounded again to fine powder. For both basalt and rhyolite compositions, small pellets of glass powder, aggregated by PVA as binder, were deposited on a Re-wire loop, after which the samples were transferred into a vertical tube furnace. Oxygen fugacity was controlled using a CO_2 / Ar-H_2 gas mixture for the reduced samples or by melting in air for the oxidized samples. The Eu^{2+}-rich samples were prepared by heating for 9.5 hours at a temperature of 1550 °C under an oxygen fugacity of IW+0.36 (27.54 % volume CO_2 and the rest Ar-H_2 at a total flow rate of 150 sccm). For synthesis of glass enriched in Eu^{3+}, the samples were heated in air for 60 minutes at a temperature of 1650 °C. All the samples were quenched by dropping them in water.

Table 4.2 Compositions of Eu-doped glass samples.

Composition	SiO_2	Al_2O_3	FeO_{tot}	CaO	MgO	Na_2O	K_2O	TiO_2	$Eu_2O_{3\ tot}$	Optical basicity	Oxygen fugacity	Eu^{3+}/Eu_{tot}
Bas Red	49.21	16.21	7.37	12.38	9.12	1.81	–	0.97	2.92	0.60	-8.02	0.48
Bas Ox	49.21	16.21	7.37	12.38	9.12	1.81	–	0.97	2.92	0.60	-0.68	0.98
Rhy Red	73.51	10.24	3.97	0.00	0.00	4.88	4.49	0.00	2.92	0.54	-8.02	0.10
Rhy Ox	73.51	10.24	3.97	0.00	0.00	4.88	4.49	0.00	2.92	0.54	-0.68	0.82

$Eu_2O_{3\ tot}$ represents the total amount of oxide doped in the powder

For Dy, we used ^{161}Dy-enriched oxide (95.8% ^{161}Dy) from Oak Ridge National Laboratory to synthesize glass of igneous rock composition. Glasses of basalt, andesite, and rhyolite composition doped with Dy (Table 4.3) were synthesized in a similar way as Eu glasses. Oxide powder (Dy_2O_3, cubic, monoclinic, triagonal) enriched in ^{161}Dy was purchased from Oak Ridge National Laboratory and was analyzed by NRIXS. The powder was mixed with the basalt, andesite, and rhyolite mixtures to achieve concentrations of 7 wt% ^{161}Dy. The glass samples were prepared in air by heating to 1650 °C. The samples were quenched by dropping them in water. Dysprosium only exists as a trivalent cation in nature and in our experiments.

Table 4.3 Compositions of Dy-doped glass samples.

Composition	SiO_2	Al_2O_3	FeO_{tot}	CaO	MgO	Na_2O	K_2O	TiO_2	Dy_2O_3
Bas	47.36	15.61	7.10	11.91	8.78	1.74	–	0.94	6.56
And	52.17	15.17	6.57	6.54	7.67	3.16	1.41	0.72	6.60
Rhy	70.75	9.85	3.82	0.00	0.00	4.69	4.32	0.00	6.56

4.2.2 Experimental Setup and Data Processing

Nuclear Resonant Inelastic X-ray Scattering was first used in Earth sciences for determining seismic velocities and phonon density of states of minerals that exist in the deep mantle and core (Mao et al., 2001; Lin et al., 2003; Mao et al., 2006). It was later adopted in stable isotope geochemistry for determining the equilibrium isotopic fractionation between minerals (Polyakov et al., 2007; Shahar et al., 2008; Polyakov, 2009; Dauphas et al., 2012; Dauphas et al., 2014; Roskosz et al., 2020). This is most widely used for Fe isotopes (Polyakov et al., 2007; Shahar et al., 2008; Polyakov, 2009; Dauphas et al., 2012; Dauphas et al., 2014;) and was applied more recently to Sn (Dauphas et al., 2018; Roskosz et al., 2020). This is the first systematic study that uses NRIXS to analyze the equilibrium isotopic fractionation for both Eu and Dy. The principles of NRIXS and its applications in isotopic geochemistry have been explained in detail in Dauphas et al. (2012) and Dauphas et al. (2018) and will only briefly described below. Mössbauer isotope ^{151}Eu has a low-lying nuclear excited state, which can be populated by incident X-ray photons that have energies of around 21.5415 keV. In NRIXS, the incident beam is pulsed. The prompt signal comes from electron scattering and is discarded. The delayed signal comes solely from de-excitation of the excited ^{151}Eu atoms. During an NRIXS measurement, the energy of the incident photons is scanned. At each energy, the X-rays scattered by nuclear de-excitation are counted. Nuclear excitation can occur while the incident photons have lower energy than the nominal resonance energy, when the solid network gives vibration energy to the atoms in a process known as phonon annihilation. Conversely, nuclear excitation can occur while the incident photon has

higher energy than the nominal resonance energy, if some of that extra energy went into exciting the solid network in a process known as phonon creation. Thus, the spectrum of scattered intensity as a function of energy of the incident X-rays allows us to probe the vibration properties of the solid network. In particular, NRIXS gives access to the mean force constant of the chemical bonds keeping Eu in position, which can be used to estimate the equilibrium isotopic fractionation of Eu. Similarly, the Mössbauer isotope ^{161}Dy has a low-lying nuclear excited state populated at 25.6515 eV (Hogarth, 1965), that can be studied using the NRIXS technique. We measured our samples at sectors 3 of the Advanced Photon Source (APS), Argonne National Laboratory. The NRIXS measurements are conducted with Nicolas Dauphas, Xike Nie, Xi Chen, Andrew Heard, Hao Zeng, Esen Alp, Michael Hu, and Jiyong Zhao. The monochromators used for those measurements were described in Toellner et al. (2006). For Eu and Dy, the energy resolutions are ~0.8 meV full width at half maximum.

All the NRIXS measurement were done at room temperature (~20 °C) and under atmospheric pressure. The pure chemical compound powders were sealed in 10 × 2 mm rectangular areas between two pieces of Kapton tape. Synthesized glass beads were placed on the top of a Kapton tubing by inserting the Pt or Re wire surrounding the bead in the hole of the tubing. Two Avalanche Photon Detectors (APD) were positioned on both sides a few millimeters away from the samples. For samples that are transparent, a third APD was placed downstream to measure the energy resolution simultaneously. Otherwise, the energy resolution used for data reduction was measured in the same period time for other samples. Typical scanning ranges for pure chemical compounds are −50 to +50 meV (energies are given relative to the resonance energy). For low concentration glasses, the acquisition ranges are −70 to +80 meV for Eu and −80 to +90 meV for

Dy. The raw data files for NRIXS and resolution functions were first added using the padd function in the Phoenix (Sturhahn, 2000) and the raw data were then further processed by SciPhon (Dauphas et al., 2012; Dauphas et al., 2018) to derive the excitation function $S(E)$ (Dauphas et al., 2018). This involves deconvolving the resolution function, interpolating the signal to remove the elastic peak, defining and subtracting a baseline interpolated between the low and high energy tails of the signal, and extrapolating the signal outside the acquisition range using a physically sound iterative procedure. The phonon density of states PDOS $g(E)$ was calculated using a Fourier-Log transform (Sturhahn et al., 1995). All the quantities that can be derived from $S(E)$ and $g(E)$ for the samples studied were calculated using SciPhon and are compiled in Table 2 for Eu and Table 3 for Dy. This includes the reduced partition function ratio β used to calculate equilibrium isotopic fractionation between phases, which can be calculated using the moments of $g(E)$ (Polyakov et al., 2005; Polyakov et al., 2007; Dauphas et al., 2012;),

$$1000\ln\beta_{I/I^*} \cong 1000\left(\frac{M}{M^*}-1\right)\left(\frac{m_2^g}{8k^2T^2}-\frac{m_4^g}{480k^4T^4}+\frac{m_6^g}{20160k^6T^6}\right), \quad (4.1)$$

where I and I^* are two isotopes of the target element of masses M and M^*, and the j^{th} moment of $g(E)$ is given by,

$$m_j^g = \int_0^{+\infty} E^j g(E)\mathrm{d}E, \quad (4.2)$$

or $S(E)$ (Dauphas et al., 2012),

$$1000\ln\beta_{I/I^*} \cong 1000\left(\frac{M}{M^*}-1\right)\frac{1}{E_R}\left[\frac{R_3^S}{8k^2T^2}-\frac{R_5^S-10R_2^SR_3^S}{480k^4T^4}+\frac{R_7^S+210\left(R_2^S\right)^2R_3^S-35R_3^SR_4^S-21R_2^SR_5^S}{20160k^6T^6}\right], \quad (4.3)$$

where the j^{th} moment of S centered on E_R is,

$$R_j^S = \int_{-\infty}^{+\infty} S(E)(E - E_R)^j \mathrm{d}E. \text{ (4.4)}$$

At high temperature, the first term in the polynomial expansion dominates and is proportional to the mean force constant $\langle F \rangle$ of the bonds that Eu and Dy forms with coordinating atoms,

$$1000 \ln \beta_{I/I^*} \cong 1000 \left(\frac{1}{M^*} - \frac{1}{M}\right) \frac{\hbar^2}{8k^2T^2} \langle F \rangle, \text{ (4.5)}$$

For Eu and Dy, this expression corresponds to,

$$1000 \ln \beta^{^{153}\mathrm{Eu}/^{151}\mathrm{Eu}} = 380.9 \frac{\langle F_{\mathrm{Eu}} \rangle}{T^2}, \text{ (4.6)}$$

and,

$$1000 \ln \beta^{^{164}\mathrm{Dy}/^{162}\mathrm{Dy}} = 331.2 \frac{\langle F_{\mathrm{Dy}} \rangle}{T^2}. \text{ (4.7)}$$

The force constant can be calculated from the second moment of $g(E)$ or the third centered moment of $S(E)$ (Lipkin, 1995; Kohn and Chumakov, 2000),

$$\langle F \rangle = \frac{M}{\hbar^2} \int_0^{+\infty} E^2 g(E) \mathrm{d}E = \frac{M}{E_R \hbar^2} \int_{-\infty}^{+\infty} (E - E_R)^3 S(E) \mathrm{d}E, \text{ (4.8)}$$

Once the reduced partition function ratio is known, one can easily calculate the isotopic fractionation between two phases A and B,

$$\Delta_{B-A}^{i/j} = \left(\delta_B^{i/j} - \delta_A^{i/j}\right)_{eq} = 1000\ln\beta_B - 1000\ln\beta_A, \quad (4.9)$$

where δ is the isotopic composition expressed as the deviation in permil of the ratio ${}^{i}E/{}^{j}E$ relative to a reference material (*e.g.*, OL-Eu and OL-Dy; Hu et al., 2021),

$$\delta^{i/j}\ (‰) = \left[\left({}^{i}E/{}^{j}E\right)_{sample}/\left({}^{i}E/{}^{j}E\right)_{standard} - 1\right]1000. \quad (4.10)$$

Because our NRIXS measurements were the first of their kind, done with the objective of estimating reduced partition function ratios of Eu and Dy, we decided to run ab initio calculations to allow us to test the validity of the values obtained by NRIXS. *Ab initio* (Density Functional Theory; DFT) calculations of chemical compounds of Eu were carried out by Hao Zeng following Zeng et al. (2019). Unless otherwise specified, structural relaxation was carried out with the Quantum ESPRESSO code (Garrity et al., 2014; Giannozzi et al., 2017), with plane-wave basis sets, pseudopotentials from Standard Solid-State Pseudopotential Library (Dal Corso, 2014; Topsakal and Wentzcovitch, 2014; Schlipf and Gygi, 2015; Lejaeghere et al., 2016; Prandini et al., 2018) and the phonon calculation was done using Phonopy (Togo and Tanaka, 2015) and a 2×2×2 supercell of the primitive lattice. The kinetic energy and charge-density cutoff were set to 75 and 750 Ry, respectively. The Monkhorst k-point grids (Monkhorst and Pack, 1976) for all materials are set to 4×4×4. A Hubbard U value (Anisimov et al., 1991; Anisimov et al., 1993; Solovyev et al., 1994) was calculated from trial and error for Eu to reproduce experimentally measured lattice parameters. The minerals investigated here are $Eu^{2+}O$, $Eu^{2+}S$, $Eu^{2+}Se$, $Eu^{3+}PO_4$ (Nowacki, 1938; Wyckoff, 1963; Ni et al., 1995). Their primitive lattice parameters were taken from experiments, and the lattice and atomic positions were relaxed until the total force and stress were smaller than 10^{-4} atomic units and 0.1 kbar, respectively.

4.3. Results

Physical and chemical properties processed from the phonon excitation probability density function $S(E)$ and PDOS $g(E)$ are presented in Table 2 for Eu and Table 3 for Dy. For the minerals analyzed in this study and those in Dauphas et al., (2018) (Fig. 4.1), Eu^{2+}-bearing minerals (EuO, EuS, EuSe, EuTe) generally show force constants at around 100 N/m, irrespective of the crystal structures and the coordination states, yielding an average of 97 ± 23 N/m. Eu^{3+}-bearing minerals ($Eu_2(CO_3)_3$, Eu_2O_3, $EuPO_4$) show substantially higher force constants with an average of 192 ± 30 N/m. The force constant of Eu^{3+} in $EuPO_4$ (174 N/m; monoclinic) is slightly lower than that in Eu_2O_3 (199 N/m; monoclinic, cubic, triagonal), possibly related to differences in coordination states.

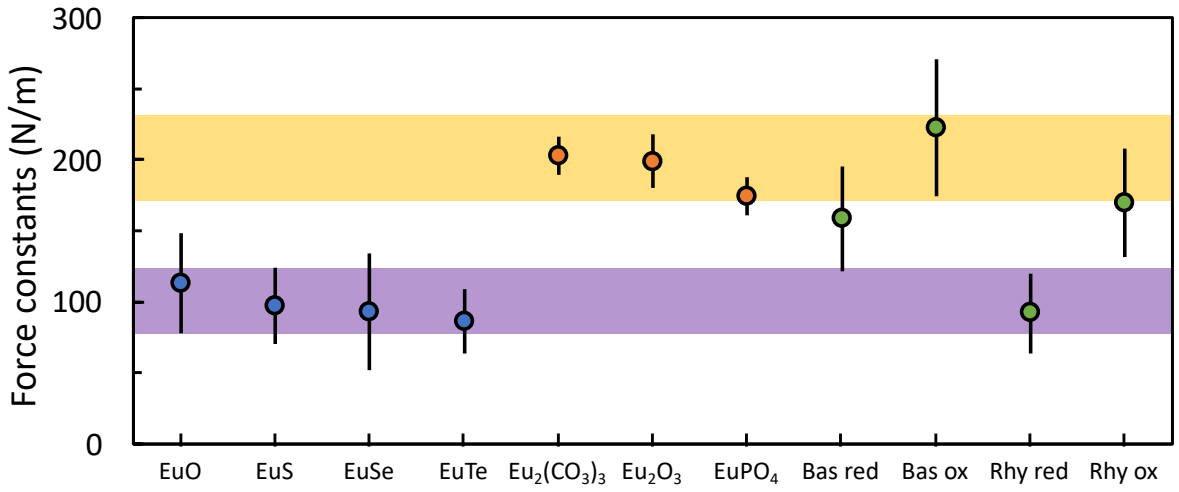

Figure 4.1 Force constants of Eu in minerals and synthesized glasses. Blue, orange, and green points represent minerals containing Eu^{2+}, minerals containing Eu^{3+}, and synthesis glass doped with Eu. The purple and orange shades represent the confidence intervals of Eu^{2+} and Eu^{3+}, respectively.

Europium in reduced synthesized glasses show force constants of 158 ± 37 and 92 ± 28 N/m for basaltic and rhyolitic compositions, while those in oxidized basaltic and rhyolitic glasses

are 222 ± 48 and 170 ± 38 N/m respectively (Fig. 4.1). Although Eu was nearly completely oxidized to Eu^{3+} during synthesis of glass of oxidized compositions, the reduced glasses contain a mixture of Eu^{2+} and Eu^{3+}. The relationship between Eu force constants and the calculated proportions of Eu^{2+} and Eu^{3+} in silicate glasses is examined in the discussion.

The force constants obtained from NRIXS are compared to those calculated using DFT for EuO, EuS, EuSe and $EuPO_4$ (Fig. 4.2). The data points fall on a 1:1 line that passes through the origin point, indicating that NRIXS and *ab initio* calculation yields consistent results. Since the systematic error on the *ab initio* calculation is unknown, only the error bars for NRIXS measurements are shown.

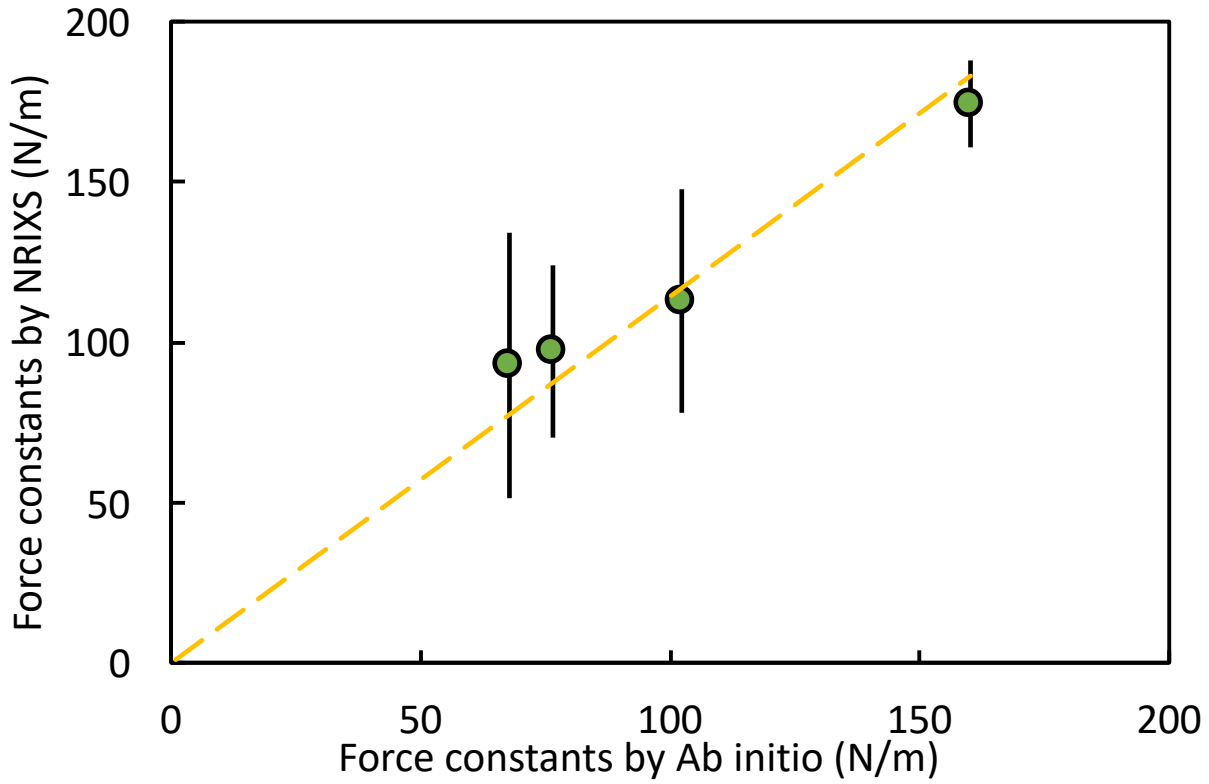

Figure 4.2 Force constants calculated by NRIXS plotted against force constants calculated by *Ab initio* calculation. The dashed line is the linear regression of all 4 samples anchored to the origin point with a slope of 1.14.

Table 4.4 Compilation of parameters derived from NRIXS spectra of Eu in minerals and synthesized glass.

Composition:	EuO	EuS	EuSe	Eu'Te	$Eu_2(CO_3)_3$	Eu_2O_3	$EuPO_4$	Bas red	Bas ox	Rhy red	Rhy Ox
Total energy range:	-39.63 - 39.67	-49.65 - 49.22	-39.7209 - 38.59	-49.71 - 49.16	-69.17 - 79.11	-64.86 - 69.79	-79.14 - 90.38	-79.0774 - 89.9425	-79.0433 - 90.2366	-69.0572 - 80.1928	-69.2319 - 79.2879
Energy cutoff (left and right in meV):	2.3 & 0.0	9.3 & 10.2	4.8 & 1.9	12.9 & 3.5	8.0 & 18.7	13.8 & 10.4	25.2 & 28.7	33.4 & 31	31 & 25.3	29.6 & 31	22.8 & 24.2
Baseline subtracted:	linear	linear	linear	linear	linear	linear	linear	linear	linear	linear	linear
a=	0.0001 ± 0.0298	0.0094 ± 0.0037	0.0141 ± 0.0179	0.0063 ± 0.0058	0.0126 ± 0.0050	0.0057 ± 0.0063	0.0044 ± 0.0025	-0.0042 ± 0.0051	0.0026 ± 0.0039	0.0037 ± 0.0053	0.0103 ± 0.0069
b=	1.5017 ± 1.1331	0.8662 ± 0.1653	4.9934 ± 0.6706	1.1467 ± 0.2581	2.8968 ± 0.3394	2.2497 ± 0.3849	2.4592 ± 0.1802	10.7851 ± 0.3553	6.1451 ± 0.2734	9.6973 ± 0.3177	14.5508 ± 0.4380
Input temperature (K):	300	300	300	300	300	300	300	300	300	300	
Temperature from detailed balance (K):	242	232	224	244	295	282	279	265	261	274	265
					From S						
lamb-mossbauer factor:	0.491 ± 0.011	0.424 ± 0.013	0.379 ± 0.017	0.354 ± 0.010	0.377 ± 0.003	0.538 ± 0.004	0.523 ± 0.003	0.422 ± 0.007	0.485 ± 0.007	0.216 ± 0.009	0.366 ± 0.007
Mean square displacement $<z^2>$ ($Å^2$):	0.00597 ± 0.00023	0.00720 ± 0.00019	0.00814 ± 0.00040	0.00872 ± 0.00019	0.00819 ± 0.00005	0.00520 ± 0.00004	0.00344 ± 0.00004	0.00724 ± 0.00011	0.00607 ± 0.00010	0.01288 ± 0.00027	0.00843 ± 0.00014
Internal energy/atom (meV):	26.48 ± 1.36	26.39 ± 1.04	26.37 ± 1.63	26.33 ± 0.89	26.96 ± 0.61	26.94 ± 0.68	26.81 ± 0.60	26.72 ± 0.99	27.06 ± 1.10	26.36 ± 0.93	26.79 ± 1.06
Kinetic energy/atom (meV):	13.24 ± 0.68	13.20 ± 0.52	13.18 ± 0.81	13.17 ± 0.44	13.48 ± 0.30	13.47 ± 0.34	13.41 ± 0.30	13.36 ± 0.50	13.53 ± 0.55	13.18 ± 0.46	13.39 ± 0.53
Force constant (N/m):	113.1 ± 34.9	97.2 ± 26.6	92.9 ± 41.3	86.4 ± 22.5	202.5 ± 13.3	199.0 ± 18.6	174.5 ± 13.4	158.0 ± 36.8	222.4 ± 47.9	91.9 ± 28.2	169.7 ± 38.0
					beta-value coefficients from S						
$1000\ln(\beta^{151}Eu/^{151}Eu)=A_1/T^2+A_2/T^4+A_3/T^6$ (T in K)											
A_1:	4.36E+04 ± 1.35E+04	3.75E+04 ± 1.03E+04	3.59E+04 ± 1.59E+04	3.33E+04 ± 8.70E+03	7.82E+04 ± 5.13E+03	7.68E+04 ± 7.18E+03	6.74E+04 ± 5.18E+03	6.10E+04 ± 1.42E+04	8.58E+04 ± 1.85E+04	3545782 ± 10870.8	6.55E+04 ± 1.47E+04
A_2:	-1.71E+07 ± 4.11E+07	-1.53E+07 ± 3.13E+07	-2.13E+07 ± 4.50E+07	-1.33E+07 ± 2.83E+07	-1.57E+08 ± 2.91E+07	-1.18E+08 ± 3.77E+07	-8.40E+07 ± 2.73E+07	-1.23E+08 ± 7.88E+07	-2.29E+08 ± 1.25E+08	-4.67E+07 ± 4.36E+07	-1.00E+08 ± 7.22E+07
A_3:	-4.32E+10 ± 2.25E+11	-2.47E+10 ± 1.75E+11	-1.15E+10 ± 2.29E+11	3.60E+10 ± 1.70E+11	8.01E+11 ± 2.97E+11	3.96E+11 ± 3.54E+11	2.26E+11 ± 2.66E+11	6.71E+11 ± 7.60E+11	1.51E+12 ± 1.44E+12	1.69E+11 ± 3.14E+11	3.43E+11 ± 6.23E+11
$1000\ln(\beta^{151}Eu_d/^{151}Eu)=B_1<r^2>/T^2+B_2<r^2>^2/T^4$ (T in K)											
B_1:	380.9	380.9	380.9	380.9	380.9	380.9	380.9	380.9	380.9	380.8562	380.9
B_2:	1374.5	1648.5	2482.8	1723.5	3620.4	2871.1	2676.5	4653.8	4306.8	5314.787	3360.4
					From g						
lamb-mossbauer factor:	0.488	0.419	0.374	0.350	0.370	0.534	0.520	0.420	0.478	0.202708	0.358
Mean square displacement $<z^2>$ ($Å^2$):	0.00603	0.00730	0.00825	0.00881	0.00834	0.00526	0.00548	0.00729	0.00619	0.013396	0.00863
$d<z^2>/dT$ ($Å^2$/K):	0.000019	0.000024	0.000026	0.000028	0.000027	0.000017	0.000017	0.000022	0.000019	4.21E-05	0.000028
Critical temperature (K):	436.2	356.4	322.2	295.4	310.1	495.7	481.7	374.6	439.3	199.591	299.9
Resilience (N/m):	71.8	58.6	53.0	48.6	51.0	81.5	79.2	61.6	72.3	32.83162	49.3
Internal energy/atom (meV):	26.49	26.40	26.39	26.34	26.98	26.95	26.82	26.72	27.07	26.39146	26.80
Kinetic energy/atom (meV):	13.25	13.20	13.20	13.17	13.49	13.48	13.41	13.36	13.53	13.19573	13.40
Vibrational entropy (kb/atom):	1.705	1.796	1.854	1.843	1.628	1.534	1.567	1.739	1.598	1.981342	1.691
Helmholtz free energy (meV):	-17.588	-20.030	-21.539	-21.295	-15.111	-12.705	-14.217	-18.233	-14.251	-24.8302	-16.911
Vibrational specific heat (kb/atom):	0.976	0.979	0.979	0.981	0.959	0.959	0.964	0.968	0.956	0.980365	0.965
lamb-mossbauer factor at T=0:	0.873	0.861	0.852	0.853	0.869	0.888	0.883	0.863	0.878	0.825774	0.863
Kinetic energy/atom at T=0 (meV):	3.398	3.117	2.992	2.965	4.093	4.247	3.998	3.573	4.206	2.769054	3.789
Force constant (N/m):	115.5	99.4	97.9	87.0	204.3	199.8	175.0	158.9	223.5	95.62596	171.1
					beta-value coefficients from g						
$1000\ln(\beta^{153}Eu/^{151}Eu)=A_1/T^2+A_2/T^4+A_3/T^6$ (T in K)											
A_1:	4.46E+04	3.84E+04	3.78E+04	3.36E+04	7.88E+04	7.71E+04	6.75E+04	6.13E+04	8.62E+04	36902.71	6.60E+04
A_2:	-2.41E+07	-2.11E+07	-3.49E+07	-1.31E+07	-1.66E+08	-1.22E+08	-8.52E+07	-1.29E+08	-2.37E+08	-5.84E+07	-1.07E+08
A_3:	3.08E+10	3.51E+10	1.15E+11	2.05E+10	1.04E+12	4.93E+11	2.55E+11	8.13E+11	1.77E+12	3.39E+11	4.90E+11

Table 4.5 Compilation of parameters derived from NRIXS spectra of Dy in minerals and synthesized glass.

Composition:	Dy	Dy_2O_3	Bas	And	Rhy
Total energy range:	-59.01 - 59.99	-80.34 - 91.06	-80.45 - 91.41	-80.46 - 90.84	-80.77 - 90.40
Energy cutoff (left and right in meV):	9.2 & 4.5	20.5 & 7.3	12.8 & 13	13.9 & 6.1	13.3 & 4.6
Baseline subtracted:	linear	linear	linear	linear	linear
a=	0.0072 ± 0.0063	0.0031 ± 0.0038	0.0199 ± 0.0072	0.0086 ± 0.0052	0.0157 ± 0.0067
b=	3.2945 ± 0.3486	2.3426 ± 0.2852	4.3161 ± 0.5740	3.1560 ± 0.4101	4.5474 ± 0.5231
Input temperature (K):	300	300	300	300	300
Temperature from detailed balance (K):	303	313	320	311	308
----------From S----------					
lamb-mossbauer factor:	0.267 ± 0.005	0.551 ± 0.004	0.440 ± 0.002	0.422 ± 0.003	0.378 ± 0.002
Mean square displacement $<z^2>$ (A^2):	0.00782 ± 0.00008	0.00353 ± 0.00003	0.00486 ± 0.00002	0.00510 ± 0.00003	0.00575 ± 0.00003
Internal energy/atom (meV):	26.42 ± 0.67	27.39 ± 0.70	27.23 ± 0.63	27.26 ± 0.64	27.23 ± 0.61
Kinetic energy/atom (meV):	13.21 ± 0.33	13.69 ± 0.35	13.61 ± 0.32	13.63 ± 0.32	13.62 ± 0.31
Force constant (N/m):	108.2 ± 14.4	301.0 ± 26.7	271.2 ± 16.5	276.5 ± 20.8	271.2 ± 17.4
----------beta-value coefficients from S----------					
$1000\ln(\beta^{164}Dy/^{162}Dy)=A_1/T^2+A_2/T^4+A_3/T^6$ (T in K)					
A_1:	3.65E+04 ± 4.86E+03	1.02E+05 ± 9.00E+03	9.15E+04 ± 5.56E+03	9.33E+04 ± 7.01E+03	9.15E+04 ± 5.87E+03
A_2:	-1.54E+07 ± 2.41E+07	-2.54E+08 ± 8.94E+07	-2.69E+08 ± 4.96E+07	-2.74E+08 ± 7.17E+07	-2.47E+08 ± 6.05E+07
A_3:	-6.49E+09 ± 2.21E+11	1.86E+12 ± 1.58E+12	2.27E+12 ± 7.78E+11	2.19E+12 ± 1.29E+12	1.65E+12 ± 1.09E+12
$1000\ln(\beta^{164}Dy/^{162}Dy)=B_1<F>/T^2-B_2<F>^2/T^4$ (T in K)					
B_1:	331.3	331.3	331.3	331.3	331.3
B_2:	1320.0	2583.2	3324.0	3267.7	3109.7
----------From g----------					
lamb-mossbauer factor:	0.259	0.545	0.437	0.415	0.369
Mean square displacement $<z^2>$ (A^2):	0.00798	0.00359	0.00490	0.00520	0.00590
$d<z^2>/dT$ (A^2/K):	0.000026	0.000011	0.000015	0.000016	0.000019
Critical temperature (K):	229.9	532.1	384.9	368.2	317.3
Resilience (N/m):	53.6	124.2	89.8	85.9	74.0
Internal energy/atom (meV):	26.43	27.40	27.24	27.27	27.26
Kinetic energy/atom (meV):	13.21	13.70	13.62	13.64	13.63
Vibrational entropy (kb/atom):	1.789	1.385	1.512	1.512	1.521
Helmholtz free energy (meV):	-19.824	-8.399	-11.848	-11.819	-12.070
Vibrational specific heat (kb/atom):	0.978	0.944	0.950	0.949	0.949
lamb-mossbauer factor at T=0:	0.816	0.873	0.853	0.852	0.848
Kinetic energy/atom at T=0 (meV):	3.173	5.003	4.558	4.589	4.563
Force constant (N/m):	108.8	301.5	272.1	277.3	272.1
----------beta-value coefficients from g----------					
$1000\ln(\beta^{164}Dy/^{162}Dy)=A_1/T^2+A_2/T^4+A_3/T^6$ (T in K)					
A_1:	3.67E+04	1.02E+05	9.18E+04	9.36E+04	9.18E+04
A_2:	-1.47E+07	-2.57E+08	-2.75E+08	-2.76E+08	-2.48E+08
A_3:	-2.57E+10	1.98E+12	2.53E+12	2.31E+12	1.71E+12

The force constants of Dy in Dy_2O_3 is 301 ± 27 N/m, about 200 N/m higher than that in metallic Dy (108 ± 12 N/m). The synthesized glass samples show slightly lower force constants compared to Dy_2O_3 at about 270 N/m (Fig. 4.3).

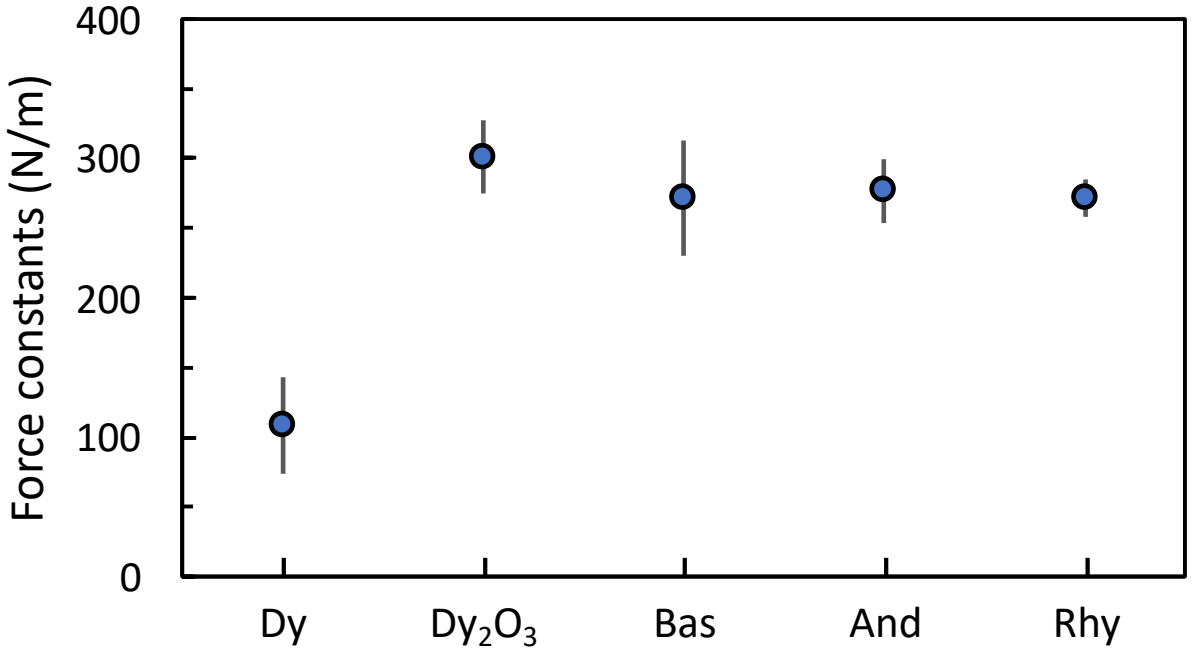

Figure 4.3 Force constants of Dy in metallic form, oxide and synthesized glass.

4.4. Discussion

4.4.1 Eu and Dy Equilibrium Isotopic Fractionation Factors in Pure Compounds and Glasses

The synthesized glass samples contain different proportions of Eu^{2+} and Eu^{3+}, which can influence the mean force constant. According to Burnham et al. (2015), the proportion of Eu^{3+} over total europium $\Sigma Eu=Eu^{2+} + Eu^{3+}$ in synthesized silicate glasses can be written as a function of oxygen fugacity fO_2, temperature T and optical basicity Λ,

$$Eu^{3+}/\Sigma Eu = \frac{1}{1+10^{-0.25\ln f_{O_2}-6410/T-14.2\Lambda+10.1}}. \qquad (4.11)$$

Optical basicity is a measure of the capacity of a silicate liquid to stabilize high charge-to-radius ratio cations, which can be calculated based on the glass chemical composition (Table 4.2; Duffy, 1993). Knowing the oxygen fugacity and temperature at which the glass samples were synthesized, and their optical basicities, one can calculate the $Eu^{3+}/\Sigma Eu$ ratio using Eq. 4.11 (Table 4.2). Accordingly, the oxidized basalt and rhyolite glass samples contain 98% and 82% Eu^{3+}, respectively. The reduced basalt and rhyolite glass samples contain 48% and 10% Eu^{3+} respectively. If one plots the force constants of Eu in the synthesized glasses against $Eu^{3+}/\Sigma Eu$ ratios, all 4 glass samples fall on a line with a slope of 131.4 and intercept of 82.5 (Fig. 4.4). The linear correlation of force constants and the Eu^{3+} fraction indicates that the variation of force constants in the glass samples is primarily controlled by the proportion of Eu^{2+} and Eu^{3+}, while the silicate composition has no significant influence. One can calculate the force constants of pure Eu^{2+} and Eu^{3+} in silicate glass by extrapolating the linear correlation to $Eu^{3+}/\Sigma Eu = 0$ and 1, yielding values of 83 ± 63 and 214 ± 68 N/m, with a difference in force constant between Eu^{2+} and Eu^{3+} glasses of 131 ± 109 N/m. These values overlap with the average force constants of Eu^{2+} (97 ± 23 N/m) and Eu^{3+} (192 ± 30 N/m) in pure chemical compounds. The force constant of Dy^{3+} in basalt, andesite, and rhyolite glasses are all very similar at ~270 N/m, which is significantly higher than the force constant of Eu^{3+} in the same glass of ~210 N/m.

X-ray absorption spectroscopy (XAS) shows that the coordination environment of the REEs can change depending on the host glass composition (Calas et al., 1987; Ponader and Brown Jr, 1989a, b). Specifically, the coordination or REEs can depend on the polymerization of the glass, the aluminum saturation index, the presence of halogen elements (F and Cl), and the nature of the REE. In general, heavier REEs tend to be in lower coordination (~5- to 6-fold) than lighter REEs

(7- to 9-fold). At the same valence, elements in lower coordination tend to form stiffer bonds than elements in higher coordination. We would therefore expect the mean force constant of heavy REE (HREE) Dy to be higher (lower coordination) than that of LREE Eu (higher coordination), which is consistent the NRIXS results ($\langle F \rangle$ = 273 N/m for Dy^{3+} vs. 214 N/m for Eu^{3+}).

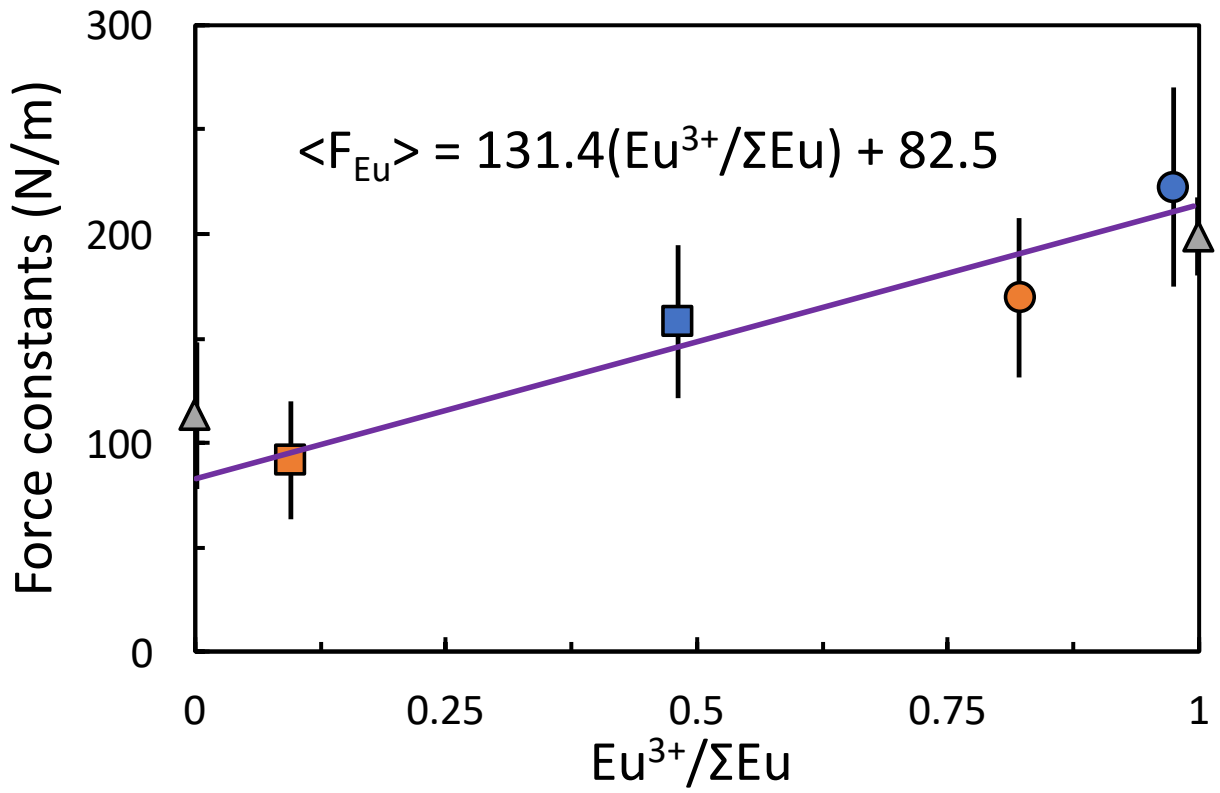

Figure 4.4 Force constants of Eu plotted as a function of Eu^{3+} fraction in synthesized glass. Blue and orange points represent synthesized glasses of basaltic and rhyolitic composition, while circles and cubes are synthesized in oxidized and reduced condition respectively. Purple line is the linear regression of all 4 synthesized glass. Grey triangles are force constants of EuO ($Eu^{3+}/\Sigma Eu = 0$) and Eu_2O_3 ($Eu^{3+}/\Sigma Eu = 100\%$).

As discussed in Sect. 4.2.2, one can calculate reduced partition function ratios using either $g(E)$ or $S(E)$, and it can be expressed as a polynomial of the even powers of the inverse of the temperature. At high temperature, $1000 \ln\beta$ is dominated by the first order term, which is proportional to the mean force constant of the bonds. As shown by Dauphas et al. (2017) and Chen

et al. (2020), one can derive an approximate expression valid at lower temperature by recognizing that the second and third coefficients in the polynomial expansions can all be related to A_1 or $\langle F \rangle$. In Fig. 4.5, we plot A_2 *vs.* $\langle F \rangle^2$ and A_3 *vs.* $\langle F \rangle^3$ for Eu and Dy in all the solids whose reduced partition function ratios were measured by NRIXS or calculated by DFT. As shown, there are clear linear relationships from which we can derive the following approximate formulas,

$$1000 \ln \beta^{^{153}\mathrm{Eu}/^{151}\mathrm{Eu}} = 380.9 \frac{\langle F_{\mathrm{Eu}} \rangle}{T^2} - 3754.9 \frac{\langle F_{\mathrm{Eu}} \rangle^2}{T^4} + 98522 \frac{\langle F_{\mathrm{Eu}} \rangle^3}{T^6}, \quad (12)$$

$$1000 \ln \beta^{^{164}\mathrm{Dy}/^{162}\mathrm{Dy}} = 331.2 \frac{\langle F_{\mathrm{Dy}} \rangle}{T^2} - 3280.2 \frac{\langle F_{\mathrm{Dy}} \rangle^2}{T^4} + 88176 \frac{\langle F_{\mathrm{Dy}} \rangle^3}{T^6}. \quad (13)$$

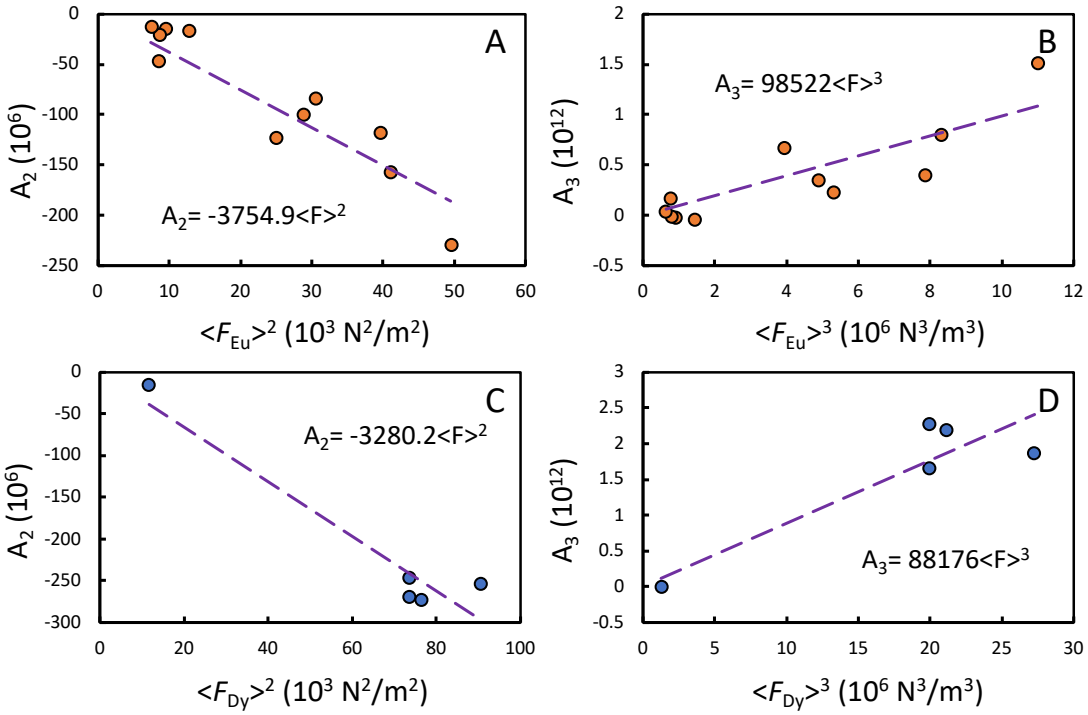

Figure 4.5 (A) A_2 *vs.* $\langle F \rangle^2$ for Eu. (B) A_3 *vs.* $\langle F \rangle^3$ for Eu. (C) A_2 *vs.* $\langle F \rangle^2$ for Dy. (D) A_3 *vs.* $\langle F \rangle^3$ for Dy. All the lines for linear regression are forced to pass through the origin point.

These formulas can be used to evaluate the temperature below which the high-temperature approximation breaks down (Fig. 4.6). Given the values of the force constants of Eu and Dy,

truncating the polynomial expansion to the first order gives reduced partition function ratios that are accurate within 5% for temperatures above ~−40 °C (accurate within 99% above ~270 °C).

In Fig. 4.7 and Fig, 4.8, we plot the $1000\ln\beta$ values of the various Eu and Dy compounds investigated. As shown, the largest equilibrium isotopic fractionation is between Eu^{3+} and Eu^{2+}. In silicate glasses, we indeed have,

$$1000\ln\alpha^{^{153}Eu/^{151}Eu}_{Eu^{3+}-Eu^{2+}} \simeq \frac{5.006\cdot10^{4}}{T^{2}} - \frac{6.485\cdot10^{7}}{T^{4}} + \frac{2.236\cdot10^{11}}{T^{6}}. \quad (4.14)$$

The absolute values remain small even at relatively low temperature, due in part to the small relative difference between the mass of the isotopes of Eu. The difference in force constant between Eu^{3+} and Eu^{2+} is the same order of magnitude as that between Fe^{3+} and Fe^{2+}, but the factor relating $1000\ln\beta$ to $\langle F\rangle$ is 2904 for the $^{56}Fe/^{54}Fe$ ratio compared to only 381 for the $^{153}Eu/^{151}Eu$ ratio. At 300°C relevant to low temperature aqueous systems, the equilibrium fractionation factor for the $^{153}Eu/^{151}Eu$ ratio between Eu^{3+} and Eu^{2+} and is +0.15 ‰, and it decreases to +0.05 ‰ at 700 °C relevant to metamorphic systems. Because Eu has only two stable isotopes, double spike cannot be used and the best currently achievable precision on $^{153}Eu/^{151}Eu$ isotopic ratio determinations is on the order of ±0.05 ‰, meaning that equilibrium isotopic fractionation should not be detectable in systems equilibrated above 700 °C, unless the Eu isotopic composition was fractionated through a distillation process. Kinetic effects can fractionate Eu isotopes, as has been documented in meteoritic refractory inclusions, driven in this case by evaporation and condensation in undersaturated and supersaturated media.

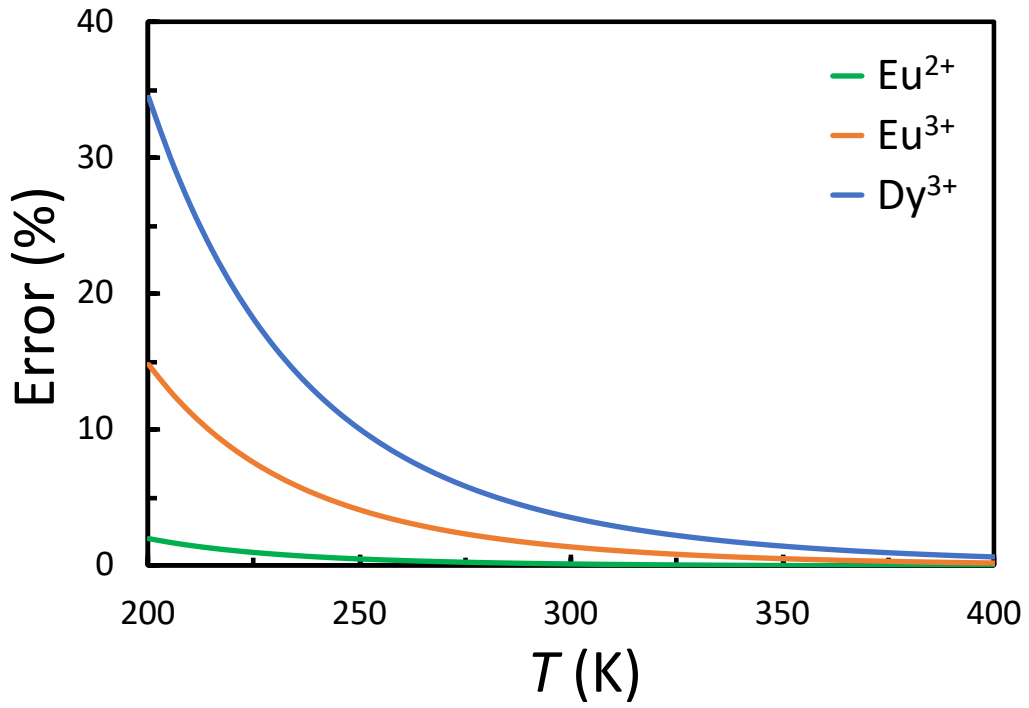

Figure 4.6 The relative error of 1000lnβ by truncating the polynomial expansion to the first order compared plotted as functions of temperature.

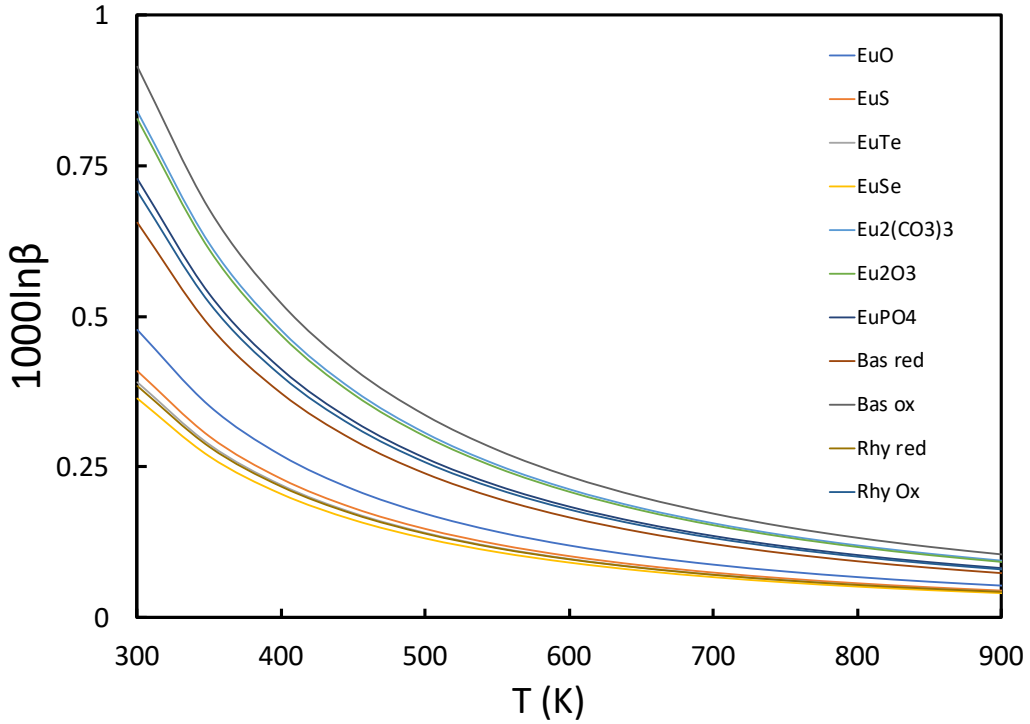

Figure 4.7 Reduce partition functions of Eu in minerals and synthesized glass. The difference of every two curves represents the equilibrium fractionation factors.

Since Dy only exists as Dy^{3+}, predicted equilibrium isotopic fractionation is more subdued than for Eu, which is influenced by Eu redox states (Fig. 4.8). The range of mean force constants for Dy from 271 to 301 N/m would allow for equilibrium isotopic fractionation of at most 0.11 and 0.02 ‰ for $\delta^{164/162}$Dy at 300 and 750 K, respectively. Current precision of Dy isotopic composition by sample-standard bracketing is approximately 0.03‰/amu (for geostandard BCR-2; Hu et al., 2021). This precision might be improved on using a double-spike approach, but in the current state of measurement capabilities, Dy equilibrium isotopic fractionation should not be detectable in natural samples unless it is magnified through a distillation process. As with Eu, kinetic processes can fractionate Dy isotopes at any temperature (*e.g.*, Hu et al., 2021)

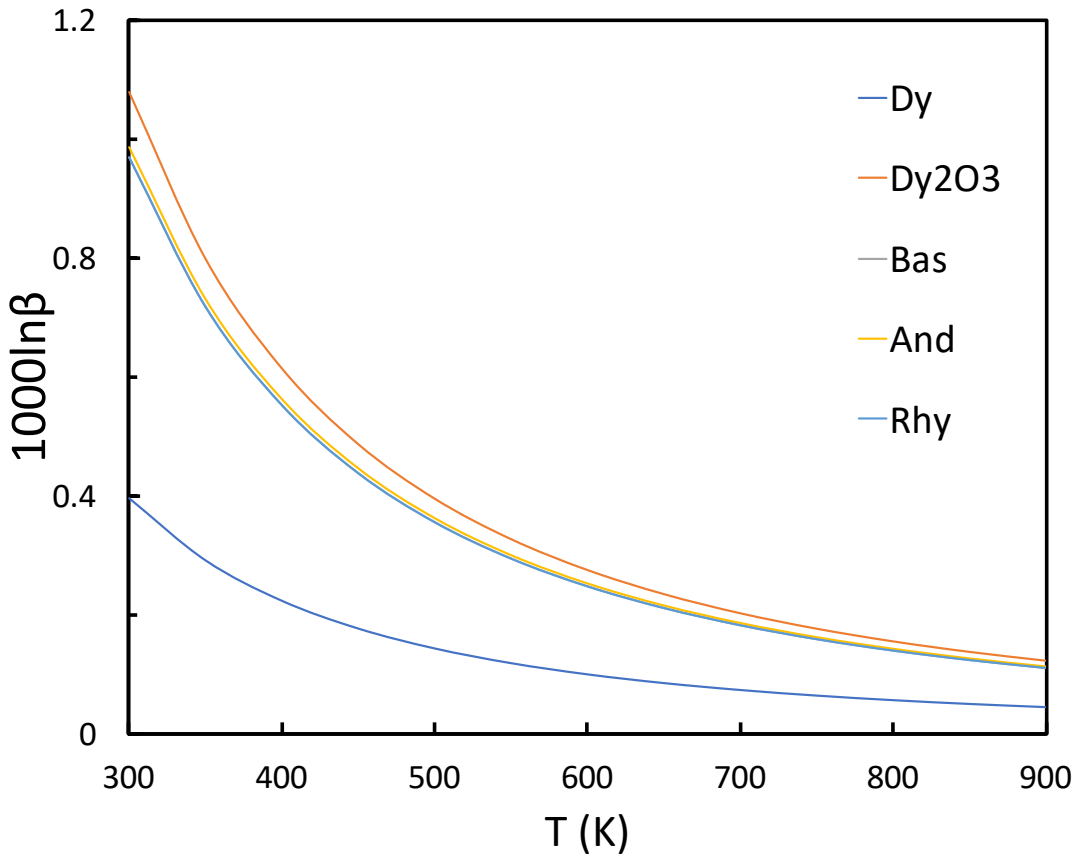

Figure 4.8 Reduce partition functions of Dy in minerals and synthesized glass. The difference of every two curves represents the equilibrium fractionation factors.

In most settings, the REEs exist in trivalent form and their properties scale smoothly with their atomic number, including their ionic radii (a phenomenon known as lanthanide contraction). One can thus interpolate and extrapolate the force constants of all REEs using those of Eu^{3+} and Dy^{3+}. To approach this question and assess how the force constant should be parameterized, we use the ionic bond model of Young et al. (2009), which gives for the mean force constant the following formula,

$$\langle F \rangle \approx \frac{z_i z_j e^2 (1-n)}{4\pi \vartheta_i \vartheta_j \varepsilon_0 {r_0}^3}, \quad (4.15)$$

where z_i and z_j are the valences of cation i and anion j, ϑ_i and ϑ_j are the CNs of i and j, e is the charge of an electron, ε_0 is the vacuum permittivity, r_0 is the interionic distance, and $n \approx 12$ is a repulsion term in the Born-Mayer interionic potential. We recognize that this formula does not provide accurate force constant estimates, but it can provide some guidance on scaling. Bond lengths tend to decrease with increasing REE atomic number in silicate glass (Fig. 5 of Cicconi et al., 2013; Ponader and Brown, 1989a) and minerals (Shannon, 1976; Cicconi et al., 2013). For a given glass composition or coordination geometry, the REE-O bond length in Å is related to the atomic number (*e.g.*, Z = 63 for Eu) through the relationship,

$$r_{0,\text{REE-O}} = a - 0.014\text{Z}, \quad (4.16)$$

with a a constant that depends on the material (glass composition) or site (6-fold, 8-fold coordination) considered. The REE-O bonds are between ~2.2 and 2.6 Å and for a given material, the difference between the lightest and heaviest REE is on the order of 0.2 Å relative. We therefore have for the force constant the following dependence on mass number,

$$\langle F \rangle \propto (a - 0.014\mathrm{Z})^{-3}. \quad (4.17)$$

If the force constant $\langle F \rangle$ is measured or calculated for a REE (Eu or Dy), one can estimate the force constant for the other REEs,

$$\langle F \rangle_i \simeq \left(\frac{a-0.014Z_{\mathrm{Eu}}}{a-0.014Z_i}\right)^3 \langle F \rangle_{\mathrm{Eu}}. \quad (4.18)$$

using the force constant for Eu^{3+} of 214 N/m and the force constant for Dy of 273 N/m, we obtain the value of a at 1.50. We use the same formula to calculate the force constants of other multi-isotope trivalent REEs, yielding values of 139 N/m for La^{3+}, 149 N/m for Ce^{3+}, 159 N/m for Pr^{3+}, 171 N/m for Nd^{3+}, 198 N/m for Sm^{3+}, 232 N/m for Gd^{3+}, 251 N/m for Tb^{3+}, 297 N/m for Ho^{3+}, 324 N/m for Er^{3+}, 355 N/m for Tm^{3+}, 390 N/m for Yb^{3+}, 429 N/m for Lu^{3+}. The reduced partition function ratios for Debye solids depend on the force constant following,

$$1000 \ln \beta^{^{139}\mathrm{La}/^{138}\mathrm{La}} = 229.1 \frac{\langle F_{\mathrm{La}} \rangle}{T^2} - 1149.7 \frac{\langle F_{\mathrm{La}} \rangle^2}{T^4}, \quad (4.19)$$

$$1000 \ln \beta^{^{142}\mathrm{Ce}/^{140}\mathrm{Ce}} = 443.1 \frac{\langle F_{\mathrm{Ce}} \rangle}{T^2} - 2177.5 \frac{\langle F_{\mathrm{Ce}} \rangle^2}{T^4}, \quad (4.20)$$

$$1000 \ln \beta^{^{146}\mathrm{Nd}/^{144}\mathrm{Nd}} = 418.9 \frac{\langle F_{\mathrm{Nd}} \rangle}{T^2} - 2001.5 \frac{\langle F_{\mathrm{Nd}} \rangle^2}{T^4}, \quad (4.21)$$

$$1000 \ln \beta^{^{152}\mathrm{Sm}/^{150}\mathrm{Sm}} = 386.1 \frac{\langle F_{\mathrm{Sm}} \rangle}{T^2} - 1771.9 \frac{\langle F_{\mathrm{Sm}} \rangle^2}{T^4}, \quad (4.22)$$

$$1000 \ln \beta^{^{158}\mathrm{Gd}/^{156}\mathrm{Gd}} = 357.1 \frac{\langle F_{\mathrm{Gd}} \rangle}{T^2} - 1576.2 \frac{\langle F_{\mathrm{Gd}} \rangle^2}{T^4}, \quad (4.23)$$

$$1000 \ln \beta^{^{168}\mathrm{Er}/^{166}\mathrm{Er}} = 315.5 \frac{\langle F_{\mathrm{Er}} \rangle}{T^2} - 1309.9 \frac{\langle F_{\mathrm{Er}} \rangle^2}{T^4}, \quad (4.24)$$

$$1000 \ln \beta^{^{174}\mathrm{Yb}/^{172}\mathrm{Yb}} = 294.1 \frac{\langle F_{\mathrm{Yb}} \rangle}{T^2} - 1178.6 \frac{\langle F_{\mathrm{Yb}} \rangle^2}{T^4}, \quad (4.25)$$

$$1000 \ln \beta^{^{176}\mathrm{Lu}/^{175}\mathrm{Lu}} = 143.0 \frac{\langle F_{\mathrm{Lu}} \rangle}{T^2} - 566.4 \frac{\langle F_{\mathrm{Lu}} \rangle^2}{T^4}. \quad (4.26)$$

At 300 and 1000 K, $1000 \ln \beta^{^{139}\mathrm{La}/^{138}\mathrm{La}}$ is 0.35 and 0.03 ‰, and $1000 \ln \beta^{^{174}\mathrm{Yb}/^{172}\mathrm{Yb}}$ is 1.25 and 0.11 ‰.

4.4.2 Negligible Equilibrium Isotopic Fractionation During Condensation and Evaporation

Equilibrium fractionation factors tend decrease rapidly with increasing temperature. However, a possible mitigating factor during evaporation and condensation processes is that many REEs under solar nebula conditions will be in different oxidation states than the solid, which can potentially induce equilibrium isotopic fractionation. This is directly relevant to REE isotopic analyses of refractory inclusions in meteorites (Hu et al., 2021). Hu et al. (2021) made the case that equilibrium isotopic fractionation between vapor and condensate would have been negligible in the solar nebula at the temperatures relevant to REE chemical fractionation. However, Hu et al. (2021) only considered Eu, while our new measurements and theoretical considerations allow us to apply the fractionation to other REEs.

According to the thermodynamic calculations, under solar nebula conditions, REEs would be present in trivalent states in host minerals such as hibonite and perovskite (Boynton, 1975; Davis and Grossman, 1979; Davis et al., 2018). For condensed REEs, we can therefore use the

force constants calculated above. In the gas, La, Pm, Nd, Gd to Dy and Lu mainly exist in the form of monoxides (2+), with a small fraction (<15%) existing as monatomic gas (0 oxidation state under solar nebular conditions). Gaseous Sm, Eu and Yb exist predominantly as monatomic species in a gas of solar composition. Gaseous Tm is a mixture of monoxide (70%) and monatomic (30%) gas. Cerium exists in the gas mostly as CeO_2 (4+), with a small fraction as CeO (2+). For the REEs present as monatomic gas, the reduced partition function ratio is 0. The REEs present in the gas as divalent monoxide can be calculated using measured vibration frequencies, as these scale directly with the force constant. The only force constant that we cannot easily constrain is that of quadrivalent CeO_2.

For REE monoxides, the vibrational frequencies in gaseous phase are known for LaO (808.3 cm^{-1}), CeO (808.3 cm^{-1}), GdO (790 cm^{-1}), HoO (741.4 cm^{-1}), and YbO (683.1cm^{-1}) (Gabelnick et al., 1974). The vibrational frequencies of the other REE monoxides in gaseous phase can be estimated using the vibrational frequencies in solid argon matrix, which are usually a few tens of cm^{-1} lower, with values of 816.9, 814.2, 807.4, 667.8, 823.9, 829, 828.5, 832, and 829.3 cm^{-1} reported for PrO, NdO, SmO, EuO, TbO, DyO, ErO, TmO, and LuO, respectively. We can convert those vibration frequencies to force constants assuming harmonic behavior using the following formula,

$$\langle F \rangle_s = 4\pi^2 m^* c^2 \nu^2, \quad (4.27)$$

where ν is the vibration wavenumber of the REE, $c = 299792458\ \mathrm{m/s}$ is the speed of light, and m^* is the reduced mass of the species. We thus calculate force constants of 552.3, 574.9, 564.9, 562.5, 555.4, 380.3, 534.0, 581.4, 589.8, 608.3, 590.6, 596.1, 402.6, and 594.0 N/m for gaseous

LaO, CeO, PrO, NdO, SmO, EuO, GdO, TbO, DyO, HoO, ErO, TmO, YbO, and LuO. Knowing the force constants for a REE i in the solid and various vapor species, we can calculate the equilibrium isotopic fractionation between vapor and solid,

$$\Delta_{i,eq,v-s} = \frac{1}{T^2}\left(\sum_p x_{i,p}\langle F\rangle_{i,p} - \langle F\rangle_{i,s}\right), \quad (4.28)$$

where p enumerates all the gas species (REE^0, REE^{2+}, REE^{4+}), $x_{i,p}$ is the fraction of REE i that is in species p, $\langle F\rangle_{i,p}$ is the force constant of the REE in the vapor, and $\langle F\rangle_{i,s}$ is the force constant in the solid. The gas speciation $x_{i,p}$ depends on temperature and oxygen fugacity (values for a gas of solar composition are shown in Fig. 4.9) (Davis and Grossman, 1979; Davis et al., 2018; Hu et al., 2021).

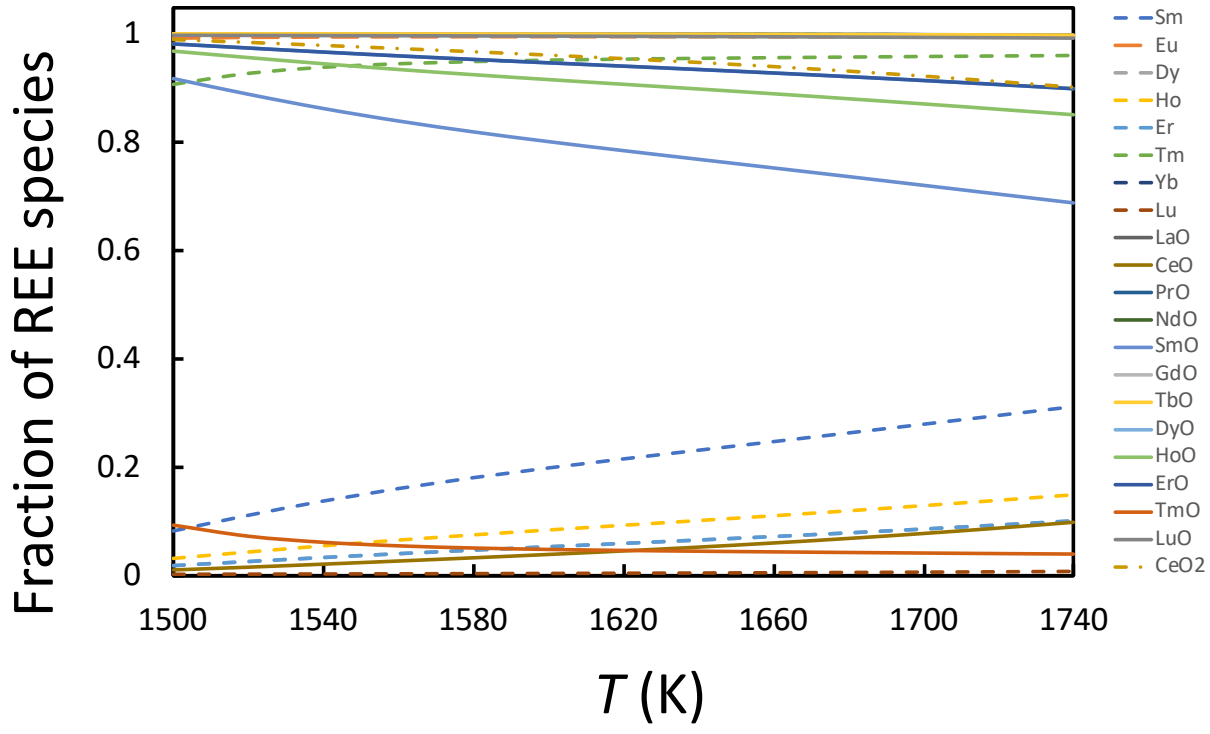

Figure 4.9 Fractions of REE gaseous species plotted at functions of temperature.

We have used this formula, the gas species proportions shown in Fig. 4.9 (calculated following Davis and Grossman, 1979; Davis et al., 2018; Hu et al., 2021), and the force constants to calculate equilibrium fractionation factors. At the temperature of 1600 K relevant to REE chemical fractionation in group II fine-grained inclusions, we find that the expected equilibrium isotopic fractionations are well within 0.02 ‰/amu. Focusing on the REEs that are most depleted and most isotopically fractionated in CAIs (Gd, Dy, and Er), we find that distillations either through evaporation or condensation could produce condensates that would be less fractionated than the values encountered in natural samples (Hu et al., 2021). This means that the isotopic large fractionations measured for selected REEs in fine-grained group II CAI must have been produced by kinetic processes (evaporation in undersaturated or condensation from supersaturated medium).

4.4.3 Europium Isotopic Fractionation during Magma Differentiation

Due to their relatively large ionic radii, REEs are generally incompatible, partitioning preferentially in the magma during melting or crystallization. Rare earth elements usually partition into major minerals by substituting elements of similar ionic radius by simple substitution (*e.g.*, $EuCa_{-1}$ meaning adding Eu and removing Ca), creating vacancies (*e.g.*, $([\ ]REE_2)Ca_{-3}$, $([\ ]REE)(CaK)_{-1}$), and concomitant or coupled substitution (*e.g.*, $REEMg(CaAl)_{-1}$, $REEAl(CaSi)_{-1}$, and $REENaCa_{-2}$) (Wood and Blundy, 1997; Witt-Eickschen and O'Neill, 2005; Lee et al., 2007; Sun and Liang, 2012; Yao et al., 2012; Liang et al., 2013; Wood and Blundy, 2014; Shimizu et al., 2013, 2017). The major repositories of REEs among major rock-forming minerals include clinopyroxene (CN = 8 in the M2 site; Sun and Liang, 2012; Wood and Blundy, 1997), garnet (CN = 8 in the X site; Sun and Liang, 2013; Westrenen et al., 2001), plagioclase (CN = 8 in the M site; Bédard, 2006; Bindeman and Davis, 2000), low-Ca pyroxene (CN = 6 in the M2 site; Yao et al.,

2012), and amphibole (CN = 8 in the M4 site; Shimizu et al., 2017). Divalent Eu has larger ionic radius than trivalent Eu and preferentially partitions into plagioclase, where it substitutes Ca^{2+} in CN = 8. Under extreme reducing conditions, the partition coefficient of Eu between plagioclase and melt is close to that of Sr.

In addition to major rock-forming minerals, a significant fraction of REE can concentrate in accessory minerals as the magma evolves. In special cases, REEs can form independent minerals especially during late-stage evolution of carbonatite and peralkaline rocks. The most common minerals include bastnaesite and monazite, which incorporate light REEs (LREEs) with CNs of 11 and 9 respectively, and xenotime, which contains HREEs with a CN of 8 (Kanazawa and Kamitani, 2006).

Among the minerals studied in this work, EuO, Dy_2O_3 and Eu_2O_3 host REEs in a CN of 6, $EuPO_4$ in a CN of 8, and EuS, EuSe, and EuTe in CNs of either 6 or 8 (Table. 4.1). The pure compounds studied capture the diversity of coordination environments for major REE-bearing minerals in nature. We find no strong control of coordination on force constants (at our current level of precision), implying that limited isotopic fractionation is expected during magmatic differentiation for REEs that exist as a single oxidation state. Europium can exist in magmas as both Eu^{2+} and Eu^{3+} (Burnham et al., 2015), potentially providing some leverage to fractionate Eu isotopes during magmatic differentiation. This is most likely to happen at the final stage of magma differentiation when plagioclase and K-felspar crystalize, sequestering and removing Eu^{2+} from the melt. The affinity of Eu^{2+} for plagioclase and K-felspar leads to fractionation of Eu^{2+} and Eu^{3+} between mineral and residual melt. The residue melt is enriched in Eu^{3+} and should concentrate heavy isotopes.

A striking example of this phenomenon is provided by the lunar magma ocean, where mare basalts acquired a negative Eu anomaly due to crystallization of plagioclase and formation of a flotation crust characterized by positive Eu anomalies (Warren, 1985 and references therein). Plagioclase crystallization and flotation is thought to have taken place through a distillation process, which can amplify equilibrium fractionation through a Rayleigh process. For a negative Eu anomaly of 0.3 ($\mathrm{Eu/Eu^*} = \sqrt{\mathrm{Sm}_N \cdot \mathrm{Gd}_N}$) and a temperature of 1000 °C, the $\delta^{153/151}$Eu isotopic composition of mare basalts could be fractionated by 0.03 ‰ relative to the bulk silicate Moon, while the anorthosite flotation crust would be fractionated by −0.01 ‰, which are less than the current precision of Eu isotope measurement ±0.05 ‰. Overall, the isotopic fractionations of Eu induced from magmatic process at over 1000 °C are negligible for the current precision.

4.4.4 Europium Isotopic Fractionation in Hydrothermal Systems

Mid-Ocean Ridge (MOR) hydrothermal fluids on basaltic substrates are characterized by positive Eu abundance anomaly and LREE enrichment normalized to chondrites. This has been interpreted to be due to exchange between the fluid and plagioclase phenocrysts, involving the transformation of anorthite to albite, a process known as albitization (Klinkhammer et al., 1994; James et al., 1995; Douville et al., 1999). Anorthite has a LREE-enriched REE pattern with a positive Eu anomaly. Due to the relatively low water/rock ratio (Michard and Albarède, 1986), REEs released from a small fraction of anorthite phenocrysts can dominate the REE pattern in the hydrothermal fluid. Hydrothermal systems in ultramafic rocks such as Lucky Strike and Snakepit fluids and the PacManus and Desmos fluids (Douville et al., 1999) also show positive Eu anomalies that cannot be ascribed to albitization and must reflect other processes. Divalent Eu is not stable in seawater at room temperature. However, its stability increases with warmer, more

acidic and reducing environment (Liu et al., 2017). The relatively high temperature as well as acidic and reducing environment of rainbow vent fluid system thus possibly allow for co-existing Eu^{2+} and Eu^{3+} (Allen and Seyfried, 2005). In that setting, the positive Eu abundance anomalies could be induced by difference in partitioning of Eu^{2+} and Eu^{3+} between the parent rock and the fluid, leading to higher leaching efficiency for Eu compared with other REEs. Although this scenario has been to some extent supported by experiments, it has not been directly observed. Europium isotopic fractionation can potentially help distinguish the effects of albitization and oxidation state change during hydrothermal fluid formation.

If the positive Eu anomalies are induced by albitization, one would expect that the fluids should inherited the Eu isotopic signature of the source rocks. According to Fig. 4.7, the stable isotopic fractionation of Eu above 600 °C is limited. Therefore, one would expect that the fluid would present a Eu isotopic signature that is very similar to igneous rocks.

If the positive Eu anomalies are instead controlled by the valence change, one could calculate the stable isotopic fractionation based on the proportion of Eu^{2+} and Eu^{3+} in the fluid and in the source rock. According to Liu et al. (2017), the proportion of Eu^{2+} and Eu^{3+} in the fluid is a function of oxygen fugacity, temperature, and pH. Canaval and Rode (2015) constrained the force constants of hydrated species of Eu^{2+} and Eu^{3+} through quantum mechanical charge-field molecular dynamics (QMCF-MD) approach. For Eu^{2+} (CN = 8) and Eu^{3+} (CN = 9), they found values of 49 and 99 N/m. Under the conditions of seafloor hydrothermal fluid circulation, a significant fraction of Eu also form as chloride complexes (Migdisov et al., 2016; Liu et al., 2017), the force constants of which are unknown. Assuming that all Eu is trivalent in the source rock, one can calculate that the fractionation factor between fluid and solid should be between 0.23‰ and

0.16‰ at 250 °C using the β-factor of Eu^{2+} and Eu^{3+} in the aqueous fluid (using the force constants of hydrous Eu as a proxy) and Eu^{3+} in rocks (214 N/m). If Eu anomalies in hydrothermal fluids are due to the stabilization of Eu^{2+} in the fluid at a low temperature below 400 °C, measurable Eu isotopic fractionation should be present. Ubiquitous positive Eu anomalies observed in the banded iron formation (BIF) older than 2.5 Ga have been generally interpreted to be a signature of hydrothermal origin, suggesting hydrothermal input be an important source of the global ocean during Archean (Danielson et al., 1992; Kato et al., 1998). The source of Eu anomaly can be either generated from the selective destruction of plagioclase (mafic) or controlled by the valence change (ultramafic). The Eu stable isotopic compositions of BIF and other Archean sediments could be used to constrain the composition of the Archean oceanic crust.

4.5. Conclusion

We conducted NRIXS measurement on minerals and for the first time, on synthesized glass samples to analyze Mossbauer isotopes ^{151}Eu and ^{161}Dy. Physical parameters related to PDOS are presented including the force constant of Eu^{2+}, Eu^{3+} and Dy^{3+}. The range of equilibrium fractionation factors obtained from force constants are in per-mil levels.

The force constants of minerals obtained from NRIXS measurement are compared with that from *ab initio* calculation and found to be consistent within the error. All the minerals analyzed in this study show similar force constants with averages of 97 ± 23 N/m for Eu^{2+} and 192 ± 30 N/m for Eu^{3+}. The force constants in the synthesized glass are controlled by the proportion of Eu^{2+} and Eu^{3+}, while the force constants of pure Eu^{2+} and Eu^{3+} do not vary with the glass chemical composition, which are 83 N/m for Eu^{2+} and 214 N/m for Eu^{3+}. Overall, force constant measurement show that Eu equilibrium isotopic fractionation is primarily controlled by redox

change while the influence of bonding environment is much more subdued. The β-factor calculated from the force constants show that equilibrium isotopic fractionation is negligible. The most likely application of Eu isotopes is to study the phase change in low temperature (less than 400 °C) hydrothermal fluid system such as MOR hydrothermal system and hydrothermal fluid related REE mineral deposits.

Dysprosium-doped synthesized glasses display highly consistent force constants at approximately 270 N/m, which are same within error from basaltic to rhyolitic composition. β-factor calculated from the force constants are the same within error for all synthesized glass and hence the isotopic fractionation of Dy during igneous process is negligible. A possible condition for Dy isotopes to be fractionated is during the condensation and evaporation in the solar nebula stage, which can be used to test the extent of deviation from equilibrium, an assumption of condensation sequence.

4.6. References

Allen, D.E., Seyfried, W.E.Jr., 2005. REE controls in ultramafic hosted MOR hydrothermal systems: an experimental study at elevated temperature and pressure. Geochimica et Cosmochimica Acta 69, 675-683.

Anisimov, V.I., Solovyev, I.V., Korotin, M.A., Czyżyk, M.T., Sawatzky, G.A., 1993. Density-functional theory and NiO photoemission spectra. Physical Review B 48, 16929-16934.

Anisimov, V.I., Zaanen, J., Andersen, O.K., 1991. Band theory and Mott insulators: Hubbard U instead of Stoner I. Physical Review B 44, 943-954.

Bédard, J.H., 2006. Trace element partitioning in plagioclase feldspar. Geochimica et Cosmochimica Acta 70, 3717-3742.

Bindeman, I.N., Davis, A.M., 2000. Trace element partitioning between plagioclase and melt: investigation of dopant influence on partition behavior. Geochimica et Cosmochimica Acta 64, 2863-2878.

Boynton, W.V., 1975. Fractionation in the solar nebula: condensation of yttrium and the rare earth elements. Geochimica et Cosmochimica Acta 39, 569-584.

Burnham, A.D., Berry, A.J., Halse, H.R., Schofield, P.F., Cibin, G., Mosselmans, J.F.W., 2015. The oxidation state of europium in silicate melts as a function of oxygen fugacity, composition and temperature. Chemical Geology 411, 248-259.

Calas, G., Brown, G.E., Waychunas, G.A., Petiau, J., 1987. X-ray absorption spectroscopic studies of silicate glasses and minerals. Physics and Chemistry of Minerals 15, 19-29.

Canaval, L.R., Rode, B.M., 2015. The hydration properties of Eu (II) and Eu (III): An ab initio quantum mechanical molecular dynamics study. Chemical Physics Letters 618, 78-82.

Chen, X., Wang, W., Zhang, Z., Nie, N.X., Dauphas, N., 2020. Evidence from Ab initio and transport modeling for diffusion-driven zirconium isotopic fractionation in igneous rocks. ACS Earth and Space Chemistry 4, 1572-1595.

Cicconi, M.R., Giuli, G., Paris, E., Courtial, P., Dingwell, D.B., 2013. XAS investigation of rare earth elements in sodium disilicate glasses. Journal of Non-Crystalline Solids 362, 162-168.

Dal Corso, A., 2014. Pseudopotentials periodic table: From H to Pu. Computational Materials Science 95, 337-350.

Danielson, A., Möller, P., Dulski, P., 1992. The europium anomalies in banded iron formations and the thermal history of the oceanic crust. Chemical Geology 97, 89-100.

Dauphas, N., Hu, M.Y., Baker, E.M., Hu, J., Tissot, F.L., Alp, E.E., Roskosz, M., Zhao, J., Bi, W., Liu, J., 2018. SciPhon: a data analysis software for nuclear resonant inelastic X-ray scattering with applications to Fe, Kr, Sn, Eu and Dy. Journal of Synchrotron Radiation 25, 1581-1599.

Dauphas, N., John, S.G., Rouxel, O., 2017. Iron isotope systematics. Reviews in Mineralogy and Geochemistry 82, 415-510.

Dauphas, N., Pourmand, A., 2015. Thulium anomalies and rare earth element patterns in meteorites and Earth: Nebular fractionation and the nugget effect. Geochimica et Cosmochimica Acta 163, 234-261.

Dauphas, N., Roskosz, M., Alp, E.E., Golden, D.C., Sio, C.K., Tissot, F.L.H., Hu, M.Y., Zhao, J., Gao, L. and Morris, R.V., 2012. A general moment NRIXS approach to the determination of equilibrium Fe isotopic fractionation factors: application to goethite and jarosite. Geochimica et Cosmochimica Acta 94, 254-275.

Dauphas, N., Roskosz, M., Alp, E.E., Neuville, D.R., Hu, M.Y., Sio, C.K., Tissot, F.L.H., Zhao, J., Tissandier, L., Médard, E. and Cordier, C., 2014. Magma redox and structural controls on iron isotope variations in Earth's mantle and crust. Earth and Planetary Science Letters 398, 127-140.

Davis, A.M., Grossman, L., 1979. Condensation and fractionation of rare earths in the solar nebula. Geochimica et Cosmochimica Acta 43, 1611-1632.

Davis, A.M., Zhang, J., Greber, N.D., Hu, J., Tissot, F.L.H., Dauphas, N., 2018. Titanium isotopes and rare earth patterns in CAIs: evidence for thermal processing and gas-dust decoupling in the protoplanetary disk. Geochimica et Cosmochimica Acta 221, 275-295.

Douville, E., Bienvenu, P., Charlou, J.L., Donval, J.P., Fouquet, Y., Appriou, P., Gamo, T., 1999. Yttrium and rare earth elements in fluids from various deep-sea hydrothermal systems. Geochimica et Cosmochimica Acta 63, 627-643.

Duffy, J.A., 1993. A review of optical basicity and its applications to oxidic systems. Geochimica et Cosmochimica Acta 57, 3961-3970.

Gabelnick, S.D., Reedy, G.T. and Chasanov, M.G., 1974. Infrared spectra and structure of some matrix-isolated lanthanide and actinide oxides. The Journal of Chemical Physics 60, 1167-1171.

Garrity, K.F., Bennett, J.W., Rabe, K.M., Vanderbilt, D., 2014. Pseudopotentials for high-throughput DFT calculations. Computational Materials Science 81, 446-452.

Giannozzi, P., Andreussi, O., Brumme, T., Bunau, O., Nardelli, M.B., Calandra, M., Car, R., Cavazzoni, C., Ceresoli, D., Cococcioni, M. and Colonna, N., Carnimeo, I., Dal Corso, A., de Gironcoli, S., Delugas, P., DiStasio, R.A.Jr., Ferretti, A., Floris, A., Fratesi, G., Fugallo, G., Gebauer, R., Gerstmann, U., Giustino, F., Gorni T., Jia, J., Kawamura, M., Ko, H-Y., Kokalj, A., Küçükbenli, E., Lazzeri, M., Marsili, M., Marzari, N., Mauri, F., Nguyen, N.L., Nguyen, H-V., Otero-de-la-Roza, A., Paulatto, L., Poncé, S., Rocca, D., Sabatini, R., Santra B., Schlipf, M., Seitsonen, A.P., Smogunov, A., Timrov, I., Thonhauser, T., Umari, P., Vast, N., Wu, X., Baroni, S., 2017. Advanced capabilities for materials modelling with Quantum ESPRESSO. Journal of Physics: Condensed Matter 29, #465901 (30 pp).

Grossman, L., 1972. Condensation in the primitive solar nebula. Geochimica et Cosmochimica Acta 36, 597-619.

Hu, J.Y., Dauphas, N., Tissot, F.L.H., Yokochi, R., Ireland, T.J., Zhang, Z., Davis, A.M., Ciesla, F.J., Grossman, L., Charlier, B. L.A., Roskosz, M., Alp, E.E., Hu, M.Y., Zhao, J., 2021. Heating events in the nascent solar system recorded by rare earth element isotopic fractionation in refractory inclusions. Science Advances 7, eabc2962.

James, R.H., Elderfield, H. and Palmer, M.R., 1995. The chemistry of hydrothermal fluids from the Broken Spur site, 29 N Mid-Atlantic Ridge. Geochimica et Cosmochimica Acta 59, 651-659.

Kanazawa, Y., Kamitani, M., 2006. Rare earth minerals and resources in the world. Journal of Alloys and Compounds 408, 1339-1343.

Kato, Y., Ohta, I., Tsunematsu, T., Watanabe, Y., Isozaki, Y., Maruyama, S., Imai, N., 1998. Rare earth element variations in mid-Archean banded iron formations: Implications for the chemistry of ocean and continent and plate tectonics. Geochimica et Cosmochimica Acta 62, 3475-3497.

Klinkhammer, G.P., Elderfield, H., Edmond, J.M. and Mitra, A., 1994. Geochemical implications of rare earth element patterns in hydrothermal fluids from mid-ocean ridges. Geochimica et Cosmochimica Acta 58, 5105-5113.

Kohn, V.G. and Chumakov, A.I., 2000. DOS: Evaluation of phonon density of states from nuclear resonant inelastic absorption. Hyperfine Interactions 125, 205-221.

Lee, C.T.A., Harbert, A., Leeman, W.P., 2007. Extension of lattice strain theory to mineral/mineral rare-earth element partitioning: an approach for assessing disequilibrium and developing internally consistent partition coefficients between olivine, orthopyroxene, clinopyroxene and basaltic melt. Geochimica et Cosmochimica Acta 71, 481-496.

Lejaeghere, K. et al., 2016. Reproducibility in density functional theory calculations of solids. Science 351, #aad3000 (7 pp).

Liang, Y., Sun, C., Yao, L., 2013. A REE-in-two-pyroxene thermometer for mafic and ultramafic rocks. Geochimica et Cosmochimica Acta 102, 246-260.

Lin, J.F., Struzhkin, V.V., Sturhahn, W., Huang, E., Zhao, J., Hu, M.Y., Alp, E.E., Mao, H-K., Boctor, N., Hemley, R.J., 2003. Sound velocities of iron-nickel and iron-silicon alloys at high pressures. Geophysical Research Letters 30, #2003GL018405 (4 pp).

Lipin, B.R., McKay, G.A., 1989. Geochemistry and mineralogy of rare earth elements. Reviews in Mineralogy and Geochemistry, Vol. 21.

Lipkin, H.J., 1995. Mössbauer sum rules for use with synchrotron sources. Physical Review B 52, 10073-10079.

Liu, W., Etschmann, B., Migdisov, A., Boukhalfa, H., Testemale, D., Müller, H., Hazemann, J.-L., Brugger, J., 2017. Revisiting the hydrothermal geochemistry of europium (II/III) in light of new in-situ XAS spectroscopy results. Chemical Geology 459, 61-74.

Lodders, K., 2003. Solar system abundances and condensation temperatures of the elements. The Astrophysical Journal 591, 1220-1247.

MacPherson, G. J., 2014, Calcium-aluminum-rich inclusions in chondritic meteorites. In Meteorites and Cosmochemical Processes (Ed. A. M. Davis), Vol. 1 Treatise on Geochemistry, 2nd Ed. (Exec. Eds. H. D. Holland and K. K. Turekian), Elsevier, Oxford, pp. 139-179.

Mao, H.K., Xu, J., Struzhkin, V.V., Shu, J., Hemley, R.J., Sturhahn, W., Hu, M.Y., Alp, E.E., Vocadlo, L., Alfè, D. and Price, G.D., Gillan, M.J., Schwoerer-Böhning, M., Häusermann, D., Eng, P., Shen, G., Giefers, H., Lübbers, R., Wortmann, G., 2001. Phonon density of states of iron up to 153 gigapascals. Science 292, 914-916.

Mao, W.L., Mao, H-K., Sturhahn, W., Zhao, J., Prakapenka, V.B., Meng, Y., Shu, J., Fei, Y., Hemley, R.J., 2006. Iron-rich post-perovskite and the origin of ultralow-velocity zones. Science 312, 564-565.

Mason, B., Taylor, S.R., 1982. Inclusions in the Allende meteorite. Smithsonian Contributions to the Earth Sciences.

Michard, A., Albarede, F., 1986. The REE content of some hydrothermal fluids. Chemical Geology 55, 51-60.

Migdisov, A., Williams-Jones, A.E., Brugger, J., Caporuscio, F.A., 2016. Hydrothermal transport, deposition, and fractionation of the REE: Experimental data and thermodynamic calculations. Chemical Geology 439, 13-42.

Monkhorst, H.J., Pack, J.D., 1976. Special points for Brillouin-zone integrations. Physical Review B 13, 5188-5192.

Ni, Y., Hughes, J.M., Mariano, A.N., 1995. Crystal chemistry of the monazite and xenotime structures. American Mineralogist 80, 21-26.

Nowacki, W., 1938. Die Kristallstruktur von EuS. Zeitschrift für Kristallographie-Crystalline Materials 99, 339-341.

Polyakov, V.B., Clayton, R.N., Horita, J. and Mineev, S.D., 2007. Equilibrium iron isotope fractionation factors of minerals: reevaluation from the data of nuclear inelastic resonant X-ray scattering and Mössbauer spectroscopy. Geochimica et Cosmochimica Acta 71, 3833-3846.

Polyakov, V.B., Mineev, S.D., Clayton, R.N., Hu, G., Gurevich, V.M., Khramov, D.A., Gavrichev, K.S., Gorbunov, V.E. and Golushina, L.N., 2005. Oxygen isotope fractionation factors involving cassiterite (SnO_2): I. Calculation of reduced partition function ratios from heat capacity and X-ray resonant studies. Geochimica et cosmochimica acta 69, 1287-1300.

Polyakov, V.B., 2009. Equilibrium iron isotope fractionation at core-mantle boundary conditions. Science 323, 912-914.

Ponader, C.W., Brown, G.E.Jr., 1989a. Rare earth elements in silicate glassmelt systems: I. Effects of composition on the coordination environments of La, Gd, and Yb. Geochimica et Cosmochimica Acta 53, 2893-2903.

Ponader, C.W., Brown Jr, G.E., 1989b. Rare earth elements in silicate glassmelt systems: II. Interactions of La, Gd, and Yb with halogens. Geochimica et Cosmochimica Acta 53, 2905-2914.

Pourmand, A., Dauphas, N., Ireland, T.J., 2012. A novel extraction chromatography and MC-ICP-MS technique for rapid analysis of REE, Sc and Y: Revising CI-chondrite and Post-Archean Australian Shale (PAAS) abundances. Chemical Geology 291, 38-54.

Prandini, G., Marrazzo, A., Castelli, I.E., Mounet, N., Marzari, N., 2018. Precision and efficiency in solid-state pseudopotential calculations. npj Computational Materials 4, 1-13.

Roskosz, M., Amet, Q., Fitoussi, C., Dauphas, N., Bourdon, B., Tissandier, L., Hu, M.Y., Said, A., Alatas, A., Alp, E.E., 2020. Redox and structural controls on tin isotopic fractionations among magmas. Geochimica et Cosmochimica Acta 268, 42-55.

Schlipf, M., Gygi, F., 2015. Optimization algorithm for the generation of ONCV pseudopotentials. Computer Physics Communications 196, 36-44.

Shahar, A., Young, E.D., Manning, C.E., 2008. Equilibrium high-temperature Fe isotope fractionation between fayalite and magnetite: an experimental calibration. Earth and Planetary Science Letters 268, 330-338.

Shannon, R.D., 1976. Revised effective ionic radii and systematic studies of interatomic distances in halides and chalcogenides. Acta Crystallographica Section A: Crystal Physics, Diffraction, Theoretical and General Crystallography 32, 751-767.

Shimizu, K., Liang, Y., Sun, C., Jackson, C.R.M., Saal, A.E., 2017. Parameterized lattice strain models for REE partitioning between amphibole and silicate melt. American Mineralogist: Journal of Earth and Planetary Materials 102, 2254-2267.

Solovyev, I.V., Dederichs, P.H. and Anisimov, V.I., 1994. Corrected atomic limit in the local-density approximation and the electronic structure of d impurities in Rb. Physical Review B 50, 16861-16871.

Sturhahn, W., 2000. CONUSS and PHOENIX: Evaluation of nuclear resonant scattering data. Hyperfine Interactions 125, 149-172.

Sturhahn, W., Toellner, T.S., Alp, E.E., Zhang, X., Ando, M., Yoda, Y., Kikuta, S., Seto, M., Kimball, C.W. and Dabrowski, B., 1995. Phonon density of states measured by inelastic nuclear resonant scattering. Physical Review Letters 74, 3832-3835.

Sun, C., Liang, Y., 2012. Distribution of REE between clinopyroxene and basaltic melt along a mantle adiabat: effects of major element composition, water, and temperature. Contributions to Mineralogy and Petrology 163, 807-823.

Sun, C., Liang, Y., 2013. The importance of crystal chemistry on REE partitioning between mantle minerals (garnet, clinopyroxene, orthopyroxene, and olivine) and basaltic melts. Chemical Geology 358, 23-36.

Tanaka, T., Masuda, A., 1973. Rare-earth elements in matrix, inclusions, and chondrules of the Allende meteorite. Icarus 19, 523-530.

Toellner, T.S., Hu, M.Y., Bortel, G., Sturhahn, W., Shu, D., 2006. Four-reflection “nested” meV-monochromators for 20-30 keV synchrotron radiation. Nuclear Instruments and Methods in Physics Research Section A: Accelerators, Spectrometers, Detectors and Associated Equipment 557, 670-675.

Togo, A., Tanaka, I., 2015. First principles phonon calculations in materials science. Scripta Materialia 108, 1-5.

Topsakal, M., Wentzcovitch, R.M., 2014. Accurate projected augmented wave (PAW) datasets for rare-earth elements (RE = La-Lu). Computational materials science 95, 263-270.

Wadhwa, M., 2001. Redox state of Mars' upper mantle and crust from Eu anomalies in shergottite pyroxenes. Science 291, 1527-1530.

Warren, P.H., 1985. The magma ocean concept and lunar evolution. Annual Review of Earth and Planetary Sciences 13, 201-240.

Westrenen, W., Wood, B.J., Blundy, J.D., 2001. A predictive thermodynamic model of garnet–melt trace element partitioning. Contributions to Mineralogy and Petrology 142, 219-234.

Witt-Eickschen, G., O'Neill, H.S.C., 2005. The effect of temperature on the equilibrium distribution of trace elements between clinopyroxene, orthopyroxene, olivine and spinel in upper mantle peridotite. Chemical Geology 221, 65-101.

Wood, B.J., Blundy, J.D., 2014. Trace element partitioning: the influences of ionic radius, cation charge, pressure, and temperature. In The Mantle and Core (Ed. R. W. Carlson), Vol. 3 Treatise on Geochemistry, 2nd Ed. (Exec. Eds. H. D. Holland and K. K. Turekian). Elsevier, Oxford, 421-448.

Wood, B.J., Blundy, J.D., 1997. A predictive model for rare earth element partitioning between clinopyroxene and anhydrous silicate melt. Contributions to Mineralogy and Petrology 129, 166-181.

Wyckoff, R.W.G., 1963. Crystal structures, Volume 1, 85-237.

Yao, L., Sun, C., Liang, Y., 2012. A parameterized model for REE distribution between low-Ca pyroxene and basaltic melts with applications to REE partitioning in low-Ca pyroxene along a mantle adiabat and during pyroxenite-derived melt and peridotite interaction. Contributions to Mineralogy and Petrology 164, 261-280.

Young, E.D., Tonui, E., Manning, C.E., Schauble, E., Macris, C.A., 2009. Spinel-olivine magnesium isotope thermometry in the mantle and implications for the Mg isotopic composition of Earth. Earth and Planetary Science Letters 288, 524-533.

Zeng, H., Rozsa, V.F., Nie, N.X., Zhang, Z., Pham, T.A., Galli, G., Dauphas, N., 2019. Ab initio calculation of equilibrium isotopic fractionations of potassium and rubidium in minerals and water. ACS Earth and Space Chemistry 3, 2601-2612.

5. A REE ISOTOPIC VIEW OF GROUP II CAI FORMATION

5.1. Introduction

It is generally accepted that the building blocks of the terrestrial planets and other inner solar system objects experienced vaporization and homogenization at high temperature at the birth of the solar system (Cameron, 1962). According to this view, solids and perhaps liquids condensed as the nebula cooled from gas of solar composition (*e.g.*, Grossman, 1972; Yoneda and Grossman, 1995). The composition of the condensates evolved during cooling following a sequence, from more refractory phases rich in Ca, Al, and Ti to more volatile phases rich in K and Na. The condensation sequence is hinted at by the mineralogical and chemical compositions of partial condensed relicts known as refractory inclusions (or Ca-, Al-rich inclusions, CAIs) that were isolated from the remaining nebular gas before major rock-forming elements such as Si, Mg, and Fe were fully condensed. This early isolation led refractory inclusions to preserve large enrichments in refractory elements such as the rare earth elements (REE), and distinctively fractionated chemical abundance patterns. A readily identifiable fractionated REE pattern in CAIs is known as group II (Tanaka and Masuda, 1973; Mason and Taylor, 1982), which is present in 40% of all CAIs, most notably those of fine-grained texture (70% of all CAIs have nonchondritic relative abundances of the REEs; Ireland and Fegley, 2000). Group II CAIs have so far only been documented in carbonaceous chondrites, but this could be due to the scarcity of CAIs in noncarbonaceous chondrites. Group II REE patterns are marked by depletions in the least refractory (Eu and Yb) and most refractory REEs (Gd–Er and Lu), while REEs of intermediate refractoriness (La–Sm and Tm) are uniformly enriched. This pattern cannot be formed by

evaporation alone and has been taken as evidence that condensation processes occurred in the early solar system.

The chemical fractionation of REEs recorded by CAIs was pervasive in the early solar system and affected planetary bodies at all scales. For example, the Earth and many meteorite parent-bodies display a resolvable depletion (~ –4.5%) in the abundance of Tm relative to CI chondrites, which is interpreted to reflect the heterogeneous distribution in the solar nebula of refractory dust carrying group II REE patterns marked by large Tm excesses (~+200% to +5400%) relative to neighboring REEs Er and Lu (Dauphas and Pourmand, 2015; Barrat et al., 2016). After formation, CAIs experienced further processing, which is reflected in their textures and compositions. Some CAIs were reheated and experienced melting and partial vaporization, which obscured signatures arising from solar nebula condensation (Richter et al., 2002; Richter et al., 2007; Shahar and Young, 2007; Grossman et al., 2008). Others, in particular fine-grained CAIs, never experienced melting and provide a more faithful record of solar nebula condensation. Due to their porous nature, fine-grained CAIs experienced extensive alteration, which modified their composition and mineralogy (Krot et al., 1995). For elements that are fluid-immobile and refractory, this is however not a significant problem. Available Ti and Sr isotopic data of fine-grained inclusions indicate that kinetic processes were at play when fine-grained CAIs formed but interpretation of these data in terms of evaporation/condensation processes is ambiguous (Simon et al., 2017; Davis et al., 2018; Charlier et al., 2019).

REEs are ideally suited for testing the theory of equilibrium condensation of the solar nebula because they are relatively fluid-immobile, display a range of 50% condensation temperatures that encompass the inferred formation temperature of CAIs (Lodders, 2003), and

their condensation behaviors are relatively well constrained. Although REE patterns can be explained by equilibrium condensation from gas of solar composition under a total H_2 pressure typical of the solar nebula of 10^{-5} to 10^{-3} bar (Boynton, 1975; Davis and Grossman, 1979; Kornacki and Fegley, 1986; Davis et al., 2018), abundances alone cannot easily tell if kinetic processes were at play during either evaporation or condensation. The reason is that evaporation kinetics are also governed by thermodynamics and equilibrium vapor pressures, through the Hertz-Knudsen equation (Hirth and Pound, 1963). Isotopes are highly sensitive to disequilibrium during evaporation and condensation (Jouzel and Merlivat, 1984; Tsuchiyama et al., 1999; Ozawa and Nagahara, 2001; Richter et al., 2002; Richter, 2004; Fedkin et al., 2012; Dauphas et al., 2015; Bourdon and Fitoussi, 2020). They can therefore be used to understand the physicochemical pathway of CAI formation.

During condensation from a supersaturated medium, the light isotopes will impinge on mineral surfaces more frequently than the heavy isotopes, resulting in a light isotope enrichment in the condensed phase relative to the vapor. Conversely during evaporation in an undersaturated medium, the light isotopes will be more readily lost than the heavy ones, resulting in a heavy isotope enrichment of the condensed phase relative to the vapor. If either evaporation or condensation take place in a vapor whose partial pressure is in close equilibrium with the condensed phase, the fluxes in and out of the condensed phase will be nearly balanced and the vapor and solid/liquid will be in isotopic equilibrium. Given the elevated temperature involved in CAI formation, the expectation is that equilibrium isotopic fractionation should be small. As such, measuring the isotopic composition of REEs in CAIs displaying group II REE patterns should theoretically (*i*) reveal if these CAIs formed under equilibrium conditions, and if they did not, (*ii*)

allow the roles played by evaporation and condensation processes to be resolved, which can help tie CAI formation and chemical fractionation of refractory elements to phenomena happening around young stellar objects.

Table 5.1 Stable isotopic fractionations of REEs in a geostandard and CAIs.

		Isotopic fractionation (‰/amu)																					
Sample	Name	δ^{φ}Ce		#	δ^{φ}Nd		#	δ^{φ}Sm		#	δ^{φ}Eu		#	δ^{φ}Gd		#	δ^{φ}Dy		#	δ^{φ}Er		#	δ^{φ}Yb		#
BCR-2		0.02	0.01	10	-0.01	0.02	15	0.00	0.01	9	0.01	0.06	4	0.02	0.03	10	0.02	0.03	8	-0.05	0.02	8	0.02	0.05	9
TS32		0.24	0.06	1	-0.03	0.05	4	-0.01	0.06	2	-0.19	0.05	2	-0.02	0.03	2	-0.02	0.07	3	-0.02	0.13	2	0.04	0.07	4
ME-3364-25.2	FG-FT-3	0.01	0.04	9	-0.14	0.01	9	-0.09	0.06	5	-1.09	0.05	1	-0.89	0.03	1	-1.04	0.07	1	-1.00	0.02	1	-0.33	0.07	3
ME-2639-16.2	FG-FT-4	0.81	0.04	12	1.10	0.01	8	0.88	0.06	3	-0.01	0.05	2	-0.61	0.03	2	-0.58	0.06	2	-2.89	0.11	1	-0.12	0.07	4
ME-2639-49.7	FG-FT-6	-0.03	0.02	9	-0.57	0.08	5	-0.37	0.06	2	-0.42	0.02	1	-1.03	0.07	3	-1.67	0.04	3	-2.02	0.05	1			
ME-2639-51.1	FG-FT-7	0.42	0.03	9				0.07	0.06	5	-0.58	0.05	1	-1.28	0.03	3	-1.64	0.07	2	-2.24	0.02	1	-0.66	0.07	1
AL3S5	FG-FT-8	0.51	0.01	9	-0.02	0.03	8	0.07	0.01	9	0.04	0.11	2	-2.26	0.01	9	-3.07	0.01	9	-1.89	0.11	2	0.01	0.05	3
AL4S6	FG-FT-9	-0.82	0.01	9	-0.93	0.02	11	-0.97	0.02	9	0.73	0.04	6	-1.05	0.07	5	-1.10	0.02	7	0.08	0.04	6	-0.32	0.01	9
AL8S2	FG-FT-10	0.35	0.05	5	-0.16	0.08	3	-0.03	0.05	1	-1.03	0.11	1	-0.35	0.07	2	-0.53	0.04	1	-3.63	0.05	1			
ME-2639-16.2	FG-FT-4*	0.96	0.07	5	0.68	0.04	8	0.88	0.06	5	0.03	0.06	4	-0.57	0.03	6	-0.55	0.02	6	-2.90	0.11	2	-0.12	0.05	9
AL3S5	FG-FT-8*	0.70	0.01	8	-0.01	0.01	15	0.11	0.01	11	0.13	0.06	3	-2.28	0.02	10	-3.08	0.02	8	-1.88	0.11	2	-0.05	0.15	2
AL4S6	FG-FT-9*	-0.62	0.07	5	-0.87	0.01	13	-0.84	0.02	7	0.82	0.06	3	-1.05	0.19	4	-1.15	0.06	5	0.01	0.11	5	-0.32	0.02	9

#Number of measurements.

*Replicates subjected to significant loss of REEs during Mo chemistry and not used for data interpretation.

The δ^{φ}E values are permil/amu variations relative to terrestrial standards (OL-REEs) calculated using Eq. 5.36 applied to ^{142}Ce/^{140}Ce, ^{146}Nd/^{144}Nd, ^{152}Sm/^{148}Sm, ^{153}Eu/^{151}Eu, ^{158}Gd/^{156}Gd, ^{164}Dy/^{162}Dy, ^{168}Er/^{166}Er, and ^{174}Yb/^{172}Yb ratios.

Here, we report the isotopic compositions of 8 REEs in 8 CAIs (including 7 fine-grained ones with group II REE patterns) from the Allende CV chondrite (Table 5.1). These measurements were made possible by the use of a new Fluoropolymer Pneumatic Liquid Chromatography system (FPLC; Fig. 5.1; Ireland et al., 2013; Dauphas et al., 2018b) to separate the REEs from one another. The REEs analyzed are Ce, Nd, Sm, Eu, Gd, Dy, Er, and Yb. The other polyisotopic REEs La and Lu were not measured, as these have only two stable isotopes, one of which is extremely minor in abundance (0.09% for ^{138}La and 2.6% for ^{176}Lu). Furthermore, large ^{138}La anomalies of probably nucleosynthetic origin have been reported (Shen and Lee, 2003), which would hamper the detection of mass-dependent fractionation for La. In CAIs with group II REE patterns, we observe significant stable isotopic fractionations of the REEs indicative of disequilibrium formation pathways.

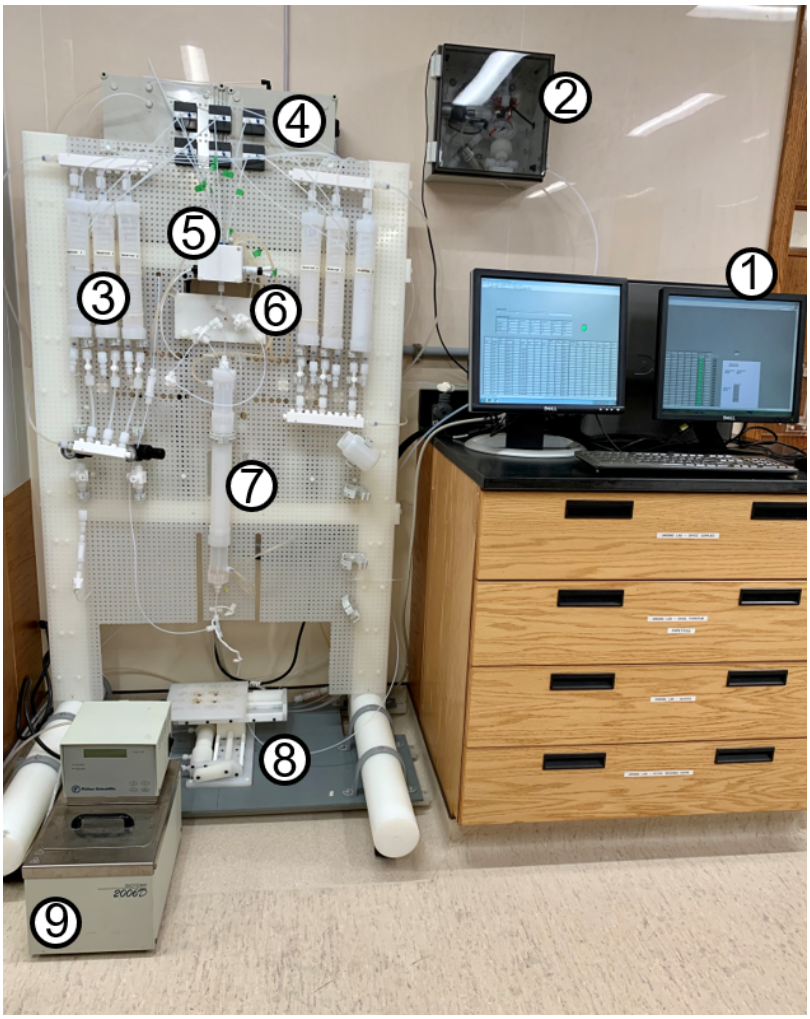

Figure 5.1 FPLC system. 1. Control station with Labview software. 2. Gas switch. If the pressure of the building-supplied high-purity N_2 from a nitrogen generator goes below 60 PSI, the gas source switches to a cylinder of compressed N_2. 3. Temperature-controlled water/reagent reservoirs. 4. Electronic bay and pneumatic PTFE positive displacement diaphragm metering pumps. The electronics are within a positively pressurized box to avoid contact with acid fumes. 5. Temperature-controlled mixing chamber. Reagents introduced by the metering pumps are mixed using a magnetic stirring bar controlled by an external pneumatic micromotor. 6. Sample introduction loop. 7. Chromatography column. The column is made of a fine PTFE tube (1.6 mm inner diameter and 70 cm length here) that runs through a Teflon jacket where water is flowing at a set temperature. 8. Stage. A 16-position pneumatic all-plastic stage is used to dispense the elution cuts in different beakers. 9. Heating circulating water bath. Many modifications were made after Ireland et al. (2013), notably the conversion to all-pneumatic actuation (including fluoropolymer metering pumps), addition of a sample introduction loop, migration of the electronics to a positively pressurized box, and development and implementation of a pneumatically-actuated plastic-made 16-position stage (Dauphas et al., 2018b).

5.2. Materials

The samples used in this study were selected from a group of CAIs that were previously studied by Tissot et al. (2016). The sampling and digestion procedures are described in detail in the supplementary section of Tissot et al. (2016) and only briefly summarized here.

The CAIs studied by Tissot et al. (2016) were mostly fine-grained CAIs extracted from a few Allende slabs using a stainless-steel dental tool. The mass of the CAIs ranged from 15 to 440 mg (Table S2 in Tissot et al., 2016). A small chip of each CAI was taken and mounted in epoxy for chemical and petrographic characterization. Most minerals have a grain size on the order of about 10 μm and are mostly composed of spinel, pyroxene, sodalite and nepheline, with minor and variable amounts of grossular, melilite and olivine. One coarse-grained CAI (TS32) was characterized in a separate study and provided in powder form. It is primarily composed of melilite, pyroxene, anorthite, and spinel, with a small amount of grossular and perovskite (Simon et al., 1999). The main mineral carriers of REEs in TS32 are pyroxene, perovskite, and melilite (Simon et al., 1999). Fine-grained CAIs in Allende have been extensively altered and to our knowledge, the distribution of REEs in these objects has rarely been studied (Huss et al., 2002).

Powdered samples were digested in a mixture of HF/HNO_3 in 3:1 proportion with a few drops of $HClO_4$ added. The samples in acid were placed on a hot plate at 160 °C for 2 weeks, after which each sample was evaporated to dryness and redissolved in a 2:1 mixture of $HCl:HNO_3$ for one week on a hot plate. These steps were performed twice to ensure complete digestion. The samples were dried down and dissolved in concentrated HNO_3. All samples were then diluted in 3 M HNO_3 and centrifuged. No residue was visible. After dissolution, 80% of the sample was

taken and processed through 2 U/TEVA columns for U extraction. The matrix cuts that contained all REEs were recovered after the U/TEVA chemistry.

5.3. Methods

5.3.1. REE Extraction and FPLC Elution

Approximately 30% of the matrix cut from the U/TEVA chemistry of Tissot et al. (2016) (equivalent to 24% fraction of the whole CAI) was passed through a prepacked TODGA column for extraction of the bulk REEs (Pourmand et al., 2012). The yields of this REE TODGA extraction step were near 100%. The bulk of the REE cut was then subjected to a 2-step Fluoropolymer-Pneumatic Liquid Chromatography (FPLC; Ireland et al., 2013; Dauphas et al., 2018b) elution to separate REEs from each other.

Another 40% from the same matrix cut of the U/TEVA chemistry was passed through a separate Mo chemistry, during which 40 to 90% of LREEs and 20 to 40% of HREEs were lost on columns. We analyzed the matrix cuts after Mo chemistry of 3 group II CAIs (FG-FT-4, 8, 9) as replicates and compare their results with the same CAIs using the 30% matrix cut so as to assess the reproducibility of the isotopic analyses (see Section Assessment of Data Accuracy below). The results from these replicates agree with those from the 30% matrix cut. They are not used however for data interpretation to avoid unnecessary influence of stable isotopic fractionation potentially induced by Mo chemistry.

As REEs behave very similarly during chromatography, difficulties in separating individual REEs from one another has hampered their isotopic analyses, especially for mass-dependent fractionation. Previous stable isotopic fractionation measurement of REEs has therefore

either focused on Sm+Eu (Moynier et al., 2006) or Er+Yb (Albalat et al., 2012). To separate all target REEs, we developed an FPLC system at the University of Chicago (Fig. 5.1; Ireland et al., 2013; Dauphas et al., 2018b). The FPLC system was modified after publication of Ireland et al. (2013) to pneumatic actuation (Dauphas et al., 2018b). Its most distinctive features are:

(*i*) The elution scheme is controlled by a computer *via* a LabView software interface, which allows one to run a fine-step gradient elution and mix as many as 6 reagents. Achieving a fine gradient elution like the one performed for the present study using traditional gravity-driven chromatography would be prohibitively labor-intensive.

(*ii*) The liquid flow path is made of solid fluoropolymer. All parts related to elution are activated pneumatically using pressurized N_2 gas. Electronics are housed in a box that is positively pressurized and spatially isolated from the reagent reservoirs and the liquid flow path. This design reduces chances of contamination and ensures that the FPLC electronics are immune to acid fumes in the clean laboratory environment. A commercial HPLC would not survive under the harsh conditions needed to perform the elution.

(*iii*) The elution temperature can be adjusted from room temperature to 80 °C through a water circulation system to achieve optimal and reproducible separation. The mixed reagents are forced through the column via pressurized high-purity N_2 gas (adjustable from 0 to 4 bar), making it possible to run elutions on extremely long columns (~70 cm for REE separation).

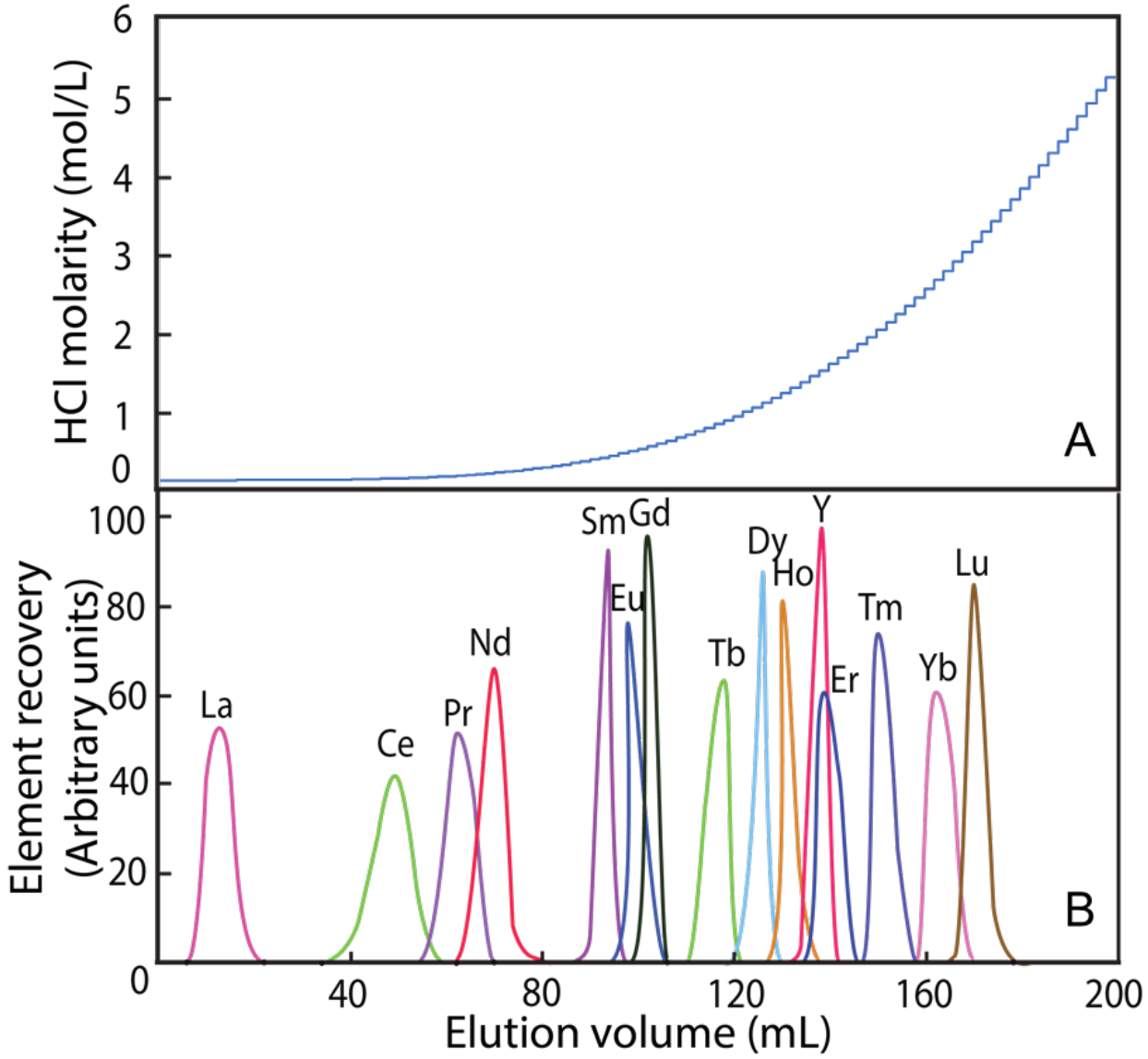

Figure 5.2 FPLC elution curve of the REEs (A) HCl molarity of the elution solution injected in the column as a function of volume. (B) REE recovery as a function of elution volume. The chromatography column is 70 cm long, 1.6 mm in diameter, filled with 1.4 mL of Ln-Spec resin (Ireland et al., 2013), and heated at 70 °C.

The sample solution is introduced in FPLC *via* a sample introduction loop composed of two fluoropolymer 3-way valves. By changing the flow paths of the two valves, samples can be injected and stored in a tube between the two valves, to be later connected to the major flow path of elution. The column used for FPLC elution of the REEs is 70 cm in length and 1.6 mm in

internal diameter, filled with 1.4 mL of 25-50 μm Ln-Spec resin (Eichrom). The overall affinity of REEs for Ln-resin decreases exponentially with increasing acid molarity (Ireland et al., 2013). The REEs are eluted sequentially from low (La) to high (Lu) atomic number by ramping up the HCl molarity (see Fig. 5.2A for the gradient elution used). The REE elution is performed at 70 °C and consists of 94 steps of 2 mL each of increasing molarity from 0.1 to 6 M HCl. The flow rate of the elution is 0.17 mL/min. The total elution volume is 188 mL and an elution lasts 16 hours. The eluting acid is automatically made by mixing Milli-Q water with any of three HCl reservoirs (0.5, 2, and 6 M respectively). The volumes of acid and water needed are automatically calculated in the LabView software and transferred into a mixing chamber using pneumatic positive displacement diaphragm metering pumps made of fluoropolymer. The elution curve was calibrated and the elution cuts were defined using 10 ppm Spex CertiPrep Multi-Element standard solution (Fig. 5.2B). The eluted fractions were collected in fluoropolymer beakers mounted on a 16-position plastic-made, pneumatically-actuated, and computer-controlled stage. The whole elution is automated and does not require operator attention after the sample is introduced.

All samples were subjected to a 2-step FPLC elution at 70 °C. In the first step, the bulk of the REEs were dried in a 6 ml PTFE beaker on a hot plate to a tiny drop (<5 μL) and then dissolved in 350 μL MQ water. The dissolved sample was then loaded onto the FPLC system and subjected to a complete elution. The eluted reagents were collected in 32 cuts ranging from 2 to 20 ml each defined by knowledge gained on a previous calibration. Approximately 5% of each cut was taken and diluted for concentration measurement by MC-ICPMS. Elution cuts that contained a given REE were then combined based on the concentration measurements. The first elution was sufficient to separate most REEs with only minor overlap of Eu/Dy and Pr/Nd (<20% Dy in the

Eu cut and 25% Pr in the Nd cut) and major overlap of Y/Er (Fig. 5.2B), none of which showed clear isobaric and matrix effects according to our doping tests. In order to achieve a better separation, a second more specific elution step was performed. In this step, REEs that are not neighbor to each other were recombined and loaded onto the FPLC system. This involves 4 FPLC elutions (Ce, Nd, Sm/Gd/Er and Eu/Dy/Yb) ranging from 92 to 188 ml (Fig. 5.3). The overall yields of the 2-step FPLC elution were higher than 95%. At the end of each elution, the column was cleaned by elution of 10 mL 6 M HCl followed by 10 ml MQ water at 70 °C to eliminate cross contamination. The same resin batch was used for all the purifications with no advert effect on the elution curves.

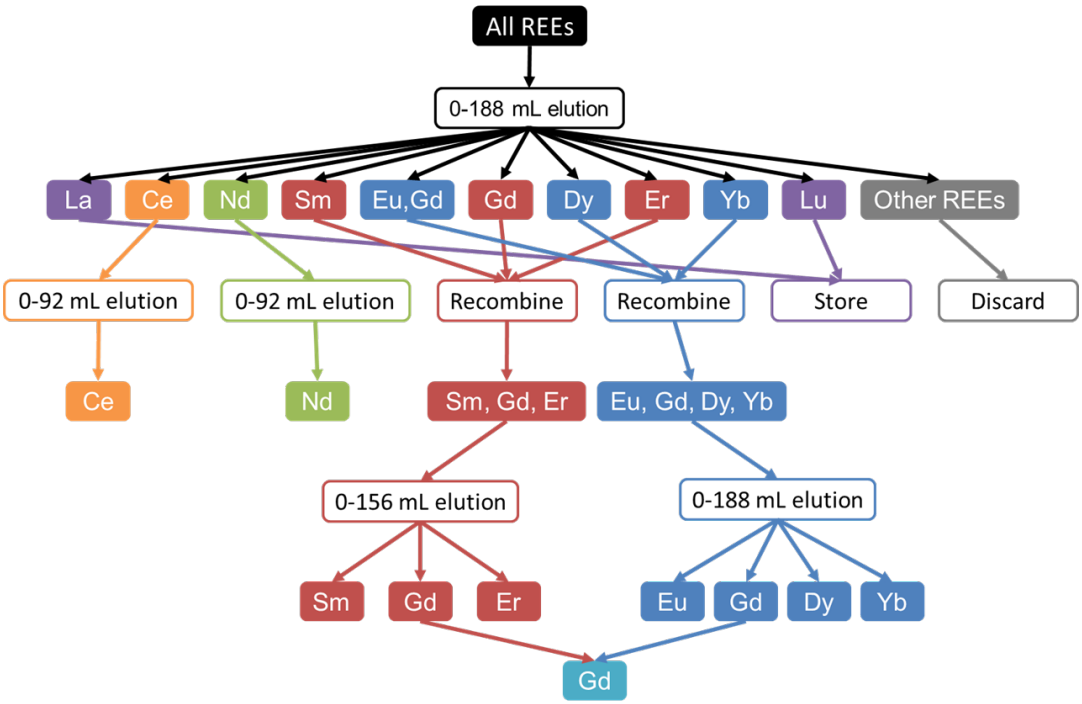

Figure 5.3 Flowchart of 2-step FPLC elution of the REEs. Each elution in the flowchart uses the same gradient elution of HCl displayed in Fig. 5.2A but ends at different acid volume. After the first elution, REEs that are not neighbor to each other (*i.e.*, Sm/Gd/Er and Eu/Dy/Yb) are recombined and loaded onto the FPLC system (Fig. 5.1) for a second elution. The Eu cut from the first 0–188 mL elution contains minor Gd, which is separated from the second 0–188 mL elution and recombined with Gd cut from the 0–156 mL elution.

5.3.2. MC-ICPMS Analysis and Data Reduction

The concentrations of all REEs and the isotopic compositions of Ce, Nd, Sm, Eu, Gd, Dy, Er, and Yb were analyzed at the University of Chicago on a Thermo Scientific MC-ICPMS upgraded to Neptune Plus specifications with the addition of an OnTool booster pump. The method for analyzing REE concentrations using an MC-ICPMS was discussed in detail in Pourmand et al. (2012).

Isotopic analyses were done using the Neptune MC-ICPMS connected to an Apex Omega desolating nebulizer. A typical measurement consisted in 60 s take-up time, 60 s baseline, and 40 cycles with an integration time of 8.184 s/cycle. The cup configurations used for isotopic analyses of the REEs are provided in Table 5.2. Most REEs were measured in static mode with the exception of Dy and Yb, for which a subconfiguration was used to monitor isobaric interferences. The subconfiguration was only measured twice at the beginning with integration times of 4.142 s each, and the average intensities were used to correct for isobaric interferences of the following 40 cycles in the main cup configuration after appropriate scaling. For example, correction of ^{162}Er and ^{164}Er on ^{162}Dy and ^{164}Dy, respectively, proceeds as follows: ^{166}Er is only measured in the subconfiguration and ^{163}Dy is measured in both the main and sub- configurations. The ratio of intensities ^{166}Er/^{163}Dy in the two subconfigurations is calculated. This ratio is then multiplied by the ^{163}Dy intensity in the main configuration. The resulting main-configuration-calculated ^{166}Er is then multiplied by the ratios ^{162}Er/^{166}Er and ^{164}Er/^{166}Er to subtract ^{162}Er and ^{164}Er from ion intensities at masses 162 and 164, which yields corrected ^{162}Dy and ^{164}Dy intensities.

Table 5.2 Cup configuration of analyzed REEs.

		Cup configurations								
		L4	L3	L2	L1	C	H1	H2	H3	H4
Ce	Main	^{131}Xe	-	^{136}Ce	^{137}Ba	^{138}Ce	^{139}La	^{140}Ce	^{142}Ce	^{145}Nd
Nd	Main	^{140}Ce	^{142}Nd	^{143}Nd	^{144}Nd	^{145}Nd	^{146}Nd	^{148}Nd	^{150}Nd	^{152}Sm
Sm	Main	^{144}Sm	^{145}Nd*	^{147}Sm	^{148}Sm	^{149}Sm	^{150}Sm	^{152}Sm	^{154}Sm	^{156}Gd*
Eu	Main	-	^{151}Eu	^{153}Eu	^{156}Dy	^{158}Dy	^{161}Dy	^{162}Dy	^{164}Dy	^{166}Er*
Gd	Main	^{150}Sm*	^{152}Gd	^{154}Gd	^{155}Gd	^{156}Gd	^{157}Gd	^{158}Gd	^{160}Gd	^{162}Dy*
Dy	Main	^{156}Dy*	^{157}Gd*	^{158}Dy	^{160}Dy	^{161}Dy	^{162}Dy	^{163}Dy	^{164}Dy	-
	Sub	-	-	-	-	^{163}Dy^{n}	^{164}Dy	-	^{166}Er	-
Er	Main	^{161}Dy	^{162}Er	^{163}Dy	^{164}Er	^{166}Er	^{167}Er	^{168}Er	^{170}Er	^{173}Yb
Yb	Main	^{168}Yb	^{170}Yb	^{171}Yb	^{172}Yb	^{173}Yb	^{174}Yb	^{175}Lu*	^{176}Yb	^{180}Hf*
	Sub	^{166}Er	-	^{169}Tm	-	^{171}Yb	^{172}Yb	^{173}Yb^{n}	-	^{178}Hf

Faraday cups with * are connected to 10^{12} Ω amplifiers while the ones unlabeled are connected to 10^{11} Ω amplifiers.
Faraday cups with ^{n} are used to normalize the signals of subconfigurations to the main configurations.

To save sample solution, the idle time between cycles with the same configurations was set to zero while the cycle after a configuration change was preceded by 10 s idle time. Isobaric effects from isotopes of neighboring elements were corrected by monitoring other isotopes of the same element, calculating intensities assuming natural abundance distribution, and subtracting the intensities from those of interfered isotopes.

As isotopic compositions of REEs in CAIs can be affected by nucleosynthetic anomalies and cosmogenic effects, we measured the isotopic composition of each REE through sample-standard bracketing (SSB). SSB is advantageous over the double-spike approach because one can distinguish mass-dependent fractionation from isotopic anomalies, which were observed in all REEs with more than two isotopes but are much smaller (and for the present purpose negligible)

compared to mass fractionation. The overall yields on the columns were over 95%. Processing of a geostandard showed that no significant isotopic fractionation was introduced by column chemistry, at least compared to the large natural variations measured in the samples. As isotopic standards of REEs are not well established, especially for HREEs, we prepared isotopic standards (referred to as OL-REE series) using high purity oxide in powder form from ESPI, which are available upon request from Hu or Dauphas. On average, LREEs were measured 9 times bracketed by OL-REE isotope standard spaced apart by 300 s rinsing time. The concentration of the sample solution was usually 15–25 ppb, corresponding to a 3.5–10 V signal for the most abundant isotope (10 V for ^{140}Ce, 4 V for ^{142}Nd, 3.5 V for ^{152}Sm). Eu and HREEs are depleted in CAIs with group II REE pattern and were usually measured 1–6 times at concentrations ranging between 1.5 and 10 ppb corresponding to 1.5–3 V for the most abundant isotope (2 V for ^{151}Er and ^{158}Gd, 3V for ^{164}Dy and 1.5 V for ^{166}Er and ^{174}Yb). Exceptions are Er measurement in FG-FT-3, 6, 7, 10, which due to the extreme Er depletion were analyzed at 1.5 ppb with a signal of 0.25 V for ^{166}Er. Despite the low abundance for some REEs in CAIs, the total procedure blanks were more than 2 orders of magnitude lower than the sample amount. The substantial isotopic fractionation of highly depleted Er in some CAIs is also evidence that the sample measurements were not plagued by contamination from matrix surrounding the CAIs as this would have shifted these Er isotopic compositions towards that of bulk Allende (~0 ‰/amu).

Isotope data reduction was done by copying the raw data into a spreadsheet and correcting for background and isobaric interferences. As documented in previous studies (Shollenberger et al., 2018), isotopic anomalies and cosmogenic effects are present for some REEs in CAIs but the variations are on the order of 0.1 ‰, which is negligible compared to the stable isotopic variations

reported here. Therefore, the choice of ratio for reporting mass-dependent fractionation is not critical. For that purpose, we use in Eq. 5.36 the two most abundant isotopes for each REE.

The measurements were performed by sample-standard bracketing, whereby sample measurements (SMP) were interspersed with measurements of standards (STD) diluted to the same concentration as the sample, in the same acid as that used for diluting the sample. The reported δ^{φ}E values were calculated based on 1 to 12 (typically 5) STD-SMP-STD bracketings, using each time the average isotopic ratio of the two STD measurements to normalize the isotopic ratio of SMP. The confidence intervals for the isotopic fractionations are reported as 95% confidence intervals using the student *t*-value and the variability of either sample δ^{φ}E values (*i.e.*, all the sequences STD-SMP-STD) for those with 6 or more values, or the variability of the δ^{φ}E values of standards bracketed by standards (*i.e.*, all the sequences STD-SMP-STD-SMP-STD) for sample measurements with less than 6 values. The threshold of 6 repeat brackets is a trade-off between the following considerations: (*i*) It is difficult to robustly assess the standard deviation based on a small number of bracketed sample measurements, and this can be estimated more robustly by using the isotopic dispersion of the numerous standard analyses performed during a session. (*ii*) The time between standard measurements is longer than that of samples bracketed by standards, which can detrimentally affect the standard deviation, meaning that using the isotopic dispersion of the samples can be preferable.

Other than stable isotopic fractionation, REE isotopes in group II CAIs can be affected by isotopic anomalies induced by nucleosynthesis, and for isotopes with large neutron capture cross sections such as ^{149}Sm, ^{155}Gd, and ^{157}Gd, cosmogenic effects (see Shollenberger et al., 2018 for examples of cosmogenic effects in CAIs). For the REEs that we analyzed in this study, all of them

except Eu have 4 or more isotopes. Hence, we were able to monitor several pairs of isotope ratios and calculate isotopic anomalies by internal normalization using an exponential fractionation law. The isotopic anomalies recorded in the CAIs were all about 2 orders of magnitude smaller compared to the stable isotopic fractionation per amu for the same REE. Eu only has two isotopes (^{151}Eu and ^{153}Eu). Thus, the stable isotopic fractionation of Eu cannot be distinguished from isotopic anomalies by monitoring different pairs of isotope ratios. ^{151}Eu has a large thermal neutron capture cross section (9200 b) but it is much lower than that of ^{157}Gd (255,000 b), which shows cosmogenic effects that would correspond to a shift of 0.05 ‰/amu if misinterpreted in terms of isotopic fractionation. Both ^{151}Eu and ^{153}Eu are mostly of *r*-process origin. Thus, we can safely assume that Eu isotopic variations are due to stable isotopic fractionation rather than nucleosynthetic anomalies or cosmogenic effects. The fact that Eu isotopic variations correlates with mass-dependent Sr isotopic fractionation (Fig. 5.4A) supports this view.

Approximately 5% of the matrix cut after U/TEVA chemistry (4% of the whole CAI) were pipetted out and used for analyzing Ti isotopic anomalies. Approximately 5% of the REE matrix cuts were also analyzed for Ti stable isotopic fractionation using the double-spike approach. The isotopic analyses and correction of isotopic anomalies were conducted by me and Zhe Zhang following Greber et al. (2017) and Hu and Dauphas (2017).

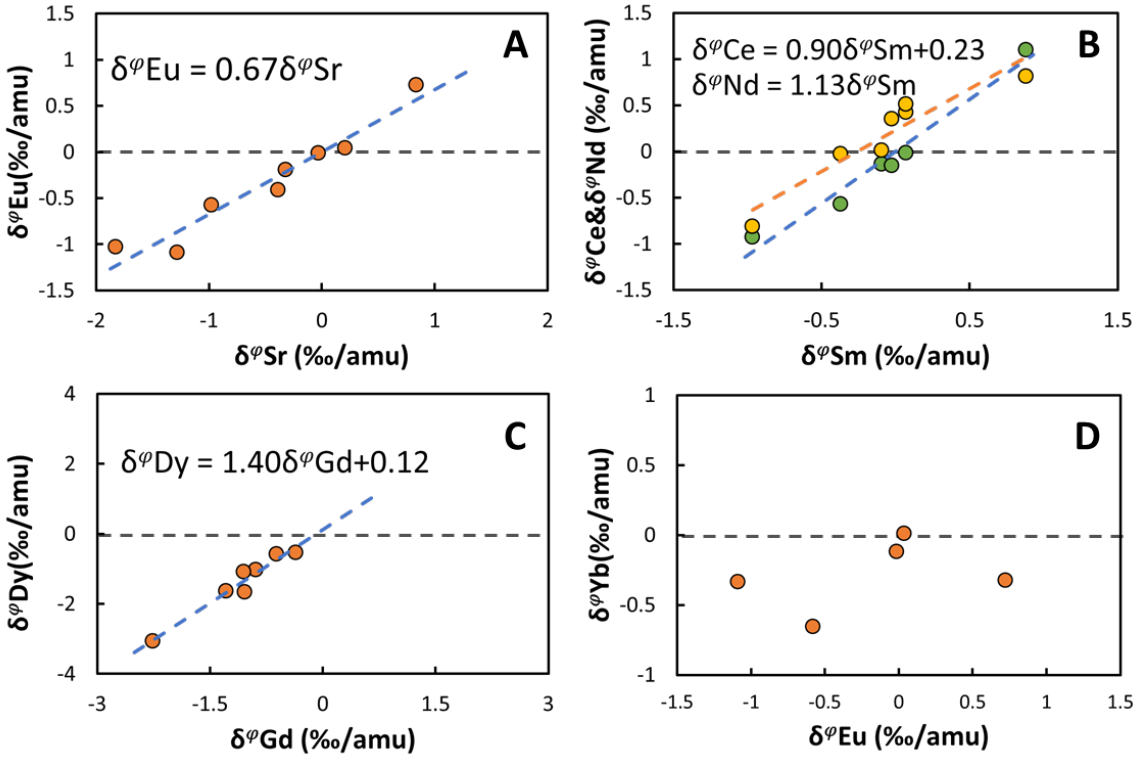

Figure 5.4 Relationship of stable isotopic fractionations of REEs. (A) Correlation of isotopic fractionations Eu *vs*. Sr in 7 CAIs with group II pattern. (B) Ce and Sm *vs*. Nd. (C) Dy *vs*. Gd. (D) Yb *vs*. Eu. See Table 5.1 caption and Eq. 5.36 for details on the δ^{φ} notation. The REE data are from Table 5.1, while the Sr data are from Charlier et al. (2019).

5.3.3. Assessment of Data Accuracy

The data quality of REE isotopic analyses was controlled by measuring the total procedural blank, a terrestrial geostandard and running replicates. The total procedural blanks for all REEs are less than 0.25 ng, which is negligible compared to the amounts of REEs in the samples. A geostandard (terrestrial basalt BCR-2) was processed with the CAIs. The stable isotopic fractionations normalized to the isotopic standards for all REEs are zero within error bars (typically less than 0.05 ‰/amu). The 3 replicates based on the matrix cut of Mo chemistry were found to yield generally consistent results compared to those of the same CAI that have not experienced significant loss of REEs. The stable isotopic compositions of LREEs in the replicates are shifted

to the heavy side by approximately 0.1 ‰/amu, while HREEs yield the same result within error bars (Table 5.1). The only exception is Nd in FG-FT-4, which is shifted by 0.4 ‰/amu. The stable isotopic fractionation of LREEs induced by Mo chemistry (possibly chromatography) is not negligible (~0.1 ‰/amu) but much less than the natural isotopic fractionations measured in these CAIs (–1 to +1 ‰/amu for LREEs).

Another piece of evidence demonstrating the accuracy of the data acquired is that our Eu isotopic variations correlate very tightly with Sr isotopic variations measuring using a double-spike approach in a different laboratory, using a completely independent chemical procedure and a TIMS for isotopic analysis (Charlier et al., 2019).

Table 5.3 Titanium isotopic fractionation (determined by double spike) and isotopic anomalies of geostandards and CAIs.

Sample	Name	ε^{46}Ti	ε^{48}Ti	ε^{50}Ti	δ^{φ}Ti (SSB)	δ^{φ}Ti (DS)
G3						0.21 ± 0.06
BCR2					0.01 ± 0.08	-0.01 ± 0.06
TS32		1.79 ± 0.06	0.45 ± 0.04	9.27 ± 0.09	0.07 ± 0.08	0.04 ± 0.06
ME-3364-22.2	FG-FT-2	1.61 ± 0.50	0.31 ± 0.30	9.76 ± 0.67	0.06 ± 0.12	0.30 ± 0.06
ME-3364-25.2	FG-FT-3	1.76 ± 0.36	0.48 ± 0.23	10.01 ± 0.32	0.24 ± 0.04	0.64 ± 0.06
ME-2639-16.2	FG-FT-4	1.77 ± 0.12	0.42 ± 0.07	9.35 ± 0.13	1.02 ± 0.07	0.99 ± 0.06
ME-2639-49.7	FG-FT-6	2.51 ± 0.55	-0.03 ± 0.40	12.98 ± 0.42	0.57 ± 0.52	0.75 ± 0.06
ME-2639-51.1	FG-FT-7	1.55 ± 0.57	0.25 ± 0.08	6.54 ± 0.30	-0.37 ± 0.19	-0.05 ± 0.06
AL3S5	FG-FT-8	1.52 ± 0.48	-0.46 ± 0.39	8.16 ± 0.88	0.32 ± 0.28	0.69 ± 0.06
AL4S6	FG-FT-9	2.02 ± 0.09	0.12 ± 0.05	13.71 ± 0.07	0.20 ± 0.05	0.36 ± 0.06
AL8S2	FG-FT-10	2.15 ± 1.98	0.53 ± 1.05	9.54 ± 1.53	-0.36 ± 0.57	-0.19 ± 0.06
AL10S1	FG-FT-11	1.97 ± 1.98	0.64 ± 1.05	9.39 ± 1.53	-0.63 ± 0.57	-0.20 ± 0.06

εTi is normalized to $^{49}Ti/^{47}Ti = 0.74977$; isotopic anomalies and stable isotopic fractionations (relative to the OL-Ti standard) using sample-standard bracketing (SSB) are published in Davis et al. (2018). Some sample names in Table 1 of Davis et al. (2018) were incorrect and are corrected in the present table.

The data quality of Ti isotope measurements was verified by measuring two geostandards BCR-2 and G-3, which yield values that are consistent with previous measurements (Millet and Dauphas, 2014; Greber et al., 2017). The Ti double-spike measurements are also compared to the

previous measurement on the same samples using SSB, which are generally consistent but are less precise (Table 5.3).

5.4. Modeling

5.4.1. Speciation of REEs during Evaporation and Condensation

In this section, we calculate the vapor pressures of the different species of a REE in equilibrium with hibonite. Hibonite is a highly refractory mineral that has been implicated in establishing the REE abundance pattern of group II CAIs (Davis and Grossman, 1979; Davis et al., 2018). According to equilibrium thermodynamics (Davis and Grossman, 1979; Davis et al., 2018), REEs can exist in the form of 6 species under solar nebula conditions, where 3 species are present in gaseous forms (noted as $M^0{}_{(g)}$, $M^{2+}O_{(g)}$, $M^{4+}O_{2(g)}$) and the other 3 species substitute for Ca in solid solution in refractory minerals such as hibonite and perovskite ($M^{2+}O_{(s)}$, $M^{3+}O_{1.5(s)}$, $M^{4+}O_{2(s)}$). At equilibrium, the partial pressures and molar densities of different species are related to each other through the following equilibria:

$$M_{(g)} + O_{(g)} = MO_{(g)},$$

$$K_1 = \frac{P_{MO}}{P_M P_O}, \tag{5.1}$$

$$2MO_{1.5(s)} = 2M_{(g)} + 3O_{(g)},$$

$$K_2 = \frac{{P_M}^2 {P_O}^3}{\left(\chi_{MO_{1.5}} n_{MO_{1.5}}/n_{Ca}\right)^2}, \tag{5.2}$$

$$M_{(g)} + 2O_{(g)} = MO_{2(g)},$$

$$K_3 = \frac{P_{MO_2}}{P_M {P_O}^2}, \tag{5.3}$$

$$MO_{2(s)} = M_{(g)} + 2O_{(g)},$$

$$K_4 = \frac{P_M {P_O}^2}{\chi_{MO_2} n_{MO_2}/n_{Ca}}, \tag{5.4}$$

$$MO_{(s)} = M_{(g)} + O_{(g)},$$

$$K_5 = \frac{P_M P_O}{\chi_{MO} n_{MO}/n_{Ca}}, \tag{5.5}$$

where $K_1 - K_5$ are the equilibrium constants of the chemical reactions, P_ℓ, χ_ℓ, and n_ℓ, are, respectively, the partial pressures, activity coefficients, and solid molar densities of the REE considered (number of moles of M, MO, MO_2), P_O is the partial pressure of atomic oxygen (the value of P_O for solar nebula conditions is provided in Davis et al. (2018) and Yoneda and Grossman (1995), and n_{Ca} is the solid molar density of Ca (condensed REEs are expected to substitute for Ca in refractory minerals). One can rearrange the equations above and write P_M, P_{MO}, P_{MO_2}, n_{MO_2}, n_{MO} as functions of P_O, K_1 to K_5, χ_M, χ_{MO}, χ_{MO_2}, $n_{MO_{1.5}}$ and n_{Ca},

$$P_M = \sqrt{K_2}\,\frac{1}{{P_O}^{1.5}}\,\frac{\chi_{MO_{1.5}}}{n_{Ca}}\,n_{MO_{1.5}}, \tag{5.6}$$

$$P_{MO} = K_1\sqrt{K_2}\,\frac{1}{\sqrt{P_O}}\,\frac{\chi_{MO_{1.5}}}{n_{Ca}}\,n_{MO_{1.5}}, \tag{5.7}$$

$$P_{MO_2} = \sqrt{K_2} K_3 \sqrt{P_O} \frac{\chi_{MO_{1.5}}}{n_{Ca}} n_{MO_{1.5}}, \tag{5.8}$$

$$n_{MO_2} = \frac{\sqrt{K_2}}{K_4} \sqrt{P_O} \frac{\chi_{MO_{1.5}}}{\chi_{MO_2}} n_{MO_{1.5}}, \tag{5.9}$$

$$n_{MO} = \frac{\sqrt{K_2}}{K_5} \frac{1}{\sqrt{P_O}} \frac{\chi_{MO_{1.5}}}{\chi_{MO}} n_{MO_{1.5}}. \tag{5.10}$$

The total molar density of a given condensed REE is given by the sum of 3 solid species,

$$n_{Mtot} = n_{MO} + n_{MO_{1.5}} + n_{MO_2}. \tag{5.11}$$

Accordingly, one can write $n_{MO_{1.5}}$ as a function of n_{Mtot} using Eqs. 5.9–5.11,

$$n_{MO_{1.5}} = \frac{n_{Mtot}}{1 + \frac{\sqrt{K_2}}{K_5} \frac{1}{\sqrt{P_O}} \frac{\chi_{MO_{1.5}}}{\chi_{MO}} + \frac{\sqrt{K_2}}{K_4} \sqrt{P_O} \frac{\chi_{MO_{1.5}}}{\chi_{MO_2}}}. \tag{5.12}$$

In the same manner, the partial pressures of $M_{(g)}$, $MO_{(g)}$ and $MO_{2\,(g)}$ can be written as a function of n_{Mtot} and P_{Mtot},

$$P_M = \frac{1}{P_O} \frac{1}{\frac{1}{K_5 \chi_{MO}} + \frac{\sqrt{P_O}}{\sqrt{K_2} \chi_{MO_{1.5}}} + \frac{P_O}{K_4 \chi_{MO_2}}} \frac{n_{Mtot}}{n_{Ca}}, \tag{5.13}$$

$$P_{MO} = K_1 \frac{1}{\frac{1}{K_5 \chi_{MO}} + \frac{\sqrt{P_O}}{\sqrt{K_2} \chi_{MO_{1.5}}} + \frac{P_O}{K_4 \chi_{MO_2}}} \frac{n_{Mtot}}{n_{Ca}}, \tag{5.14}$$

$$P_{MO_2} = K_3 P_O \frac{1}{\frac{1}{K_5 \chi_{MO}} + \frac{\sqrt{P_O}}{\sqrt{K_2} \chi_{MO_{1.5}}} + \frac{P_O}{K_4 \chi_{MO_2}}} \frac{n_{Mtot}}{n_{Ca}}, \tag{5.15}$$

$$P_M = \frac{1/P_O}{1/P_O+K_1+K_3P_O} P_{Mtot} = x_M P_{Mtot}, \quad (5.16)$$

$$P_{MO} = \frac{K_1}{1/P_O+K_1+K_3P_O} P_{Mtot} = x_{MO} P_{Mtot}, \quad (5.17)$$

$$P_{MO_2} = \frac{K_3P_O}{1/P_O+K_1+K_3P_O} P_{Mtot} = x_{MO_2} P_{Mtot}. \quad (5.18)$$

where x_ℓ are the mole fraction of the various gas species. We also have for the total vapor pressure of a REE,

$$P_{Mtot} = \frac{1/P_O+K_1+K_3P_O}{\frac{1}{K_5\chi_{MO}}+\frac{\sqrt{P_O}}{\sqrt{K_2}\chi_{MO_{1.5}}}+\frac{P_O}{K_4\chi_{MO_2}}} \frac{n_{Mtot}}{n_{Ca}} = \kappa \frac{n_{Mtot}}{n_{Ca}}, \quad (5.19)$$

where κ is a factor that relates the equilibrium vapor pressure to the concentration (molar density) in the solid. Equations 5.13–5.15 can be used to calculate the equilibrium pressures of gaseous species if the molar density of the REEs in solid, temperature, thermodynamic constants, and oxygen partial pressure are known.

5.4.2. REE Abundance and Stable Isotopic Fractionation during Evaporation

In this section, our goal is to develop a quantitative model of the depletions and stable isotopic fractionations of all REEs during evaporation. Most REEs are thought to have been quantitative evaporated during the first stage of evaporation envisioned here. The only REEs that were not quantitatively evaporated are the most refractory ones, notably Gd and Dy. In fine-grained CAIs, we find that these REEs are highly depleted relative to moderately refractory REEs and have light isotopic compositions. This is more readily explained if the signature of group II REE patterns

in CAIs were inherited from an episode of evaporation, whereby the most refractory REEs were only partially evaporated in an undersaturated medium, resulting in their light isotope enrichment in the gas phase, which latter partially re-condensed to form CAIs with group II REE patterns. For this first evaporation stage, we are therefore primarily interested in the isotopic composition of the vapor. Our primary aim here is to use the isotopic composition of the most refractory REEs to put constraints on the rate of heating and duration of the evaporation episode. According to the Hertz-Knudsen equation, the net flux for each REE i during evaporation is given by,

$$J_i = \sum_\ell \frac{\gamma_{\ell,i}\left(P_{eq,\ell,i} - P_{\ell,i}\right)}{\sqrt{2\pi m_{\ell,i} RT}}, \tag{5.20}$$

where ℓ enumerates the gaseous species $M_{(g)}$, $MO_{(g)}$ and $MO_{2\,(g)}$, $\gamma_{\ell,i}$ and $m_{\ell,i}$ are the condensation/evaporation coefficients and masses of the corresponding species, R is the gas constant, $P_{\ell,i}$ and $P_{eq,\ell,i}$ are the partial and equilibrium vapor pressures, respectively. The equilibrium vapor pressure $P_{eq,\ell,i}$ in Eq. 5.20 is the partial pressure that is in equilibrium with the condensate at temperature T, as is derived in Eqs. 5.13–5.15.

We consider a model where refractory inclusions of similar sizes and evenly distributed in space are evaporated. This model is similar to those applied to closed-system condensation/evaporation and chondrule formation (Tsuchiyama et al., 1999; Ozawa and Nagahara, 2001; Richter, 2004; Fedkin et al., 2012; Bourdon and Fitoussi, 2020). Under these conditions, we do not need to track a whole ensemble of refractory inclusions and can only consider a single CAI of radius r surrounded by a parcel of gas of finite volume $V_g = 4\pi\mathcal{R}^3/3$ with no-flux boundary conditions at the boundaries ($\mathcal{R}$ is the radius of the system inclusion+gas,

which is much larger than the radius r of the inclusion itself). From a practical point of view, this is equivalent to considering a local closed-system. We assume that the driver for evaporation is heating, with the temperature increasing linearly with time, $T(t) = T_0 + \Phi t$, where T_0 is the initial temperature, Φ is the heating rate, and t is the time elapsed since the onset of heating. If inclusion and gas form a closed system, the evaporation flux must be balanced by a change in the vapor pressure $dP_{\ell,i}$ (we use the ideal gas law here),

$$\sum_\ell \frac{4\pi\mathcal{R}^3 dP_{\ell,i}}{3RT} = \sum_\ell \frac{\gamma_{\ell,i}\left(P_{eq,\ell,i} - P_{\ell,i}\right)}{\sqrt{2\pi m_{\ell,i} RT}} 4\pi r^2 dt. \tag{5.21}$$

Different gas species can be lost at different rates depending on their masses and evaporation coefficients, so the speciation of the vaporized gas does not necessarily reflect equilibrium vapor pressures. We assume that once in the gas, the different gas species have the opportunity to re-equilibrate and we have,

$$P_{\ell,i} = \frac{P_{eq,\ell,i}}{P_{eq,i}} P_i. \tag{5.22}$$

with $P_i = \sum_\ell P_{\ell,i}$ and $P_{eq,i} = \sum_\ell P_{eq,\ell,i}$. Using Eqs. 5.21 and 5.16-5.18 ($P_{eq,\ell,i} = x_{\ell,i} P_{eq,i}$), we can rewrite Eq. 5.21 as,

$$\frac{dP_i}{dt} = 3\Upsilon_i\left(P_{eq,i} - P_i\right)\sqrt{\frac{RT}{2\pi}}\frac{r^2}{\mathcal{R}^3}, \tag{5.23}$$

with $\Upsilon_i = \sum_\ell \gamma_{\ell,i} x_{\ell,i}/\sqrt{m_{\ell,i}}$. P_i is related to the total number of moles of i in the gas $\eta_{g,i}$ by the ideal gas law, and $P_{eq,i}$ is related to the total number of moles of i in the solid $\eta_{s,i}$ through Eq. 5.19. We thus have,

$$\frac{d\eta_{g,i}}{dt} = 3\Upsilon_i \left(\kappa_i \frac{4\pi\mathcal{R}^3 \eta_{s,i}}{3RT\eta_{s,Ca}} - \eta_{g,i} \right) \sqrt{\frac{RT}{2\pi}} \frac{r^2}{\mathcal{R}^3}, \tag{5.24}$$

where $\eta_{s,Ca}$ are the total number of Ca substitution sites in the solid. We consider that before vapor dissipation, gas and solid form a closed system, so we have $\eta_{g,i} + \eta_{s,i} = \eta_{tot,i}$ with $\eta_{tot,i}$ a constant. If we introduce $f_{g,i} = \eta_{g,i}/\eta_{tot,i}$ the fraction of i that has been evaporated, we have,

$$\frac{df_{g,i}}{dt} = 3\Upsilon_i \left[\kappa_i \frac{4\pi\mathcal{R}^3 (1-f_{g,i})}{3RT\eta_{s,Ca}} - f_{g,i} \right] \sqrt{\frac{RT}{2\pi}} \frac{r^2}{\mathcal{R}^3}. \tag{5.25}$$

If we assume that the precursor is made of hibonite, one can calculate the number of moles of Ca sites using the density ρ_{hib} and molar mass m_{hib} of hibonite,

$$\eta_{s,Ca} = \rho_{hib} \frac{4}{3} \pi r^3 / m_{hib}. \tag{5.26}$$

We therefore have for Eq. 5.25,

$$\frac{df_{g,i}}{dt} = \Upsilon_i \left[\frac{3m_{hib}\kappa_i}{\sqrt{2\pi RT}\rho_{hib} r} (1 - f_{g,i}) - 3\sqrt{\frac{RT}{2\pi}} \frac{r^2}{\mathcal{R}^3} f_{g,i} \right]. \tag{5.27}$$

If we change the differentiation variable from t to T and write $T = T(t)$, Eq. 5.27 becomes,

$$\frac{df_{g,i}}{dT} = \frac{\Upsilon_i}{\dot{T}}\left[\frac{3m_{hib}\kappa_i}{\sqrt{2\pi RT}\rho_{hib}r}(1 - f_{g,i}) - 3\sqrt{\frac{RT}{2\pi}}\frac{r^2}{\mathcal{R}^3}f_{g,i}\right]. \quad (5.28)$$

Assuming that the temperature increasing linearly with time, $T(t) = T_0 + \Phi t$, $\dot{T} = \Phi$. Equation 5.28 takes the form,

$$\frac{df_{g,i}}{dT} = \frac{\Upsilon_i}{\Phi}\left[\frac{3m_{hib}\kappa_i}{\sqrt{2\pi RT}\rho_{hib}r}(1 - f_{g,i}) - 3\sqrt{\frac{RT}{2\pi}}\frac{r^2}{\mathcal{R}^3}f_{g,i}\right]. \quad (5.29)$$

Equation 5.29 can be integrated starting at a low temperature with the initial condition $f_{g,i} = 0\ at\ T = T_0$, and we get the fraction of element i evaporated,

$$f_{g,i} = e^{-\int_1^T \frac{\Upsilon_i}{\Phi}\left(\frac{3m_{hib}\kappa_i}{\sqrt{2\pi RT}\rho_{hib}r} + 3\sqrt{\frac{RT}{2\pi\mathcal{R}^3}}\right)dT} \int_{T_0}^{T} \frac{\Upsilon_i}{\Phi}\frac{3m_{hib}\kappa_i}{\sqrt{2\pi RT}\rho_{hib}r} e^{\int_1^T \frac{\Upsilon_i}{\Phi}\left(\frac{3m_{hib}\kappa_i}{\sqrt{2\pi RT}\rho_{hib}r} + 3\sqrt{\frac{RT}{2\pi\mathcal{R}^3}}\right)dT} dT. \quad (5.30)$$

The isotopic composition was calculated by applying Eq. 5.30 to different isotopes of the REEs using $\delta_{g,i,2/1} = 1000\ln(f_{g,i,2}/f_{g,i,1})/(m_{i,2} - m_{i,1})$, where $m_{i,1}$ and $m_{i,2}$ are the molecular mass of isotope 1 and 2 of REE i respectively. The parameters that can differ in Eq. 5.29 between two isotopes are Υ_i and κ_i, where Υ_i is a function of $\gamma_{\ell,i}$, $x_{\ell,i}$ and $m_{\ell,i}$. We only vary $m_{\ell,i}$ and keep the other parameters constant. The fraction and the isotopic fractionation of the element evaporated are both functions of the heating rate and final temperature (duration) of the evaporation episode. We can therefore constrain the heating rate and duration from the depletion of the element considered relative to Sm (fraction evaporated), and the isotopic composition of the CAIs with group II REE patterns (corresponding to the composition of the gas except for Eu and Yb).

For numerical calculations, the precursor is assumed to be a sphere with radius *r* of 40 μm, a typical size for hibonite inclusions in Murchison (70 to 150 μm in their longest dimensions; Ireland, 1988). The ambient pressure during evaporation is set to 10^{-3} bar H_2. We assume that the system has solar bulk composition. To calculate the whole system radius, we use $\aleph_{Ca}$ the number of moles of Ca condensed per unit volume of the system solid + gas, which is from an Excel spreadsheet provided as supplementary online material in Davis et al. (2018). Indeed, we have $\aleph_{Ca} 4\pi\mathcal{R}^3/3 = n_{Ca} 4\pi r^3/3$ and $\mathcal{R} = r(n_{Ca}/\aleph_{Ca})^{1/3}$ where $n_{Ca} = 5.42$ mol/L is the Ca molar density of hibonite. The density ρ_{hib} and molar mass m_{hib} of the host mineral hibonite are 3.84 g/cm^3 and 708.8 g/mol, respectively. The radius of the system inclusion + gas $\mathcal{R}$ used is accordingly ~5 m. The sticking coefficients $\gamma_{\ell,i}$ of the REEs are not known and set to 0.1 based on the range of the sticking coefficients of Mg and SiO in melt of CAI composition (Richter et al., 2002). The oxygen fugacity P_O is from a previous condensation calculation (Yoneda and Grossman, 1995) and is provided in an Excel spreadsheet in the Supplementary Online materials of Davis et al. (2018). The molar masses $m_{M,i}$ of REEs used for calculation in g/mol are 138.91 (La), 140.12 (Ce), 140.91 (Pr), 144.24 (Nd), 150.36 (Sm), 151.96 (Eu), 157.25 (Gd), 158.93 (Tb), 162.50 (Dy), 164.93 (Ho), 167.26 (Er), 168.93 (Tm), 173.04 (Yb), 174.97 (Lu), respectively. Other thermodynamic data for the REEs, such as the Gibbs free energy and activity coefficients ($\chi_{\ell,i}$) can be found in the supplementary material of Davis et al. (2018). The choice of the precursor size and thermodynamic data have little effect on the interpretation of the thermal event given the great difference in terms of timescales for the astrophysical events that are considered.

5.4.3. REE Abundance and Stable Isotopic Fractionation during Condensation

We envision a two-step process for establishing group II REE pattern. In the first step, all REEs except the most refractory ones are quantitatively evaporated (Sect. 5.4.2). This means that Eu and Yb are in the vapor. In the second step, the vapor thus produced is partially condensed. Moderately refractory REEs are uniformly enriched in CAIs and display subdued stable isotopic fractionations. We therefore expect that during this condensation step, only the least refractory Eu and Yb remain in the vapor, while other REEs are quantitatively condensed.

Eu and Yb are depleted in CAIs with group II REE patterns but show rather subdued isotopic fractionations. This observation can be explained if condensation occurred under near-equilibrium conditions. Cooling must have been protracted to prevent the buildup of large supersaturation, thereby limiting the extent of kinetic isotopic fractionation. Indeed, if cooling had been fast, the equilibrium vapor pressure would have decreased rapidly and the rate of condensation of gas atoms would not have been sufficient to keep up with this decrease. Large kinetic isotope effects associated with supersaturation would have developed, which is not seen for Eu and Yb. Below, we present a model to translate our measurements into a quantitative assessment of cooling rates and timescales. We model condensation assuming closed-system behavior (also see Richter, 2004; Bourdon and Fitoussi, 2020) until gas dissipation.

We assume that the CAIs are of equal sizes and evenly distributed in space. We assume that during cooling and condensation, gas and CAI form a closed system. Elements condense following linear cooling until a time/temperature when vapor is dissipated. If the CAIs are all identical and evenly distributed, we do not need to track a whole ensemble of CAIs and can instead only consider a single CAI of radius r surrounded by a parcel of gas of finite volume $V_g = 4\pi\mathcal{R}^3/3$

with no-flux boundary conditions at the boundaries, which from a practical point of view is equivalent to considering a local closed-system. The decrease in the amount of element i in the gas residue is related to the condensation net flux,

$$-\sum_{\ell}\frac{4\pi\mathcal{R}^3 dP_{\ell,i}}{3RT}=\sum_{\ell}\frac{\gamma_{\ell,i}\left(P_{\ell,i}-P_{eq,\ell,i}\right)}{\sqrt{2\pi m_{\ell,i}RT}}4\pi r^2 dt. \tag{5.31}$$

The steps in the derivation of the differential equation governing condensation are similar to those used to derive Eq. 5.27 and will not be repeated here,

$$\frac{df_{s,i}}{dt}=\Upsilon_i\left[3\sqrt{\frac{RT}{2\pi}}\frac{r^2}{\mathcal{R}^3}\left(1-f_{s,i}\right)-\frac{3m_{hib}\kappa_i}{\sqrt{2\pi RT}\rho_{hib}r}f_{s,i}\right]. \tag{5.32}$$

Changing the differentiation variable from t to T, and writing $T=T(t)$, we have,

$$\frac{df_{s,i}}{dT}=\frac{\Upsilon_i}{\dot{T}}\left[3\sqrt{\frac{RT}{2\pi}}\frac{r^2}{\mathcal{R}^3}\left(1-f_{s,i}\right)-\frac{3m_{hib}\kappa_i}{\sqrt{2\pi RT}\rho_{hib}r}f_{s,i}\right]. \tag{5.33}$$

If we parameterize cooling as $T(t)=T_0+\Phi t$, like in the evaporation section, with T_0 the starting temperature and Φ (a negative number) the cooling rate, we can write an equation similar to Eq. 5.29 for the solid condensate,

$$\frac{df_{s,i}}{dT}=\frac{\Upsilon_i}{\Phi}\left[3\sqrt{\frac{RT}{2\pi}}\frac{r^2}{\mathcal{R}^3}\left(1-f_{s,i}\right)-\frac{3m_{hib}\kappa_i}{\sqrt{2\pi RT}\rho_{hib}r}f_{s,i}\right]. \tag{5.34}$$

Integrating Eq. 5.29 or 5.34 starting at a high temperature with the initial condition $f_{s,i}=0\ at\ T=T_0$, we can calculate the fraction of i that has condensed as a function of temperature,

$$f_{s,i} = e^{-\int_1^T \frac{\Upsilon_i}{\Phi}\left(\frac{3m_{hib}\kappa_i}{\sqrt{2\pi RT}\rho_{hib}r}+3\sqrt{\frac{RT}{2\pi\mathcal{R}^3}}\right)dT} \int_{T_0}^{T} 3\frac{\Upsilon_i}{\Phi}\sqrt{\frac{RT}{2\pi}}\frac{r^2}{\mathcal{R}^3} e^{\int_1^T \frac{\Upsilon_i}{\Phi}\left(\frac{3m_{hib}\kappa_i}{\sqrt{2\pi RT}\rho_{hib}r}+3\sqrt{\frac{RT}{2\pi\mathcal{R}^3}}\right)dT} dT. \quad (5.35)$$

The numerical values used in the condensation calculation are very similar to those used during evaporation. The free parameters are the heating rate and duration of the evaporation, which can be constrained by combining measurements of the depletion and isotopic fractionation of Eu and Yb. In our calculation, we assume a starting temperature of 1700 K, at which hibonite is thought to have started condensing but REEs are still mostly in the gas phase.

5.5. Results

The abundances of Ce, Nd, Sm, Eu, Gd, Dy, Er, and Yb in group II CAIs (Table 2 in Davis et al., 2018) are normalized to Sm abundance and CI chondrites (Pourmand et al., 2012) and plotted in Fig. 5.5A in order of increasing refractoriness according to their condensation temperatures under solar nebula conditions in 10^{-4} bar H_2 (Lodders, 2003; see Fig. 5.6 for the REE abundance pattern plotted as a function of atomic mass). Both the least refractory (Eu and Yb) and most refractory REEs (Gd, Dy, and Er) are depleted while the moderately refractory REEs (Ce, Nd, and Sm) display uniform enrichment relative to CI chondrites, which are characteristics of group II patterns (Mason and Taylor, 1982).

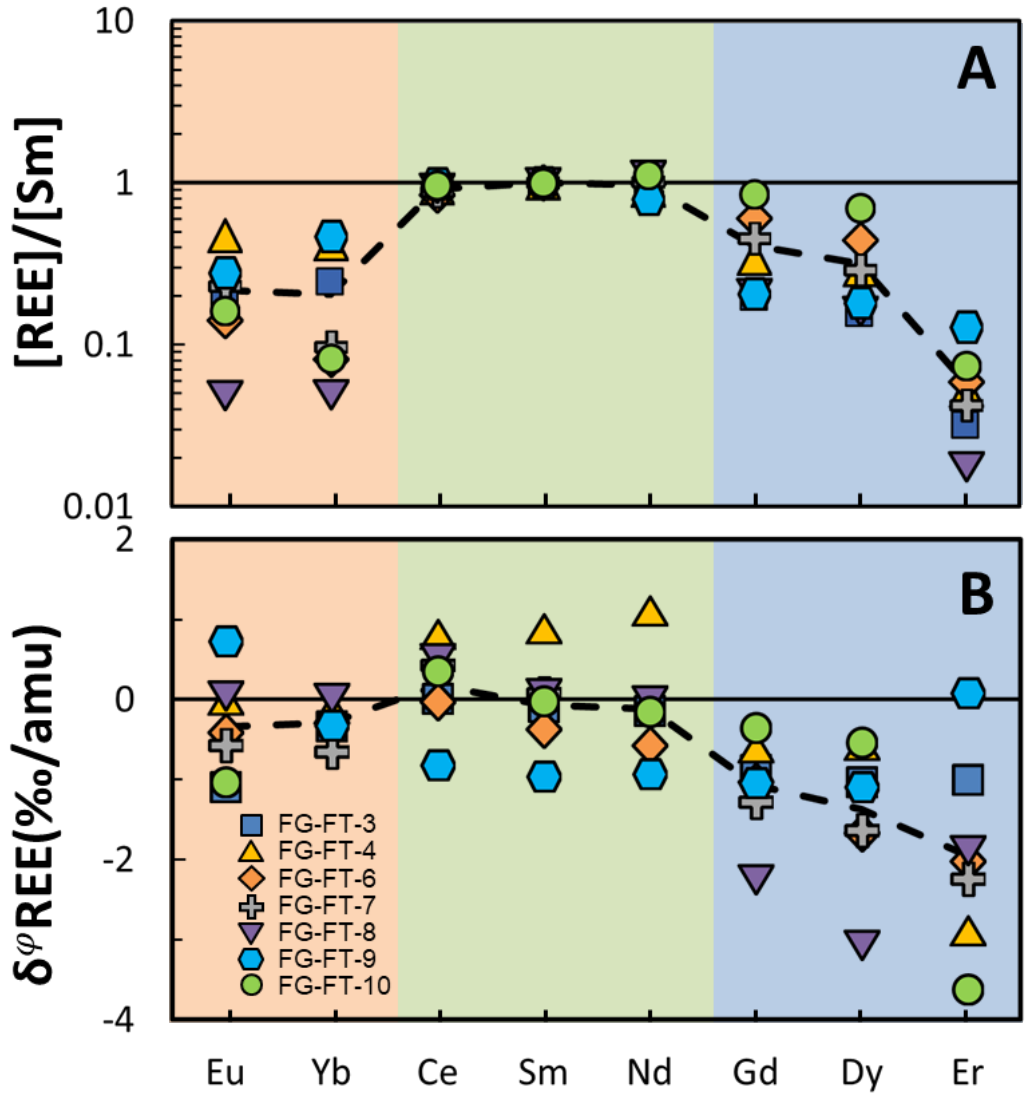

Figure 5.5 Abundances and stable isotopic fractionations of REEs ordered by increasing refractoriness (from the least refractory on the left to the most refractory on the right). (A) Abundances of REEs in 7 fine-grained CAIs with group II REE patterns (Table 2 in Davis et al., 2018) normalized to Sm abundance and chondrites (Dauphas and Pourmand, 2015). Orange, green and blue shades are least refractory, moderately refractory, and most refractory REEs respectively. Each symbol corresponds to one CAI. The dashed line is the average abundance of 7 CAIs for each REE. (B) Isotopic fractionations of REEs in the same 7 CAIs (Table 5.1). The dashed line is the average isotopic fractionations of the 7 CAIs analyzed. Note that one CAI with a flat REE abundance and isotopic pattern (TS32) is not plotted here (Table 5.1). See Table 5.1 caption and Eq. 5.36 for details on the δ^{φ} notation.

For a given REE, the isotopic fractionation is expressed as permil per atomic mass unit (‰/amu) deviations relative to terrestrial standard solutions using the following notation (the φ superscript refers to the δ notation on a per atomic mass unit basis),

$$\delta^{\varphi}\mathrm{E}\ (‰/\mathrm{amu}) = \left[\frac{\left({}^{i}\mathrm{E}/{}^{j}\mathrm{E}\right)_{Sample}}{\left({}^{i}\mathrm{E}/{}^{j}\mathrm{E}\right)_{Standard}} - 1\right]\frac{1000}{m_i - m_j}, \tag{5.36}$$

where m_i and m_j are the atomic masses of isotopes ${}^{i}\mathrm{E}$ and ${}^{j}\mathrm{E}$, respectively (*e.g.*, Ce isotopic fractionation $\delta^{\varphi}\mathrm{Ce}$ in ‰/amu is reported as $\delta^{142/140}\mathrm{Ce}$ divided by the atomic mass difference 142 – 140 = 2). The reason for expressing isotopic variations on a ‰/amu basis is that the magnitude of mass-dependent fractionation of an element scales to first order with the difference in mass of the isotopes involved, so this notation allows easier comparison of the isotopic variations of several REEs covering different mass ranges. The terrestrial standard solutions used for normalization in the $\delta^{\varphi}\mathrm{E}$ notation have isotopic compositions that are close to those of terrestrial basalts, which are presumably close to the bulk Earth values (Table 5.1; Albalat et al., 2012). The REE isotopic compositions in group II CAIs (Table 5.1) are plotted in order of increasing refractoriness in Fig. 5.5B. The most refractory REEs (Gd, Dy, and Er) show significant negative stable isotopic fractionations ranging from 0 to –3.6 ‰/amu with averages approximately at –1.5 ‰/amu. The least refractory Eu and Yb and moderately refractory REEs Ce, Nd, and Sm range from –1 to +1 ‰/amu and define averages near 0. A CAI with a flat REE abundance pattern was also measured and shows isotopic compositions within ±0.25 ‰/amu of 0.

Although Sr has a nominal 50% condensation temperature (1464 K) that is ~100 K higher than that of Eu (1356 K; Lodders, 2003), the elemental enrichment factors of Eu and Sr in CAIs

normalized to CI chondrites are tightly correlated, meaning that during evaporation and condensation the two elements have very similar behaviors (Charlier et al., 2019). Comparing our new Eu isotopic analyses with previous Sr stable isotopic fractionation data measured on the same sample digestion using a double-spike approach shows that δ^{φ}Eu and δ^{φ}Sr also correlate closely over a range of δ^{φ}Sr values from –1.8 to +0.8 ‰/amu with a slope of 0.67 (Fig. 5.4A). This is further evidence that Eu and Sr have very similar behaviors during condensation in the nebula. Linear correlations between isotopic compositions were also observed for Ce and Nd *vs*. Sm (with slopes of 0.90 and 1.13, respectively; Fig. 5.4B), and Dy *vs*. Gd (with a slope of 1.40; Fig. 5.4C). The Ti stable isotopic fractionation in this set of CAIs were reported in Davis et al. (2018) using sample-standard bracketing and were remeasured in this study using the double-spike approach to achieve higher precision (Table 5.3). The 50% condensation temperature of Ti is 1582 K under solar nebula conditions (at 10^{-4} bar total pressure of H_2), which overlaps with that of LREEs (Lodders, 2003). The isotopic fractionation of Ti ranges from –0.2 to +1.0 ‰/amu but shows no clear correlation with any of the REEs. Since Ti is a major element, its behavior during evaporation and condensation is likely to be decoupled from the REEs, which usually substitute into host minerals as trace elements. Correlation matrices showing all possible bivariate correlations for abundances and isotopes of the elements investigated in this set of CAIs are shown in Fig. 5.7. The correlations highlighted above (Eu-Sr, Ce-Nd-Sm, and Dy-Gd) are the only ones that are statistically significant. Yb and Eu, which are among the least refractory REEs, are not correlated isotopically (Fig. 5.4D). The stable isotopic composition of U also does not correlate with that of any REE including Yb, whose abundance correlates with that of U (Fig. 5.8; Tissot et al., 2016).

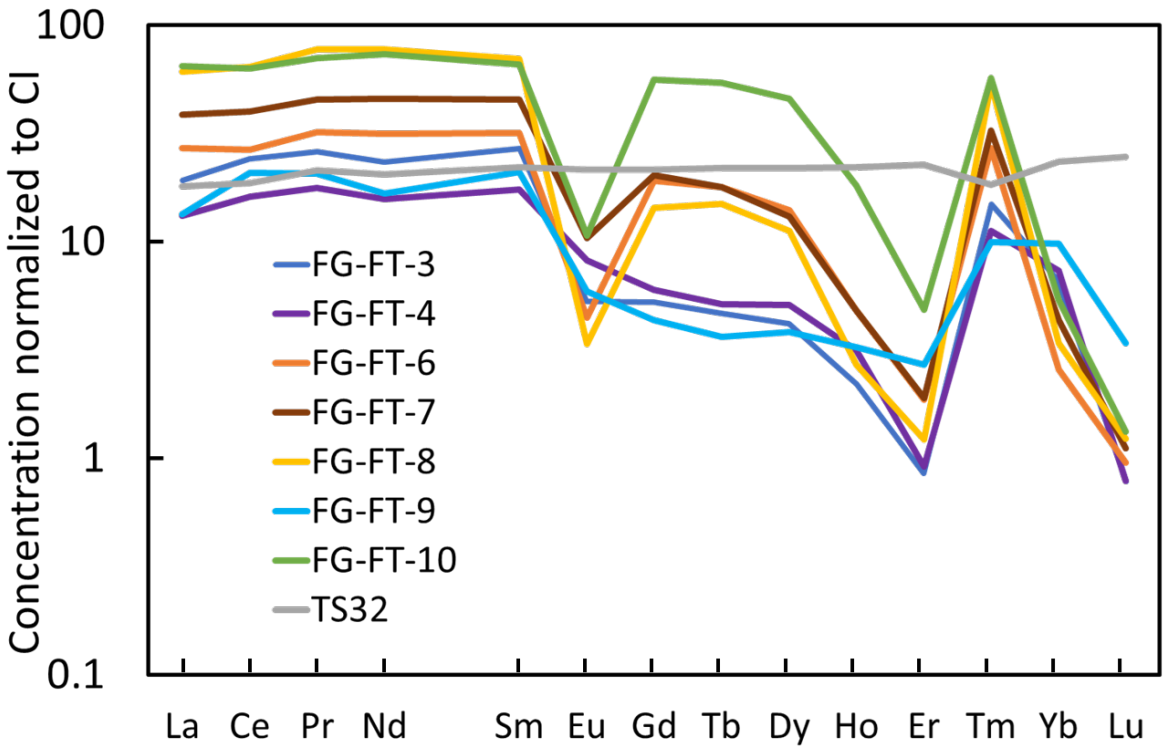

Figure 5.6 REE abundance patterns of the 8 CAIs (7 with group II REE patterns) studied here, in order of atomic number (Tissot et al., 2016; Davis et al., 2018).

Little data is available in the literature to compare with our results (Moynier et al., 2006; Albalat et al., 2012). A previous study (Albalat et al., 2012) reported measurements of the stable isotopic compositions of Er and Yb in a variety of terrestrial rocks and bulk meteorites. They found limited variations in meteorites, which span ~0.3 ‰/amu for δ^{φ}Yb and ~0.15 ‰/amu for δ^{φ}Er. The isotopic variations documented in CAIs are much larger, spanning ~0.7 and ~3.6 ‰/amu for Yb and Er, respectively. The largest isotopic variations are found in the least REE-enriched CAIs, which contribute the least to the bulk inventory of these elements in CAI-bearing meteorites. This could explain the limited isotopic variations documented by Albalat et al. (2012) in bulk meteorites.

Figure 5.7 Scatter plot matrix of 7 group II CAIs. The top left plots are correlations of the abundances normalized to CI chondrites, while the bottom right plots are the correlations of the stable isotopic fractionations (‰/amu). Circles in grey, red, green, yellow, blue, black, purple and orange correspond to CAIs TS32, FG-FT-3, 4, 6, 7, 8, 9 and 10, respectively. Note that in this diagram, none of the plots displays enrichment factor *vs*. isotopic composition (or vice versa).

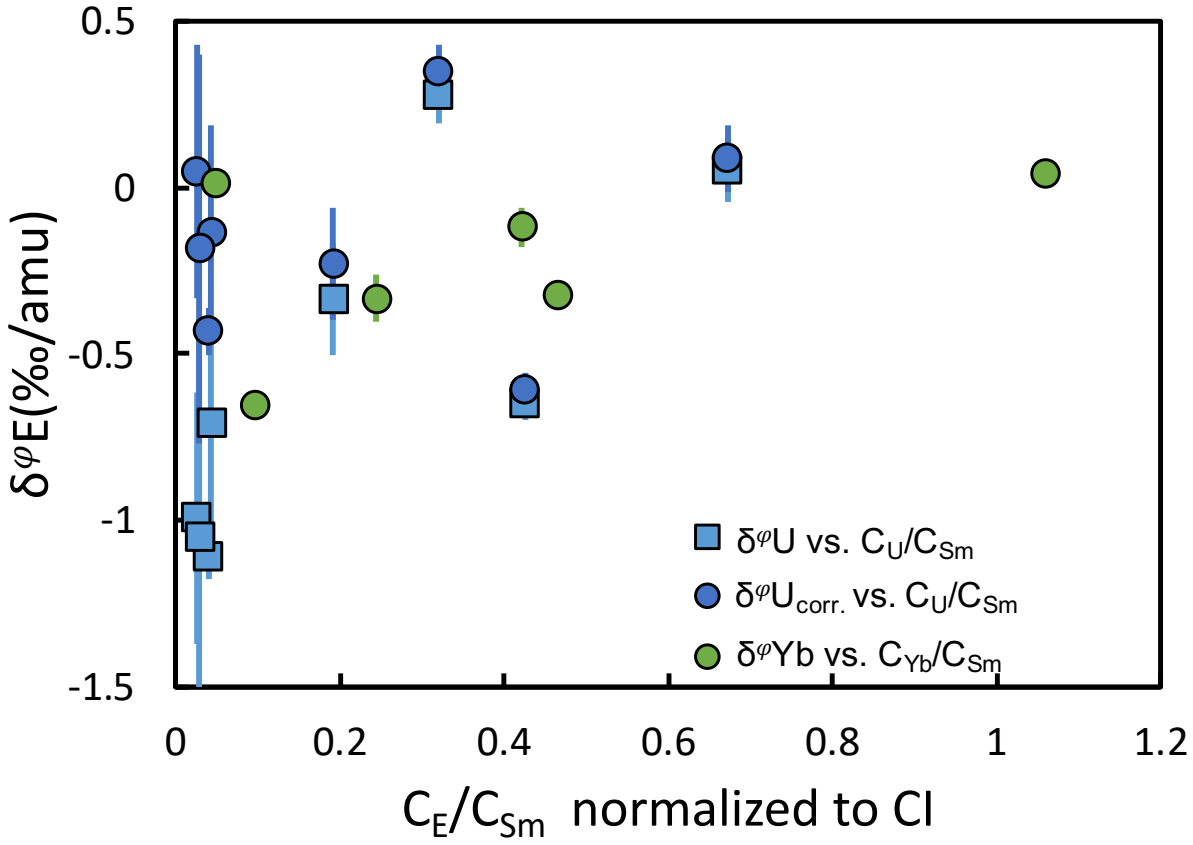

Figure 5.8 Yb (green) and U (blue) isotopic compositions plotted as a function of their depletions relative to Sm in CAIs. The Yb isotopic data are from Table 5.1, while the U isotopic data are from Tissot et al. (2016). The blue-filled squares are raw U isotopic data (δ^{φ}U), while the blue filled-circles ($\delta^{\varphi}U_{corr.}$) have been corrected for decay of ^{247}Cm ($t_{1/2}$ = 15.6 My) using an initial $^{247}Cm/^{235}U$ ratio of 7.0×10^{-5} (Brennecka et al., 2010; Tissot et al., 2016; Tang et al., 2017) and using the Nd/U ratio as a measure of the fractionation of the Cm/U ratio. As shown, the CAIs show no correlation between δ^{φ}Yb and δ^{φ}U, despite the broad logarithmic correlation of their concentrations Tissot et al. (2016). It is worth noting that the correlation in Tissot et al. (2016) is visible in logarithmic scale but the scatter in the data points around the 1:1 line spans an order of magnitude. The lack of correlation between δ^{φ}Yb and δ^{φ}U could be due to their distinct volatilities or due to U mobilization during aqueous alteration of fine-grained CAIs (Tissot et al., 2016).

Another study (Moynier et al., 2006) reported measurements of the Sm and Eu isotopic compositions of several chondrites and CAIs. They found limited variations, with δ^{φ}Sm and δ^{φ}Eu values in CAIs that span ranges of less than 0.04 and 0.06 ‰/amu, respectively. The δ^{φ}Sm

and δ^{φ}Eu values measured here span ranges of ~1.9 and 1.8 ‰/amu, respectively. The difference could be due to the fact that we focused on CAIs with highly fractionated REE patterns, while Moynier et al. (2006) may have measured samples with mostly flat (unfractionated) REE abundance patterns (the REE pattern is known for only one of the four CAIs that they measured and it is a flat group I; Mason and Taylor, 1982). Highly fractionated group II REE patterns are most commonly found in fine-grained CAIs that are difficult to extract from meteorites, and it is conceivable that the CAIs studied by Moynier et al. (2006) were of the more readily extractable coarse-grain kind. We indeed measured negligible isotopic fractionation in one CAI with a flat REE abundance pattern (TS32; Table 5.1).

5.6. Discussion

5.6.1. A Kinetic Origin for the Isotopic Fractionation of the REEs

Although the various isotopic patterns for each group II CAI reflect their unique formation histories, they still share similarities, among which the most distinctive feature is that the most refractory REEs (Gd, Dy, and Er) are all enriched in the light isotopes with average isotopic compositions of approximately –1.5 ‰/amu. In contrast, the less refractory REEs show smaller isotopic variations, centered around 0 (Fig. 5.5B).

The isotopic fractionations of the REEs could be due to equilibrium or kinetic processes, or a combination of both during evaporation and condensation. The extent of equilibrium isotopic fractionation can be estimated based on thermodynamic considerations. During evaporation or condensation of CAIs under solar nebula conditions, REEs in minerals (presumably hibonite or perovskite) exist as 3+, except for Eu, for which a significant fraction may exist as 2+ (Simon et

al., 1991). In the vapor, La, Pr, Nd, Gd-Er, and Lu are predominantly composed of monoxides (2+), with less than 15% present as monatomic gas (0 oxidation state). Gaseous Eu and Yb are nearly all monatomic, while Sm and Tm are predominantly monatomic species with only moderate fractions (~30% and 5% respectively) of monoxides. The majority (*i.e.*, ~90%) of Ce exists in the vapor as CeO_2 (4+) and the rest as CeO (2+). There are no data or calculations that we are aware of to estimate equilibrium isotopic fractionation between Ce^{4+} in the vapor and Ce^{3+} in minerals, but we can estimate the other fractionation factors. All trivalent REEs have similar geochemical behavior and it is likely that they form chemical bonds of similar strengths. The technique of Nuclear Resonant Inelastic X-ray Scattering (NRIXS) applied to the Mössbauer isotope ^{151}Eu in solid EuO and Eu_2O_3 gives force constants of Eu^{2+} and Eu^{3+} of 114 and 196 N/m, respectively (Dauphas et al., 2018a). The formula that relates reduced partition function ratio to force constant for Eu is (Dauphas et al., 2018a and references therein),

$$1000\ln\beta_{\mathrm{Eu}}^{\varphi} = 193\frac{\langle F_{\mathrm{Eu}}\rangle}{T^2}, \tag{5.37}$$

with $1000\ln\beta_{\mathrm{Eu}}^{\varphi} = 1000\ln\beta_{\mathrm{Eu}}^{1/(m_i-m_j)}$ the equilibrium fractionation factor in ‰/amu in the compound of interest relative to monoatomic gas, $\langle F_{\mathrm{Eu}}\rangle$ the force constant in N/m and T the temperature in K. Using this formula, we estimate that at 1750 K, relevant to CAI formation, the equilibrium isotopic fractionation between Eu^{2+} and Eu^{3+} in solid and monatomic Eu in gas will be +0.007 and +0.012 ‰/amu, respectively. The force constant of gaseous EuO is not known but it can be calculated using the formula relating vibration wavenumber to bond force constant for diatomic molecules,

$$\langle F_{\mathrm{Eu}}\rangle = 4\pi^2 m^* c^2 \nu^2, \tag{5.38}$$

where ν = 668 cm^{-1} is the vibration wavenumber of EuO in an argon matrix (Gabelnick et al., 1974), c = 299792458 m/s is the speed of light, and $m^* = 2.404 \times 10^{-26}$kg/amu is the reduced mass of EuO. This gives a force constant of 381 N/m, corresponding to $1000\ln\beta_{\mathrm{Eu}}^{\varphi}$ =+0.024 ‰/amu for gaseous EuO. The equilibrium isotopic fractionations between Eu^{2+} and Eu^{3+} in solid and EuO in gas at 1750 K are therefore –0.017 and –0.012 ‰/amu, respectively. Regardless of the speciation of the REEs in the vapor or minerals, the expected equilibrium isotopic fractionation is always smaller than ~0.02 ‰/amu (Fig. 5.9). Even if a Rayleigh distillation was involved in the depletion of some REEs relative to others, the resulting isotopic fractionation would be 0.1 ‰/amu at most, assuming a depletion factor of 100. This calculation shows that equilibrium isotopic fractionation cannot explain the REE isotopic fractionation observed in group II CAIs, thus demonstrating that these CAIs are not simple solar nebula equilibrium condensates but that kinetic processes associated with evaporation and/or condensation played some role.

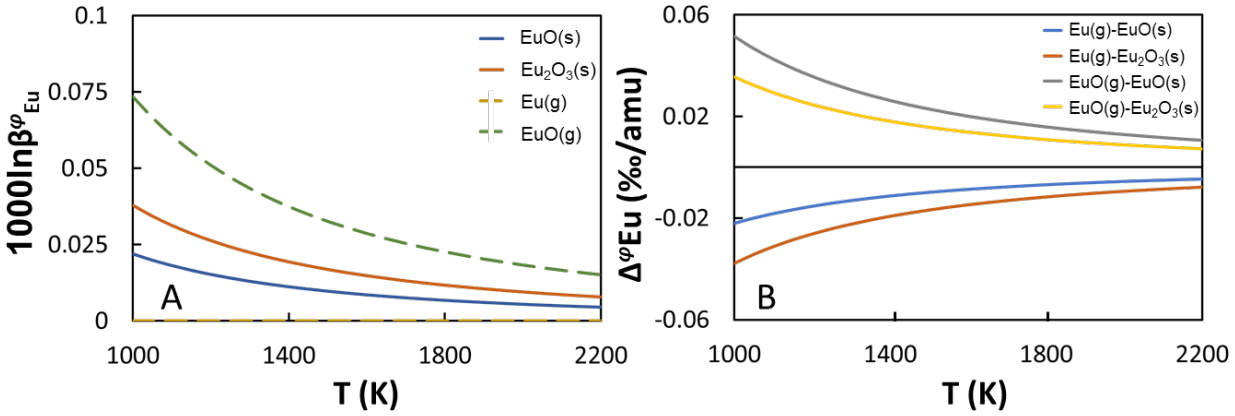

Figure 5.9 Equilibrium isotopic fractionations of Eu. (A) Calculated reduced partition function ratios (in ‰/amu) of Eu compounds as a function of temperature. (B) Equilibrium isotopic fractionation between gas and solid phases of Eu as a function of temperature. See text for details.

5.6.2. Isotopic Fractionation of the Most Refractory REEs

As discussed in the introduction, the isotopic fractionation experienced by solids or liquids during evaporation and condensation is characteristic of the process involved, and the saturation conditions. In the canonical view of the origin of the group II pattern, the most refractory REEs are sequestered in ultrarefractory grains that are removed from the system. Below, we discuss several scenarios for the removal of this ultrarefractory component and show how only the partial evaporation scenario (*iii*) is viable:

(*i*) If these ultrarefractory grains (distinct from the refractory CAIs investigated here) condensed under supersaturated conditions, the vapor left behind would have been isotopically heavy. This signature would have been imparted to the highly refractory REEs in CAIs condensed from this vapor, which is the opposite to what is observed (Fig. 5.5B).

(*ii*) An alternative scenario is that ultrarefractory grains formed in near-equilibrium conditions, leaving behind vapor depleted in the most refractory REEs but with near-normal isotopic composition. If group II CAIs condensed under supersaturated conditions from such unfractionated gas, the most refractory REEs could have acquired a light isotopic composition, consistent with observations. However, for isotopic fractionation to be expressed during condensation, mass-balance requires that only a fraction of the refractory REEs be condensed. In that case, we would expect a significant fraction of the more volatile moderately refractory REEs (Ce, Nd, and Sm) to remain in the gas residue, leading to elemental depletion and isotopic fractionations of moderately refractory REEs in group II CAIs, which is not observed.

(*iii*) The most plausible scenario is therefore that the refractory heavy REE acquired their light isotope enrichments by near-complete condensation of vapor produced by a prior stage of nonequilibrium evaporation that left behind material akin to ultrarefractory grains.

The magnitude of stable isotopic fractionation during partial evaporation depends on the fraction of the target element left in the residue, the kinetic fractionation factor that describes the difference in evaporation rates for two isotopes, and the degree of undersaturation of the vapor (Richter et al., 2002; Richter, 2004; Dauphas et al., 2015). The finding of large kinetic isotopic fractionation for refractory REEs Gd and Dy means that evaporation took place in a medium that was undersaturated, which provides constraints on the timescale of this evaporation episode. Indeed, if the surrounding vapor is highly undersaturated, evaporation is faster and isotopic fractionation is larger, than when vapor is near equilibrium and the fluxes in and out of the residue are nearly balanced.

To quantify the evaporation timescale, we have built a simple scenario (Fig. 5.10A; see Sect. 5.4 for details) whereby ultrarefractory grains of equal sizes are evenly distributed in space, and evaporation is driven by a temperature increase $T(t) = T_{h,0} + \Phi_h t$ with $T_{h,0}$ the initial temperature and Φ_h the heating rate (a positive number). The value of $T_{h,0}$ has little influence on the model result provided that it is low enough that all REEs are fully condensed at the beginning of the calculation. In our simulations, we adopt a value of 1350 K. Evaporation happens in a closed system until a time (temperature) when ultrarefractory grains are physically separated from the vapor. Some meteorites like Allende display a group II REE pattern at a bulk scale (Stracke et al., 2012; Dauphas and Pourmand, 2015; Barrat et al., 2016), supporting the view that ultrarefractory inclusions with REE patterns complementary to group II were physically separated at large scales

from lower temperature refractory materials. We define the timescale of the evaporation event as the time span between 5% evaporation of the least refractory REE (Eu), and the time of ultrarefractory solid removal.

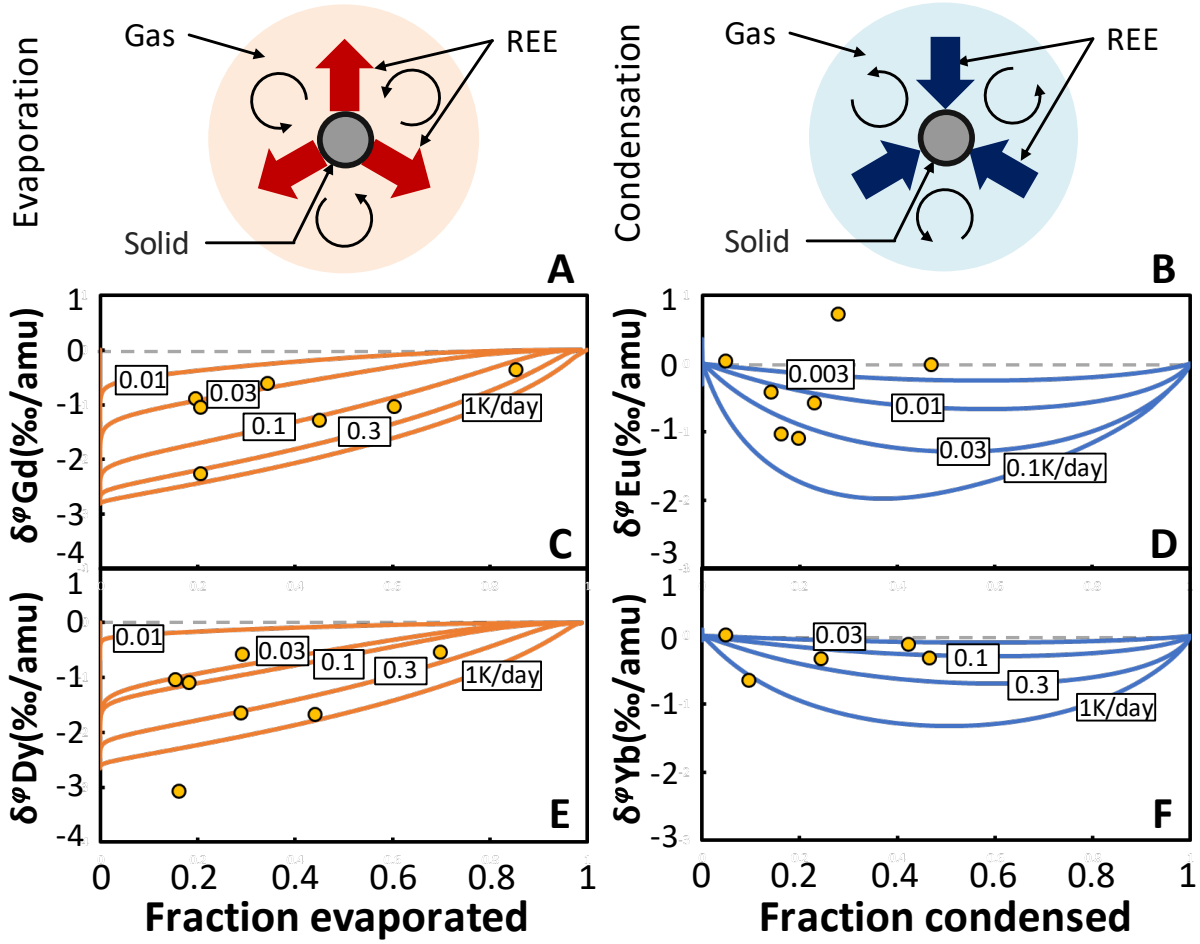

Figure 5.10 Trajectories of chemical depletion and isotopic fractionation in the evaporation (left panels) and condensation (right panels) stages considered to explain the composition of group II CAIs (see Sect. 5.4 for details). Schematics of the models envisioned for evaporation (A) and condensation (B). (C) Gd and (E) Dy isotopic fractionations and depletions during closed-system evaporation for different heating rates. (D) Eu and (F) Yb isotopic fractionations and depletions during closed-system condensation for different cooling rates. The labels on the curves are the heating rates (evaporation) and cooling rates (condensation) used in the calculations.

This model shares similarities with those applied to closed-system condensation/evaporation and chondrule formation (Tsuchiyama et al., 1999; Ozawa and Nagahara, 2001; Richter, 2004; Fedkin et al., 2012; Bourdon and Fitoussi, 2020). The chemical depletions and isotopic fractionations of the REEs evaporated depend on the heating rate and duration of the evaporation episode. If temperature increases slowly, the vapor pressure is always close to equilibrium, evaporation is slow, and isotopic fractionation approaches equilibrium, which is small at the temperatures considered. Conversely, if temperature increases rapidly, evaporation is fast but insufficient to keep up with the increasing equilibrium vapor pressure, leading to undersaturation and light isotope enrichment in the vapor (Richter, 2004). The two unknowns of the model are the heating rate and duration, which can be solved for using the two observables chemical depletion and isotopic fractionation of Gd and Dy; the two highly refractory REEs most affected by this evaporation episode.

The fractions of Gd and Dy evaporated from the ultrarefractory residue can be estimated for each CAI using their abundances normalized to chondrites over that of the moderately refractory REE Sm, which like other moderately refractory REEs would have been lost quantitatively from the precursors of ultrarefractory inclusions and fully condensed in the CAI. We have used thermodynamic modeling to calculate the isotopic fractionations and depletions of Gd and Dy for different heating rates and compare model predictions with our measurements (details of the modeling are provided in Sect. 5.4). The thermodynamic data, oxygen fugacity, and number of moles of Ca condensed per unit volume of the system used for modeling evaporation are from Davis et al. (2018) assuming that the mineral host of REEs during evaporation is hibonite. Although hibonite is rare in the fine-grained CAIs that we studied, we have adopted it as the REE

solid carrier as (*i*) hibonite is the highest temperature mineral that incorporates significant REEs, (*ii*) it is the only likely REE host phase over a 55 K range (MacPherson and Davis, 1994), (*iii*) it could have been present as a precursor mineral before disappearing by reaction with the vapor during cooling and is found in some ultrarefractory inclusions in CM chondrites (Ireland and Fegley, 2000), and (*iv*) perovskite is another option but it cannot explain Tm anomalies (Davis and Grossman, 1979). We find that the heating rates of Gd (Fig. 5.10C) and Dy (Fig. 5.10E) in most CAIs fall in the range ~0.03 to 0.3 K/day, for a duration of the evaporation episode of hundreds to thousands of days.

5.6.3. Stable Isotopic Fractionation of the Least Refractory REEs (Eu and Yb)

The uniform enrichment of the moderately refractory REEs and the relative depletion of the least refractory REEs can potentially be explained by either evaporation or condensation. In the evaporation scenario, the vapor produced by evaporation of an ultrarefractory component as described above was quantitatively condensed in a second generation of refractory inclusions that were subsequently reheated and lost the least refractory REEs (Eu and Yb) to the vapor. In the condensation scenario, during cooling of the parcel of vapor produced by evaporation of an ultrarefractory component, the moderately refractory LREEs were quantitatively condensed but vapor was separated from the solid before the least refractory REEs condensed.

Overall, Eu and Yb show limited stable isotopic fractionations, with most Yb data displaying negative δ^{φ}Yb values consistent with partial condensation being the dominant process. A likely explanation for the limited isotopic variations but large elemental depletions of Eu and Yb is that their condensation took place under near-equilibrium conditions. The degree of isotopic fractionation during condensation (Jouzel and Merlivat, 1984; Richter, 2004; Dauphas et al., 2015;

Simon et al., 2017) is related to the degree of chemical depletion, the kinetic isotopic fractionation factor associated with condensation, and the degree of supersaturation. As with evaporation, isotopic fractionation during condensation can provide constraints on the timescale of this condensation episode. Indeed, if the surrounding vapor is highly supersaturated, condensation is faster and isotopic fractionation is larger, than when vapor is near equilibrium and the fluxes in and out of the condensate are nearly balanced.

To quantify the condensation timescale, we have built a simple scenario (Fig. 5.10B; see Sect. 5.4 for details) whereby vapor produced during the first evaporation episode condenses in a second generation of refractory inclusions, and condensation is driven by a temperature decrease $T(t) = T_{c,0} + \Phi_c t$ with $T_{c,0}$ the initial temperature and Φ_c the cooling rate (a negative number). The value of $T_{c,0}$ has little influence on the model result provided that it is high enough that all REEs are fully evaporated at the beginning of the calculation. In our simulations, we adopt a value of 1700 K. Condensation happens in a closed system (also see Richter, 2004; Bourdon and Fitoussi, 2020) until a time or temperature at which the vapor is dissipated and the remaining least refractory REEs are lost. We define the timescale of the condensation event as the time span between 5% condensation of highly refractory REE (Dy), and the time of gas dissipation. The chemical depletions and isotopic fractionations of the condensed REEs depend on the cooling rate and duration of the condensation episode. If temperature decreases slowly, the vapor pressure is always close to equilibrium, condensation is slow, and isotopic fractionation approaches equilibrium, which is small at the temperatures considered. Conversely, if temperature decreases rapidly, condensation is fast but insufficient to keep up with the decreasing equilibrium vapor pressure, leading to oversaturation and light isotope enrichment in the condensate (Richter, 2004).

Moderately refractory REEs are present in near-chondritic proportions and show little isotopic fractionations (Fig. 5.5A and Fig. 5.6), so they were most likely quantitatively condensed during this stage. Highly refractory REEs were also quantitatively condensed. The only REEs affected by this stage are the least refractory Eu and Yb. Despite their large elemental depletions (Fig. 5.5A), these REEs show little isotopic fractionations (Fig. 5.5B), meaning that cooling must have been protracted and condensation occurred under near-equilibrium conditions. We calculated the cooling rate (Φ_c) and overall duration t (time of vapor dissipation after the onset of condensation) needed to explain the large depletions and small isotopic fractionations of Eu and Gd depletions (Fig. 5.10D). We find that the cooling rates relevant to most CAIs are lower than 0.1 K/day for Eu and 1 K/day for Yb (Fig. 5.10F). The duration of this condensation episode must have been at least a few hundreds of days.

5.6.4. Evaporation-Condensation Scenario Inferred from REE Isotope Systematics

The isotopic compositions and depletions of the most refractory and least refractory REEs are most readily explained in the context of a two-stage evaporation-condensation scenario (Fig. 5.11).

In the first stage, nebular dust with chondritic REE abundances was subjected to closed-system evaporation. The least refractory and moderately refractory REEs were quantitatively vaporized and the vapor inherited the isotopic composition of the solid precursor for these elements. The most refractory REEs were only partially vaporized. The partial evaporation of the most refractory REEs induced significant negative isotopic fractionations in the vapor because the lighter isotopes evaporated more readily than heavy ones during kinetically controlled evaporation.

In the second stage, vapor was physically isolated from the solid residue and subsequently condensed to form CAIs with group II REE patterns under near-equilibrium conditions. The most refractory REEs and the moderately refractory REEs were completely condensed at this stage and inherited the abundance and isotopic compositions from the gas phase. The least refractory REEs were only partially condensed, which resulted in their depletion in CAIs. The limited isotopic fractionations observed in the least refractory REEs required that the cooling that induced condensation must have been slow enough to maintain near-equilibrium conditions.

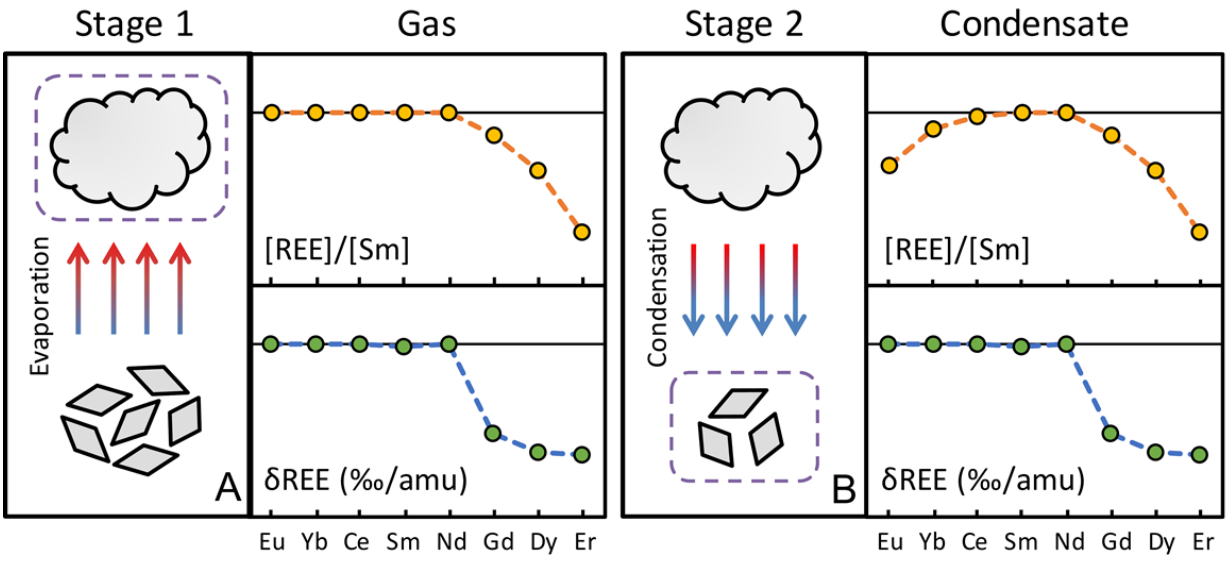

Figure 5.11 Schematics of group II REE fractionation in CAIs. (A) Stage 1: Nebular dust with chondritic proportions of the REEs evaporates in an undersaturated medium, which leaves behind an ultrarefractory residue and produces vapor depleted in the heavy most refractory REEs that are also characterized by light isotope enrichments. (B) Stage 2: The vapor from Stage 1 partially condenses. The highly refractory (HREE except Tm and Yb) and moderately refractory (light REEs and Tm) are completely condensed. The least refractory REEs Eu and Yb remain in the gas and are not completely condensed. The condensation during that stage occurs in near equilibrium conditions.

We have modelled the REE abundance and isotopic pattern predicted by this two-stage scenario and it can quantitatively reproduce the composition of group II CAIs. In this 2-stage

scenario, the elemental abundances of the most refractory REEs were fractionated due to prior isolation of an ultrarefractory component, which had a REE pattern complementary to group II pattern except for Eu and Yb. Such ultrarefractory REE patterns are rare but are found in a few refractory inclusions from carbonaceous chondrites such as Murchison and Ornans (*e.g.*, Palme et al., 1982; Simon et al., 1996). A prediction of our model is that ultrarefractory inclusions should be evaporation residues and as such they should be enriched in the heavy isotopes of the REEs, especially the least refractory and moderately refractory (Ce, Nd, Sm, Eu, and Yb). The view that ultrarefractory inclusions are evaporation residues agrees with the W depletion measured in an ultrarefractory inclusion from Ornans, as this feature requires relatively oxidizing condition, which is more easily achieved through evaporation than condensation of solar nebula gas (Palme et al., 1982). Analyzing the stable isotopic fractionation of REEs in these refractory inclusions will shed light on their genetic relationship with group II CAIs.

5.6.5. Early Solar System Events Responsible for the Formation of CAIs

According to the 2-stage scenario outlined above, CAIs characterized by group II patterns were formed by heating above 1600 K for hundreds to thousands of days of dust with initially chondritic REE composition, followed by cooling of the vapor formed by the first evaporation stage for at least a few hundred days. It is difficult to tie this thermal history to specific early solar system events, but we speculate that such a heating history could have taken place during rapid solar outbursts when the young Sun went through EXor or FUor events akin to those documented in remote stars. EXors are a group of pre-main-sequence stars characterized by intense, episodic increases in brightness separated by quiescent periods (Audard et al., 2014). They are named after the prototype EX Lupi, which is a low-mass, Sun-like young star located in the Lupus cloud

(Herbig, 2007). FUors are eruptions in FU Orionis objects, another group of pre-main-sequence stars that see episodes of brightening of higher intensity and longer duration than EX Lupi (Hartmann and Kenyon, 1996; Audard et al., 2014). Observations of accretion tracers such as spectral lines and veiling indicate that these large, repetitive outbursts are caused by episodic increase of mass accretion from the protoplanetary disk onto the star. Taking EX Lupi as an example, the typical timescale of the outburst ranges from several months to a few years, during which the brightness of the star can increase by 2–5 magnitudes (Herbig, 2007). The brightness during the outburst can fluctuate significantly, possibly leading to rapid temperature swings in the inner region of the protoplanetary disk.

The increase in brightness during FUors and EXor outbursts is presumably associated with intense thermal processing of pre-existing dust in the central region of the protoplanetary disk. This is supported by the discovery in 2008 of in situ formation of crystalline silicates in one of the largest outbursts that happened in the circumstellar disk of EX Lupi (Ábrahám et al., 2009). Objects like CAIs might have been subjected to similar thermal processing near the protostar during FUors or EXor outbursts. The increased luminosity of the Sun and internal dissipation associated with higher mass flux through the disk would both lead to higher temperatures in the solar nebula. We propose that FUors and EXor outbursts or similar events happened in the early solar system and are responsible for the formation of group II CAIs and refractory dust of similar composition.

The periods of the optical light luminosity of FUors and EXor outbursts range from hundreds of days to 100 years (Hartmann and Kenyon, 1996; Audard et al., 2014), which is consistent with the time required for evaporation of the most refractory REEs and the condensation

of the least refractory REEs. During the outburst, only part of the most refractory REEs (and all the least refractory and moderately refractory REEs) were vaporized at the peak luminosity, leading to significant light isotope enrichments of the most refractory REEs in the vapor. When the outburst subsided, most REE condensed except the least refractory REEs, prohibited by the relatively high ambient temperature. The chemical and isotopic compositions of CAIs with group II patterns might reflect the influence of several cycles of evaporation and condensation before final condensation in refractory inclusions. During or after the FUors or EXor outburst, newly formed CAIs would have been distributed to the outer regions of the solar system through extensive radial transport, where they were incorporated in comets and other low-temperature outer solar system objects (Brownlee et al., 2006; Lisse et al., 2006; McKeegan et al., 2006; Zolensky et al., 2006).

5.7. References

Ábrahám, P., Juhász, A., Dullemond, C.P., Kóspál, Á., Van Boekel, R., Bouwman, J., Henning, Th., Moór, A., Mosoni, L., Sicilia-Aguilar, A. and Sipos, N., 2009. Episodic formation of cometary material in the outburst of a young Sun-like star. Nature 459, 224-226.

Albalat, E., Telouk, P., Albarède, F., 2012. Er and Yb isotope fractionation in planetary materials. Earth and Planetary Science Letters 355, 39-50.

Audard, M., Abrahám, P., Dunham, M.M., Green, J.D., Grosso, N., Hamaguchi, K., Kastner, J.H., Kóspál, A., Lodato, G., Romanova, M.M., 2014. Episodic accretion in young stars. In Protostars and Planets VI (Eds. Beuther, H, Klessen, R.S., Dullemond, C.S., Henning, Th.), 387-410.

Barrat, J.-A., Dauphas, N., Gillet, P., Bollinger, C., Etoubleau, J., Bischoff, A., Yamaguchi, A., 2016. Evidence from Tm anomalies for non-CI refractory lithophile element proportions in terrestrial planets and achondrites. Geochimica et Cosmochimica Acta 176, 1-17.

Bourdon, B., Fitoussi, C., 2020. Isotope fractionation during condensation and evaporation during planet formation processes. ACS Earth and Space Chemistry 4, 1408-1423.

Boynton, W.V., 1975. Fractionation in the solar nebula: condensation of yttrium and the rare earth elements. Geochimica et Cosmochimica Acta 39, 569-584.

Brennecka, G.A., Weyer, S., Wadhwa, M., Janney, P.E., Zipfel, J. and Anbar, A.D., 2010. $^{238}U/^{235}U$ variations in meteorites: Extant ^{247}Cm and implications for Pb-Pb dating. Science 327, 449-451.

Brownlee, D., et al., 2006. Comet 81P/Wild 2 under a microscope. science 314, 1711-1716.

Cameron, A.G.W., 1962. The formation of the sun and planets. Icarus 1, 13-69.

Charlier, B.L.A., Tissot, F.L.H., Dauphas, N. and Wilson, C.J.N., 2019. Nucleosynthetic, radiogenic and stable strontium isotopic variations in fine-and coarse-grained refractory inclusions from Allende. Geochimica et Cosmochimica Acta 265, 413-430.

Dauphas, N., Hu, M.Y., Baker, E.M., Hu, J., Tissot, F.L.H., Alp, E.E., Roskosz, M., Zhao, J., Bi, W., Liu, J., Lin, J-F., Nie, N.X., Heard, A., 2018a. SciPhon: a data analysis software for nuclear resonant inelastic X-ray scattering with applications to Fe, Kr, Sn, Eu and Dy. Journal of Synchrotron Radiation 25, 1581-1599.

Dauphas, N., Poitrasson, F., Burkhardt, C., Kobayashi, H., Kurosawa, K., 2015. Planetary and meteoritic Mg/Si and $\delta^{30}Si$ variations inherited from solar nebula chemistry. Earth and Planetary Science Letters 427, 236-248.

Dauphas, N., Pourmand, A., 2015. Thulium anomalies and rare earth element patterns in meteorites and Earth: Nebular fractionation and the nugget effect. Geochimica et Cosmochimica Acta 163, 234-261.

Dauphas, N., Tissot, F.L.H., Yokochi, R., Ireland, T.J., Hu, J., 2018b. Fluoropolymer pneumatically/hydraulically actuated liquid chromatographic system for use with harsh reagents. U.S. Patent No. 9,884,266 (OrLab Chromatography LLC).

Davis, A.M., Grossman, L., 1979. Condensation and fractionation of rare earths in the solar nebula. Geochimica et Cosmochimica Acta 43, 1611-1632.

Davis, A.M., Zhang, J., Greber, N.D., Hu, J., Tissot, F.L.H., Dauphas, N., 2018. Titanium isotopes and rare earth patterns in CAIs: evidence for thermal processing and gas-dust decoupling in the protoplanetary disk. Geochimica et Cosmochimica Acta 221, 275-295.

Fedkin, A.V., Grossman, L., Ciesla, F.J., Simon, S.B., 2012. Mineralogical and isotopic constraints on chondrule formation from shock wave thermal histories. Geochimica et Cosmochimica Acta 87, 81-116.

Gabelnick, S.D., Reedy, G.T. and Chasanov, M.G., 1974. Infrared spectra and structure of some matrix‐isolated lanthanide and actinide oxides. The Journal of Chemical Physics 60, 1167-1171.

Greber, N.D., Dauphas, N., Puchtel, I.S., Hofmann, B.A., Arndt, N.T., 2017. Titanium stable isotopic variations in chondrites, achondrites and lunar rocks. Geochimica et cosmochimica acta 213, 534-552.

Grossman, L., 1972. Condensation in the primitive solar nebula. Geochimica et Cosmochimica Acta 36, 597-619.

Grossman, L., Simon, S.B., Rai, V.K., Thiemens, M.H., Hutcheon, I.D., Williams, R.W., Galy, A., Ding, T., Fedkin, A.V., Clayton, R.N. and Mayeda, T.K., 2008. Primordial compositions of refractory inclusions. Geochimica et Cosmochimica Acta 72, 3001-3021.

Hartmann, L., Kenyon, S.J., 1996. The FU orionis phenomenon. Annual Review of Astronomy and Astrophysics 34, 207-240.

Herbig, G.H., 2007. EX Lupi: history and spectroscopy. The Astronomical Journal 133, 2679.

Hirth J. P. and Pound G. M.,1963. Condensation and Evaporation. Pergamon, Oxford, 192 pp.

Hu, J.Y., Dauphas, N., 2017. Double-spike data reduction in the presence of isotopic anomalies. Journal of Analytical Atomic Spectrometry 32, 2024-2033.

Huss G. R., MacPherson G. J., Davis A. M., Krot A. N. & Ulyanov A. A. (2002) Microdistribution of REE in fine-grained group II Ca-Al-rich inclusions in the reduced CV chondrite Efremovka. Meteoritics Planet. Sci. 37, A68.

Ireland, T.J., Tissot, F.L.H., Yokochi, R., Dauphas, N., 2013. Teflon-HPLC: A novel chromatographic system for application to isotope geochemistry and other industries. Chemical Geology 357, 203-214.

Ireland, T.R., 1988. Correlated morphological, chemical, and isotopic characteristics of hibonites from the Murchison carbonaceous chondrite. Geochimica et Cosmochimica Acta 52, 2827-2839.

Ireland, T.R., Fegley, B.Jr., 2000. The solar system's earliest chemistry: Systematics of refractory inclusions. International Geology Review 42, 865-894.

Jouzel, J., Merlivat, L., 1984. Deuterium and oxygen 18 in precipitation: Modeling of the isotopic effects during snow formation. Journal of Geophysical Research: Atmospheres 89, 11749-11757.

Kornacki, A.S., Fegley, B.Jr., 1986. The abundance and relative volatility of refractory trace elements in Allende Ca, Al-rich inclusions: implications for chemical and physical processes in the solar nebula. Earth and Planetary Science Letters 79, 217-234.

Krot, A.N., Scott, E.R.D., Zolensky, M.E., 1995. Mineralogical and chemical modification of components in CV3 chondrites: Nebular or asteroidal processing? Meteoritics 30, 748-775.

Lisse, C.M., VanCleve, J., Adams, A.C., A'hearn, M.F., Fernández, Y.R., Farnham, T.L., Armus, L., Grillmair, C.J., Ingalls, J., Belton, M.J.S., Groussin, O. McFadden, L.A., Meech, K.J., Schultz, P.H., Clark, B.C., Feaga, L.M., Sunshine, J.M., 2006. Spitzer spectral observations of the Deep Impact ejecta. Science 313, 635-640.

Lodders, K., 2003. Solar system abundances and condensation temperatures of the elements. The Astrophysical Journal 591, 1220.

MacPherson, G.J., Davis, A.M., 1994. Refractory inclusions in the prototypical CM chondrite, Mighei. Geochimica et Cosmochimica Acta 58, 5599-5625.

Mason, B., Taylor, S.R., 1982. Inclusions in the Allende meteorite. Smithsonian Contributions to the Earth Sciences 25, 1-30.

McKeegan, K.D. et al., 2006. Isotopic compositions of cometary matter returned by Stardust. Science 314, 1724-1728.

Millet, M.-A., Dauphas, N., 2014. Ultra-precise titanium stable isotope measurements by double-spike high resolution MC-ICP-MS. Journal of Analytical Atomic Spectrometry 29, 1444-1458.

Moynier, F., Bouvier, A., Blichert-Toft, J., Telouk, P., Gasperini, D., Albar ède, F., 2006. Europium isotopic variations in Allende CAIs and the nature of mass-dependent fractionation in the solar nebula. Geochimica et Cosmochimica Acta 70, 4287-4294.

Ozawa, K., Nagahara, H., 2001. Chemical and isotopic fractionations by evaporation and their cosmochemical implications. Geochimica et Cosmochimica Acta 65, 2171-2199.

Palme, H., Wlotzka, F., Nagel, K., El Goresy, A., 1982. An ultra-refractory inclusion from the Ornans carbonaceous chondrite. Earth and Planetary Science Letters 61, 1-12.

Pourmand, A., Dauphas, N., Ireland, T.J., 2012. A novel extraction chromatography and MC-ICP-MS technique for rapid analysis of REE, Sc and Y: Revising CI-chondrite and Post-Archean Australian Shale (PAAS) abundances. Chemical Geology 291, 38-54.

Richter, F.M., 2004. Timescales determining the degree of kinetic isotope fractionation by evaporation and condensation. Geochimica et Cosmochimica Acta 68, 4971-4992.

Richter, F.M., Davis, A.M., Ebel, D.S., Hashimoto, A., 2002. Elemental and isotopic fractionation of Type B calcium-, aluminum-rich inclusions: experiments, theoretical considerations, and constraints on their thermal evolution. Geochimica et Cosmochimica Acta 66, 521-540.

Richter, F.M., Janney, P.E., Mendybaev, R.A., Davis, A.M., Wadhwa, M., 2007. Elemental and isotopic fractionation of Type B CAI-like liquids by evaporation. Geochimica et Cosmochimica Acta 71, 5544-5564.

Shahar, A., Young, E.D., 2007. Astrophysics of CAI formation as revealed by silicon isotope LA-MC-ICPMS of an igneous CAI. Earth and Planetary Science Letters 257, 497-510.

Shen, J-S., Lee, T., 2003. ^{138}La anomaly in the early solar system. The Astrophysical Journal Letters 596, L109.

Shollenberger, Q.R., Render, J., Brennecka, G.A., 2018. Er, Yb, and Hf isotopic compositions of refractory inclusions: An integrated isotopic fingerprint of the solar system's earliest reservoir. Earth and Planetary Science Letters 495, 12-23.

Simon, J.I., Jordan, M.K., Tappa, M.J., Schauble, E.A., Kohl, I.E. and Young, E.D., 2017. Calcium and titanium isotope fractionation in refractory inclusions: tracers of condensation and inheritance in the early solar protoplanetary disk. Earth and Planetary Science Letters 472, 277-288.

Simon, S.B., Davis, A.M., Grossman, L., 1999. Origin of compact type A refractory inclusions from CV3 carbonaceous chondrites. Geochimica et Cosmochimica Acta 63, 1233-1248.

Simon, S.B., Davis, A.M., Grossman, L., 1996. A unique ultrarefractory inclusion from the Murchison meteorite. Meteoritics & Planetary Science 31, 106-115.

Simon, S.B., Grossman, L., Davis, A.M., 1991. Fassaite composition trends during crystallization of Allende Type B refractory inclusion melts. Geochimica et Cosmochimica Acta 55, 2635-2655.

Stracke, A., Palme, H., Gellissen, M., Münker, C., Kleine, T., Birbaum, K., Günther, D., Bourdon, B., Zipfel, J., 2012. Refractory element fractionation in the Allende meteorite: Implications

for solar nebula condensation and the chondritic composition of planetary bodies. Geochimica et Cosmochimica Acta 85, 114-141.

Tanaka, T., Masuda, A., 1973. Rare-earth elements in matrix, inclusions, and chondrules of the Allende meteorite. Icarus 19, 523-530.

Tang, H., Liu, M.-C., McKeegan, K.D., Tissot, F.L.H., Dauphas, N., 2017. In situ isotopic studies of the U-depleted Allende CAI Curious Marie: pre-accretionary alteration and the co-existence of 26Al and 36Cl in the early solar nebula. Geochimica et Cosmochimica Acta 207, 1-18.

Tissot, F.L.H., Dauphas, N., Grossman, L., 2016. Origin of uranium isotope variations in early solar nebula condensates. Science Advances 2, #e1501400 (7pp).

Tsuchiyama, A., Tachibana, S., Takahashi, T., 1999. Evaporation of forsterite in the primordial solar nebula; rates and accompanied isotopic fractionation. Geochimica et Cosmochimica Acta 63, 2451-2466.

Yoneda, S., Grossman, L., 1995. Condensation of CaO-MgO-Al_2O_3-SiO_2 liquids from cosmic gases. Geochimica et Cosmochimica Acta 59, 3413-3444.

Zolensky, M.E. et al., 2006. Mineralogy and petrology of comet 81P/Wild 2 nucleus samples. Science 314, 1735-1739.

6. CONCLUSION

CAIs are the oldest objects in the solar system. These ceramic-like meteoritic inclusions have recorded processes that might have shaped the compositions of the building blocks of the planets, meteorites, and other solar objects. This study provided an opportunity to re-interpret the theory of equilibrium condensation of elements from the solar nebula, a central hypothesis of cosmochemistry since 1970s that had never been tested other than through thermodynamic calculations.

Analyzing the isotopic compositions of REEs adds another dimension to the REE pattern and provides insights into various aspects including but not limited to volatility-controlled processes, redox change, nucleosynthesis and cosmic-ray exposure. However, a major problem related to the accurate isotopic measurements of individual REEs is the difficulty in the proper separation of individual REEs from each other by ion exchange chromatography since their behaviors are extremely similar during column chemistry.

I have been one of the inventors of a unique Fluoropolymer Pneumatic-actuated Liquid Chromatography (FPLC) system in the lab, which has been patented and successfully used to separate elements that are difficult to separate using conventional columns. The FPLC system is mainly composed of custom designed and machined parts. I have adapted the system to my REE work and achieved a complete separation of 8 REE isotopes for isotopic analyses.

The typical levels of stable isotopic fractionation for REEs are subtle (often on sub-‰ level) due to their relatively high mass number. I therefore developed double-spike approaches for Ce, Nd, Sm, Gd, Dy and Er to attain a precision as high as 0.03 ‰/amu. This involved extensive work

including (1) preparation of isotopic reference materials, (2) mixing and calibration of the double-spike solutions, and (3) doping tests on isobaric interferences and matrix effects for each element. Since the double-spike approach is only valid for samples that can be related with the isotopic standard through a fractionation line, I also did a mathematic derivation to obtain an analytical formula to correct the isotopic fractionation for samples with isotopic anomalies.

The analytical methods I developed were first tested by measuring a series of terrestrial igneous geostandards and a few low-temperature samples like carbonates and ferromanganese nodules, which serves to define the isotopic composition of the bulk silicate Earth (BSE). Specially, ferromanganese nodules were found to be enriched in light isotopes of cerium, suggesting change of redox state (Ce^{3+} to Ce^{4+}) during adsorption and precipitation. The isotopic fractionation has shown that Ce isotopes are sensitive to a relatively oxidizing environment, which could be used as a redox indicator in ocean environments.

The NRIXS technique provides a unique insight into Eu stable isotopic fractionation by directly measuring the strength of the chemical bonds (*i.e.*, the mean force constant), which controls the equilibrium isotopic fractionation between co-existing phases. I have analyzed a series of pure oxides, minerals and synthesized glass doped in various proportions of Eu^{2+} and Eu^{3+} using NRIXS technique, which has suggested measurable equilibrium isotopic fractionation between Eu^{2+} and Eu^{3+} at a temperature relevant to hydrothermal system. The potential stable isotopic fractionations of Eu could be used as indicator for hydrothermal redox processes such as ocean floor weathering and REE deposit formation.

Force constants of Eu oxides and synthesized glasses can only provide estimation on the level of equilibrium isotopic fractionation of Eu alone, while with Dy NRIXS study, I can estimate the equilibrium isotopic fractionation of for each REE via interpolation and extrapolation based on the force constants of Eu and Dy. The NRIXS study on pure oxides, minerals, and synthesized glasses doped with Dy has shown negligible equilibrium isotopic fractionation, suggesting that isotopes of heavy HREEs are unlikely to be fractionated by equilibrium processes, which is important for the interpretation of isotopic fractionations I found in group II CAIs.

The condensation origin of group II CAIs has been the cornerstone to support the traditional condensation sequence. I tested this scenario by analyzing 8 REEs (Ce, Nd, Sm, Eu, Gd, Dy, Er and Yb) in 7 group II CAIs, and I found quite the opposite of the expectation above. Refractory REEs displayed remarkable negative isotopic fractionations (up to 3 ‰/amu), suggesting that group II CAIs were actually formed by gas generated from kinetic evaporation of a precursor with chondritic REE composition, followed by complete condensation of REEs in the gas except for the least refractory REEs (*i.e.*, Eu and Yb). This suggests an intense, large-scale heating event at the earliest stage of the solar system formation. The timescales of REEs calculated from their depletion levels and isotopic fractionation suggest that the most likely candidates of such intense heating events are FU Orionis and EX Lupi outbursts of eruptive pre-main-sequence stars.